ABSTRACT

Title of Dissertation:	DYNAMIC MELT PROCESSES IN THE LITHOSPHERES OF MARS AND IO
	Joseph William Schools, Doctor of Philosophy, 2020
Dissertation directed by:	Professor Laurent G. J. Montési, Department of Geology

The interior structures of planetary bodies beyond the Earth are broadly unknown. Our observational capacity is largely limited to surface imagery from spacecraft. The work presented in this dissertation uses novel modeling methods of melt migration and melt focusing processes to illuminate the thermal and structural characteristics of the lithospheres of Mars and Jupiter's moon Io. Models are constrained by, and inform observations of, surface volcanism.

Coupled petrological-geodynamical models of one-dimensional melt migration are performed to determine the depth of impermeable boundaries, known as permeability barriers, in the lithosphere of Mars. Relatively deep permeability barriers are found to be prevalent throughout Martian history unless in regions of high strain rate (10^{-13} s^{-1}), or a wet mantle (25-1000 ppm H_2O). Permeability barrier depth is suggested to be linked to the style of volcanic edifice seen at the surface, with deep

barriers creating larger edifices like shield volcanoes, and shallower barriers creating widespread flows.

Similar petrological-geodynamical models performed for the lithosphere of Io reveal that permeability barriers always form at the base of the lithosphere due to the cold temperatures caused by geologically rapid resurfacing (~1 cm/yr) and subsidence. Melt may ascend closer to the surface in areas with a low subsidence rate (0.02 cm/yr)

Two-dimensional numerical models of melt migration in the Martian lithosphere suggest that convection in a highly porous layer beneath a permeability layer (a decompaction channel) focuses melt over the convective wavelength. Melt ascends in the lithosphere at this wavelength which is reflective of volcano spacing at the surface for Hesperian aged terrains.

Numerical and analytical models of melt flow through the asthenosphere and lithosphere of Io constrain the lifespan of its volcanic plumbing systems. A 1 km conduit will fully close within ~10,000 years while a 25 km conduit of melt will close within 6-7 million years. Solid convection in the asthenosphere is found to be necessary for melt focusing to heat pipe centers at the base of the lithosphere, however it is counterintuitively found that an arrangement with downwelling undeath the eruptive center is the most efficient for melt extraction.

DYNAMIC MELT PROCESSES IN THE LITHOSPHERES OF MARS AND IO

by

Joseph William Schools

Dissertation submitted to the Faculty of the Graduate School of the
University of Maryland, College Park, in partial fulfillment
of the requirements for the degree of
Doctor of Philosophy
2020

Advisory Committee:
Professor Laurent G. J. Montési, Chair
Assistant Professor Megan E. Newcombe
Research Scientist Philip M. Piccoli
Assistant Professor Nicholas C. Schmerr
Professor Wenlu Zhu
Professor Derek Richardson (Dean's Representative)

Dedication

To Mom and Dad. I guess all those trips to the libary paid off.

Acknowledgements

I must start my acknowledgments by thanking my advisor Laurent Montési. Even when you were managing six grad students at a time, teaching two classes, living in Oslo, and/or serving as the Editor-in-chief of JGR Planets, you somehow always had time to maintain an open-door policy and could turn around conference abstract edits quicker than I could refresh my email. I've only come this far due to your mentorship and I am forever grateful.

I would also like to thank the faculty and staff of the Geology department for making these last ~~five~~ six years of my life a fantastic experience. In particular I'd like to thank Todd Karwoski for his help and tolerance of my stupid questions about the Geodynamics Lab's computing cluster. Thank you to my committee members, Wenlu Zhu, Megan E. Newcombe, Philip Piccoli, Derek Richardson, and especially Nicholas Schmerr who suffered through too many letters of recommendation on my behalf.

Every visitor to our department comments on how connected our grad student community is. I would name almost every graduate student in the department from the last six years, but I've only got a few hours until I have to submit this, so here's a few highlights. Past and current members of the Geodynamics Lab: Hailong Bai, Kristel Izquierdo, Alexis Martone, Mark McAdam, Stephanie Johnston Kruckvich, Kevin Miller, Jiangyi Hou, Goeun Ha, James Bader, Karla Nunez, and Edward Williams; a few good friends: Erin Cunningham, Willy Nicklas, Al Greaney, and Scott Wipperfurth; a few awful roommates: Kayleigh Harvey, Rebecca Butcher, Jonathan Guandique, Rahbert Nicklas, Jack Hollingsworth, Phillip Goodling; the

loves of my life: Angela Marusiak and Wallie Nicklas; and the very good dogs of the department: Erebos, Roxy, Khari, Willie Nicklas, Roxy, Limon, and many others.

I would like to thank my family, Grandma Schools and Uncle Frank who welcomed me into the family with open arms, my brothers who replaced me at home, and finally my parents: the mom who fought for me and the dad who chose me. (Do I get on the mantel now?)

As for the science: The Mars projects presented in this dissertation were supported by NASA Grant NNX14AG51G. The Io projects were supported by a NASA Earth and Space Science Fellowship, Grant 80NSSC17K0486.

The work presented here is possible due to the development of codes and software by folks with a lot more mathematical and programming knowledge than me. I would specifically like to thank the primary developers of ASPECT, Wolfgang Bangerth, Juliane Dannberg, Rene Gassmoeller, and Timo Heister for their development undertaking, as well as thoughtful conversations at two of the ASPECT Hackathons and at conferences. ASPECT itself is hosted by the Computational Infrastructure for Geodynamics (CIG) which is supported by the National Science Foundation award EAR-1550901.

As Chapter 2 is adapted from a published manuscript, I wish to thank Editor David Baratoux, reviewer John Rudge, and an anonymous reviewer for their constructive comments, as well as Steven A. Hauck II for sharing the model data of *Hauck and Phillips* [2002] and Justin Filiberto for correspondence on the water content of the Martian mantle.

Table of Contents

List of Tables

List of Figures

Chapter 1: Introduction: Volcanism as a Window to Planetary Interiors

1.1 Introduction

The interior structure of planetary bodies besides the Earth is largely a mystery. This dissertation focuses on constraining the thermal and structural characteristics of the lithospheres of Mars and Jupiter's moon Io (Figure 1.1), through petrological and geodynamic models of silicate melt transport. By linking the modeling results with simple surface observations, such as the morphology and distribution of surface volcanism, constraints can be made on planetary interiors in the absence of complex seismic networks or high-resolution gravity data, as on the Earth.

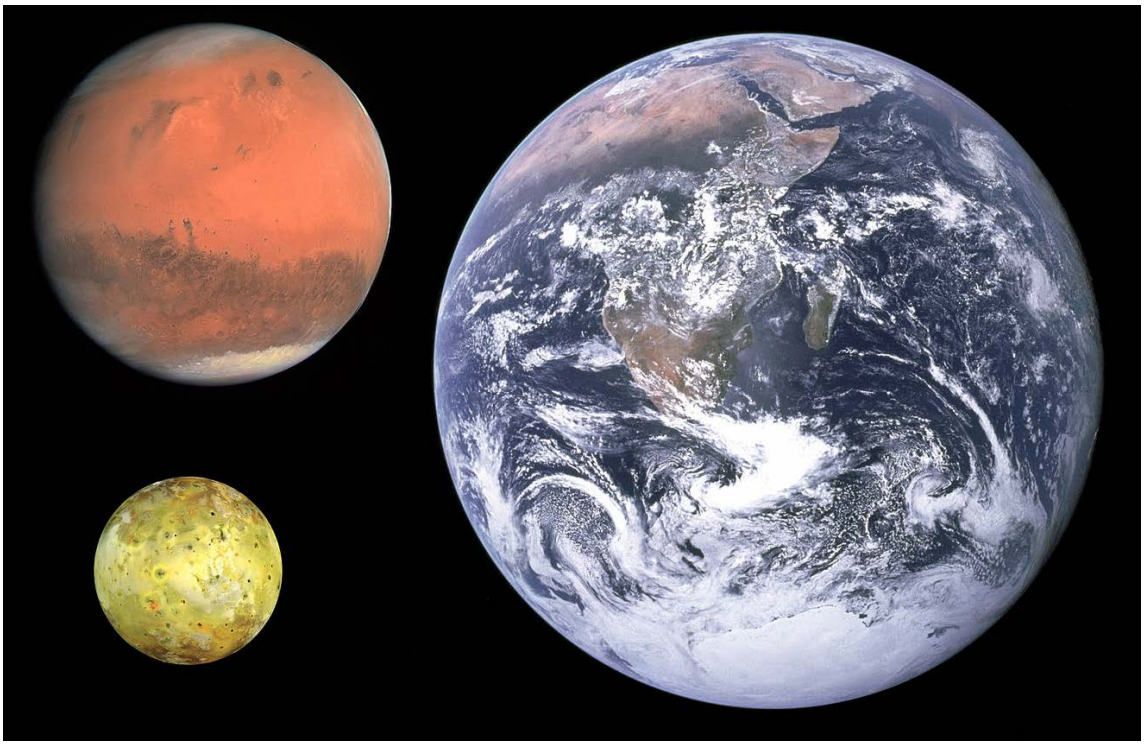

Figure 1.1 - Earth, Mars, and Io to scale [*NASA/ESA/JPL/University of Arizona*]

1.2 Limitations to the Exploration of Planetary Interiors

On the Earth, a large number and density of seismometers allow for relatively detailed constraints to be placed on the interior physical and thermal structure of the planet, both at global scales [e.g. *Dziewonski and Anderson*, 1981; *Rawlinson et al*., 2010] and regional scales such as the Cascadia Initiative [*Toomey et al.,* 2014] and the AlpArray Seismic Network [*Hetényi et al.,* 2018]. Planetary missions such as the Apollo program, NASA's InSight lander, and the Soviet Venera landers have also allowed for limited seismological exploration of the Moon [*Garcia et al.,* 2019], Mars [*Banerdt et al.,* 2020; *Lognonné et al.,* 2020], and Venus [*Ksanfomaliti et al.,* 1982] respectively. Despite the success of these missions, each comes with restrictions in observational duration, regional coverage, and data resolution. Due to the complex logistics and extreme costs of missions involving seismic networks, alternative techniques must be used to peer inside the other bodies in our solar system.

Interior structure can also be determined via gravitational field mapping by orbiting spacecraft such as the GRAIL mission around Earth's moon [*Zuber et al*., 2013]. This method has yielded otherwise inaccessible constraints on the composition and structure of the lunar crust [*Wieczorek et al.,* 2013], with the potential for observing deeper structures [*James et al.*, 2019; *Izquierdo et al.,* 2020]. Due to atmospheric drag, high resolution gravity is unfortunately limited to airless bodies, reducing its usefulness for the study of planets such as Mars and Venus. The intense radiation environment around Jupiter prevents long-duration orbital missions that would be necessary to probe in detail the gravity field of other large bodies of interest

such as Io. Thus, with the exception of the Moon, gravity data is of limited use for interrogating lithosphere scale processes associated with surface geological activity

1.3 Modeling as a Tool for Constraining Planetary Interiors

In the absence of complex seismic networks or high-resolution gravity data, as on the Earth or the moon, the most robust scientific option left is modeling based on physical and chemical principles. Specifically, by linking the results of numerical and analytical modeling of interior processes with orbital observations of surficial features, such as spectroscopy, radar, and simple visual imagery, constraints can be made on the geological processes active in planetary interiors.

Geodynamic modeling methods also allow for insights beyond geophysical measurements. Geophysical observations such as seismological and gravitational measurements are essentially snapshots of large-scale conditions in the present day. The models presented in this dissertation interrogate the evolution of planetary interiors through time and constrain the past interior structure. The models also involve processes occurring at the scale of mineral grains, much smaller than observable with geophysical imaging.

The focus of this dissertation is on the structure of planetary lithospheres. The term “lithosphere” originates from *Barrell* [1914] and describes the outermost rigid shell of a planetary body, which overlies a weak, ductile mechanical layer called the “asthenosphere”. On the Earth, the lithosphere consists of the crust and upper mantle, under which exists the convecting mantle, or asthenosphere. The concept of the lithosphere can be further refined into two types: the thermal lithosphere and the elastic lithosphere [*Turcotte and Schubert,* 2014]. The thickness of the thermal

lithosphere is primarily related to the temperature profile of planetary body, with the lithosphere-asthenosphere boundary associated with a brittle ductile transition at some isotherm. The elastic lithosphere refers to the thickness which bends when subjected to a load at the surface. This dissertation primarily deals with the thermal lithosphere.

Previous studies have modeled and constrained the structure of the lithospheres of planetary bodies using a variety of modeling and observational techniques. Beyond seismic and gravity data, geophysical techniques include measuring flexural signals of larges masses on planetary lithospheres [e.g. *Solomon and Head,* 1982; *McGovern et al.,* 2002; *Taylor et al.,* 2020], examinations of stress state due to horizontal compression [*Montési and Zuber*, 2003*; Bland and MicKinnon*, 2016], observing volcanic output to constrain resurfacing rates as a mechanism for lithosphere recycling [e.g. *O'Reilly and Davies,* 1981], and thermal evolution modeling [e.g. *Hauck and Phillips*, 2002; *Nimmo*, 2002].

A relatively recent development is the ability to model the generation, migration, and crystallization of melt through planetary interiors. Melt is the liquid generated by melting solid rock. The generation of melt, or melting, occurs when the temperature of the solid rock surpasses a compositionally dependent temperature known as the solidus temperature, at a set pressure. The initially solid rock fully melts (100% liquid) at a higher temperature known as the liquidus. On the modern Earth, melting is limited to regions which possess one or more of the following conditions [*Wilson*, 2007]:

1) The temperatures are elevated for a given pressure. In this simple case, regions with higher temperatures surpass the solidus, and melting occurs. On the Earth, this partially accounts for melting associated with mantle plumes.
2) Pressures are lower for a given temperature. In regions where the hot mantle is relatively close to the surface, such as terrestrial mid-ocean ridges, the reduced pressures allow for melting to initiate at relatively low temperatures.
3) Volatiles are included in the composition. Volatiles such as water lower the solidus compared to a volatile free composition. Regions with higher water contents, such as above subducting plates on Earth, melt at lower temperatures than surrounding material, creating arc volcanism.

For petrological modeling, the MELTS thermodynamic calculator was released to the scientific community at large in 1995 [*Ghiorso and Sack*, 1995]. However, ongoing development from 2005 resulted in the alphaMELTS calculator [*Smith and Asimow*, 2005; *Thompson et al., 2007*; *Antoshechkina and Asimow*, 2010; *Antoshechkina et al*., 2010] which allows for an unlimited number calculations to be looped and integrated into simple geodynamic models [Chapter 2 of this dissertation; *Schools and Montési,* 2018]. The increasing availability of high-performance computing and the development of new finite element packages such as ASPECT [*Kronbichler et al.,* 2012; *Heister et al.,* 2017] have also allowed for numerical modeling of melt migration in viscously deforming solids in planetary interiors [*Dannberg and Heister*, 2016; *Dannberg et al.,* 2019]. The research presented in this

dissertation focuses on modeling melt migration processes in planetary lithospheres, using these recent hardware and software developments, constrained by surface imagery of volcanic terrains. Specifically, petrological and numerical models representing melt migration in the lithosphere and asthenosphere of Mars and Jupiter's moon Io are performed.

The melt migration modeling presented here builds on many similar Earth-based projects. The compaction physics which are central to all my dissertation chapters were derived in *McKenzie* [1984] and subsequently adapted for a variety of modeling efforts. Much effort has focused on melt migration at mid-ocean ridges (Figure 1.2), starting with *Sparks and Parmentier* [1991], who proposed a semi-analytical model of melt rich channels formation under impermeable cold boundaries which focus melts from large areas to the ridge axis. Evolutions of this modeling have produced various modeling efforts including integrated geodynamical-petrological models *[Hebert and Montési*, 2010] and numerical models [*Bai et al.,* 2017; *Keller et al.,* 2017] each providing new insights or explaining unique features such as ultraslow spreading ridges [*Montési and Behn*, 2007] and the relation between ridge segmentation and crustal thickness [*Montési et al.,* 2011; *Bai et al.,* 2015]. Modeling these processes at mid-ocean ridges has the benefit of observational confirmations, as the geological evidence of impermeable melt boundaries at the crust-mantle transition of ophiolites [*Ceuleneer and Rabinowicz*, 1992; *Kelemen and Aharonov*, 1998; *Korenaga and Kelemen*, 1997].

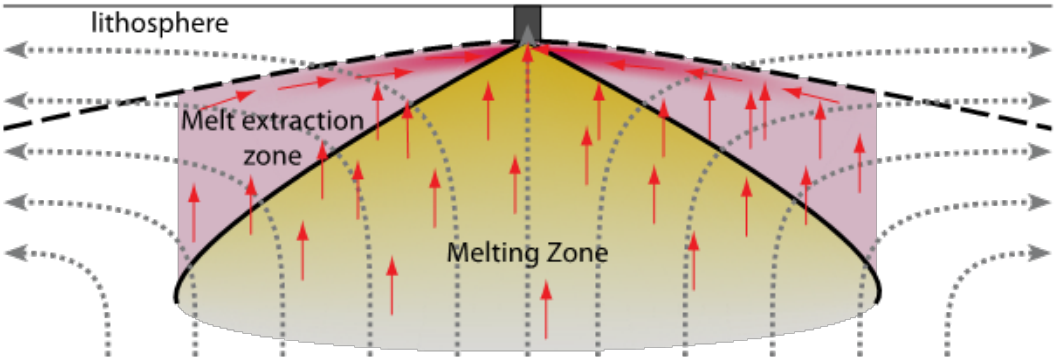

Figure 1.2 - Schematic illustration showing melt focusing processes in a mid-ocean ridge. Melt is produced in the melting zone (yellow shading) and rises buoyantly (red arrows) into the base of the lithosphere. Here they crystallize, potentially forming a permeability barrier (black dashed line). Melts migrate along the permeability layer, following the sloped basal topography, to the ridge axis where they can be erupted. Pink-red shading represents permeability in the melt extraction zone, where the deepest red is a porosity maximum representing a decompaction channel. Dotted gray arrows represent the solid flow streamlines. [*Hebert and Montési*, 2010]

Other efforts have looked at melt focusing at subduction zones [*England and Katz*, 2010; *Ha et al*., in prep], the chemical evolution of mantle plumes [*Dannberg and Gassmöeller*, 2018], and dike generation at the lithosphere-asthenosphere boundary [*Havlin et al*., 2013; *Cai and Bercovici*, 2016]. Ongoing experimental efforts on terrestrial samples also provides critical information on the transport property of partially molten samples, which is parameterized into modeling efforts [*Miller et al.,* 2014]. At the depths of interest in this dissertation, which corresponds to the base of the lithosphere, solid minerals are expected to be in textural equilibrium with melt. Thus, the melt is present in networks of tubules and pores that follow grain edges (Figure 1.3) [e.g. *von Bargen and Waff*, 1986; *Zhu et al.,* 2011].

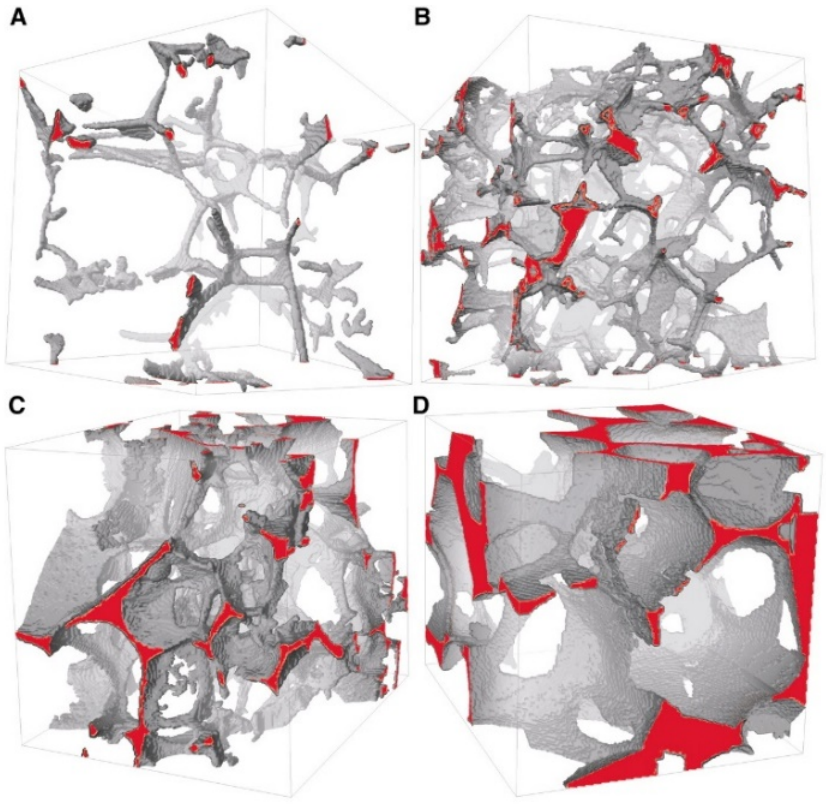

Figure 1.3 - Volume renderings of melt distribution in olivine-basalt samples equilibrated at 1350°C and 1.5 GPa, then imaged by Synchrotron X-ray microtomography. Sample melt fractions are (A) 0.02, (B) 0.05, (C) 0.10, and (D) 0.20. Gray represents the melt phase, empty space represents the solid olivine grains, and red represents the intersection of melt regions and the bounds of the box. From [*Zhu et al.,* 2011]. Reprinted with permission from AAAS.

1.4 Volcanism on Mars

One of the defining features of Mars is the Tharsis Bulge, a topographic rise accounting for one quarter of the surface of the planet (Figure 1.4) [*Carr,* 1974; *Wise et al*., 1978]. This region is home to Olympus Mons, the largest volcano by volume in the solar system at almost 22 km tall and encompassing an area of 840 x 640 km [*Plescia*, 2004]. The Tharsis region also contains Alba Patera, a massive low relief shield volcano larger in area than Olympus Mons [*Ivanov and Head*, 2006], and the three Tharsis Montes (Arsia, Pavonis, and Ascraeus Mons), each significantly larger

than any Earth volcano [*Crumpler and Aubele*, 1978; *Zimbelman and Edgett,* 1992]. Several other shield volcanoes exist on the Tharsis Bulge, possibly partially buried by subsequent lava flow, so their true dimensions are unknown [*Plescia and Saunders*, 1979; *Montési*, 2001; *Plescia*, 2004]. A second cluster of four large shield volcanoes exists in the Elysium region of Mars [*Mouginis-Mark et al.,* 1984; *Plescia*, 2004].

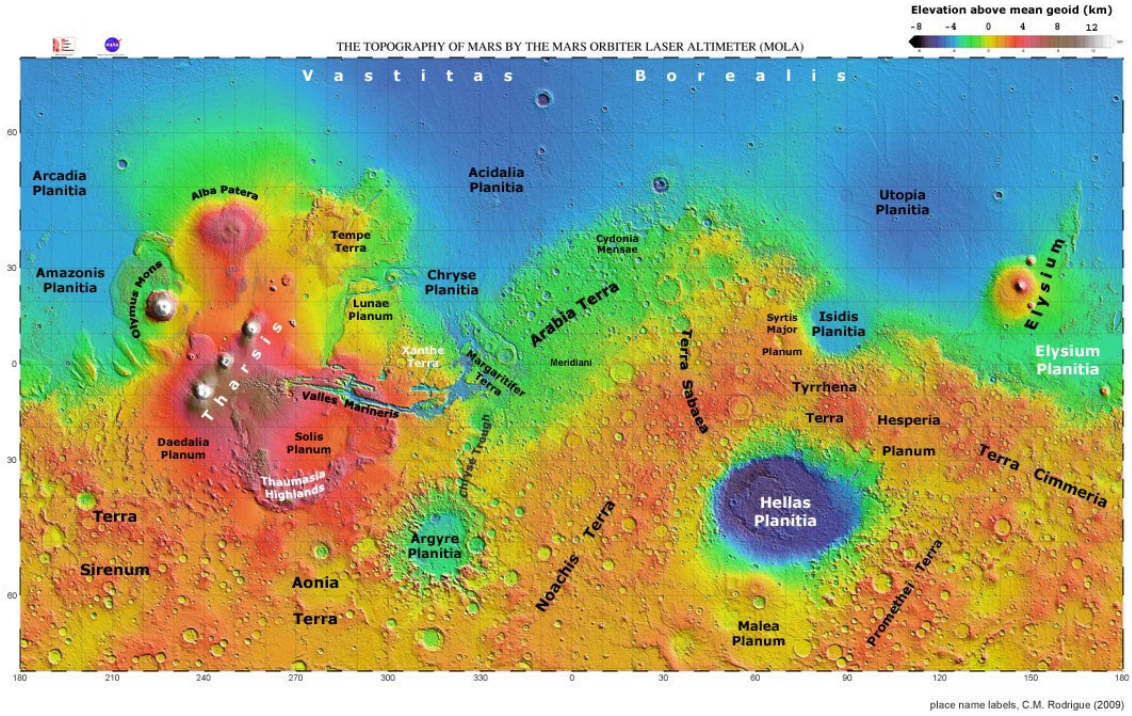

Figure 1.4 - Topographic map of the surface of Mars. Areas of relevance to this project are the Tharsis Rise, taking up most of the western hemisphere, and the Elysium region to the east. [Map: *MOLA Science Team/NASA Goddard*; Labels: *Rodrigue*, 2009]

Beyond the large shield volcanoes, Mars also features many large-scale volcanic flows. The majority of the surface of Mars consists of volcanic flows, although covered in craters and sediment (Figure 1.5) [*Head et al.,* 2002; *Hiesinger and Head,* 2004; *Schaber,* 1982; *Tanaka et al.,* 2014; *Williams et al.,* 2009]. According to crater counting, most surface flows appear to have been emplaced between 3.7 and 3.0 Ga [*Carr and Head*, 2010; *Greeley and Spudis,* 1981; *Werner,*

2009]. This period appears to represent a global transition, as early volcanism on Mars was widespread and produced a variety of edifice types [*Carr,* 1973; *Carr et al.,* 1977; *Plescia and Saunders,* 1979; *Williams et al*., 2009; *Xiao et al.,* 2012], while later volcanism appears limited to possible episodic eruptions of the large shield volcanoes of the Tharsis Bulge [*Hauber et al.,* 2011; *Werner, 2009*; *Wilson et al.,* 2001].

Based on the shield morphology of major edifices and the presence of fluid lava flows and lava channels, most of Martian volcanism is assumed to be basaltic [*Greeley,* 1973; *Zimbelman,* 1985; *Mouginis-Mark and Yoshioka*, 1998; *Greeley et al.,* 2000, 2005; *Garry et al.,* 2007; *Jaeger et al.,* 2007; *Vaucher et al.*, 2009]. The lava flow morphology on the flanks of major edifices suggests basaltic to andesitic compositions [*Hulme*, 1976; *Moore et al.,* 1978; *Zimbelman*, 1985; *Cattermole*, 1987; *Warner and Gregg*, 2003; *Baloga et al*., 2003; *Glaze et al.,* 2003; *Hiesinger et al.,* 2007; *Baptista et al.,* 2008*; Baratoux et al*., 2009; *Pasckert et al.,* 2012].

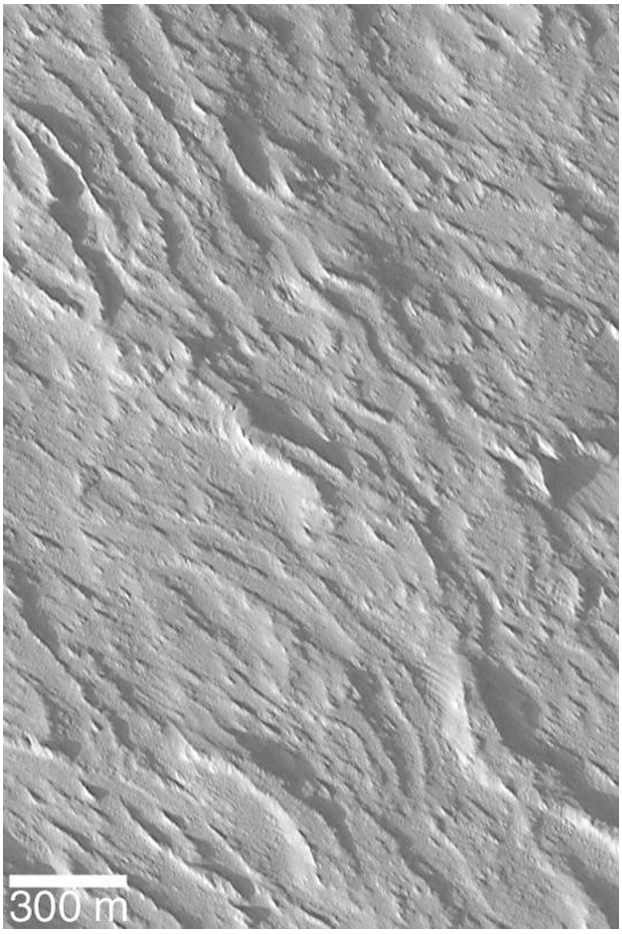

Figure 1.5 - Overlapping lava flows on the western flank of Olympus Mons. [NASA/JPL/Malin Space Science Systems, PhotoID: PIA04583]

These estimates are consistent with remote sensing data [*Bandfield et al.,* 2000*; Hamilton et al.,* 2001; *Wyatt and McSween,* 2002; *Wyatt et al.,* 2004], laboratory analysis of Martian meteorite composition [*Longhi*, 1990; *McSween*, 1985; 1994], and in-situ measurements of volcanic rocks [*Rieder et al*., 1997; *McSween et al.*, 1999, 2004*; Greeley et al.,* 2005].

The apparent prevalence of mafic compositions in Martian lavas suggest that the likely origin of melting is a combination of plume activity and decompression melting in the Martian mantle. As Mars lacks evidence of plate tectonics, more evolved compositions may be the result of fractional crystallization in magma chambers.

The Mars portions of this dissertation are focused on identifying a link between melt processes at depth in the lithosphere with the surface expression of volcanism through time, as related to the cooling of the planet. Specifically, we focus on the evolution of Martian volcanoes from the large, ancient, singular shield volcanoes of Tharsis and Elysium to the smaller vent fields and expansive lava flows of younger Mars. We also link model results to the spacing of volcanoes at the surface to determine the structure of the lithosphere during volcano emplacement.

1.5 Volcanism on Io

Io is the smallest and innermost of the Galilean moons of Jupiter (Figure 1.6) [*Galilei,* 1610]. Due to a mean motion resonance with the other moons of Jupiter [*de Sitter*, 1928], Io is tidally heated with enough intensity to partially melt its silicate interior [*Peale et al.,* 1979; *Khurana et al.,* 2011]. This constant heating and melting makes Io the most volcanically active body in the solar system The entirety of the surface of Io is made of emplaced volcanic flows, uplifted volcanic flows, and eruption debris, and has no observable impact craters. [*Hanel et al.,* 1979; *Morabito et al.,* 1979; *Smith et al.,* 1979; *McEwen et al.,* 1998; *Davies,* 2007]. It is estimated that the average resurfacing rate for the moon is ~1 cm/year, mostly from lava flows [*Johnson et al*., 1979; *Blaney et al*., 1995*; McEwen et al.,* 2004]. At this rate it takes only 10^6 years to bury the entire surface of Io to a depth of 10 km [*Turtle et al.,* 2007].

Figure 1.6 - An active eruption from Pilan Patera on Io. [*NASA/JPL/University of Arizona,* PhotoID: PIA01081]

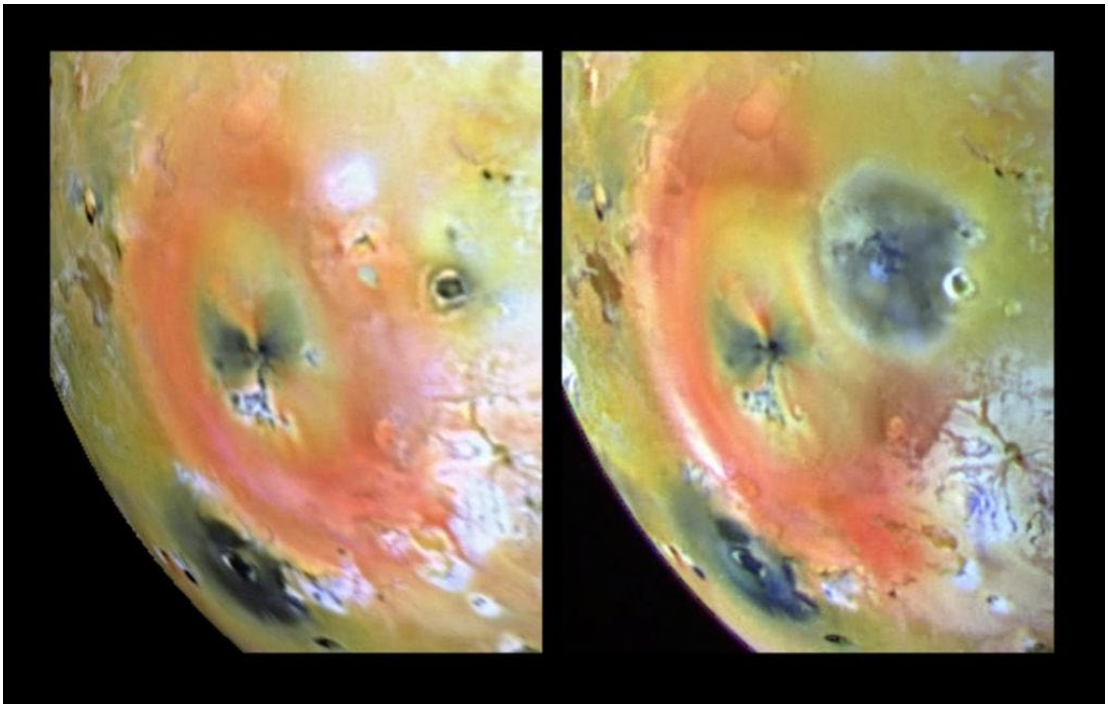

Figure 1.7 - Eruption of Pilan Patera Left image taken April 1997, right taken September 1997. The new dark spot is approximately 400 km in diameter. [*NASA/JPL/University of Arizona,* PhotoID: PIA00744]

Currently the expression of volcanism on Io is represented by 173 thermal anomaly hotspots, and 423 paterae [*Hamilton et al.,* 2013]. The thermal anomaly hot spots represent active areas of active volcanism. A patera (Figure 1.7), the singular form of paterae, is a shallow semicircular feature that is the surface expression of collapsed magma chamber [*Keszthelyi et al.,* 2004]. The identified paterae represent the past million years of volcanic history on Io. Hot spot location, as determined by infrared spectrography, corresponds to currently active paterae. One such currently active unit is Loki Patera, which is an active, 202 km diameter lava lake [*Rathbun et al.,* 2002]. Observations of Io's volcanic activity are obtained from spacecraft flybys, initially from the Voyager 1 infrared spectrometer [*Hanel et al.,* 1979] and later sustained observations from the Galileo spacecraft orbiting Jupiter [*McEwan et al.,*

1998]. Ground and space telescopes have provided regular observation of volcanic activity over the last 30 years [e.g. *Veeder et al*., 1994; *Rathbun and Spencer*, 2006; *de Pater* et al., 2017]. Decades of consistent records of volcanic activity may suggest a periodicity [~470 days] of volcanic eruptions at Loki Patera [*de Kleer et al.,* 2019].

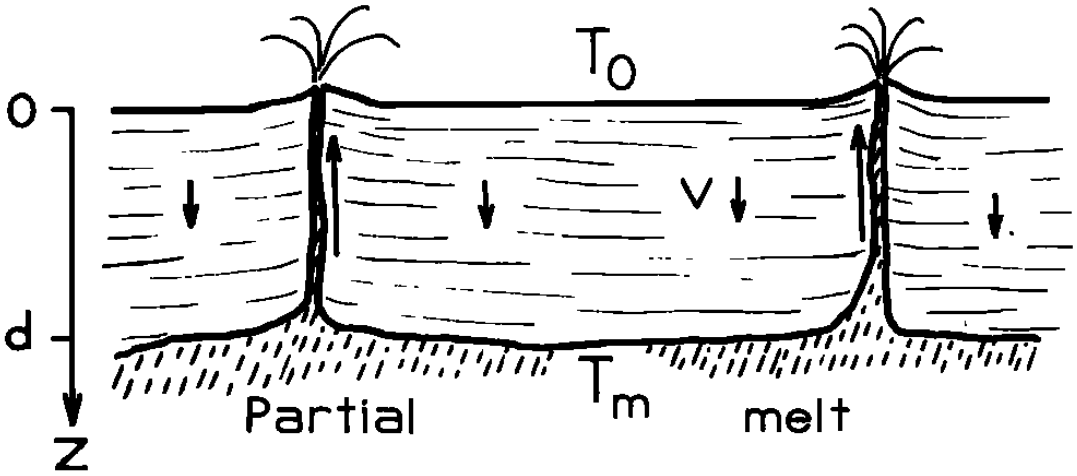

Figure 1.8 – Heat pipe model of the Ionian lithosphere. Magma of temperature T_m rises through the heat pipe and is erupted onto the surface. As it deposits on the surface, it cools to T_0 and is buried by subsequent flows and eruptions, resulting in a subsidence velocity, or resurfacing rate, of v. From *O'Reilly and Davies* [1981].

A recent estimate of average heat flow from the surface of Io is 2.24±0.45 W/m^2 [*Davies et al.,* 2015], which is about 20 times higher than the Earth's [*Turcotte and Schubert, 2014*]. Heat in Io is lost predominantly by advection through ascending magma in heat pipes rather than conduction through the lithosphere (Figure 1.8) [*O'Reilly and Davies,* 1981; *McEwen et al.,* 2004]. This large heat flow and long history of tidal heating have had significant effects on the interior structure and composition of the Jovian moon. Io has the smallest moment of inertia of any body in the solar system, ~0.377, suggesting that it is very well differentiated into separated layers [*Anderson et al.,* 2001]. Moment of inertia is a measure of an object's resistance to a change in angular velocity, which can be calculated from mass and

gravity, and informs us about the interior density structure. The mean density is 3528 kg/m^3, much higher than other satellites in the outer solar system [*Anderson et al.,* 2001]. This means that Io has been significantly heated over its history so that it kept molten enough to completely differentiate into distinct layers and to lose most of its water. Both traits tie Io more to the silicate planets than the satellites of the outer solar system, which are primarily water ice. Based on eruption temperature, tidal flexure calculations and, induced magnetic field measurements, Io is believed to have a significant "magma ocean" reservoir of 20 to 30% melt, ~50 km thick underneath the entirety of the surface [*Keszthelyi and McEwen*, 1997; *Keszthelyi et al., 2007*; *Khurana et al.,* 2011; *Spencer et al.,* 2020].

In addition to the volcanic features, Io possesses many nonvolcanic mountains, some of which exceed 18 km in height [*Schenk et al.,* 2001; *Turtle et al.,* 2001]. The mountains are not correlated with hot spots [*Carr et al.,* 1998] and dwarf most volcanoes on the planet, all of which have less than 3 km relief [*Schenk et al.,* 2004]. Mountains and volcanoes on Io actually appear to be anticorrelated, meaning the mountains exist further away from the volcanic centers than if they were randomly distributed [*Schenk et al.,* 2001; *Kirchoff et al.,* 2011]. Despite this anticorrelation, the rapid resurfacing rate due to volcanic output of Io is thought to cause the creation of the mountains. The resulting subsidence creates excessive compressive stresses in the lithosphere, which creates mountain building thrust faults [*Schenk and Bulmer*, 1998; *Jaeger et al.,* 2003; *Kirchoff and McKinnon*, 2009; *Bland and McKinnon,* 2016].

The portions of this dissertation that deal with Io focus on how melt in the interior of Io interacts with heat pipes in the lithosphere in order to form the active volcanism observed on the surface. This includes melt intrusion to the base of the lithosphere which may initiate heat pipes, the closure of heat pipes due to freezing and crystallization of melt, and convective processes in the asthenosphere to focus melt to heat pipes.

1.6 Modeling Projects Presented in this Dissertation

There are four main projects presented in this dissertation. In Chapter 2, an integrated petrological-geodynamical model of melt migration in one-dimension is used to determine likely horizons of melt accumulation in the Martian lithosphere through time. The depths of these horizons are linked to the types of volcanic edifices produced on the surface of Mars through time. Chapter 3 utilizes a similar methodology as Chapter 2 but focuses on the depth of melt accumulation in the lithosphere of Io and how it varies with volcanic resurfacing. This accumulation is linked to the creation of new heat pipes in the lithosphere of Io. Chapter 4 uses numerical modeling involving two-phase flow to show the probability of convecting channels of melt in the lithosphere of Mars, and how surface spacing of volcanoes is linked to the wavelength of convection. Chapter 5 also uses numerical modeling of solid and melt flow to constrain the lifespan of heat pipes in the Ionian lithosphere and reveals the most efficient pattern of asthenosphere convection for melt extraction.

Chapter 2: The Generation of Barriers to Melt Ascent in the Martian Lithosphere

This chapter has been published as:

Schools, J. W., & Montési, L. G. (2018). The generation of barriers to melt ascent in the Martian lithosphere. *Journal of Geophysical Research: Planets*, *123*(1), 47-66. https://doi.org/10.1002/2017JE005396

Abstract

Planetary mantles can be regarded as an aggregate of two phases: a solid, porous matrix and a liquid melt. Melt travels rapidly upwards through the matrix due to its buoyancy. When this melt enters the colder lithosphere it begins to crystallize. If crystallization happens at a high rate, the newly formed crystals can clog the pore space, reducing its permeability to essentially zero. This zone of zero permeability is the permeability barrier. We use the MELTS family of thermodynamic calculators to determine melt compositions and the crystallization sequence of ascending melt throughout Martian history and simulate the formation of permeability barriers. At lower strain rates (10^{-17} – 10^{-15} s^{-1}) permeability barriers form deep in the lithosphere, possibly contributing to the formation of localized volcanic edifices on the Martian surface once fracturing or thermal erosion enables melt to traverse the lithosphere. Higher strain rates (10^{-13} s^{-1}) yield shallower permeability barriers, perhaps producing extensive lava flows. Permeability barrier formation is investigated using an anhydrous mantle source or mantle sources that include up to 1000 ppm H_2O. Introducing even small amounts of water (25 ppm H_2O) reduces mantle viscosity in a manner similar to increasing the strain rate, and results in a shallower barrier than in

the anhydrous case. Large amounts of water (1000 ppm H_2O) yield very shallow weak barriers or no barriers at all. The depth of the permeability barrier has evolved through time, likely resulting in a progression in the style of surface volcanism from widespread flows to massive, singular volcanoes.

2.1 Introduction

The three massive Tharsis Montes were the first features of Mars observed by the Mariner 9 orbiter in 1971 [*McCauley et al*., 1972]. Large volcanoes, like the Tharsis Montes, are concentrated in two main provinces: the extensive Tharsis Rise and the smaller Elysium province. Smaller edifices in these regions are likely the exposed summits of partially buried, large volcanoes [*Plescia and Saunders*, 1979; *Montési*, 2001]. In addition to volcanic edifices, Mars also features many large-scale volcanic flows. Most of the surface of the planet is probably composed of volcanic flows, although covered by sediment in many places, especially in the northern hemisphere [*Schaber*, 1982; *Head et al*., 2002; *Hiesinger and Head*, 2004; *Williams et al*., 2009; *Tanaka et al*., 2014]. Based on crater counts, the bulk of surface flows were emplaced in the Hesperian (3.7 – 3.0 Ga), a period that marks a transition in volcanic intensity [*Greeley and Spudis*, 1981; *Werner*, 2009; *Carr and Head*, 2010]. Early volcanism on Mars was widespread and produced a variety of edifice types [*Carr*, 1973; *Carr et al*., 1977; *Plescia and Saunders*, 1979; *Williams et al*., 2009; *Xiao et al*., 2012]. However, later volcanism appears limited to just the large shield volcanoes of the Tharsis Rise and was possibly episodic in nature [*Wilson et al*., 2001; *Werner*, 2009; *Hauber et al*., 2011]. Here we hypothesize that the transition of volcanic style from a variety of edifices to volcanic flows to shield building may have

been induced by a change in the depth at which ascending melts may stall in the Martian lithosphere.

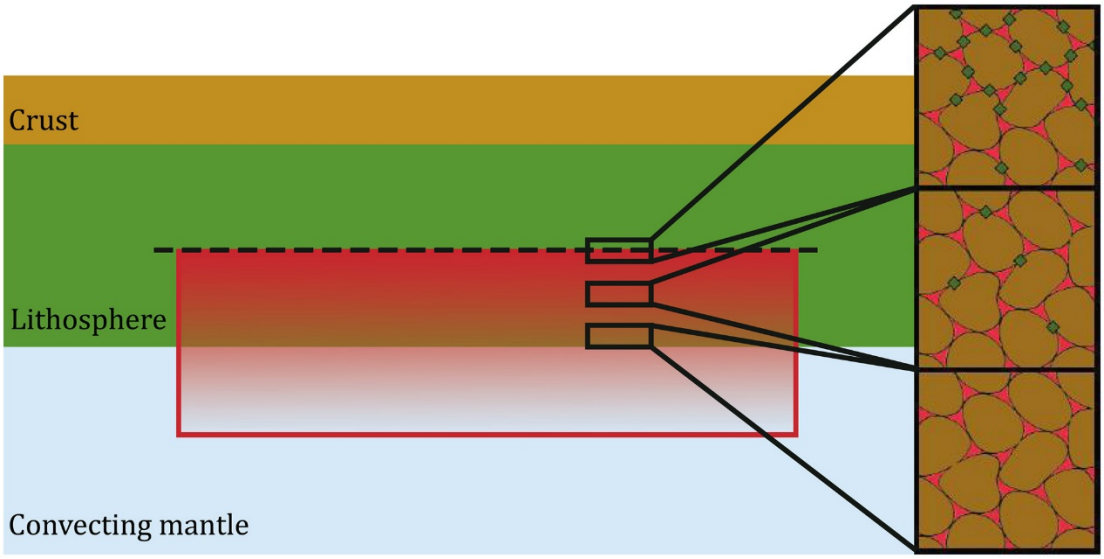

Figure 2.1 -Schematic diagram of permeability barrier formation. Melt (red box) produced in the convecting mantle (blue) percolates up through the lithospheric mantle (green). This melt crystallizes as it cools, eventually reaching a crystallization rate sufficiently high for all melt pathways to close (insets). This is the level of the permeability barrier (thick dashed black line). Subsequent melt cannot rise past this barrier. Figure not to scale.

Permeability barriers are a natural consequence of magma rising upward into the lithosphere. The sub-lithospheric mantle is often considered as an aggregate of two phases: a solid, porous matrix and a liquid melt [*McKenzie*, 1984; *Bercovici et al*., 2001]. Recent studies of partially molten aggregates have imaged the topology of pore networks in which melt resides in three dimensions [*Zhu et al*., 2011] and concluded that melt easily travels upwards through the matrix due to its buoyancy [*Miller et al.,* 2014]. When this melt enters the colder lithosphere, it begins to crystallize. If the crystallization happens a high rate, the newly formed crystals can clog the pore space, reducing its permeability to essentially zero [*Korenaga and*

Kelemen, 1997; Figure 2.1]. This zone of zero permeability is the permeability barrier.

The concept of a permeability barrier was introduced by *Sparks and Parmentier* [1991] to explain the observation that magma is produced over a wide area (hundreds of kilometers) under mid-ocean ridges but only reaches the surface within 2 km of the ridge axis [*Detrick et al*., 1987, *Vera et al*., 1990]. Melt must be focused to the ridge and the permeability barrier provides a way to explain that focusing. A lack of significant horizontal pressure gradient makes it difficult to explain how melt can travel laterally over long distances toward the ridge axis [*e.g.*, *Spiegelman,* 1993; *Kelemen et al.,* 1997]. The permeability barrier model of *Sparks and Parmentier* [1991] solves this problem by placing a thermally controlled cap on the system and forcing the melt to travel along the sloping permeability barrier towards the ridge axis. Possible geological evidence for permeability barriers has been reported at the crust-mantle transition zone of the Oman ophiolite [*Ceuleneer and Rabinowicz*, 1992; *Korenaga and Kelemen*, 1997; *Kelemen and Aharonov*, 1998]

Previous studies of permeability barriers were conducted in the context of the Earth's magmatism and plate motions, specifically mid-ocean ridges and seafloor crustal evolution [*Sparks and Parmentier*, 1991; *Spiegelman*, 1993; *Magde and Sparks,* 1997; *Magde et al.,* 1997; *Kelemen and Aharonov,* 1998; *Hebert and Montési*, 2010, 2011; *Weatherley and Katz*, 2010; *Montési et al.,* 2011; *Bai and Montési*, 2015]. In this setting, the depth of the permeability barrier is related to the thickness of the oceanic lithosphere. As the lithosphere cools and thickens over time as it moves away from the ridge axis, the permeability barrier in most terrestrial

tectonic settings is likely sloped. Permeability barriers may also form in subduction zones [*Rondenay et al.*, 2010; *England and Katz*, 2010] where they are also likely associated with a significant slope due to the complex mantle flow and temperature variations in this setting. By contrast, Mars and other planets do not display significant plate movement; therefore, permeability barriers in other planetary lithospheres would be essentially horizontal. Focusing of melt to volcanic centers must operate under a different process than on the Earth. This work is the first to look at the development of a permeability barrier outside the context of plate boundaries. The methods developed here may be applicable to other planetary bodies, including the Earth in relation to plume related processes or volcanic vent fields.

We report here on models of permeability barrier development where we determine the crystallization sequence and crystallization rate of melts that rise through the Martian lithosphere and cool progressively during their ascent. The depth at which a permeability barrier forms is reported as a function of mantle potential temperature and lithospheric thickness assuming various water contents in the mantle and various strain rates in the lithosphere. The results are discussed in term of potential surface volcanic activity and linked to the thermal and geological history of the planet.

2.2 Methods

The primary goal of this project is to determine under what conditions permeability barriers form in the Martian lithosphere. Modifying the technique of *Hebert and Montési* [2010], we used the MELTS [*Ghiorso and Sack*, 1995; *Asimow*

and Ghiorso, 1998], pMELTS [*Ghiorso et al*., 2002], and phMELTS [*Asimow et al*., 2004] thermodynamic calculators with the alphaMELTS front-end interface [*Smith and Asimow*, 2005] to determine melt compositions and the crystallization sequence of melts ascending along a pressure-temperature path that represents the structure of the upper mantle at different times throughout Martian history.

The MELTS family of algorithms calculates equilibrium mineral assemblages based on a minimization of Gibbs free energy [*Ghiorso and Sacks*, 1995]. pMELTS is required to perform calculations at pressures greater than 3 GPa [*Ghiorso et al*., 2002], which is desirable to calculate initial decompression melts on Mars. MELTS is optimized for calculations at pressures of 3 GPa or less and is found to be sufficient to cover the majority of crystallization cases for Mars. phMELTS, which consider the storage of water in nominally anhydrous minerals [*Asimow et al*., 2004], is used in models involving high concentrations of water. The alphaMELTS front-end interface allows for scripted loops of MELTS calculations, so that the calculation of thousands of MELTS runs can be automatized [*Smith and Asimow*, 2005].

MELTS and pMELTS were not designed for Martian application and were calibrated using experiments involving terrestrial basaltic and peridotitic compositions. *El Maarry et al.* [2009] compared pMELTS calculations involving the bulk silicate Mars composition of *Dreibus and Wänke* [1985] to experimental results involving the same composition [*Bertka and Holloway*, 1994]. That work concluded that pMELTS adequately replicated oxide composition trends, especially SiO_2, FeO, CaO, and Al_2O_3, with the caveat that the absolute value of the oxide in the liquid may need a small correction factor (< 3 wt.% for SiO_2 and FeO). *Balta and McSween*

[2013] performed a more detailed study, focusing on the replication of parental melt crystallization paths of Martian meteorites. That paper also concluded that MELTS and pMELTS are effective at predicting Martian crystallization paths, with additional caveats.

This model of permeability barrier formation is computed in three steps. First, a melt is generated through the adiabatic decompression melting of a composition representing bulk silicate Mars. Next, batch crystallization of the resulting melt aggregate is simulated along a user-imposed pressure-temperature path representing ascent through the lithosphere. Finally, the permeability barrier is located by comparing the crystallization rate and the rate at which the porous matrix can expand (decompact) to accommodate crystallization products. Due to the focus of this project on crystallization rate rather than composition, we do not apply the correction factors mentioned above, although they must be remembered if one were to compare the compositions of magma present at the barrier with Martian volcanic products. The model is repeated for different mantle potential temperatures, lithospheric thicknesses, and initial mantle water contents.

2.2.1 Melt Generation

Starting with a bulk silicate composition appropriate for Mars (Table 2.1), each model run performs a series of continuous (fractional) melting calculations to determine the composition of the aggregate melt generated upon decompression along a mantle isentrope with potential temperature (θ) to a final depth (H) representing the base of the thermal lithosphere. Temperature decreases as the mantle decompresses

due to the compressibility of mineral phases and also to heat generated or consumed by phase changes, including melting. Therefore, MELTS outputs not only the composition of the aggregate melt and residual solid but also the temperature T at each depth. In particular, we record the temperature T_{base} at depth H, the base of the lithosphere.

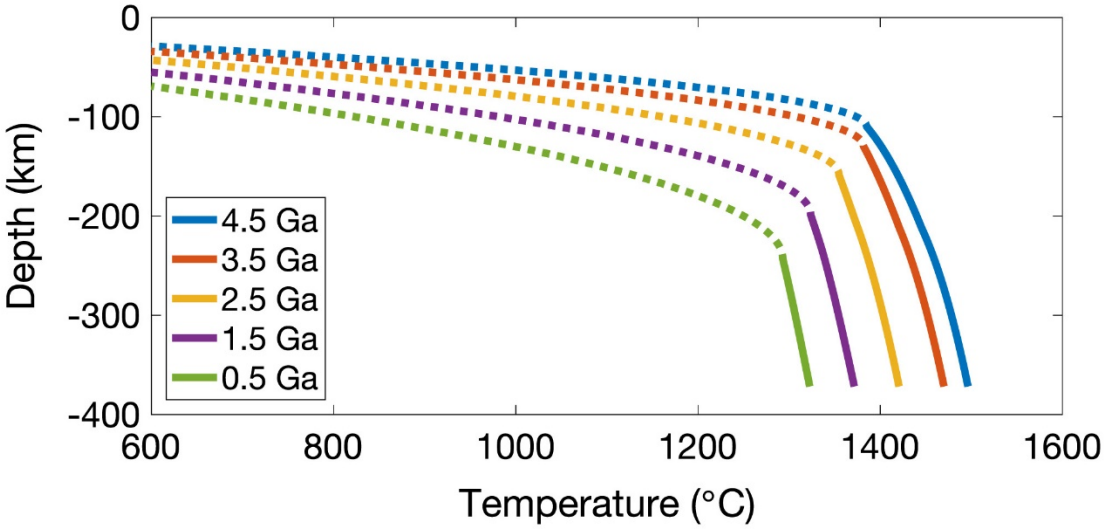

Figure 2.2 - Example pressure-temperature paths including mantle adiabats (solid lines), and lithosphere geotherms (dashed lines) truncated at 600°C, the lowest temperature for which MELTS is reliable. The mantle potential temperatures and lithosphere thickness values used in these examples correspond to approximate ages in the thermal models of *Hauck and Phillips* [2002].

Over the course of Mars's thermal history, H has progressively increased while θ decreased [*e.g.*, *Hauck and Phillips*, 2002; *McGovern et al.*, 2002]. Therefore, the thermal history of the planet can be regarded as a trajectory in the θ-H space (Appendix A, Table A1). Each θ value creates a different mantle isentrope that we follow to a depth H (Figure 2.2). Although we consider many possible combinations of θ and H, the thermal model of *Hauck and Phillips* [2002] is used as a reference to ascribe combinations of θ and H to specific times in Martian history. For example, they predict $H \approx 100$ km and $\theta \approx 1450$ ºC at 4.5 Ga, while at present day, $H \approx 275$ km and $\theta \approx 1200$

ºC. Note that we consider a wider range of θ and *H* than prescribed in these models to cover the uncertainty in thermal evolution models [*e.g.*, *Ruedas et al,* 2013a, 2013b].

The mantle potential temperature likely varies across Mars, especially under the Tharsis Rise where a superplume is thought to elevate temperatures. *H* likely also differs from the reference value in the Tharsis region, where volcanic activity has thickened the crust and the plume may thermally erode the lithosphere [*Kiefer and Li*, 2009]. In order to account for spatial variations and possible excess temperature mantle plume conditions, we perform MELTS runs with θ between 1200 ºC and 1670 ºC with 5 ºC intervals and *H* between 50 km and 275 km with 5 km intervals. Systematically varying θ and *H* generates a continuum of possible melt amounts and compositions, with each application involving ~4000 melting scenarios covering a wide range of conditions possible over Martian history.

Several bulk silicate and mantle compositions of Mars have been proposed [see *Taylor*, 2013 for a review]. The composition most used in the literature is that of *Wänke and Dreibus* [1994], and its predecessor [*Dreibus and Wänke*, 1985], estimated from element correlations in Martian meteorites and chondritic abundances. Additionally, the use of this composition with the MELTS and pMELTS calculator has been previously performed and defended [*El Maarry et al.*, 2009; *Baratoux et al.*, 2011; 2013], albeit with the previously mentioned correction factor. Therefore, this study primarily uses the composition of *Wänke and Dreibus* [1994] (Table 2.1) for consistency when comparing results to literature values. We conducted a few exploratory calculations using other bulk Martian compositions. Crystallization rates

and permeability barrier depths based on the Martian bulk silicate composition of *Taylor* [2013] show no significant difference from those based on *Wänke and Dreibus* [1994], while models using the *Lodders and Fegley* [1997] composition typically create permeability barriers up to 10 km shallower than discussed here, depending on the thickness of the lithosphere. However, not enough calculations were performed to make a definitive statement.

SiO_2	44.4
TiO_2	0.14
Al_2O_3	3.53
Cr_2O_3	0.76
FeO[a]	17.9
MnO	0.46
MgO	30.2
CaO	2.45
Na_2O	0.50
K_2O[b]	0.04
P_2O_3[b]	0.16

[a] All Fe represented as FeO.

[b] Not included in calculations due to limitations in pMELTS.

Table 2.1 - Major Element Concentrations for Bulk Silicate Mars (Wänke & Dreibus, 1994)

The water content of the Martian mantle is a topic of much debate. *Dreibus and Wänke* [1987] calculated only 39 ppm H_2O in bulk silicate Mars. Studies on hydrous mineral inclusions in Martian meteorites yield water concentrations from 15 to 2870 ppm in the melt source [*McCubbin et al*., 2012; *Hallis et al*., 2012; *Usui et al*., 2012]. Estimates from concentrations of H_2O and Cl on the surface of Mars place the water content in the Martian mantle at 330 ± 10 ppm [*Boynton et al*., 2008]. *Taylor* [2013] estimates 300 ± 150 ppm H_2O in the Martian mantle, based on an assessment of surface observations, meteorite composition, and geophysical requirements. In order to account for the large variation seen in the literature we repeated our calculations with water contents of 25, 100, 200, 500, and 1000 ppm.

Most model runs were performed with an oxygen fugacity buffer of FMQ -2.5 in the pMELTS adiabatic melting calculations, and left unbuffered in the MELTS

lithosphere crystallization calculation. Ideally, to replicate expected Martian mantle fugacity conditions model runs would be performed a FMQ -3.5 or lower [*Herd et al*., 2002]. However, pMELTS could not perform initial calculations at many temperatures under conditions more reducing than FMQ -2.5. Smaller subsets of the desired 1200 ºC to 1670 ºC temperature range buffered in pMELTS and MELTS at FMQ -1.5 and -2.5 were generated, as well as subsets where initial calculations at depth were set to FMQ -1.5, -2.5, and -3.5, but were unbuffered during their evolution (Appendix A, Figure A1). The results from these subsets are essentially the same as the FMQ -2.5 data set and suggest that permeability barrier formation conditions are not strongly dependent on oxygen fugacity.

2.2.2 Crystallization of Melt

Each produced melt composition is inputted to a second MELTS calculation under batch conditions and decreasing pressure P and temperature T following a lithospheric geothermal gradient (or areothermal gradient as it should be named for Mars). The lithosphere temperature is approximated using the equation:

$$T = T_{\text{surface}} + \left\{ (T_{\text{base}} - T_{\text{surface}}) * \cos\left[\sin^{-1}\left(\frac{P - P_{\text{base}}}{P_{\text{base}}} \right) \right]^2 \right\} \quad (2.1)$$

where T_{surface} is the surface temperature of Mars (-60 ºC), T_{base} is the temperature at the base of the lithosphere from the end conditions of the adiabatic (isentropic) melting MELTS calculation, P is the lithostatic pressure, and P_{base} is the pressure at the base of the lithosphere. Other temperature profiles may be derived, using steady-state conduction or transient plate cooling. However, uncertainty in the thickness of the crust and its concentration of heat-producing element limits the usefulness of

these profiles. Equation 2.1 produces a profile that transitions smoothly to the adiabatic temperature profile in the actively melting mantle, which helps modeling the transition from melting to crystallizing with MELTS, and is linear through much of the lithosphere (Figure 2.2), which is likely to be appropriate near the surface. For the crystallization calculation, temperature is calculated at every 100 meters, corresponding to increments of 10.76 bar.

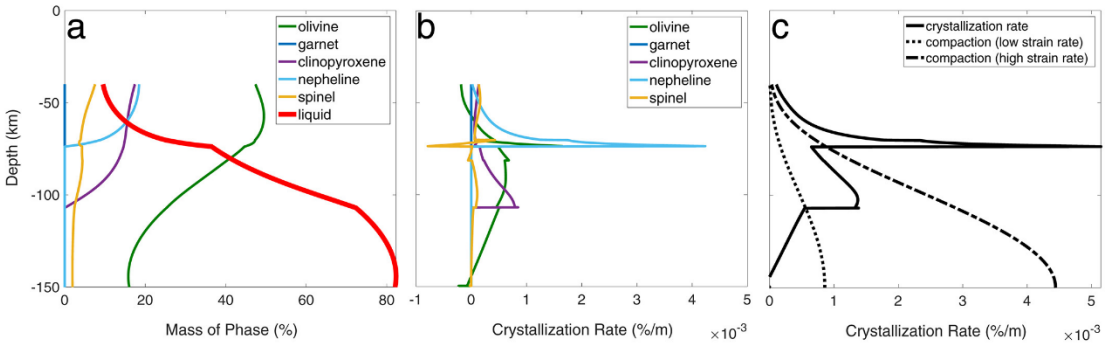

Figure 2.3 - Crystallization sequence for melt rising through a 150 km thick lithosphere, a mantle potential temperature of 1350°C, and anhydrous conditions. (a) Phase abundance expressed as a percentage of the original melt mass in the calculation. (b) Crystallization rate of the mineral phases as mass percentage changes per meter. Crystallization is due mainly to the cooling during ascent. Negative crystallization rates are possible due to phase changes. (c) Total crystallization rate (solid line) of all the solid phases compared to the equivalent crystallization rate due to decompaction of the lithosphere with low (10^{-15} s^{-1}) or high (10^{-13} s^{-1}) background strain rate (dotted and dash-dotted lines). Permeability barriers form at the intersection of the bulk crystallization rate and decompaction-induced equivalent crystallization. High strain rates cause this intersection to occur shallower in the lithosphere than with low strain rates.

As melt rises and cools along this path, mineral phases crystallize. An example calculation of this crystallization sequence is presented in Figure 2.3 using $\theta = 1350$ °C and $H = 150$ km. A portion of the melt, here about 20% in mass, crystallizes instantaneously at the base of the lithosphere because the initial melt composition, obtained as the aggregate of the partial melts, is not in equilibrium with the P-T conditions. This initial compositional adjustment is an artifact of our two-step solution

strategy and should not be interpreted in term of permeability barrier formation. The adjustment is typically produced by crystallizing olivine and spinel, as in the example calculation (Figure 2.3a). Later crystallization does represent the further rise of the melt batch through the lithosphere.

In this example calculation, a small fraction of the initially crystallized olivine is reabsorbed into melt at the bottom 10 km of the lithosphere as the geotherm at that location is almost isothermal and pressure decreases. Olivine crystallization resumes when the batch enters the parts of the lithosphere where temperature drops more rapidly. The crystallization rate is defined as the mass of minerals (as a percent of the mass of the initial melt from the adiabat calculation) crystallized per meter in the lithosphere. The olivine crystallization rate increases progressively during ascent between ~140 and ~110 km depth in the example calculation (Figure 2.3b).

At ~110 km depth, the batch becomes saturated in clinopyroxene (cpx). Spinel also enters the crystallization products at this point. The crystallization rate of cpx and spinel is highest when they first become saturated and decreases progressively as the batch continue to rise. Olivine crystallization decreases slightly at the cpx/spinel crystallization point but otherwise continues to increase as the batch rises. The total crystallization rate reflects the mass of all the mineral phases that crystallize for each depth increment (Figure 2.3c). It displays a sudden jump at the multiple crystallization point around 110 km in this example, and generally decreases as the batch continues to rise, whereas is was progressively increasing when only olivine was saturated.

As the batch reaches shallower and shallower depths, new mineral phases enter the solution. Nepheline and olivine crystallize at the expense of spinel starting at about 70 km depth in the example calculation (Figure 2.3a). Negative crystallization rates for mineral phases, such as spinel, here, and olivine, starting at about 60 km depth, are possible as the thermodynamic conditions may become less favorable for some phases as the batch ascends so that the mineral can be reabsorbed into melt or solid-state reactions take place.

Nepheline frequently appears in the calculation with a high crystallization rate. This may be a miscalibration of MELTS and not representative of reality. Nepheline generally appears late in the sequence when more than half of the initial melt has already crystallized. Nepheline crystallization rate is typically very high at its saturation point (Figure 2.3b) even though little melt is present at that point because most of the precipitation takes place within a few degrees of the saturation point.

We suspect three possible issues in the MELTS and pMELTS which may cause this unrealistic nepheline crystallization rate peak, all related to late residual enrichment of aluminum and sodium. First, while MELTS is well calibrated for peridotite derived compositions near the liquidus, the evolved aluminum and sodium rich melt seen in the late stages of our calculation, when cooling has proceeded well past the liquidus, exists beyond the calibration space of MELTS. Second, due to known MELTS issues in the handling of the spinel system [*e.g.*, *Balta and McSween*, 2013; *Hamecher et al.*, 2013], nepheline is added late in the crystallization sequence to accommodate the aluminum that would otherwise be hosted in spinel. Third, our

initial composition omits potassium from the initial bulk composition, as it is not compatible in pMELTS. A lack of potassium does not affect the earlier crystallization of olivine or clinopyroxene, but probably alters the crystallization behavior of late residual melts, where potassium should be enriched along with aluminum and sodium. The newer rhyolite-MELTS calculator [*Gualda et al.*, 2012] may be capable of accurately handling these late residual melt compositions. However, at the time of writing, there is no reliable way to transition calculations between MELTS and rhyolite-MELTS.

Eventually, it is expected that the batch would be completely crystallized but the calculations are stopped at 600 °C, as MELTS is unreliable at lower temperatures, or the melt evolves to a composition well outside the domain of MELTS. In principle, though, melt ascent should be stopped when a permeability barrier is reached. Typically, we detect permeability barrier formation before the end of calculation, invalidating the late stage of crystallization. Eventually melt may reach the crust where assimilation of surrounding rock may occur, however this process is not modeled in this work.

2.2.3 Permeability Barrier Detection

A permeability barrier is expected to form where the compaction length (δ_c) is larger than the critical compaction length (δ_c^*) [*Korenaga and Kelemen,* 1997; *Hebert and Montési*, 2010]:

$$\delta_c \geq \delta_c^* \tag{2.2}$$

The compaction length is the length scale over which a fluid moving through a viscous porous matrix may support a pressure gradient [*McKenzie*, 1984]:

$$\delta_c = \sqrt{\frac{k_\phi \left(\xi + \frac{4}{3}\eta\right)}{\mu}} \tag{2.3}$$

where k_ϕ is permeability, ξ is the bulk viscosity of the matrix, η is the shear viscosity of the matrix, and μ is the fluid viscosity. The equation used for permeability in this model is:

$$k_\phi = \frac{\phi^n d^2}{C} \tag{2.4}$$

where ϕ is the porosity, *n* is a power law exponent, *d* is grain size, and *C* is a geometric factor related to the dihedral angle [*Cheadle*, 1989; *Connolly et al*., 2009; *McKenzie*, 1984; *Ricard et al*., 2001; *von Bargen and Waff*, 1986; *Wark and Watson*, 1998]. This model assumes a grain size of 3 mm and porosity of 1%, typical values observed in the Earth [*e.g. Avé Lallemant et al*., 1980; *Karato*, 1984; *Kelemen et al*., 1997]. In this work grain size and porosity are considered constant for simplicity. From *Miller et al*. [2014]: C = 56 and *n* = 2.6. Fluid viscosity (μ) is assumed to be 1 Pa*s. Bulk and shear viscosities are related through the porosity:

$$\xi = \frac{\eta}{\phi} \tag{2.5}$$

while the shear viscosity can be expressed as:

$$\eta = \left[\frac{(2\dot{\varepsilon})^{1-m}\exp\left(\frac{Q}{RT}\right)}{2A}\right]^{\frac{1}{m}} \tag{2.6}$$

modified from *Kirby and Kronenberg* [1987], where $\dot{\varepsilon}$ is the strain rate, m is a power law exponent, Q is the activation energy, R is the gas constant (8.314 J mol^{-1} K^{-1}), T is the temperature given by Equation 2.1, and A is a pre-exponential factor. We use the flow law parameters of *Hirth and Kohlstedt* [2003] for m, Q, and A for either wet or dry conditions, as needed (Table 2.2).

Over broad areas of the tectonically active Earth, $\dot{\varepsilon}$ is estimated to range from 10^{-15} to 10^{-12} s^{-1} [*e.g.*, *Buck* 1991; *Tesauro et al.*, 2007; *Karato*, 2010]. Generally, strain rate calculations over broad areas of Mars yield smaller values from 10^{-20} to 10^{-16} s^{-1} [*e.g.*, *Soloman and Head*, 1990; *McGovern et al.*, 2002; *Wilkins et al.*, 2002; *Nahm and Schultz*, 2010]. However, just like on Earth, small, localized areas such as shear zones likely produce higher strain rates. For example, the strain rates near large faults, as exist around the Tharsis bulge, may be as high as 10^{-11} s^{-1} [*e.g., Schultz and Lin*, 2001]. In order to assess the significance of strain rate to the formation of potential permeability barriers over all scales, we use values of 10^{-17}, 10^{-15}, and 10^{-13} s^{-1}.

Name	Symbol	Value	Unit	Equation
Compaction length	δ_c		m	2.2 and 2.3
Critical compaction length	δ_c^*		m	2.2 and 2.7
Permeability	k_θ		m^2	2.3 and 2.4
Bulk viscosity of the matrix	ξ		Pa s	2.3 and 2.5
Shear viscosity of the matrix	η		Pa s	2.3, 2.5, and 2.6
Fluid viscosity	μ	1	Pa s	2.3
Porosity	ϕ	0.01	unitless	2.4 and 2.5
Power law exponent	n	2.6	unitless	2.4
Grain size	d	3	mm	2.4
Geometric factor from dihedral angle	C	56	unitless	2.4
Strain rate	$\dot{\varepsilon}$	10^{-17} (low), 10^{-15}, 10^{-13} (high)	s^{-1}	2.6
Power law exponent	m	3.5	unitless	2.6
Activation energy	Q	535 (dry), 480 (wet)	kJ mol^{-1}	2.6
Gas constant	R	8.314	J mol^{-1} K^{-1}	2.6
Temperature	T		K	2.6 and 2.7
Preexponential factor	A	1.1×10^4 (dry), 3.6×10^5 (wet)	MPa^{-n} s^{-1}	2.6

Table 2.2 - Parameters and Variables Used in the Identification of Martian Permeability Barriers in MELTS Output Files

The critical compaction length is simply the inverse of the crystallization rate:

$$\delta_c^* = \left(\frac{dT}{dz}\frac{df}{dT}\right)^{-1} \tag{2.7}$$

where f is the melt fraction. The crystallization rate df/dT is provided by MELTS.

The parameters entering Equations 2.2 through 2.7 are listed in Table 2.2.

To better understand the relation between the crystallization rate and compaction, we compute an equivalent crystallization rate from compaction

$$X_e = \left(\delta_c \frac{dT}{dz}\right)^{-1} \tag{2.8}$$

Where δ_c is given by Equation 2.3. The location of the permeability barrier is defined as the deepest intersection of the resulting δ_c^* and δ_c curves or equivalently the deepest intersection between the equivalent crystallization rate and the actual crystallization provided by MELTS.

Viscosity is lowest at the base of the lithosphere and increases upward. Therefore, the compaction length increases upward and the equivalent crystallization rate decreases upward. In the example calculation of Figure 2.3, as in most cases, crystallization rate is low at the base of the lithosphere and increases upward as long as olivine is the only crystallizing phase. As the equivalent crystallization rate has the opposite trend, it is possible for the two to intersect and form a permeability barrier. That will often be the case at low strain rate, when X_e is particularly low (Figure 2.3c).

If multiple saturation is reached before a permeability barrier forms, crystallization rate increases dramatically. It makes it likely that a permeability barrier forms at a multiple saturation point. *Hebert and Montési* [2010] assumed that the multiple saturation point of plagioclase and cpx is the location of the permeability barrier at mid-ocean ridges. For Mars, the first spike in crystallization rate is also associated with cpx saturation.

If the strain rate is high enough, which lowers viscosity and increases the effective crystallization rate, even that spike may not have sufficient amplitude to result in a permeability barrier. Crystallization rate decreases after the spike, so a permeability barrier only rarely forms before the next multiple saturation point, which typically corresponds to the crystallization of nepheline, is reached (Figure 2.3c). The crystallization rate at the nepheline saturation point is usually larger than at the cpx saturation point, so that, combined with the reduced effective crystallization rate due to the lower ambient temperature and higher mantle viscosity, it is highly unusual that crystallization proceeds past this point without encountering a barrier.

If the nepheline saturation point is overcome, crystallization rate decreases dramatically, and we never observe a later barrier. In that case, melt crystallizes progressively and either becomes entirely solid in the mantle or reaches the crust, as which point assimilation can further facilitate the upward ascent of melt, a process that we do not consider in detail here.

As previously noted, nepheline is likely an artifact of the limitations of the MELTS algorithms, therefore the intense crystallization spike and associated permeability barrier predicted here are unlikely to exist in nature. Therefore, conditions where a permeability barrier forms only at the nepheline saturation point may equally represents conditions for which the melt crystallizes completely or reaches the crust without encountering a permeability barrier.

By systematically varying mantle potential temperature and lithospheric thickness, we generate a dataset identifying the formation conditions and

characteristics of permeability barriers for different temporal and spatial possibilities on Mars. From MELTS, we also record the composition of the melt present at the barrier, which likely represents the primitive magma that source lava flow and volcanic edifices at the surface of Mars.

2.3 Results

2.3.1 Melt Generation

The adiabatic melting calculations yield a broad range of melt amounts and compositions (Figure 2.4; Appendix A, Figures A2 and A3). The hottest mantles and thinnest lithospheres considered in this model (θ = 1665 ºC and H = 50 km) produce upwards of 50% partial melt of the mantle but for more realistic situations, especially the conditions predicted by *Hauck et al.,* [2002], the degree of melting is less than 20% (Figure 2.4a). Cold mantles and thick lithospheres such as those forming the quasi-triangular region from 1200 to 1300 ºC and 150 to 275 km in Figure 2.4a produce no melt in the anhydrous model. This area of no melt encompasses the estimated last 1.5 billion years of Martian conditions including the present day estimate of θ = 1200 ºC and H = 275 km according to the calculation of *Hauck and Phillips* [2002]. Today, anhydrous melting is expected only if the mantle temperature exceeds their model by at least 100 °C. By comparison, mantle plumes on Earth are likely 100 to 300 °C hotter than the source region of mid-ocean ridge basalts [*Herzberg et al.,* 2007; *Putirka et al.,* 2008]. Therefore, it is possible that melting today is restricted to anomalously hot regions of the mantle, such as mantle plumes.

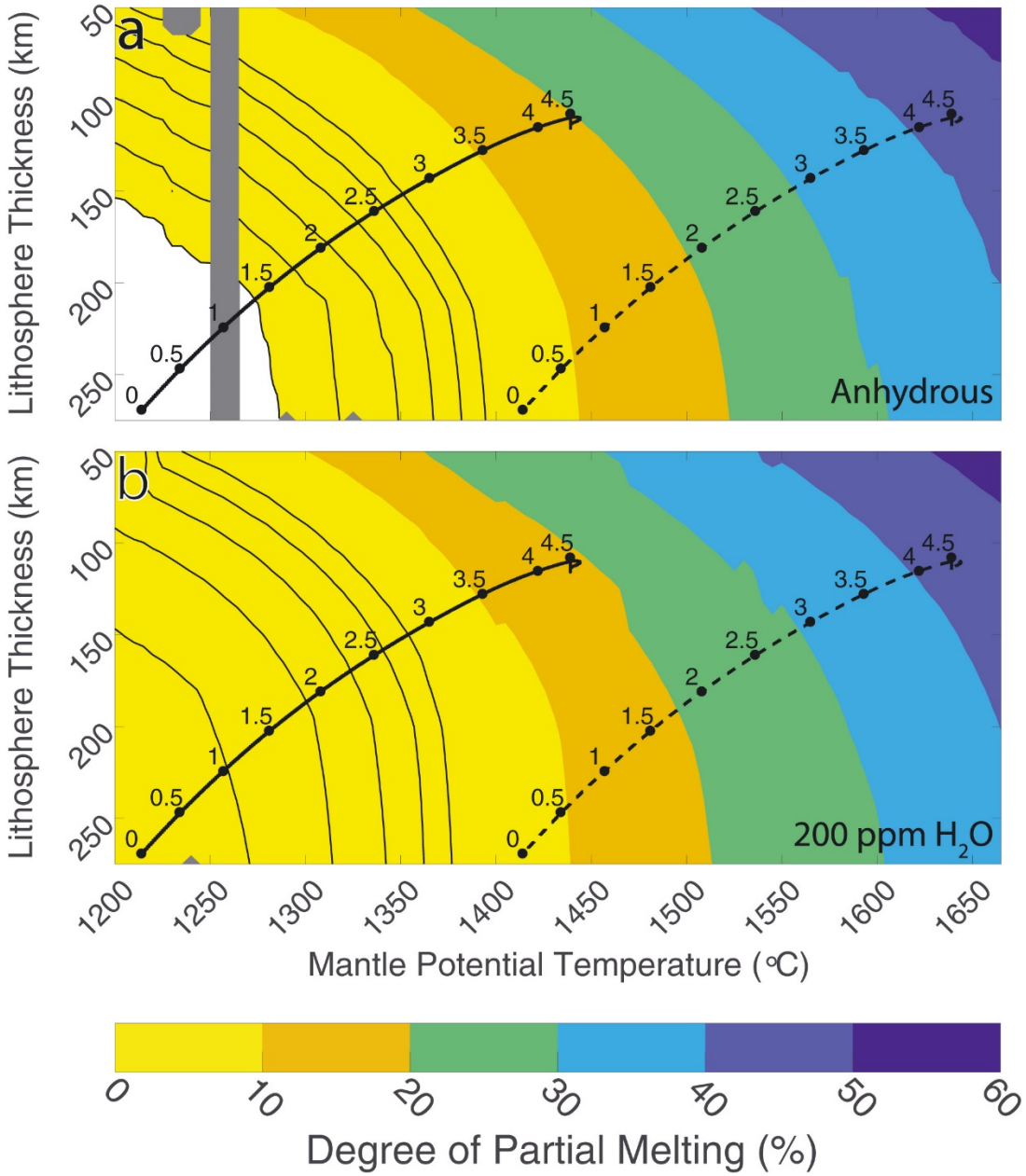

Figure 2.4 - Degree of melting produced by decompression melting of (a) anhydrous Martian mantle and (b) Martian mantle containing 200 ppm H_2O, as a function of mantle potential temperature and lithospheric thickness. The black contours indicate the first 5% of partial melting. The gray bars represent fields where the MELTS calculator could not perform calculations. White space indicates no melt. The numbered, thick, solid black lines follow the thermal model of *Hauck and Phillips* [2002] with labels indicating time before present in billions of years. The dashed black lines represent the same thermal evolution model with 200°C added to the mantle temperature to represent an anomalously hot mantle, as may be present at mantle plumes. Plumes may also thin the lithosphere; however, the magnitude of this effect was not estimated or applied to the dashed curve.

Increasing the mantle water content allows melting to take place with thicker lithospheres and colder mantles (Figure 2.4b), however in the 25 ppm H_2O case, mantle temperatures below 1245 ºC could not be assessed due to pMELTS stability issues under these conditions (Appendix A, Figure A2). Increasing water content to 100 ppm results in some melting in all the considered θ-*H* space, with a minimum partial melt of 0.03% at θ = 1200 ºC and *H* = 275 km but it may not be possible to extract such small melt fractions. Higher concentrations of water produce higher partial melts at present day, reaching about 1.5% partial melt with the highest considered water concentration of 1000 ppm. Increased water content has a more negligible effect to melting at higher mantle temperatures and thinner lithospheres due to water having partitioned into the melt phase at early stages of melting [*e.g.*, *Asimow et al.,* 2004]. Therefore, water influences melting most for recent Mars but is not expected to substantially effect melt generation in the Noachian and most of the Hesperian (Figure 2.4 and Appendix A, Figure A2).

2.3.2 Permeability Barrier Formation Conditions

2.3.2.1 Effect of Strain Rate in anhydrous conditions

At low strain rates ($\dot{\varepsilon} = 10^{-17}, 10^{-15}$ s^{-1}) and anhydrous conditions, permeability barriers form only deep in the lithosphere (Figures 2.5a, 2.5b, and Appendix A, Figures A4 and A6). Higher mantle temperatures and shallower lithospheres form permeability barriers during the steady crystallization of olivine, whereas lower mantle temperatures and thicker lithospheres form barriers at the onset of clinopyroxene crystallization. As pyroxene appears early in the crystallization sequence, which exact phase is crystallizing at permeability barrier does not have a

marked effect on our results. In the 10^{-17} s^{-1} case, the barrier develops at essentially the base of the lithosphere (Figure 2.5a; Appendix A, Figure A6, left column), while in the 10^{-15} s^{-1} case, the barrier develops approximately one quarter of the way into the lithosphere, regardless of mantle temperature (Figure 2.5b; Appendix A, Figure A6, middle column). Barriers formed due to the crystallization of later phases, such as feldspar, are observed only for lithospheres thinner than 60 km and low mantle potential temperature. However, the existence of these conditions in reality is unlikely based on thermal evolution models [*Hauck and Phillips*, 2002]. The depth of the permeability barrier depends predominantly on the thickness of the lithosphere only very little on mantle temperature.

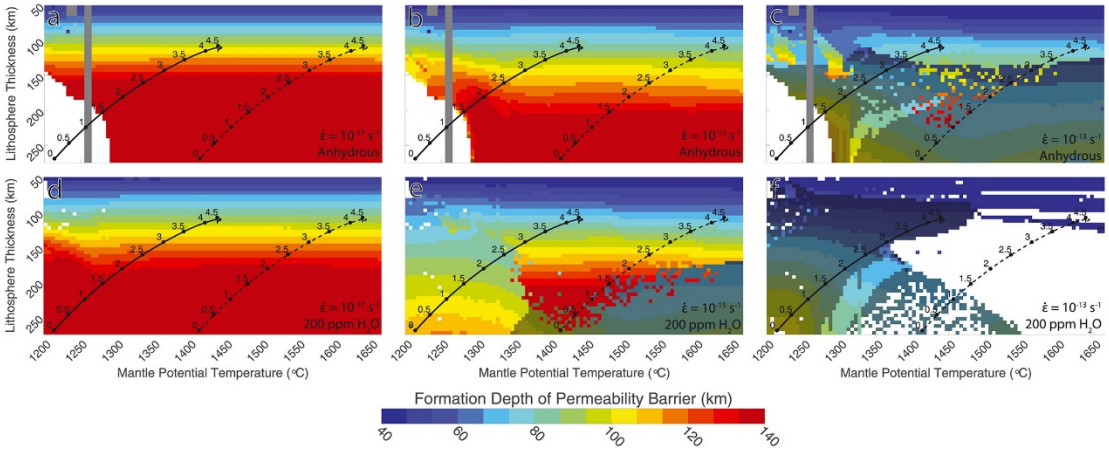

Figure 2.5 - Depth of the permeability barrier as a function of mantle potential temperature and lithospheric thickness assuming a background strain rate of (a and d) $\dot{\varepsilon} = 10^{-17}\ s^{-1}$, (b and e) $\dot{\varepsilon} = 10^{-15}\ s^{-1}$, or (c and f) $\dot{\varepsilon} = 10^{-13}\ s^{-1}$ and various water contents: anhydrous mantle (Figures 2.5a–2.5c) with a dry rheology in the lithosphere and 200 ppm H_2O (Figures 2.5d–2.5f) in the mantle with a fully wet rheology in the lithosphere. The color bar is saturated at 140 km for comparison. White indicates that no barrier forms. Gray bars indicate conditions for which the MELTS calculator could not perform calculations or predicted no melt. Colors with a gray mask represent permeability barriers formed at the crystallization peak of nepheline and are likely unreliable. The solid black lines are as in Figure 2.4.

Higher strain rates ($\dot{\varepsilon} = 10^{-13}$ s^{-1}) and anhydrous conditions produce two distinct results, depending on lithosphere thickness (Figure 2.5c). When the lithosphere is thinner than ~135 km, the permeability barrier is relatively deep and usually forms during crystallization of olivine or clinopyroxene. Barrier formation is similar to the low strain rate case, although slightly delayed due to the increased strain rate and lower viscosity of the matrix. Barriers form about one third of the way into the lithosphere, regardless of mantle potential temperature. By contrast, lithospheres thicker than ~135 km produce permeability barriers at relatively shallower depth. For example, if the mantle temperature is about 1375 °C, the barrier forms at about 75 km depth when the lithosphere is 115 km thick but at 65 km depth when the lithosphere is 140 km thick. The shallow barriers form primarily when late phases such as nepheline or spinel enter the crystallization sequence, and therefore may be unrealistic. The crystallization of initial olivine ± cpx did not occur at a rate sufficient to form a permeability barrier when considering the reduced viscosity of the mantle deforming at a high strain rate. Later phases may produce a barrier because they take place at colder temperature, when the mantle is more viscous. However, due to the presence of nepheline we cannot assess these later phases. Permeability barriers created due to the crystallization of feldspar are prevalent for low mantle potential temperature and thin lithospheres. However, once again, these conditions are unlikely to represent Mars at any time of its history.

2.3.2.2 Effect of Water Content

The inclusion of water into the models does not change much the crystallization sequence of the melt, in part because during most of the Martian

history, water in the melt source has only a minor effect on melt composition (Section 3.1). Using the viscosity law for a dry Martian mantle, but with melt derived from wet (200 ppm H_2O) mantle results in the same permeability barrier depth as for the anhydrous model shown in Figure 2.5a, 2.5b, and 2.5c with the addition of permeability barrier depth estimates with low mantle potential temperature and thick lithospheres (Appendix A, Figures A4 and A6).

This situation (wet melt source, dry lithosphere) is realistic if one assumes that the lithosphere which the melt traverses is dry, perhaps due to an earlier melting episode, like the oceanic lithosphere on Earth [*Hirth and Kohlstedt,* 1996; *Evans et al.*, 2005]. However, if the lithosphere is not the residuum of melting but is simply the thermal boundary layer on top of the convective mantle, it may be that water is present in the solid matrix. The effect of water on viscosity and therefore on the compaction rate of the solid matrix changes significantly the depth at which permeability barriers form.

To capture the effect of water in the solid mantle matrix, we adopt the flow law parameters for wet olivine listed in *Freed and Bürgmann* [2004]. Water lowers the viscosity of the matrix and therefore influences permeability barrier formation in a similar way to increasing the strain rate: it is possible for olivine and clinopyroxene to crystallize without forming a barrier. Instead, for at least some θ-*H* conditions, the barrier forms when later phases crystallize. At the lowest strain rate (10^{-17} s^{-1}), a wet mantle rheology slightly elevates the barrier in thicker lithospheres (Figure 2.5e; Appendix A, Figures A5 and A7). In the 10^{-15} s^{-1} strain rate models the barrier is shallower than the reference anhydrous calculations (Figure 2.5b; Appendix A,

Figures A4), when the lithosphere is thick and the mantle potential temperature is either lower than ~1350 °C or higher than ~1500 °C (Figure 2.5e; Appendix A, Figures A5 and A7). When strain rate is higher (10^{-13} s^{-1}), the permeability barrier is always shallower than in the anhydrous models and may never form if the mantle temperature is too high (Figure 2.5f; Appendix A, Figures A5, and A7). We describe here the various domains in the θ-*H* space that may be identified in terms of permeability barrier depth systematics.

First, at the 10^{-15} s^{-1} strain rates, water does not affect much permeability barrier formation when the mantle potential temperatures is between 1350 and 1550 ºC, regardless of lithospheric thickness, or when the lithosphere is shallower than ~120 km, regardless of mantle temperature (Figure 2.5e). Under these conditions, the barrier forms upon crystallization of olivine or clinopyroxene in the lower third or quarter portion of the lithosphere, as in the anhydrous case.

Second, when the lithosphere is thick and the mantle hotter than ~1500 °C (depending on lithospheric thickness), the barrier forms at much shallower depths than predicted for an anhydrous lithosphere. For example, the barrier is only at 60 km deep when the lithosphere is 200 km thick and the mantle potential temperature is 1550 °C. The barrier under these conditions is typically associated with saturation of nepheline and spinel and therefore may not develop at all in reality.

Third, when the lithosphere is thick and the mantle cooler, as may be representative of the last 2.5 billion years of Martian history, the barrier forms during the progressive crystallization of olivine and clinopyroxene, although later than the

crystallization rate maximum associated with clinopyroxene saturation. The barrier is shallower than in the anhydrous case but not as shallow as when controlled by late-crystallizing phases. For example, the barrier is about 90 km deep for a 200 km thick lithosphere and a mantle potential temperature of 1300 °C (Figure 2.5e).

Increasing the strain rate of the model to $\dot{\varepsilon} = 10^{-13}$ s^{-1} drastically changes the results. Under these conditions, the permeability barrier forms at shallow depths regardless of lithosphere thickness or mantle potential temperature (Figure 2.5f). The majority of these barriers are formed due to the late crystallization of nepheline and, as argued before, may not exist in reality. In addition, permeability barriers do not form at all when mantle temperature exceeds ~1350 °C and the lithosphere is thicker than ~100 km. Increasing the water content increases the likelihood that no barrier forms even for thicker lithospheres and cooler temperatures. The permeability barrier does not form when the strain rate and water content in the solid matrix are high because the viscosity is small enough for the matrix to decompact and accommodate the crystallization products generated by the cooling melt.

2.3.2.3 Composition of Melt at the Depth of the Permeability Barrier

Once a permeability barrier is formed, the subsequent melt immediately below the barrier is trapped. The composition of this melt, which is likely the parent melt to surface lava flows, is systematically recorded. Its silica content depends on the depth of the barrier, with deeper barriers holding more ultramafic melt and shallower barriers holding more mafic melt. In both the 10^{-17} and 10^{-15} s^{-1} strain rate cases (Figure 2.6a, 2.6b; Appendix A, Figures A8, and A9; anhydrous mantle), following the silica content of the sub-barrier melt along profile of *Hauck and Phillips* [2002]

shows an evolution from ultramafic (<35% SiO_2) to less mafic (>55% SiO_2) as the mantle cools and lithosphere thickens. At the +200 °C conditions of a mantle plume, the melt stays ultramafic (between 35 and 40% SiO2) throughout Martian history.

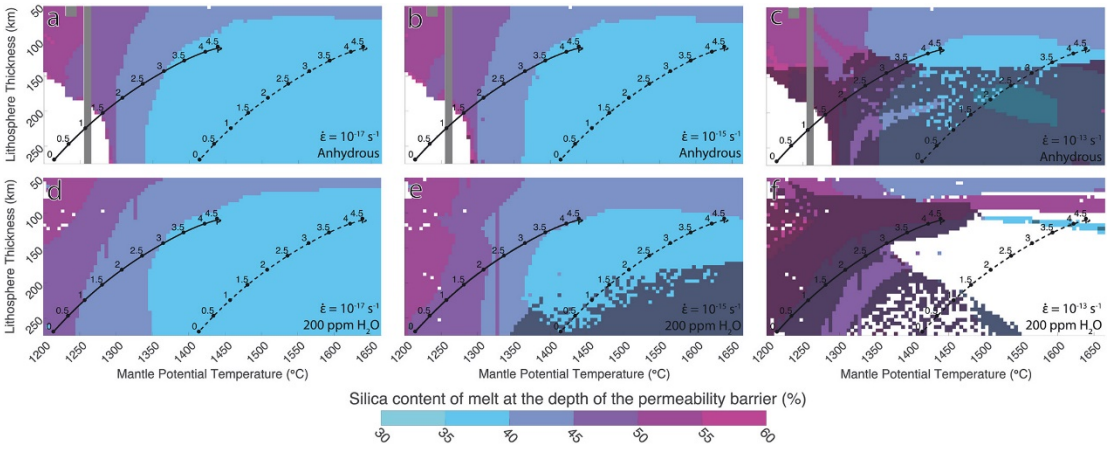

Figure 2.6 - Silica content of melt at the level of the permeability barrier predicted. Run conditions, gray and white areas, gray mask, and black lines are as in Figure 2.5. The values displayed here are the values obtained from our pMELTS-MELTS model run; however, it should be noted here that in another pMELTS-related project *(El Maarry et al.,* 2009), dealing with the Martian composition of *Dreibus and Wänke* (1985), a correction factor of +2.91 wt % SiO2 in the melt was determined through comparison with applicable experimental results (*Bertka & Holloway*, 1994). Therefore, the melt compositions may be slightly more felsic than presented here.

As previously discussed, increasing the strain rate to 10^{-13} s^{-1} raises the permeability barrier to shallower depths, especially after 3.5 Ga in both the nominal and higher temperature cases. In these times of elevated barrier, the trapped melt slightly more felsic (50-55% SiO_2) than seen at the lower strain rate case (Figure 2.6c; Appendix A, Figures A8 and A9).

Adding water the mantle was also previously shown to raise the level of the permeability barrier, especially at the nominal temperature age profile. Accordingly, the silica content of the trapped melt is higher than in equivalent anhydrous cases (Figures 2.6d, 2.6e, 2.6f; Appendix A, Figures A8 and A9). A combination of higher

strain rates in the lithosphere and water in the mantle always result in melt with more than 50% SiO_2 if the barrier forms at all.

2.4 Discussion

As the melt generated by decompression in the Martian interior rises through the lithosphere, it is highly likely that it forms a permeability barrier and stalls, unless the lithosphere is sufficiently wet and/or it deforms at a high strain rate, signifying some active tectonics. Under most conditions, the permeability barrier is deep, in the lower third of the lithosphere, and appears upon initial crystallization of olivine or at cpx saturation. A barrier can form more shallowly if viscosity is reduced, whether by including water in the solid matrix or by increasing strain rate. It is possible for the elevated barrier to still be associated with later olivine + cpx crystallization, especially when the mantle is cold and the lithosphere is thick (Figure 2.5e) but elevated barriers typically form late in the crystallization sequence, upon the unrealistic saturation of nepheline.

From this summary, it is clear that melt usually stalls at some level in the lithosphere. However, some amount of melt must evidently reach the surface of Mars to create the observed volcanic edifices and plains. We propose here three possible methods to overcome the permeability barrier. Then, we associate different volcanic expressions to these methods. Finally, we discuss how changes in the formation conditions of permeability barrier linked to the thermal history of Mars can explain the general trends of volcanism observed at the surface.

2.4.1 Overcoming the Permeability Barrier

There are three principal ways for melt to rise to shallow levels in the lithosphere and reach the surface: thermal erosion, cracking, and assimilation. We describe each of these processes and explain under what conditions they are likely to take place.

First, the permeability barrier may be overcome thanks to the feedback between the thermal structure of the lithosphere and the location of the barrier. Crystallizing melt releases latent heat, which can increase slightly the temperature of the lithosphere. This effect is strongest at the permeability barrier, where melt accumulates and crystallization rates are high. Due to the increased temperature, crystallization is slightly delayed, so that melt can rise past the nominal permeability barrier level. This process might create a thermal instability whereby melt would be focused to any location where the barrier is slightly elevated [*e.g.*, *Sparks and Parmentier,* 1991; *Montési et al.* 2011], release more heat from crystallization, which further elevates the barrier at that point. The process may become unstable but would also be limited by the horizontal transport towards locations where the barrier is elevated. Although a detailed model of this process is not yet available, it is conceivable that the competition between thermal erosion and melt supply gives rise to a preferred wavelength of instability.

Second, melt may cross the permeability barrier by cracking. Because crystallization products are typically less dense than the melt, crystallization results in a net volume increase of the pore space. At the permeability barrier, where, per definition, the solid matrix is too strong to decompact and accommodate this pore

volume increase, pore fluid pressure increases instead. It is possible that the overpressure develops to the point of initiating cracks and dikes that carry the residual melt through the overlying lithosphere [*Havlin et al*., 2013; *Cai and Bercovici*, 2016].

Finally, melt may bypass the nominal level of a permeability barrier via assimilation of the surrounding wall rock. On the one hand, the mantle would not be greatly subjected to assimilation, as the melt temperature is similar to the mantle solidus. Even so, a melt-rock reaction, specifically the incongruent melting of pyroxene by rising melt as the equilibrium mineral assemblage changes with decreasing pressure, has been proposed as the origin of dunite conduits in the Earth mantle [*Kelemen et al*., 1995]. On the other hand, crustal assimilation may affect the formation of the permeability barrier. Assimilation has been recognized on Earth, even in oceanic settings [*Nicholson et al.,* 1991; *Coogan,* 2003; *Wanless et al*., 2010], where the composition of the crust, as on Mars, is mafic. By incorporating crustal materials into the melt, the barrier may rise or not form at all, resulting in either case in melt reaching the surface unimpeded.

The three processes described here generally take place at different depths. Assimilation is most effective when the melt reaches the crust, at typical depths of 30 km in the northern hemisphere and 60 km in the southern hemisphere of Mars [*Neumann et al.,* 2004]. Such shallow permeability barriers are predicted only when the lithosphere is less than 100 km thick (Figure 2.5), which is unlikely to represent actual conditions in the Martian interior [*Hauck and Phillips,* 2002]. Permeability barrier depths approaching 60 km with more realistic lithosphere may be possible when strain rate is high (Figure 2.5c, 2.5f). This may be sufficient to reach the base of the

crust in the southern hemisphere, but as that hemisphere does not show as much signs of tectonic activity, the strain rate there is likely too low for the barrier to be elevated enough. However, elevated permeability barriers are associated with crystallization of nepheline and may not exist in reality, allowing melt to reach the crust if the lithosphere is not too thick.

Under most conditions, permeability barriers form deep into the mantle (Figure 2.5), leaving thermal erosion and cracking as the most likely mechanisms associated with crossing the barrier. Cracking should be favored for relatively shallow barriers, where the overburden pressure is less. Thermal erosion should be favored for the deeper barriers, where not only cracking is suppressed, but also the less intense background temperature gradient is more easily perturbed by the heat anomaly. Detailed models should be developed to constrain the actual depth at which the mode of permeability crossing changes.

2.4.2 Surface Manifestations of Permeability Barrier

The depth and characteristics of the permeability barrier clearly change with lithospheric thickness and mantle potential temperature (Figure 2.5). To evaluate the relevance of these models for the geology of Mars, we discuss here how the position of the barrier in relation to lithospheric thickness may result in different styles of volcanism. To do this, we consider four cases for each combination of the barrier being deep or shallow and the lithosphere being thick or thin. Schematic diagrams for each case are presented in Figure 2.7.

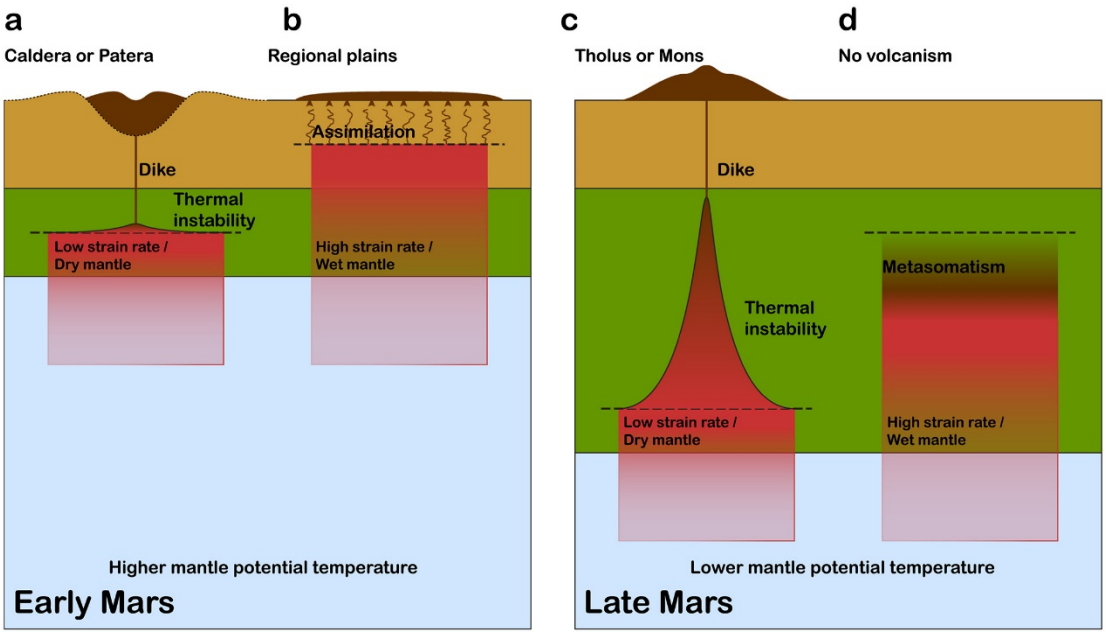

Figure 2.7 - Schematic representation of the four permeability barrier configurations and their potential volcanic expression. (a) The lithosphere is thin, the barrier (dashed black line) has formed in the lithospheric mantle (green), beneath the crust (tan), possibly due to a low strain rate and/or being dry in the lithospheric mantle. To reach the surface, the permeability barrier must be broken via melt overpressure or thermal erosion and transported by dikes or fractures to form a localized edifice. A caldera or patera may form due to flexure of the thin plate. (b) The lithosphere is thin with a likely high strain rate and/or some amount of water; the barrier may form in the crust where crustal assimilation and a weak barrier may allow melt to travel above the nominal barrier to form widespread flows. (c) The lithosphere is thick, and the barrier deep due to low strain rate and/or lack of water, melt must be focused, likely via thermal erosion, and the barrier level must be elevated to a shallow enough level so that dikes and fractures may occur. In this case, the thickness of the plate may support the volcano with minimal flexure, creating Mons or Tholus style volcanoes. (d) The lithosphere is thick and has a high strain rate or is wet; shallow barrier formation is unlikely. Slow crystallization of the melt metasomatizes the lithospheric mantle.

A thin lithosphere corresponds to early Mars (*e.g.*, Noachian, early Hesperian). When the permeability barrier is deep, as may occur in low strain rate, dry rheology, young environment (Figures 2.5a, 2.5b, and 2.5d), it likely to be located in the mantle, removing the possibility of assimilation. The barrier can be overcome by an instability process, with cracking being the most likely candidate. Melt is focused to the instability

point and carried to the surface by dikes and fractures. The melt would reach the surface at discrete points forming a central volcanic edifice. The thin elastic plate at that time cannot support the growing topography of the volcano [*McGovern et al.*, 2015] so that the resulting edifice is likely a caldera or patera (Figure 2.7a). *Baratoux et al.*, [2013] created MELTS models which let a batch melt of the mantle solidify at a constant 1 bar. In the cases of a thin lithosphere and hot mantle characteristic of the Noachian their models appear to match the composition of the Martian surface as represented by ALH84001 [*Larpen et al.*, 2010]. This scenario suggests quick extraction of melt via cracking to the near surface so that mineralogical evolution at depth does not occur.

When the lithosphere is thin and the permeability barrier is shallow, it is possible for the melt to reach the crust. This situation appears possible in higher strain rate, wet rheology, early environments (Figures 2.5c, 2.5e, and 2.5f). Assimilation of crustal material may raise the barrier or prevent its formation, allowing melt to reach the surface essentially unimpeded over wide areas. The distributed source may give rise to volcanic plains (Figure 2.7b).

Three objections may be raised concerning this association. First off, the composition of the melt present at the location of most likely barrier formation under these conditions contains more than 50 wt% SiO_2 (Appendix A, Figures A8 and A9), which is more evolved than the Martian surface [*Karunatillake et al.*, 2009; *Baratoux et al.,* 2011]. Here, it should be noted that we assumed that the magma equilibrates thermally with its surrounding. This may not be the case, leading to melts at the surface that are more mafic than predicted. In addition, assimilation of the mafic crust of Mars may actually reduce the SiO_2 content of the melt, a counterintuitive result if one is used

to think about the less mafic continental crust on Earth. Secondly, if the volcanic plains are thought to form by long lava flows, the eruption rate should be high enough to overcome heat loss [*e.g.*, *Zimbelman et al*., 1998; *Garry et al*., 2007] and high eruption rates have often been linked with deep reservoirs [*Gregg and Williams*, 1996]. However, the high rate eruption of continental flood basalts on Earth [*e.g.*, *Svensen et al.,* 2012; *Self et al.*, 2014] are typically associated with the silicic members, which are stored at a shallow level in the crust, whereas the eruption of the more mafic members did not take place at exceptionally high rates [*White et al.*, 2009*; Bryan et al*., 2010]. Therefore, volcanic plains do not require high eruption rates. Here we argue that the large size and uniformity of volcanic plains implies a widespread source of lava, one that would not be possible if magma was stopped at a permeability barrier, as means of overcoming the barrier would result in localized melt outpouring at the surface. Third, the higher strain rates required on a regional scale for widespread flows may be excessive. It may be more likely that many individual localized shear zones serve as melt sources for lava flows in a region. For example, localized wrinkle ridges are present throughout the early Hesperian aged lava flows of Lunae Planum, indicating localized areas of high strain through the lithosphere [*Plescia*, 1991; *Zuber* 1994]. The permeability barrier may be elevated near the thrust associated with each individual wrinkle ridge, allowing melt to reach the surface. Different flows associated with different shear zones in a region may have aggregated to form the terrain visible today.

A thick lithosphere corresponds to later Mars (*e.g.*, late Hesperian, Amazonian). Here again, the permeability may be deep or shallow relative to the lithosphere but in

either case, it is unlikely to encounter the crust. Therefore, it becomes impossible to form a widespread plain.

If the barrier is deep within the thick lithosphere, as may occur in a low strain rate, dry rheology, more recent environment (Figures 2.5a, 2.5b, and 2.5d), melt may take advantage of an instability to overcome the barrier. Like the thin lithosphere and deep barrier case, melt delivery is probably localized over the site of the instability, forming a central volcanic edifice. However, as the barrier is deeper than before, a thermal instability is more likely than cracking. It may be that as the perturbed barrier reaches shallower and shallower depths, cracking becomes increasing possible, but the start of the instability if likely dominated by thermal processes. The volcanic edifice can build a conical shape due to the strength of the lithosphere [*McGovern et al.,* 2015] so that the expression of these conditions is probably a tholus or mons (Figure 2.7c). *Baratoux et al.*, [2013] also match a model of near-surface isobaric crystallization of primary Amazonian melt to 1.3 Ga Nakhiltes [*Bouvier et al.*, 2009]. Melt must therefore ascend quickly past the level of the permeability barrier as opposed to stalling and evolving at depth.

Finally, if the barrier is relatively shallow in a thick lithosphere, we have argued earlier that it may not exist at all. This outcome is likely in high strain rate, wet rheology, ancient areas of Mars (Figures 2.5c and 2.5e), especially if the temperature is elevated (Figure 2.5f). As assimilation is not an option at these depths, it is likely that melts crystallizes completely and metasomatizes the lithospheric mantle, yielding no surface volcanism (Figure 2.7d). Trapped melts are commonplace in abyssal peridotites [*Hellebrand et al.,* 2002; *Le Roux et al.*, 2007].

2.4.3 Permeability Barriers Throughout Martian History

Thanks to thermal history models, the various permeability barrier configurations and their surface volcanic expressions can be associated with various time periods on Mars. We show in Figures 2.5, 2.6, and Appendix A, Figures A4 to A9 the results of *Hauck and Phillips* [2002] that predict a Martian mantle that cools from ~1450 °C to 1200 °C from 4.5 billion years ago to present, while the thickness of the lithosphere increases from 100 to 250 km. We use the model results of *Hauck and Phillips* [2002] as a reference to associate lithospheric thicknesses and mantle potential temperature. Alternative thermal evolution models have been developed based on different assumption about the importance of the core, melt-induced differentiation and dehydration of the interior, and initial conditions. For example, *Ruedas et al.* [2013a, 2013b] used two-dimensional models and predict higher temperatures in the Martian mantle, reaching 1450 °C at present. The ages discussed in the following section are model-dependent and should not be as precise estimate of the time in Martian history when the configuration of permeability barrier in the Martian lithosphere changes. The thermal evolution of Mars is imperfectly understood, and thermal models, in particularly, do not explain the very thick lithosphere (>300 km) inferred below the north pole at present [*Phillips et al.*, 2008].

Mantle plumes, which are likely present underneath Tharsis and Elysium, would also result in higher temperature and possibly thinner lithosphere [*Kiefer and Li*, 2011]. Based on petrological modeling, *Baratoux et al.* [2011] infer temperatures of nearly 1400 °C in the older volcanic provinces of Sinai and Solis Planum and a cooler Martian interior (1340 °C) for the younger Alba Mons and Olympus Mons,

which is close to the *Hauck and Phillips* [2002] model. Therefore, although we can roughly follow the evolution of the Martian interior in the θ-*H* plots presented earlier, the exact temperature of the interior and lithosphere thicknesses have to be regarded as somewhat uncertain.

If the lithosphere is dry and deforms at a strain rate of 10^{-17} or 10^{-15} s^{-1} (Figures 2.5a and 2.5b), the permeability barrier is always at the base of the lithosphere and becomes deeper and deeper over time, whether mantle temperature follows the nominal value of *Hauck and Phillips* [2002] or is higher. Central volcanoes (Figures 2.7a and 2.7c) are expected throughout the Martian history, and they would become progressively higher and steeper as their shape is controlled by the elastic thickness, as observed. It may be expected that at some point, the barrier is too deep for magma to be able to pass through and reach the surface, but the transition would be progressive. It is not known if the volcanic regime would change as the manner that melt cross the permeability changes from cracking to thermal erosion. The permeability barrier is identical on top of regular mantle or mantle plumes.

By contrast, model results that use 10^{-13} s^{-1} strain rate and a dry rheology (Figure 2.5c) display a change in the characteristics of the permeability barrier about 3.5 billion years ago. Before then, the permeability barrier is deep, as in the lower strain rate case, but after that, the barrier is elevated or may not exist at all. The switch can be delayed by a couple hundred million of years if the mantle is a couple hundred degrees hotter than the "normal" case (Figure 2.5c). It is possible that this switch explains the abundance of volcanic plains emplaced in the Hesperian. Right at

the transition, the barrier jumps up and might even reach crustal levels, resulting in the emplacement of volcanic flood plain (Figure 2.7b). As time goes on, the barrier becomes deeper, following the lithosphere thickness, and may reach the point where it is too deep for the melt to reach the crust and flood volcanism should stop (Figure 2.7d). The shallow permeability barriers form only 3.5 to 3.0 billion years ago and in areas of high strain rate, implying tectonic activity or shear zones. The barrier is always more elevated in higher mantle temperature regions, so that flood volcanism may continue above mantle plumes later than over "normal" mantle, possibly contributing to the late Hesperian / early Amazonian plain volcanism on the Tharsis Rise.

If the lithosphere follows a wet rheology and the strain rate is 10^{-15} s^{-1}, the depth of the permeability barrier experiences a similar transition as in the previous case, at least with nominal mantle temperature. Approximately 3 to 2.5 billion years ago, the barrier transitioned from deep to shallow conditions (Figure 2.5e). However, even after the transition, the barrier is still controlled by the crystallization of olivine and cpx and is therefore likely to exist in reality, unlike the late elevated permeability barriers of the dry rheology, high strain rate case. Therefore, no transition in the style of volcanism is expected in this model. However, the melt trapped at the barrier becomes less ultramafic. This transition would not take place above mantle plumes, as, in this case, deep barriers are predicted throughout the Martian history.

Increasing the strain rate while still assuming a wet rheology results only in elevated permeability barriers, which may not be effective at concentrating volcanism, or generates no barrier at all (Figure 2.5f). In this model, we expect to see

flood volcanism (Figure 2.7b) dominating throughout Martian history until the lithosphere is so cold that melt is trapped at depth and metasomatizes the mantle (Figure 2.7d). That cessation of volcanic activity takes place somewhat later than in the high strain rate, anhydrous models and when mantle temperature is high. This model inspires an alternative view of the Hesperian and Amazonian activity in which melt simply rose unimpeded through the lithosphere above mantle plumes and forms widespread volcanic flows throughout that period. It does not explain the formation of central edifices.

Strain rate, mantle temperature, and, to some extent, hydration levels, are expected to vary from place to place. We see that over the first billion year of Martian history, the permeability barrier was likely to be at the base the lithosphere, unless strain rate was high and the mantle hydrated. Low-relief central volcanoes and regional plains are expected at the surface. From 3.5 to 2.5 billion years ago, elevated barriers become increasingly more likely, increasing the likelihood of plain volcanism, especially where strain rate is high. Although central volcanoes are still possible, the lithosphere becomes generally more permeable, which may explain the abundance of plain volcanism in the Hesperian. Later on, as the lithosphere becomes progressively colder, melt is arrested at deeper and deeper depths and plain volcanism is replaced by widespread mantle metasomatism. In a sense, melt is trapped in an underground cycle, being generated at the base of the lithosphere but rising only halfway towards the surface. Central volcanoes are still possible but only where mantle temperature is elevated, perhaps explaining why volcanism localizes toward Elysium and Tharsis.

2.5 Conclusion

Permeability barriers have likely formed in the Martian lithosphere throughout its geologic history. Areas of tectonic activity and particularly wet regions of the mantle may produce shallower permeability barriers or prevent their formation. Deep permeability barriers may cause the formation of localized volcanic edifices such as the Tharsis Montes while shallow permeability barriers may be linked to dispersed lava flows. Permeability barriers may be breached by processes such as thermal erosion, cracking, or crustal assimilation. Further work is needed to assess the significance of these mechanisms.

Chapter 3: Barriers to Melt Ascent in the Lithosphere of Io with Applications to Heat Pipe Formation

Abstract

Melt from the presumed magma ocean in Io's interior reaches the surface at well documented paterae and hotspots. To do so, melt needs to cross the thermal lithosphere of Io, even though, as it loses heat, it may stall inside the lithosphere. The heat pipe model of Io allows for melt to travel from the molten asthenosphere to the surface at discrete points, however unless these heat pipes are billions of years old and constant in both location and flux, melt must ascend through the cold lithosphere at other locations to form new melt conduits. We model here the crystallization sequence of melts as they rise through the lithosphere of Io and determine under what conditions a permeability barrier may form. The barrier is generally deep, near the base of the lithosphere regardless of lithospheric thickness or mantle temperature, but can be elevated 100s of meters to several kilometers in areas of high strain rate ($\dot{\varepsilon}$=10^{-9} s^{-1}) or low resurfacing rate (v=0.02 cm/yr). We propose a feedback mechanism where regions closer to a heat pipe experience a higher resurfacing rate, driving the permeability barrier deeper, while regions away from a heat pipe experience a lower resurfacing rate allowing the permeability barrier to elevate. Melt flows up the resulting regional slope of the lithosphere, concentrates to elevated pockets, releases heat as it crystallizes, and changes the thermal profile so that melt can ascend further, eventually creating a new heat pipe through the lithosphere while the old heat pipe closes. Melt may also ascend along planes of deformation such as proposed lithosphere scale thrust faults.

3.1 Introduction

Io, the smallest and innermost of the Galilean moons of Jupiter, is the most volcanically active body in the solar system. Intense internal heating driven by tidal dissipation causes melting in the Ionian interior [*Peale et al.,* 1979], likely yielding 20-30 volume % melt in the upper mantle [e.g. *Moore,* 2001; *Keszthelyi et al*., 2007; *Khurana et al*., 2011]. This melt reaches the surface of Io through heat pipes, which are channelized conduits of melt, reaching through the lithosphere from the asthenosphere to the surface [*O'Reilly and Davies,* 1981; *Moore and Webb*, 2013]. Due to the frequency and volume of volcanic eruptions, and a lack of detectable impact craters, it is estimated that the moon buries its surface at an average rate of ~1 cm/year [*Johnson et al*., 1979; *Blaney et al.,* 1995; *Phillips*, 2000; *McEwen et al.,* 2004]. At this rate it takes only 10^6 years to bury the entire surface of Io to a depth of 10 km [*Turtle et al.,* 2007]. For comparison Phanerozoic terrestrial convergent settings bury material at a rate of 0.03-0.3 cm/yr [*Nicoli et al.,* 2016].

Advective heat transfer in heat pipes appears to serve as the dominant mechanism for heat transport through the Ionian lithosphere [*O'Reilly and Davies*, 1981]. Assuming a 1 cm/yr burial rate, heat transfer through conduction is negligible (Figure 3.1). Therefore, away from heat pipes, the lithosphere is expected to be very cold relative to the partially molten asthenosphere underneath it. Essentially the surface temperature (-160˚C) is maintained through the entire thickness of the lithosphere until a sudden thermal boundary layer and the onset of melting (Figure 3.1). The continuous cycle of crustal burial and remelting implies that the crust and lithosphere of Io are equivalent.

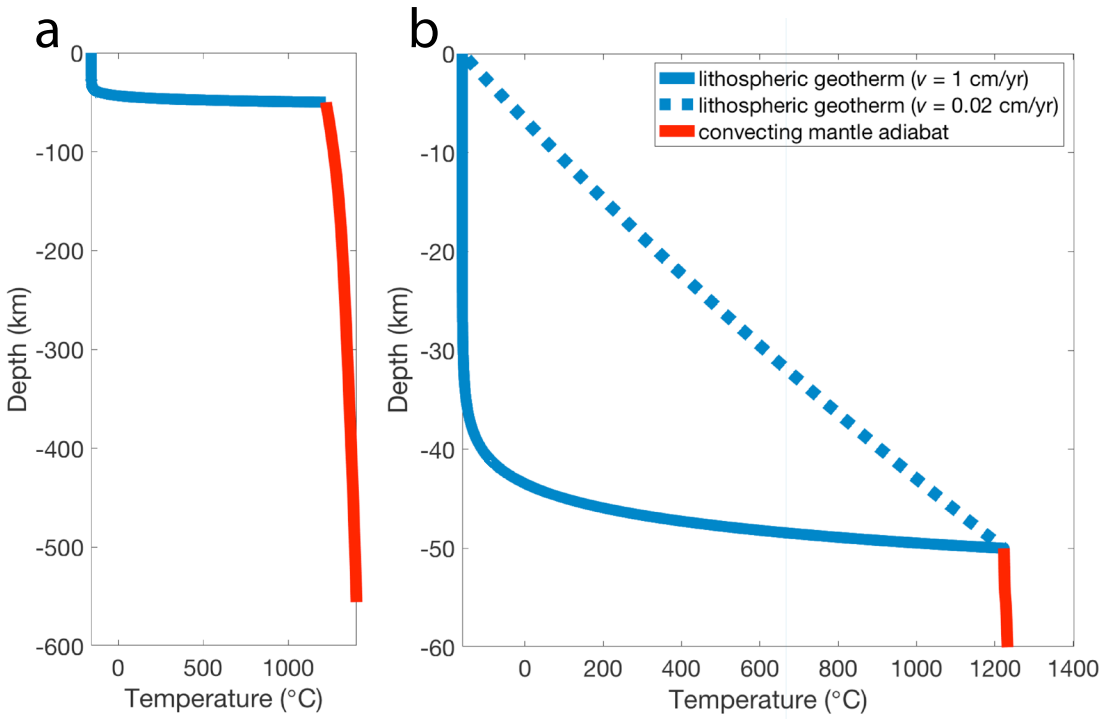

Figure 3.1 - Example temperature profile of the lithosphere (blue) and adiabatic convecting mantle (red). Lithosphere thickness is 50 km and mantle potential temperature is 1350˚C. (a) Whole profile from the surface to a pressure of 3 GPa corresponding to ~550 km depth. (b) Zoomed-in profile highlighting the different lithospheric geotherms from Equation 3.1. The solid blue line uses a burial rate of 1 cm/yr and the dashed blue line uses a burial rate of 0.02 cm/yr.

A permeability barrier may form in the thermal boundary layer, blocking melt from ascending in regions away from preexisting heat pipes, blocking the formation of new conduits for melt ascent in the lithosphere. *Spencer et al.* [2020] studied the formation of a decompaction channel at the base of a permeability assumed to form at the solidus of the downgoing lithosphere. They demonstrated the importance of considering this decompaction channel as well as magmatic intrusions into its crust to reconcile Io's elastic thickness estimates and high melt fraction inferred in its asthenosphere. Here we model the crystallization sequence of melts as they rise

through the lithosphere of Io and determine under what conditions a permeability barrier may form.

Permeability barriers are a likely byproduct of melt transport through planetary lithospheres. As melt is buoyant compared to solid mantle, it ascends along the porous network of inter-grain boundaries in the asthenosphere [*McKenzie*, 1984; *Bercovici et al.,* 2001], cools when it enters the lithosphere, and crystallizes. At some depth the crystallization may reach a quick enough rate where the available melt pathways are clogged by crystals and permeability is essentially reduced to zero, creating a permeability barrier [*Sparks and Parmentier*, 1991; *Korenaga and Kelemen*, 1997]. Melt is unable to rise through the barrier and accumulates underneath it. The pressure in this accumulation zone increases and forces the solid matrix to expand (decompact), forming a decompaction channel [*McKenzie,* 1984; *Sparks and Parmentier*, 1991; *Spiegelman,* 1993; *Spencer et al.,* 2020]. At mid-ocean ridges on Earth, the permeability barrier is likely associated with the multiple saturation point of pyroxene and plagioclase in crystallizing basaltic magma [*Kelemen and Aharonov*, 1998; *Hebert and Montési,* 2010].

In addition to the volcanic features, Io possesses many non-volcanic mountains, some of which exceed 18 km in height [*Schenk et al.,* 2001]. These mountains are thought to exist due to the rapid rate of resurfacing. The resulting subsidence creates excessive compressive stresses in the lithosphere, which creates mountain-building thrust faults [*Schenk and Bulmer*, 1998; *Turtle et al*., 2001; *Jaeger et al.*, 2003; *Kirchoff and McKinnon*, 2009; *Bland and McKinnon*, 2016; *Kirchoff et al.*, 2020]. Due to the coldness of the lithosphere, these thrusts may penetrate to the

molten asthenosphere, serving as a potential conduit for melt ascent. A lack of continuous observation or surface seismic data means that the length and timescales of lithospheric deformation are largely a mystery. The constant subsidence of the surface may result in large regional or localized rates of deformation.

3.2 Methods

The methodology of this paper generally follows that of *Hebert and Montési* [2010] and *Schools and Montési* [2018] (Chapter 2 of this dissertation), who modeled permeability barrier formation in mid-ocean ridges on Earth and in the lithosphere of Mars, respectively. Here we use the MELTS calculator to determine melting and crystallization along many lithospheric geotherms representing a continuum of possible pressures and temperatures inside of Io. Potential permeability barriers in the Ionian lithosphere are then located using a compaction length scale analysis.

The MELTS software collection operates by calculating equilibrium mineral assemblages and melt composition based on a minimization of the Gibbs free energy [*Ghiorso and Sack*, 1995; *Asimow and Ghiorso*, 1998]. MELTS is well calibrated to mantle and chondrite compositions for pressures under 3 GPa, appropriate for the lithosphere of Io. It has been previously used in studies of the magmatic differentiation of Io [*Keszthelyi and McEwen*, 1997] and Ionian eruption temperatures [*Keszthelyi et al.,* 2007]. We use the alphaMELTS front-end interface in order to create scripted loops of MELTS calculations, allowing for thousands of automated calculations [*Smith and Asimow*, 2005].

3.2.1 Melt Generation

Each individual model run begins by performing a continuous (fractional) melting calculation along a mantle isentrope starting from a potential temperature T_a at 3 GPa (~550 km depth) to the depth of the base of the lithosphere. In the isentropic melting calculation, MELTS calculates the composition of the melt, the composition and mineralogy of the residual solid, and the temperature, which is lowered by decompression, phase changes, and melting as the pressure decreases. While the lithosphere of Io is descending, the asthenosphere convects independently of this downward motion [e.g. *Moore*, 2001; 2003; *Tackley*, 2001] resulting in adiabatic melting of the mantle.

Melt is less dense than the solid rock of the mantle, therefore as it is generated, it rises buoyantly through the asthenosphere. The aggregate of ascending melt accumulates at the base of the lithosphere [*Spencer et al.,* 2020]. To model this, the solid composition is calculated, and the generated melt composition is extracted at each calculation step. When the calculation reaches the base of the lithosphere, the temperature T_b is recorded. The resulting aggregate melt composition at the base of the lithosphere is calculated by subtracting the mass of remaining, unmelted solid composition from the mass of the initial mantle composition.

Based on the very high observed surface heat flow, early models estimated that the lithospheric thickness of Io, H, is between 8 and 18 km [*Peale et al.,* 1979]. The presence of the large mountains, which appear to be isostatically compensated at depth [*Turtle et al.,* 2007], yield estimates for H in excess of 50 km. H likely varies across Io, for example it is likely thinner near active hotspots, where the heat flow is

higher, and thicker in colder, non-volcanic regions [*O'Reilly and Davies,* 1981]. We perform runs using values of H from 5 km to 75 km, every 5 km in order to encompass the two end member estimates. It should be noted that due to Io's low gravity (1.796 m s^{-2}; 0.18 Earth gravity) internal pressures are much lower than those assessed in the Earth or other terrestrial planets (only ~27 MPa in the H = 5 km model). The MELTS calculator is well equipped to handle these pressures whereas the high-pressure pMELTS calculator [*Ghiorso et al*., 2002] typically used in terrestrial mantle melting calculations would be inappropriate for this study.

Keszthelyi et al. [2007] stipulated that the maximum possible mantle potential temperature of Io must be 1500ºC, otherwise too much of the mantle would be molten to generate significant tidal heat. There is a minimum mantle potential temperature of 1250ºC, as at any temperature lower than this Io would become less dissipative, leading to a decrease in heating [*Moore*, 2001; *Keszthelyi et al.,* 2007]. We use the range of 1250ºC to 1500ºC, every 5ºC. Note that Io does not cool with time in the traditional sense of other planetary bodies. Due to the tidal heating from Jupiter and the other moons, Io has likely not experienced a large degree of cooling, other than after initial formation. Therefore, the range of mantle potential temperatures considered should not be associated with a potential thermal evolution of Io through time. Instead, the models shown here interrogate the effect of poorly constrained internal conditions on present day permeability barrier formation and the implications for volcanic activity.

We use the estimates of *Keszthelyi and McEwen* [1997] and *Keszthelyi et al.* [2007] for the composition of the bulk silicate Io (Table 3.1). They assumed Io formed from chondritic material, like the rest of the solar system, but was depleted in volatiles due to the temperature extremes around Jupiter [*Lunine and Stevenson*, 1982]. Moment of inertia measurements suggest that Io has an iron-rich core, likely a Fe-Ni-S alloy, that makes up 20 wt.% of the moon [*Anderson et al*., 1996]. The final composition estimate was made by subtracting this core from a CII/CM chondritic composition. We use bulk silicate Io as opposed to the Ionian mantle as a simplification of crustal recycling and mixing with mantle. We assume a dry composition and do not consider the effects of trace elements on melting.

SiO_2	44.24
TiO_2	0.16
Al_2O_3	3.53
Cr_2O_3	0.68
FeO[a]	16.27
MnO	0.33
MgO	31.01
CaO	2.95
Na_2O	0.90

*All Fe represented as FeO. MELTS calculates Fe_2O_3 content from set oxygen fugacity.

Table 3.1 - Major Element Concentrations for Bulk Silicate Io (from Keszthelyi et al., 2007)

It has been suggested that due to high eruption temperatures and exposure to vacuum, a loss of silicon and other elements may result in a mantle composition similar to a calcium-aluminum inclusion (CAI) in chondrules [*Kargel et al.,* 2003]. This composition is well outside the MELTS calibration space, and most Io literature suggests a broadly peridotitic mantle with a basalt/komatiite crust, therefore we do not model this composition.

The MELTS calculator is not calibrated for compositions with sulfur and we therefore do not include the effects of sulfur in our models. We recognize that the majority of the detectable surface of Io is made of sulfur, SO_2, and other sulfur-based

compounds, and early Voyager interpretations suggested that the volcanism and topography of Io could be entirely sulfur based [*Sagan,* 1979]. However, Voyager and Galileo papers suggested that the topography of Io must be supported by a silicate crust [*Carr et al.,* 1979; *Clow and Carr,* 1980; *Turtle et al.,* 2001]. Galileo observations confirmed that the bulk of Ionian volcanism does appear to be silicate [*McEwen et al.,* 1997; *McEwen et al.,* 1998; *McEwen et al*., 2000]. Sulfur and SO_2 volcanism likely occurs as a secondary process due to melting of crustal sulfur sources [e.g. *Williams and Howell*, 2007]. Additionally, due to increasing compressive stresses in the lithosphere with depth, volatiles such as SO_2 may be squeezed out of the system, resulting in sulfur surface volcanism that is not reflective of deeper magmatism [*Jaeger et al.,* 2003; *Turtle et al*., 2007]. Sulfur compounds cover much of the surface and have a strong signature in remote sensing datasets but may not represent the bulk of the Ionian crust.

We assume an oxygen fugacity at the Iron-Wüstite (IW) buffer. *Zolotov and Fegley* [1999] concluded that the magma source region of modern lava flows is likely significantly more oxidized than the IW buffer, but possibly closer to IW at depth. The oxygen fugacity of the magma source may not be representative of the whole mantle, and *Schools and Montési* [2018] (Chapter 2 of this dissertation) determined that oxygen fugacity is not a significant factor in the development of permeability barriers. Therefore, oxygen fugacity is fixed at the IW buffer and not varied in this study.

3.2.2 Melt Crystallization

The melt generated in step 1, which represents the accumulated aggregate melt composition, is used as the starting composition for a MELTS calculation of batch crystallization along a fixed decreasing pressure and temperature path representing a lithosphere geotherm. The geotherm is calculated from *O'Reilly and Davies* [1981], assuming negligible heating in the lithosphere:

$$T = (T_b - T_s)\frac{e^{z/l} - 1}{e^{D/l} - 1} + T_s \tag{3.1}$$

where T_s is the surface temperature (-160 ºC) and z is the depth. T_b is the temperature at the base of the lithosphere (top of the asthenosphere), which is taken from end conditions of the mantle melting calculation. D is the thickness of the thermal lithosphere. Due to the transition from cold, solid lithosphere to hot, molten asthenosphere, the thermal lithosphere and elastic lithosphere are essentially the same thickness, therefore $D = H$ in these models. The parameter l is defined as $l = \kappa/v$ where κ is the thermal diffusivity (10^{-6} m^2/s) and v is the surface burial rate. The temperature profile is calculated every 0.27 bar corresponding to every 5 m depth, in order to observe crystallization behaviors occurring at depths with large temperature gradients.

The ascent rate of the melt is assumed to be slow enough so that the temperature of the melt and solid matrix are in equilibrium. As a simple check on the equilibrium assumption, we use the Péclet number for heat transfer between solid and melt in a porous medium [e.g. *Spiegelman and Kenyon*, 1992; *Schmeling et al*., 2018]:

$$\mathrm{Pe} = \frac{wd}{\kappa} \tag{3.2}$$

where w is the melt velocity relative to the solid matrix, d is the grain size, and κ is the thermal diffusivity. The Péclet number shows the ratio of thermal advection to thermal diffusion. If Pe < 1, the system is in thermal equilibrium between the solid matrix and melt, and when Pe > 1, the system is in thermal disequilibrium. Assuming the velocity of the melt flowing through the porous matrix is $\sim 10^{-9}$ m/s, as has been suggested for melt percolation velocities under mid-ocean ridges [*Petford et al*., 1995; *Keller et al*., 2017; *Schmeling et al*., 2018], a length scale equal to the grain size (3 mm), and a thermal diffusivity of 10^{-6} m^2/s, the Péclet number is 3×10^{-6}, indicating that the melt and solid are in thermal equilibrium. The upwards melt velocity can be increased up to 3.33×10^{-4} m/s, or 10.5 km/yr and remain in equilibrium.

The multicomponent, two-phase chemical equilibrium required to justify the batch crystallization calculation is more complex to determine than thermal equilibrium. Using the simplified, diffusion-controlled Damköler number of *Korenaga and Kelemen* [1998], we can make a rough, order of magnitude constraint on the equilibrium requirements:

$$\mathrm{Da} = \frac{\tau_{\mathrm{ma}}}{\tau_{\mathrm{sd}}} = \frac{L/w}{d^2/D_s} \tag{3.3}$$

where τ_{ma} is the melt advection timescale and τ_{sd} is the solid diffusion timescale. Therefore for large Damköler number values, where the melt advection timescale is larger than the diffusion timescale, the system can be considered to be in chemical

equilibrium. L is the length scale of melt migration, w is the melt velocity through the solid matrix, d is the grain size, and D_s is the solid diffusion rate. The solid diffusion rate will vary depending on many factors including the mineral components involved and the temperature, but for this simple justification we use the interdiffusion rate of Fe-Mg in olivine at 1200˚C, which is 10^{-15} m^2/s. Using the same grain size (3 mm) and melt velocity (10^{-9} m/s) as in Equation 3.2, and using a small length scale of 1 km (See Fig. 3.2), yields a Damköler number of ~100. Further increasing the length scale increases the Damköler number, suggesting that the system can be considered in chemical equilibrium, appropriate for batch crystallization. For a more sophisticated analysis of disequilibrium melting calculations involving a multicomponent system, including Damköler numbers, refer to *Spiegelman et al.* [2001] and *Rudge et al.* [2011].

The melt both cools and decompresses as it rises along this path. Due to the sharpness of the thermal boundary layer in most cases (Figure 3.1) cooling is a much more significant factor than the decompression and therefore mineral phases begin to crystallize. In the example of Figure 3.2a, a small mass of olivine has crystallized before reaching the base of the lithosphere at 50 km depth as the aggregate melt adjusted to the temperature and pressure conditions at the top of the asthenosphere. Once cooling begins at the base of the lithosphere, olivine starts to crystallize at a faster rate (Figure 3.2b). It is followed by clinopyroxene a few hundred meters higher in elevation. In this example calculation the onset of clinopyroxene crystallization corresponds to a dramatic increase in crystallization rate (Figure 3.2b). A second

phase of clinopyroxene, more enriched in titanium and aluminum follows, crystallizing at a lower rate.

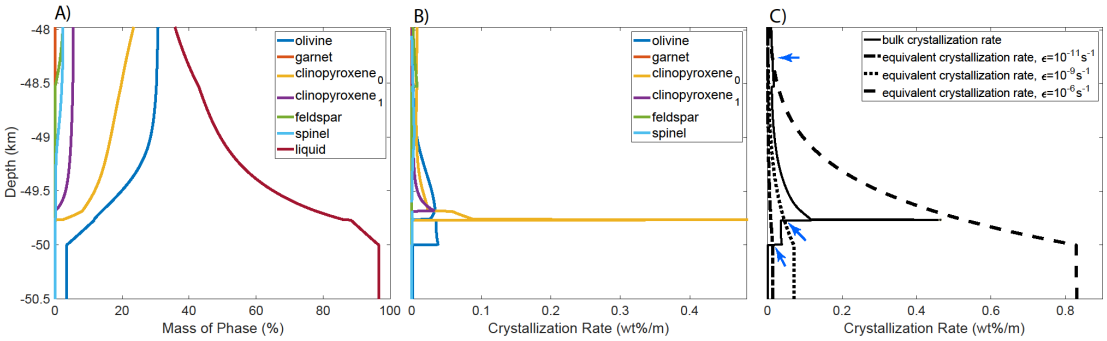

Figure 3.2 - Crystallization of melt derived from a mantle with a potential temperature of 1350˚C through a 50 km thick lithosphere and a resurfacing rate of 1 cm/yr. (a) Phase abundance expressed as a percentage of the original mass of the melt in the calculation. Liquid mass is not at 100% at the base of the lithosphere due to the stability of some olivine. Liquid mass does not reach 0% due to the calculation exiting the MELTS calibration space. Crystallization occurs as melt cools. (b) Crystallization rate of individual minerals, expressed as the weight percent of original melt crystallized at each pressure step (every 0.27 bar; 5 m). (c) Bulk crystallization rate of all mineral phases combined (solid line), compared to the decompaction-induced equivalent crystallization rate, X_e, given by Equation 3.9 assuming various strain rates (thin dashed and dotted lines). The intersection of bulk and equivalent crystallization rate (blue arrows) indicates the depth of possible permeability barriers. Lower strain rates in the lithosphere result in permeability barriers at the base of the lithosphere while higher strain rates result in barriers at shallower depths. The "nominal" strain rate of 10^{-15} s^{-1} plots between the crystallization rate and the 10^{-15} s^{-1} decompaction, not resolvable at the displayed scaling of the figure.

As the more iron- and magnesium-rich crystals of olivine and clinopyroxene form, the remaining melt becomes silica-saturated and feldspar and spinel begin to crystallize one kilometer above the base of the lithosphere. The calculation terminates with less than 40% of the melt remaining as the composition of the remaining melt exits the calibration space. Other calculations may terminate due to the calculation reaching the lower MELTS temperature limit of ~600ºC. Compared to previous calculations for the Earth or Mars, this crystallization sequence takes place over a

very narrow depth range, due to the sharp thermal boundary layer considered in this specific example.

The total crystallization rate (Figure 3.2c) is the aggregate of all the individual mineral phases. The two primary features of the example, and most of the other calculations, are a moderate rate increase at or just above the base of the lithosphere where olivine begins to crystallize, and a dramatic crystallization rate peak corresponding to the onset of clinopyroxene crystallization. Under most conditions permeability barriers will be detected at these two crystallization features (see section 3.2.3), and therefore the melt composition and minerals above these two points are not considered realistic.

The calculations in this paper suppress nepheline as possible output mineral. When not suppressed, nepheline is a common output mineral late in the crystallization sequence when there is a relative enrichment in SiO_2, Al_2O_3, Na_2O, and K_2O. However, this composition is outside the MELTS calibration space and its output should be considered unrealistic. In particular, nepheline appears to compensate for known limitations in the compositional space of spinel considered by MELTS [*Hamecher et al.,* 2013]. When nepheline is suppressed, a more realistic feldspar is generated; however, the melt composition is still outside the calibration space. See *Schools and Montési* [2018] (Chapter 2 of this dissertation) for a more detailed commentary on nepheline in MELTS calculations. In all but the most extreme cases, the permeability barrier is detected deeper in the lithosphere, earlier in the calculation, relative to the appearance of nepheline. Therefore, nepheline and melt compositions shallower than that point are considered irrelevant.

3.2.3 Permeability Barrier Identification

Ionian permeability barriers are located in the MELTS crystallization output where the compaction length is greater than the critical compaction length [*Korenaga and Kelemen*, 1997; *Hebert and Montési*, 2010]

$$\delta_c \geq \delta_c^* \tag{3.4}$$

The compaction length is the length scale over which a fluid moving through a viscous, porous matrix may support a pressure gradient [*McKenzie*, 1984]:

$$\delta_c = \sqrt{\frac{k_\phi\left(\xi + \frac{4}{3}\eta\right)}{\mu}} \tag{3.5}$$

where ξ is the bulk viscosity of the matrix, η is the shear viscosity of the matrix, and μ is the viscosity of the fluid (the melt). Permeability, k_ϕ, in this model is defined as

$$k_\phi = \frac{\phi^n d^2}{C} \tag{3.6}$$

where ϕ is the porosity, n is a power law exponent, d is grain size, and C is a geometric factor related to the dihedral angle [*McKenzie,* 1984; *von Bargen and Waff*, 1986; *Cheadle*, 1989; *Wark and Watson,* 1998; *Ricard et al.,* 2001; *Connolly et al.,* 2009]. Porosity is assumed to be 0.01 and grain size is assumed to be 3 mm. Model parameters n and C are taken from *Miller et al.* [2014] and are listed in Table 3.2.

Melt viscosity (μ) is assumed to be 1 Pa s. The bulk and shear viscosities of the matrix are related through the porosity: $\xi = \eta/\phi$. The shear viscosity is modified from *Kirby and Kronenberg* [1987] as:

$$\eta = \left[\frac{(2\dot{\varepsilon})^{1-m}\exp\left(\frac{Q}{RT}\right)}{2A}\right]^{\frac{1}{m}} \quad (3.7)$$

where $\dot{\varepsilon}$ is the strain rate, m is a power law exponent, Q is the activation energy, R is the gas constant (8.314 J mol^{-1} K^{-1}), T is the temperature given by Equation 3.1, and A is a pre-exponential factor. We utilize the dry flow law parameters of *Hirth and Kohlstedt* [2003] for m, Q, and A (Table 3.2).

While several studies have been published focusing on the stress state and structure of the Ionian lithosphere, as pertaining to mountain building [e.g. *Bland and McKinnon et al.,* 2016], constraints on the strain rate are limited. On the Earth, actively deforming continents exhibit regional strain rates of 10^{-15} to 10^{-12} s^{-1} [*Pfiffner and Ramsay*, 1982; *Buck*, 1991; *Karato,* 2010; *Fagereng and Biggs*, 2018]. The rapid resurfacing of Io may lend itself to higher regional strain rates, but a definitive statement cannot be made on this topic. As this model is one dimensional and not time dependent, we use a range of strain rates encompassing many possible lengthscales and magnitudes of deformation. Our primary results use strain rates of 10^{-15}, 10^{-13}, 10^{-11}, and 10^{-9} s-^{1}, representing regional deformation to potential shear zones.

Name	Symbol	Value	Unit	Equation
Temperature	T	$(T_a - T_s)\frac{e^{z/l} - 1}{e^{D/l} - 1} + T_s$	˚C	(3.1) (3.6)
Temperature at base of lithosphere	T_b		˚C	(3.1)
Surface temperature	T_s	-160	˚C	(3.1)
Depth	z		m	(3.1) (3.8) (3.9)
Thickness of lithosphere	D		m	(3.1)
Conduction length scale	l	κ/v	m	(3.1)
Thermal diffusivity	κ	10^{-6}	m^2s^{-1}	(3.1) (3.2)
Surface burial rate	v	1 (nominal), 0.02 (slow)	ms^{-1}	(3.1, within l)
Grain size	d	3	mm	(3.2) (3.3) (3.6)
Melt velocity	w	10^{-9}	ms^{-1}	(3.2) (3.3)
Lithospheric melt migration length scale	L	1	km	(3.3)
Solid diffusion rate	D_s	10^{-15}	m^2s^{-1}	(3.3)
Compaction length	δ_c	$\sqrt{\frac{k_\phi\left(\xi + \frac{4}{3}\eta\right)}{\mu}}$	m	(3.4) (3.5) (3.9)
Critical compaction length	δ_c^*	$\left(\frac{\mathrm{d}T}{\mathrm{d}z}\frac{\mathrm{d}f}{\mathrm{d}T}\right)^{-1}$	m	(3.4) (3.8)
Permeability	k_ϕ	$\frac{\phi^n d^2}{C}$	m^2	(3.5) (3.6)
Bulk viscosity of matrix	ξ	η/ϕ	Pa s	(3.5)
Shear viscosity of matrix	η	$\left[\frac{(2\dot{\varepsilon})^{1-m}\exp\left(\frac{Q}{RT}\right)}{2A}\right]^{\frac{1}{m}}$	Pa s	(3.5) (3.7)
Melt viscosity	μ	1	Pa s	(3.5)
Porosity	ϕ	0.01	unitless	(3.6)
Power law exponent	n	2.6	unitless	(3.6)
Geometric factor	C	56	unitless	(3.6)
Power law exponent	m	3.5	unitless	(3.7)
Activation energy	Q	535	kJ mol^{-1}	(3.7)
Gas constant	R	8.314	J $mol^{-1}K^{-1}$	(3.7)
Pre-exponential factor	A	1.1×10^4	$MPa^{-n}s^{-1}$	(3.7)

Table 3.2 - Parameters and Variables Used in the Identification of Ionian Permeability Barriers in MELTS Output Files

The critical compaction length is essentially the inverse of the crystallization rate:

$$\delta_c^* = \left(\frac{\mathrm{d}T}{\mathrm{d}z}\frac{\mathrm{d}f}{\mathrm{d}T}\right)^{-1} \tag{3.8}$$

where f is the melt fraction by weight and $\mathrm{d}f/\mathrm{d}T$ is the crystallization rate provided by the MELTS calculator.

In order to create a direct comparison to crystallization and compaction, we formulate a decompaction-induced equivalent crystallization rate of the lithosphere:

$$X_e = \left(\delta_c \frac{\mathrm{d}T}{\mathrm{d}z}\right)^{-1} \tag{3.9}$$

where δ_c is the compaction length from Equation 3.5. The depth of a permeability barrier is defined as the deepest intersection of the equivalent crystallization rate X_e and the thermodynamically inferred crystallization rate $\mathrm{d}f/\mathrm{d}T$.

3.3 Results

3.3.1 Composition of mantle melt

The adiabatic melting calculation of section 3.2.1 yields a range of melt compositions, dependent on the mantle potential temperature and lithospheric thickness. The mantle potential temperature is the primary driver of melt composition, with small deviations to lower percent melts in models with thicker lithospheres (Appendix B, Figure B1). As represented by the degree of partial melting, the generated melts ranged from a ~4 to ~18% melt of bulk silicate Io. The

SiO_2 content of the melts range from an intermediate ~55% at mantle potential temperatures of 1225°C to an ultramafic ~40% at 1500°C (Appendix B, Figure B2).

This methodology produces melt fractions systematically lower than those generated in MELTS modeling of *Keszthelyi et al*. [2007]. For example, at a depth of 50 km and a mantle potential temperature of 1400°C, this methodology produces a melt fraction of ~9 vol%, whereas *Keszthelyi et al.* [2007] reported ~35 vol% melt at similar conditions. This difference is likely due to differing methodologies in calculating the thermal profiles of the asthenosphere. Their methodology assumed that the surface eruption temperature is equal to the potential temperature, whereas this methodology calculates the potential temperature via a metastable one bar calculation to obtain a corresponding entropy (S) for the isentropic mantle melting calculation. As the solid decompresses (representing rising from depth), the solid melts and the isentropic path cools, reaching temperatures down to 1100ºC near the base of the lithosphere.

3.3.2 Permeability Barrier Formation Conditions: Nominal Model

Our nominal model, where the resurfacing rate (v) is 1 cm/yr, leads to results that are representative of the crystallization behavior for all modeled lithospheric thicknesses and mantle potential temperatures (Figure 3.2). As described in section 3.2.2, olivine crystallization increases at the base of the lithosphere, followed by the onset of clinopyroxene, then a second clinopyroxene phase, feldspar, and finally spinel and garnet. Each phase enters the crystallization sequence in rapid succession due to the compressed temperature gradient at the base of the lithosphere that results

from burial and downwelling (Figure 3.1). Generally, these crystallization sequences yield crystallization rates similar to those seen in Figure 3.2b, of the order of 0.1 wt%/m where two main peaks can be seen: the first smaller olivine peak at the base of the lithosphere, and the second larger peak at the onset of clinopyroxene crystallization.

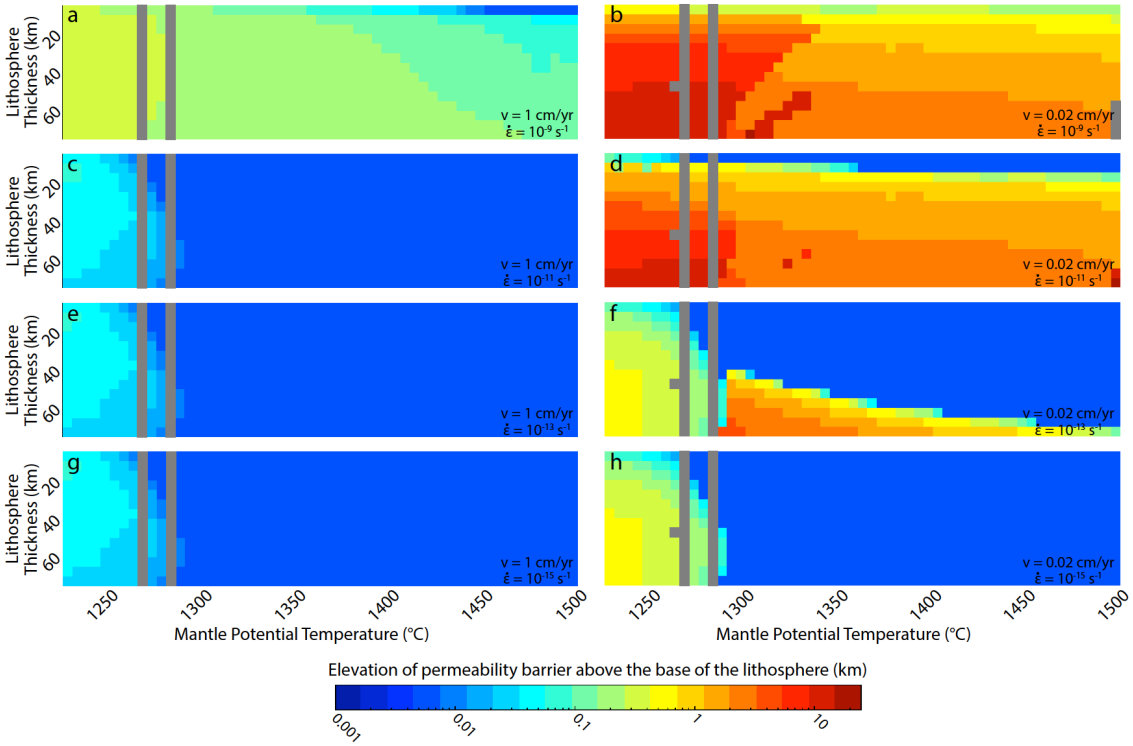

Figure 3.3 - Elevation of the permeability barrier above the base of the lithosphere as a function of lithosphere thickness and mantle potential temperature. Larger elevations correspond to shallower barrier depths. Each row represents an assumed lithospheric strain rate. a and b: $\dot{\varepsilon} = 10^{-9}\ s^{-1}$; c and d: $\dot{\varepsilon} = 10^{-11}\ s^{-1}$; e and f: $\dot{\varepsilon} = 10^{-13}\ s^{-1}$; and g and h: $\dot{\varepsilon} = 10^{-15}\ s^{-1}$. Each column represents a burial rate. a, c, e, and g: $v = 1\ cm/yr$; b, d, f, and h: $v = 0.02\ cm/yr$. Note the color bar is on a logarithmic scale. The grey bars represent conditions where the MELTS calculator could not compute the initial conditions.

Figure 3.2c shows the bulk crystallization rate (solid line) plotted along with the equivalent crystallization rate X_e from Equation 3.9 for different lithospheric strain rates. The nominal model assumes a strain rate of 10^{-15} s^{-1}, comparable to

terrestrial continental values. Decompaction at a strain rate of 10^{-15} s^{-1}leads to an equivalent crystallization rate that intersects the bulk crystallization rate peak of olivine at the base of the lithosphere. This indicates that a permeability barrier is expected at the very base of the thermal lithosphere (Figure 3.3g). Note that in our temperature profiles (Figure 3.1) the transition from lithosphere and asthenosphere is abrupt. Details of convection in the asthenosphere and consideration of latent heat of fusion and crystallization would smooth that transition. Nevertheless, the barrier under the nominal conditions of slow strain rate and rapid burial would be expected to develop as soon as the temperature starts to decrease.

Slightly higher barrier elevations (50-100 m above the base of the lithosphere) occur with mantle potential temperatures lower than 1300°C. These slight differences in elevation are due to a delay in olivine crystallization to cooler temperatures. This behavior may be due to the melt being more felsic at lower mantle potential temperatures.

As the majority of the melt is trapped beneath the permeability barrier at the base of the lithosphere and did not ascend, cool, and crystallize, its composition is effectively the same as the results of the melting calculation (Section 3.3.1). The SiO_2 content ranges from 55 wt% at lower mantle potential temperatures to 40 wt% at higher mantle potential temperatures (Appendix B, Figure B3). Mg# ranges from 32 to 38 (Appendix B, Figure B4).

3.3.2.1 Effect of strain rate

A permeability barrier forms where the crystallization rate of the ascending melt is larger than the decompaction-induced equivalent crystallization rate of the

solid matrix, which is dependent on the compaction length. In turn, the compaction length is primarily dependent on the bulk and shear viscosities of the solid matrix (Equation 3.5), which themselves are primarily dependent on the strain rate (Equation 3.7). Increasing the strain rate in the lithosphere should decrease viscosity and compaction length, and therefore increase the magnitude of the decompaction-induced equivalent crystallization rate of the solid matrix and bypass smaller crystallization peaks. Thus, increasing strain rate may lead to permeability barriers that form at shallower depths than in the nominal case above.

Assuming the same burial rate of 1 cm/yr as before, raising the strain rate several orders of magnitude to $\dot{\varepsilon}=10^{-13}$ s^{-1} (Figure 3.3e) or 10^{-11} s^{-1} (Figure 3.3c) does not change the depth of the permeability barrier compared to the nominal case of $\dot{\varepsilon}=10^{-15}$ s^{-1} (Figure 3.3g). Under these conditions the magnitude of the decompaction-induced equivalent crystallization rate is not large enough to overcome the crystallization rate peak of olivine (Figure 3.2b). The matrix is still too viscous to accommodate the newly crystallized olivine crystals. In order to observe a significant difference in permeability barrier depth, the strain rate must be raised to $\dot{\varepsilon}=10^{-9}$ s^{-1}. With a lithospheric strain rate to $\dot{\varepsilon}=10^{-9}$ s^{-1} (Figure 3.3a) the magnitude of X_e is increased enough to exceed the crystallization rate of olivine at the base of the lithosphere. Thus, the permeability barrier rises to the depth of initial clinopyroxene crystallization, typically 100-300 m above the base of the lithosphere, which exhibits much faster crystallization rates than olivine (Figure 3.2b).

Due to the high crystallization rate typically associated with the initial formation of clinopyroxene crystals, the matrix strain rate must be much higher than

$\dot{\varepsilon}=10^{-9}$ s^{-1} to let melt ascend past the clinopyroxene onset peak. In the example of Figure 3.2c, the strain rate in the lithosphere must be $\dot{\varepsilon}=10^{-6}$ s^{-1} in order to for melt to ascend. In this case the permeability barrier typically forms ~ 3 km above the base of the lithosphere at the crystallization peak of feldspar. Crystallization rate in that region is low, but the mantle temperature is significantly lower than at the base of the lithosphere. The mantle is cold and viscous enough that even the slowly crystallizing late phases can lead to the formation of a permeability barrier. We do not explore these models in detail in part because this late crystallization sequence is not particularly reliable but mainly because such high strain rates are unlikely to be maintained over regional scale. Instead they might occur in localized areas, possibly in shear zones associated with slip along Io's mountain building thrust faults.

Under conditions of nominal resurfacing rate and strain rates of $\dot{\varepsilon}=10^{-13}$ s^{-1} or 10^{-11} s^{-1}, the melt compositions under the barrier are identical to the nominal model, as the melt does not ascend or crystallize more than in the nominal model. The melt compositions alter slightly in the $\dot{\varepsilon}=10^{-9}$ s^{-1} model, as the melt can cool and crystallize for several hundred meters further into the lithosphere. As the main minerals to crystallize are the more Fe and Mg-rich minerals (olivine and clinopyroxene), the melts present at the permeability barrier typically yield SiO_2 concentrations 1-2 wt% higher and Mg numbers ~5 units lower than at the base of the lithosphere. Higher strain rates yield increasingly felsic melts as the more mafic minerals crystallize deeper at higher temperatures.

3.3.2.2 Effect of resurfacing rate

The resurfacing rate is the primary control on lithosphere temperature for regions away from heat pipes (Equation 3.1). Lowering the resurfacing rate from the nominal 1 cm/yr to a minimum 0.02 cm/yr (required to prevent preservation of impact craters; Johnson et al., 1979) results in a much more progressive temperature profile throughout the lithosphere (Figure 3.1). The melt cools much more slowly as it ascends past the base of the lithosphere and crystallization is allowed to occur over a larger depth range (Figure 3.4). As crystallization rates at the base of the lithosphere decrease, permeability barriers are expected to form at shallower depths.

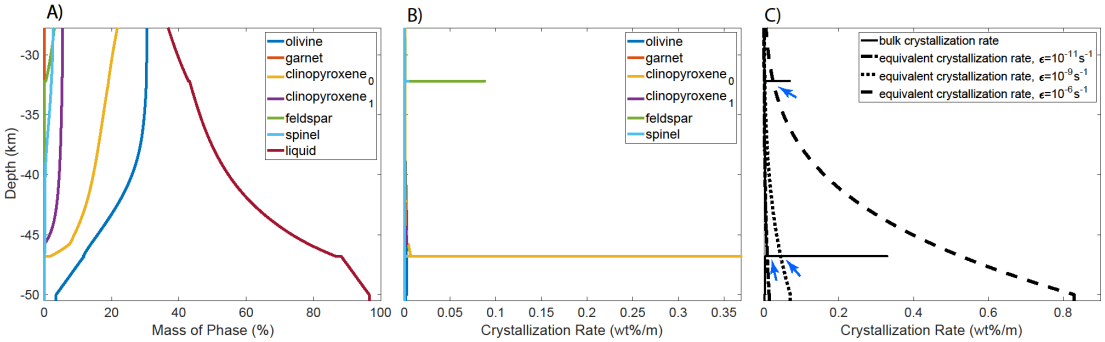

Figure 3.4 - Crystallization of melt derived from a mantle with a potential temperature of 1350˚C through a 50 km thick lithosphere and a resurfacing rate of 0.02 cm/yr. Other than the reduced resurfacing rate, conditions and figure explanations are the same as Figure 3.2

In the model with nominal strain rate of 10^{-15} s^{-1}, but a decreased resurfacing rate of 0.02 cm/yr (Figure 3.3h), the results are largely similar to those of the nominal model (Figure 3.3g). The individual crystallization profiles resemble that of Figure 3.2, however the crystallization rates are lower and occur over a depth range of tens of km instead of 1 to 2 km. The permeability barrier is still typically detected at the base of the lithosphere in this case as the initial olivine crystallization peak is too large for deformation at low strain rates to counter. A more progressive and realistic

transition from asthenosphere may be able to reduce the crystallization rate of olivine to the point that a permeability barrier would not form at the base of the lithosphere, but this concept cannot be tested quantitatively at this point. Permeability barriers in calculations with lower mantle potential temperatures are slightly more elevated (up to 700 meters) compared to the nominal case due to the olivine crystallization onset is delayed to slightly lower temperatures. The effect is more pronounced than in the nominal model due the lower temperature gradient at the base of the lithosphere.

Increasing the strain rate in the decreased resurfacing rate models drastically changes the depth of the permeability barrier. With a lithospheric strain rate of 10^{-13} s^{-1} (Figure 3.3f and 3.4), the permeability barrier forms several kilometers higher in the calculations with higher lithosphere thicknesses and mantle temperature. The most elevated barrier forms 10 km above the base of the lithosphere for a mantle potential temperature of 1290˚C and a lithosphere thickness of 70 km. These barriers form at the first clinopyroxene crystallization rate peak, which is several km above the base of the lithosphere due to the more progressive temperature profile compared to the nominal model. The elevated barriers are not observed in the models with smaller lithospheric thickness as the shorter temperature gradient yields a more rapid crystallization of olivine that the decompaction cannot overcome. The barrier is also not elevated at temperatures less than ~1300°C as the olivine crystallization rate is still high enough to form a barrier.

Further increasing the strain rate to 10^{-11} s^{-1} with a low resurfacing rate (Figure 3.3d and 3.4) yields more elevated permeability barriers in thinner lithospheres. Most of the calculations show permeability barriers located at least 1 km

above the base of the lithosphere except for the thinnest lithospheres. The initial olivine crystallization peak is overcome even for models with mantle potential temperatures lower than 1300˚C. In this case the permeability barriers can located tens of kilometers higher than the base of the lithosphere, and several km than the barrier predicted for higher mantle potential temperatures with similar lithosphere thicknesses. These crystallization profiles show the first crystallization of clinopyroxene occurring at a slower rate than the higher temperature mantle models. Therefore, the deformation profile intersects higher on the temperature profile either at depth were olivine and clinopyroxene crystallize simultaneously, without forming a peak or at the onset of feldspar crystallization (Figure 3.4). The models with a strain rate of 10^{-9} s^{-1} (Figure 3.3b. and 3.4) continue the behavior of the $\dot{\varepsilon}=10^{-11}$ s^{-1} model, extending to thinner lithosphere the conditions for which kilometer scale barrier elevations are observed. The region of non-peak or feldspar associated permeability barriers extends to higher mantle potential temperatures in thinner lithosphere models.

The models with low resurfacing rate and low strain rates ($\dot{\varepsilon}=10^{-15}$ s^{-1} and 10^{-13} s^{-1}) show similar compositions of melt underneath the permeability barrier as in the nominal model. As the temperature change near the base of the lithosphere is drastically reduced, less minerals crystallize out during ascent, even if the permeability barrier is higher than in the nominal model. In the models with strain rates of 10^{-11} s^{-1} and 10^{-9} s^{-1} and cooler mantle potential temperature, the melt composition at the permeability does differ from that in the nominal model. The melts here appear more felsic, with SiO_2 up to 60 wt%. The models with higher mantle

potential temperatures also lead to melts that are again slightly more elevated in SiO_2 but remain in the mafic range with 40-50 wt% SiO_2. Mg numbers in the felsic region as low as ~5 whereas the most mafic melts show Mg numbers around 30.

3.4 Discussion

3.4.1 Melt ascent above the nominal permeability barrier

Melt clearly reaches the surface of Io, implying that melt is able, at least locally, to rise above the permeability barrier. Transport above the barrier does not need to take place everywhere in the lithosphere and could be limited to heat pipes. Heat pipes deliver much of the heat flux to the surface of Io, and much of that heat is advected by melt rather than conduction or solid-state advection [*Moore and Webb,* 2013; *Spencer et al.,* 2020]. However, it is unlikely that the same heat pipes and eruptive centers of Io could continuously operate for billions of years as the entire lithosphere is recycled over just a few millions of years. Heat pipes may slowly close as melt crystallizes on the edges or they may be truncated due to lithosphere scale thrust faults and associated deformation. New heat pipes must form in order to continuously extract melt to the surface of Io; however in our models a permeability barrier always forms near the base of the lithosphere, or much closer to the base of the lithosphere than to the surface, blocking melt ascent. We discuss here three possibilities that may enable melt to ascent past the barrier and form a heat pipe: thermal erosion, cracking, and faulting.

3.4.1.1 Thermal Erosion

Thermal erosion is a possible feedback between the thermal structure of the lithosphere and the location of the permeability barrier [*England and Katz,* 2010]. As melt collects and crystallizes beneath the permeability barrier, heat is released due to the phase change from liquid to solid. Heat released by melt crystallization may increase the temperature at the base of the lithosphere, allowing some melt to rise past the nominal permeability barrier level at some locations. As melt buoyantly rises, it would be focused to any location where the barrier is slightly elevated [e.g. *Sparks and Parmentier*, 1991; *Spiegelman*, 1993; *Montési et al.,* 2011], release more heat from crystallization, and elevate the barrier further [*England and Katz*, 2010]. This process has not yet been modeled in detail. However, it may allow for melt to ascend along a perturbed permeability barrier to some depth where another structure, such as a more traditional heat pipe, forms to allow melt to access the surface.

Thermal erosion may become unstable, however it is limited by the available melt supply from below. Further work is needed, but it is possible that competition between melt supply and thermal erosion may result in a wavelength instability of permeability barrier peaks [*Schools and Montési*, 2018] (Chapter 2 of this dissertation). These apices of melt would presumably lead to volcanic centers at the surface, in a way similar to the way that volcanic arc location may represent melt collection at the apex of a permeability barrier at terrestrial subduction zones [*Ha et al.,* in prep]. Once melt collects at a specific location at the base of the lithosphere, it can further rise either through the same process of thermal erosion or as a melt diapir [*Keller et al.,* 2013]. Focusing to a thermal eroded base of the lithosphere may

explain the non-random spacing of volcanoes observed on the surface of Io [*Hamilton et al*., 2013].

3.4.1.2 Cracking

While the base of the lithosphere may be hot and ductile, the rest of the lithosphere is colder and within the brittle regime. Overpressure develops in the decompaction channel as buoyant melts rise and forces open the pore space [*Spiegelman,* 1993; *Spencer and Katz*, 2020]. Cracking and diking may result from this overpressure, allowing melt to ascend quickly in a disequilibrium fashion through the lithosphere [*Cai and Bercovici*, 2016; *Havlin et al.,* 2013].

Both thermal erosion and cracking are more likely when melt is focused and concentrated to specific points. Both processes may act in tandem, for example thermal erosion may operate within the first few kilometers above the base of the lithosphere, allowing melt to accumulate and focus. The collected melt then may build pressure and crack, initializing the traditionally envisioned heat pipe style of melt transport. Numerical models of diapiric rise accommodated by tensile fractures or cracking tend to form a vertical conduit [*Keller et al.,* 2013] that best resembles conceptually a heat pipe.

3.4.1.3 Faulting

While the mountains of Io are largely non-volcanic, patera (caldera) are frequently observed in contact with the edges of mountain blocks [*Jaeger et al.,* 2003], e.g. Hi'iaka patera, Mekala patera, and the Hi'aka Montes [*Bunte et al*., 2010]. The mountain building thrust faults of Io, and associated extensional features, may serve as direct conduits of melt to the surface [*Bland and McKinnon*, 2016]. These

faults, or, if appropriate their downward extension as a ductile shear zone, may serve as a conduit for melt propagation, as is commonly observed on Earth in the form of melt-rich shear zones and dikes deviated by preexisting fractures and faults [*Hollister and Crawford*, 1986; *Hutton*, 1988; *Brown and Solar*, 1998; *Valentine and Krogh*, 2006; *Le Corvec et al.,* 2013]. At least in the case of rapid burial, the lithosphere of Io is cold enough that faults are expected to remain brittle throughout. As these thrusts may reach all the way through the lithosphere to the asthenosphere, they may bypass all permeability barrier processes as mantle melt travels rapidly upward without thermal equilibration. Melt may not travel all the way to the surface in all cases. Stratification of the crust has been observed to stop upward melt propagation [e.g. *Gudmundsson*, 2005] and should be expected in the case of Io, due to the constant (but not continuous) deposition of volcanic deposit layers and the possible intercalation of silicate flows and sulfur deposit horizons [*Schenk and Bulmer,* 1988; *Turtle et al.,* 2001]. Differential vertical motion across dip-slip faults may also serve as an initial perturbation through the nominal permeability barrier for thermal erosion or cracking to take place.

3.4.2 Linking heat pipe lifecycle with permeability barriers

The potential melt focusing processes discussed above should be more effective at breaching the shallow permeability barriers that form when burial rate is reduced that than the deeper barriers expected at the nominal burial rate. Thermal erosion will be suppressed by the competing downward advection of rapidly buried cold lithosphere. Cracking and faulting are generally harder under the increased confining pressure conditions expected deeper in the lithosphere. Thus, diapiric rise

and the formation of a heat pipe is easier if burial rate is reduced. Here we propose a coupled conceptual model of permeability barrier evolution and heat pipe formation and closure, based on the results about permeability barrier depth at various resurfacing rates and strain rates and literature-based understanding of melt migration processes (Figure 3.5).

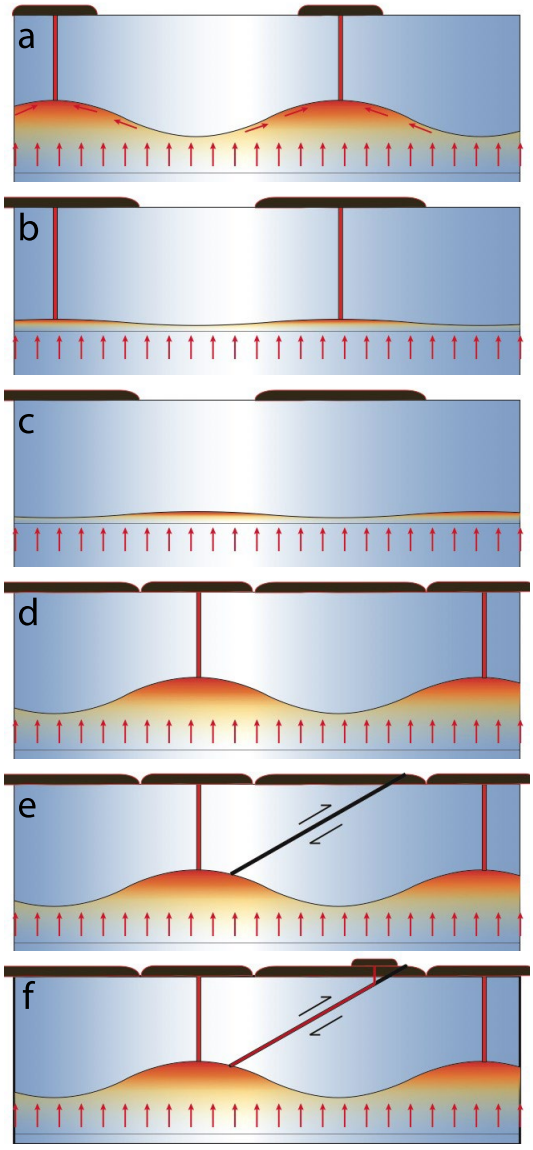

Figure 3.5 - Schematic diagram of proposed heat pipe evolution model (not to scale): a) In an initial state, with a preexisting heat pipe (red vertical line), the permeability barrier (solid black line) near the heat pipe is likely elevated due to higher temperatures or a thinner lithosphere. Melt (red arrows) is focused (red gradient) to the heat pipe by the deflection of the permeability barrier. b) As material is erupted onto the surface, the burial rate around the pipe increases, pushing the permeability barrier down, due to decreasing temperatures or a thickening lithosphere. Conversely, the lithosphere between the pipes heats up as it adjusts to a lower burial rate, and the permeability barrier rises. c) The slope of the permeability barrier is reversed compared to the initial conditions, so that volcanism through the initial heat pipe is shut off. d) Thermal erosion, diapiric rise, and cracking bring melt higher into the lithosphere and leads to the formation of a new heat pipe. e) Separately from the process in panels a to d, stress due to resurfacing builds in the lithosphere, forming large thrust faults that cuts through the whole lithosphere. f) Due to the increased strain rate the permeability barrier is elevated and melt is focused to the fault. Melt may then travel along the plane of the thrust fault, or region of deformation, towards the surface and from a patera at the surface.

In an initial system with a preexisting heat pipe and an underlying elevated permeability barrier, melt would focused to the base of the pipe, perhaps following the slope of the permeability barrier, rise quickly through the lithosphere, and erupt on the surface, forming a volcanic plume that rapidly buries the surface at local scale (Figure 3.5a). As the lithosphere cools due to this high burial rate, the barrier becomes deeper around the initial heat pipe (Figure 3.5b). By contrast, the lithosphere away from the heat pipe does not experience a similar resurfacing rate. The lithosphere heats up, which eventually leads to an elevated permeability barrier (Figure 3.5c). The preexisting heat pipe may close due to cooling from the outside in, or its magma supply may be shunted to locations away from the pipe where the permeability barrier newly reached a shallower level in the lithosphere. Melt supply in that new location leads to a thermal erosion feedback that drives a melt pool to shallower depths where diapiric rise, especially if facilitated by cracking, initiates a heat pipe to the surface, creating a new eruptive center (Figure 3.5d). This process would presumably be cyclical, as the new eruptive center would increase resurfacing rate above the permeability barrier and cool the lithosphere, pushing the barrier back down to restart the process. While melt ascent in a heat pipe can be rapid, the time scale of this cycle is related to the thermal equilibration. Considering a typical thermal conductivity of $\kappa = 10^{-6}$ m^2/s and the need to cool the lithosphere over length scales L of several km gives a time scale $\tau \approx L^2/\kappa$ of the order of 100,000 years. This cycle would not be observable in historical records, unlike the more rapid but less dramatic changes in volcanic activity linked to orbital cycles [*de Kleer et al.,* 2019]. However, the long-lived stability of volcanic centers over the observational

record [*Rathbun and Spencer*, 2010; *de Pater et al.,* 2017] is at least consistent with the expected duration of the cycle described here. Further two- and three-dimensional modeling is needed to investigate the viability of this proposed cycle.

A secondary effect due to strain rate may create a positive feedback loop. As Io resurfaces, it generates large tectonic stresses resulting in its thrust-driven, large, non-volcanic, mountain ranges. Areas of tectonic activity deep in the lithosphere, and therefore laterally distant from the mountains themselves, would have an increased strain rate, which, if large enough, would raise the local permeability barrier. Although this effect may be small, it may be sufficient to initiate melt focusing, breaching the barrier, and increasing the resurfacing. Differential burial rates on either side of the fault may also perturb the thermal structure in the permeability barrier level, initiating melt focusing. Finally, the faults themselves, if they penetrate deep enough in the Ionian lithosphere, may also tap melt otherwise trapped by a permeability barrier (Figure 3.5e and 3.5f).

3.4.3 Mantle potential temperature and the composition of surface volcanism

Our modeling suggests the mantle potential temperature of Io must be hotter than ~1350˚C, otherwise the reservoir of melt under the permeability barrier is too felsic to represent the presumed mafic volcanology of Io [e.g. *McEwen et al.,* 2000]. Melt collects at the base of the lithosphere or in the decompaction channel and is directed to the eruptive center/heat pipe, therefore the composition of melt below the permeability barrier is likely close to or less evolved than the erupted melt composition. The 60 wt% SiO_2 melt under the permeability barrier in the low

resurfacing rate, higher strain rate scenario is simply too felsic to create surface basalt or komatiite flows. Assimilation of more mafic lithosphere is not likely to counter evolved melt compositions, as the lithosphere of Io consists entirely of erupted lava flows. The melt can only assimilate material that is compositionally similar to the melt itself. Finally, the issue is made worse if melt stalls in the lithosphere after having crossed the barrier. Stalled magma would cool and differentiate, becoming less and less mafic [e.g. *McBirney*, 1995]. Note that stalled magma or evolved magma could be present as magmatic intrusions. The general downward motion of the Ionian lithosphere would make it unlikely to observed deeply emplaced bodies at the surface. However, the presence of these evolved bodies is necessarily speculative and should not be used as a constraint on our heat pipe development model.

3.5 Conclusion

Permeability barriers likely form near the base of the Ionian lithosphere away from heat pipes. New heat pipes must form and therefore melt must ascend past the permeability barrier. Regions of lower resurfacing rates and increased strain rates may allow melt to rise past the nominal depth of the permeability barrier, where thermal erosion, cracking, and faults may allow the formation of new heat pipes. Further modeling is needed to evaluate the contributions of these three processes. An Io dedicated mission, such as the Io Volcano Observer [IVO; *McEwen et al.,* 2014] is desirable to observe lithosphere deformation in real time, observe volcanic eruption temperatures, and constrain the surface compositions beyond “silicate”.

Chapter 4: Convection in a Deep Melt-Rich Channel and the Spacing of Volcanic Vents on the Surface of Mars

Abstract

The spacing of volcanic edifices on the surface of Mars can be used to constrain the interior conditions of the planet during edifice emplacement. We create numerical models of melt migration and document the development of high porosity channels, also called decompaction channels, deep in the Martian lithosphere. Crystallization-driven convection initiates in the channel due to density differences between the solid material and the more buoyant melt. The wavelength of convective cells focuses melt to discrete points at the top of the channel and allow melt to rise past an otherwise impermeable boundary. The spacing of the resulting raised points may be linked to the spacing of volcanic edifices at the surface. The volcanic vents of the Hesperian-aged Syria Planum have a nearest-neighbor spacing of 16.5 km which approximately matches numerical model the 18.2 km convective wavelength result using expected Hesperian interior conditions of a mantle temperature of 1650 K and a lithospheric thickness of 150 km. Larger spacings such as those between the large Tharsis shield volcanoes are not replicated and may be caused by an alternative process.

4.1 Introduction

Some of the most striking geological features of Mars are the enormous volcanic edifices, including Alba Mons and Olympus, the largest central volcanoes in the solar system. The three Tharsis Montes volcanoes (Ascreus, Pavonis, and Arsia Mons) in the Tharsis region of Mars are remarkable aligned and regularly spaced

(Figure 4.1) [*McCauley et al*., 1972]. Each of the Tharsis Montes volcanos is 350 to 500 km in diameter, lies in a northeast trending line, and is spaced ~700 km to its neighbor [*Carr et al., 1977*; *Crumpler and Aubele*, 1978; *Plescia*, 2004]. An additional cluster of volcanoes, the Uranius group composed of Uranius Tholus, Ceraunius, and Uranius Patera is located along the same line, ~750 km to the northeast of Ascraeus Mons [*Plescia*, 2000]. Other volcanoes like Tharsis Tholus and the cluster of Ulysses Patera and Biblis Patera are also separated by 700 to 800 km from their nearest major volcanic edifice, although they are not located along the same line as the Tharsis Montes.

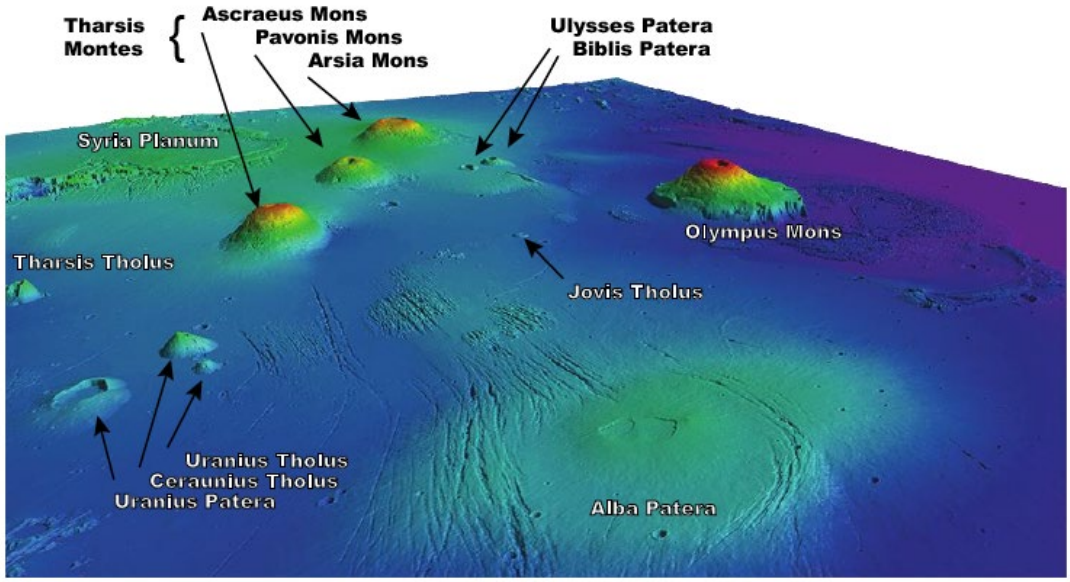

Figure 4.1 - Perspective view of the Tharsis Rise from the northwest, looking towards the southeast. This map was generated using Fledermaus™ and color-coded MOLA topographic information. The scale is variable due to perspective. Alba Patera and Arsia Mons are separated by 3,000 km.

The linear sequence of the Tharsis Montes is not an age progression, as seen at Hawaii on the Earth, as each volcano appears to have developed contemporaneously and each has erupted episodically through time [*Wilson et al*.,

2001; *Carr and Head*, 2010]. It may reflect an underlying major rift system, cropping out in Tempe Terra to the Northeast and Mangala and Syrenum Fossae to the Southwest (Mège and Masson, 1996; Montési, 2001). Some melt focusing process must have occurred during the formation of the Tharsis Montes which created the observed wavelength spacing of these edifices, instead of creating a continuous linear volcanic feature such as a mid-ocean ridge.

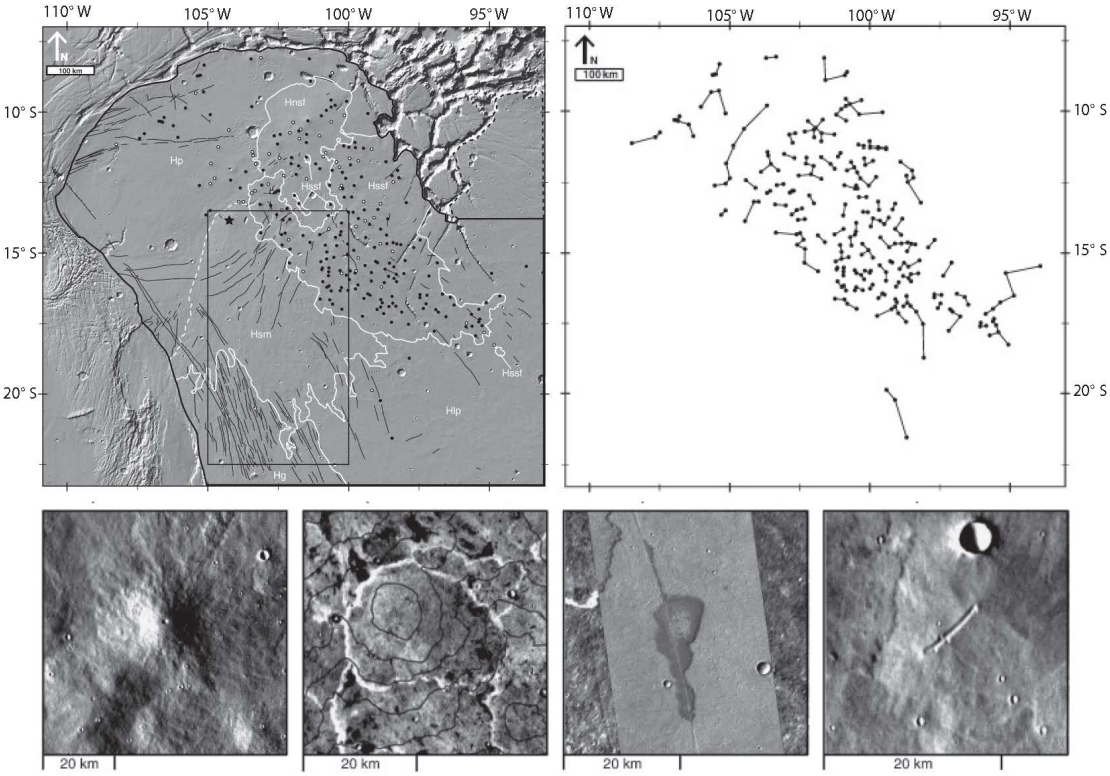

Figure 4.2 - Locations of volcanic vents at Syria Planum Mars. Top left: Geologic map of Syria Planum. Each black point is a volcanic vent and, each point circled in white is a likely volcanic vent, and the star is Syria Mons. Top right: a visual representation of the nearest neighbor spacing of volcanic vents at Syria Planum. Bottom row: Examples of likely volcanic vents in Syria Planum. Adapted from *Richardson et al*. [2013]. "Reprinted from *Journal of volcanology and geothermal research, Vol. 252*, Authors J. A. Richardson, J. E. Bleacher, and L. S. Glaze, The volcanic history of Syria Planum, Mars, Pages 1-13, Copyright (2012), with permission from Elsevier.

On a smaller scale, volcanic terrains such as Syria Planum on Mars also display statistically significant spacings of volcanic edifices. Syria Planum possesses

a non-random distribution spacing of its 263 volcanic vents (Figure 4.2) [*Richardson et al,* 2013]. Syria Planum is a high-elevation region in the Southeast corner of the Tharsis province. Surrounded to the North by the chasms of Noctis Labyrinthus and to the West by Claritas Fossae, the region forms the highest elevation of the sloping Thaumasia Plateau. It was a Hesperian age center of volcanic activity with a volcanic flux similar to that of the Tharsis Montes, emplaced on top of the already thickened crust at the center of the Tharsis Bulge [Baptista et al., 2008].

Some process must have focused melt to singular points at depth underneath Syria Planum, as a random distribution of volcanic centers, expected from random dikes accessing a spatially continuous melt source can be ruled out on statistical grounds [*Richarson et al.,* 2013]. We take inspiration from terrestrial melt focusing processes and investigate the role that a permeability barrier and associated decompaction channel at the base of the lithosphere may play in focusing melt on Mars.

Permeability barriers are a likely byproduct of melt transport through planetary lithospheres. At depth where the mantle is hot and melt is generated, melt occupies and travels along a porous network that follows solid grain boundaries [*Von Bargen and Waff*, 1986; *McKenzie*, 1984]. Melt rises due to its buoyancy and reaches the lithosphere, where it cools and crystallizes. At some depth the crystallization may reach a quick enough rate where the available melt pathways are clogged by crystals and permeability is reduced to zero, thereby creating a permeability barrier [*Sparks and Parmentier*, 1991; *Korenaga and Kelemen*, 1997]. Melt is unable to rise through the barrier and accumulates underneath it. The pressure in this accumulation zone

increases and forces the solid matrix to expand (decompact), forming a decompaction channel [*McKenzie*, 1984; *Sparks and Parmentier*, 1991; *Spiegelman*, 1993].

On the Earth, porous flow through a decompaction channel has been invoked to explain melt focusing to mid-ocean ridges. Aging, cooling plates create a sloped permeability barrier and melt flows upslope through the decompation channel to the ridge axis [e.g. *Sparks and Parmentier*, 1991; *Spiegelman*, 1993, *Kelemen and Aharanov*, 1998; *Hebert and Montési,* 2010]. On Mars, horizontal permeability barriers are likely developed relatively deep in the lithosphere through time [*Schools and Montési*, 2018; This Dissertation, Chapter 2]. At all but the earliest Martian epochs, melt is trapped at depth, and is too deep to be accessed by faults, dikes, or any kind of brittle deformation. Some process must exist to allow melt to ascend to shallower depths where fracturing and diking can lead to surface volcanism.

One possible process for melt ascension is the thermal erosion of the permeability barrier due to heat release from crystallization. Here we create two-dimensional, numerical models of decompaction channel evolution and document the development of crystallization-driven convection in the solid-melt aggregate in the decompaction channel. This convection forces a length scale on thermal erosion that can focus melt to elevated portions of the barrier and may be expected to be reflected in the spacings of volcanoes at the surface of Mars. We discuss how this length scale matches the spacing of small volcanoes in Syria Planum but cannot explain the separation between the larger edifices of Tharsis Montes.

4.2 Methodology

Using the finite element code ASPECT 2.0.1 [*Kronbichler et al.,* 2012; *Heister et al.,* 2017; *Bangerth et al., 2018*; *Bangerth et al*., 2019] we model the formation and evolution of permeability barriers and underlying decompaction channels. The model is set up in two dimensions with no initial variations in temperature or any other parameters, as is appropriate for a single plate planetary lithosphere. For models with melt migration [*Dannberg and Heister*, 2016; *Dannberg et al.,* 2019], ASPECT operates by solving a series of equations for velocity, pressure, temperature, and porosity representing the behavior of silicate melt flowing through a viscously deforming solid matrix. Please refer to Appendix C for a more detailed description of the relevant solved equations.

Each numerical model consists of a two-dimensional rectangular box representing the thermal lithosphere and upper portion of the asthenosphere of Mars (Figure 4.3). The rectangular box is 200 km wide with periodic boundaries, so that the model represents a horizontal continuum. The thickness of the box is typically 400 km, but a thicker domain of 500 km was necessary to accommodate deeper melting in the hottest models (mantle temperature of 1900K). The upper portion of the box has thickness H and represents the thermal lithosphere. The remaining lower portion of the box represents the upper asthenosphere. The top and bottom boundaries are closed and do not affect the calculation.

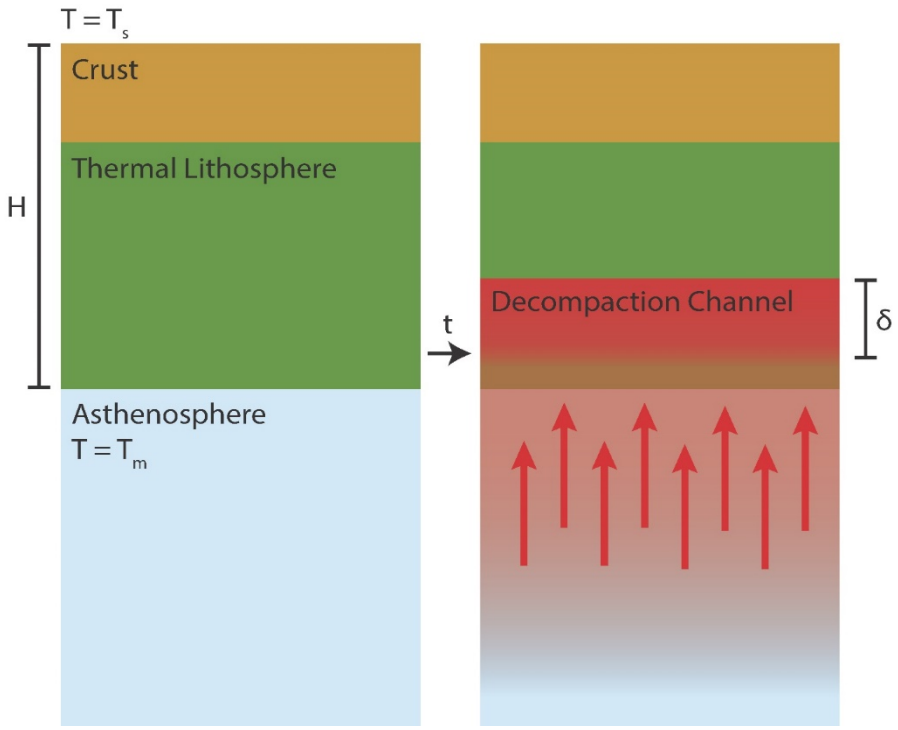

Figure 4.3 - Schematic diagram of model set up. The model domain consists of two boxes, a lithosphere of thickness $\boldsymbol{H}$, comprising the crust (brown) and the thermal lithosphere (green), overlying the asthenosphere (blue). Temperature decreasing along a geotherm from $\boldsymbol{T_m}$ at the base of the lithosphere and in the asthenosphere to $\boldsymbol{T_s}$ at the surface. Over the initial timesteps, melting occurs in the asthenosphere and melt ascends and enters the lower lithosphere (red arrows). Melt collects in a region known as the decompaction channel (red shading) of thickness $\boldsymbol{\delta}$, where the accumulation increases porosity (more intense red). As all the melt processes occur below the expected depth of the crust, crustal assimilation is not expected or modeled, and the crust is assumed in our models to have the same composition and the thermal lithosphere and the asthenosphere.

The initial temperature of the asthenosphere is set to a temperature, T_m. The initial temperature of the lithosphere follows the equation:

$$T = T_s + \left((T_m - T_s) \cdot \left\{ \cos \left[\arcsin \left(\frac{p - p_b}{p_b} \right) \right] \right\}^2 \right) \tag{4.1}$$

where T_s is the surface temperature, p is the lithostatic pressure with depth, and p_b is the pressure at the base of the lithosphere (at depth H). This is the same lithospheric temperature profile as used in Chapter 2.

Asthenosphere (mantle) temperature, T_m, and thermal lithosphere thickness, H, are the two primary variables in the model. Models were run with $T_m = 1450$ K to $T_m = 1900$ K every 50 K and with $H = 50$ km to $H = 300$ km every 50 km, encompassing 60 total model runs.

The crust is not considered as separate from the mantle in these models in order to focus on the deeper processes that take place at the lithosphere-asthenosphere boundary. Therefore we initiate the entire model with uniform peridotitic composition which follows the melting parameterization of *Katz et al.* [2003] for dry peridotite. Crystallization follows the same model even though melting is not rigorously reversible [e.g. *Hebert and Montési*, 2010]. Throughout this calculation, melt is given one density and the solid another, without consideration of the progressive depletion of the residuum or variations in melt composition. Thermal expansion is considered, which changes the buoyancy terms that drive solid and melt flow, according to the Boussinesq approximation.

The only source of heat is assumed to be from latent heat changes from crystallization and melting. Therefore, the heat equation becomes:

$$\bar{\rho} C_p \left(\frac{\partial T}{\partial t} + \mathbf{u}_s \cdot \nabla T \right) - \nabla \cdot k_{\text{thermal}} \nabla T = T \Delta S \Gamma \tag{4.2}$$

Refer to Table 4.1 and Appendix C for descriptions of model variables and parameters. Note that in this formulation, the solid and melt always have the same temperature. Therefore, melt temperature adjusts instantaneously to the temperature of the solid through which it travels. This assumption would break down if the melt travels too rapidly or if there is too much melt in the partially molten aggregate considered here. In melt fraction exceeds ~35%, it may be expected that the

solid/melt mixture disaggregates, at which point, the physical model that underlies our numerical results loses its validity [*Costa et al.,* 2009]. Therefore, our model cannot capture eruption dynamics and is limited to deep melt migration models.

Name	Symbol	Value	Unit	Equation
Temperature	T			(4.1)(4.2) Appendix C
Surface temperature	T_s	210	K	(4.1)
Asthenosphere temperature	T_m		K	(4.1) (4.6)
Lithostatic pressure	p		Pa	(4.1)
Lithostatic pressure at the base of the lithosphere	p_b		Pa	(4.1)
Lithosphere thickness	H		km	(4.1) (4.6)
Phase weighted average density	$\bar{\rho}$		$\frac{kg}{m^3}$	(4.2) Appendix C
Thermal conductivity	$k_{thermal}$	4.7	$\frac{W}{m\,K}$	(4.2)
Specific Heat	C_p	1250	$\frac{J}{kg\,K}$	(4.2)
Solid velocity	$\boldsymbol{u}_s$			(4.2) Appendix C
Darcy Coefficient	K_D	$\frac{k}{\eta_f}$		Appendix C
Melting/Freezing Rate	Γ	From melting model [Katz et al., 2003]		(4.2) Appendix C
Peridotite melting entropy change	ΔS	300	$\frac{J}{kg\,K}$	(4.2)
Time	t			(4.2) Appendix C
Reference solid density	ρ_{s_0}	3000	$\frac{kg}{m^3}$	(4.3)(4.4) Appendix C
Gravity	g	3.7	$\frac{m}{s^3}$	(4.3)(4.4) Appendix C
Thermal expansivity	α	2×10^{-5}	$\frac{1}{K}$	(4.3) Appendix C
Temperature contrast over decompaction channel	ΔT		K	(4.3)
Decompaction channel thickness	δ		km	(4.3)(4.4)(4.5)
Thermal diffusivity	κ	$\frac{k_{thermal}}{\rho_s C_p}$		(4.3)(4.4) Appendix C
Reference melt density	ρ_{f_0}	2500	$\frac{kg}{m^3}$	(4.4) Appendix C
Porosity	ϕ			(4.4) Appendix C
Convective wavelength	λ		km	(4.5)
Convective cell aspect ratio	R		unitless	(4.5)
Reference permeability	k_0	10^{-7}	m^{-2}	Appendix C
Reference bulk viscosity	ξ_0	4×10^{20}	$Pa\,s$	Appendix C
Reference shear viscosity	η_0	1×10^{18}	$Pa\,s$	Appendix C
Melt viscosity	η_f	1	$Pa\,s$	Appendix C
Melt weakening parameter	a	27	$unitless$	Appendix C
Reference temperature	T_0	1600	K	Appendix C
Melt velocity	$\boldsymbol{u}_f$			Appendix C

Table 4.1 – Variables and parameters for the decompaction channel convection model and associated calculations

4.3 Results

For models with low mantle temperatures and large lithosphere thicknesses no melt was generated (19 models), or too little melt was generated to initiate significant observable processes other than slow cooling and crystallization (8 models). For models with high mantle temperatures and thin lithospheres, too much melt is generated, and the calculations are terminated without results (11 models). This leaves 22 "just right" models, of the performed 60, where convective processes are observed. These 22 models are the models referred to in the rest of this chapter.

In the 22 convective models, melt is generated in the initial timesteps and ascends through the asthenosphere and lower lithosphere. At some depth in the lithosphere the temperature is too low causing crystallization, reducing permeability to zero, and creating a permeability barrier. The subsequently ascending melt continues to rise and collect underneath this permeability barrier, resulting in decompaction of the matrix and high porosities of 25-30% melt, a high value but probably not enough to cause disaggregation of the melt/solid mixture. The depths of these channels are highly dependent on lithosphere thickness, with 50 km thick lithospheres having the tops of decompaction channels at ~35 km depth and 300 km thick lithospheres creating channels at ~200 km depth. Lower temperatures generate less overall melt, yielding a minimum decompaction channel thickness of 5 km (in the $T_m = 1550$ and $H = 50$ km model) and a maximum of 26.5 km (in the $T_m = 1900$ and $H = 200$ km model).

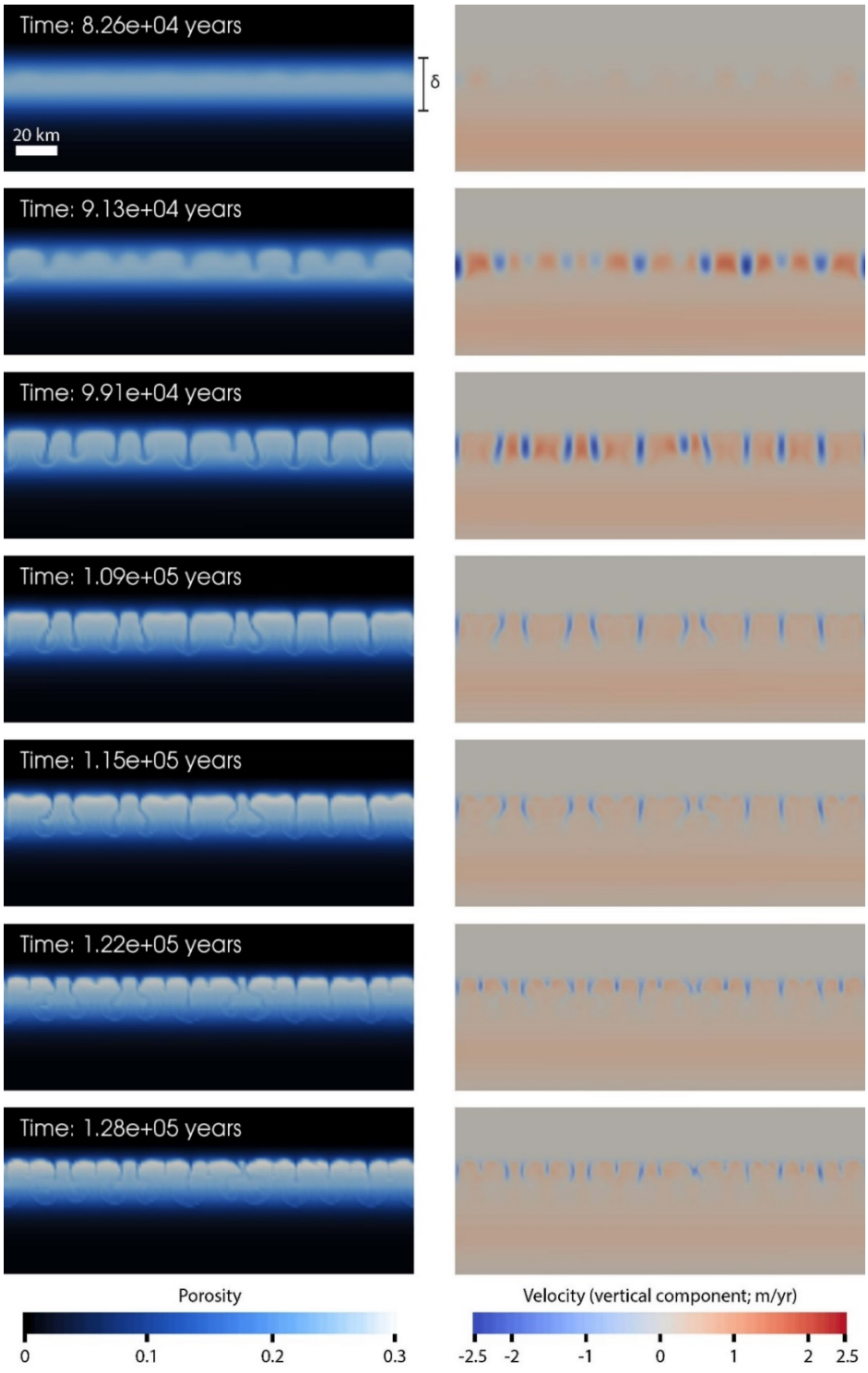

Figure 4.4 - Example results of a model with a lithospheric thickness (H) of 150 km and asthenosphere temperature (T_m) of 1650 K. Left column displays porosity, showing development of the decompation channel and partially solidified downwellings. Right column displays the vertical component of the melt velocity, to highlight the locations of downwellings and upwellings.

Once the decompaction channels reach a porosity of 25 to 30%, a new dynamical regime begins in the form of density driven convection (Figure 4.4). Cold downwellings, or drips consisting of both solid matrix and trapped melt, descend from the top of the decompaction channel. As these downwellings reheat from the surrounding warm material, melting occurs, and the drips vanish. Less dense, melt-rich upwellings bring hot melt and accompanying solid back to the highly porosity region near the top of the decompaction channel. New drips form near the top of the channel as the newly arrived melt cools in contact with the lithosphere and crystallizes. Melt is thus focused to the upwelling locations and accumulation further increases porosity in these pockets. In this process, heat is carried as latent heat. It is liberated when the upwelling crystallizes and slightly thermally erodes the roof of the decompaction channel. Model runs are terminated as porosity increases upwards of ~35%, beyond ASPECT's capabilities.

The average spacing, or wavelength, of the convective cells is affected by the initial conditions of the model. Thicker channels yield larger spacings between downwellings (Figure 4.5), with an average convection cell aspect ratio of $R_\lambda \sim 2.7\delta$ for all the models. Figure 4.6 displays the time of onset for convection, the depth of the decompaction channel, the thickness of the decompaction channel, the observed spacing of downwellings in the models, and the aspect ratio of the convective cells.

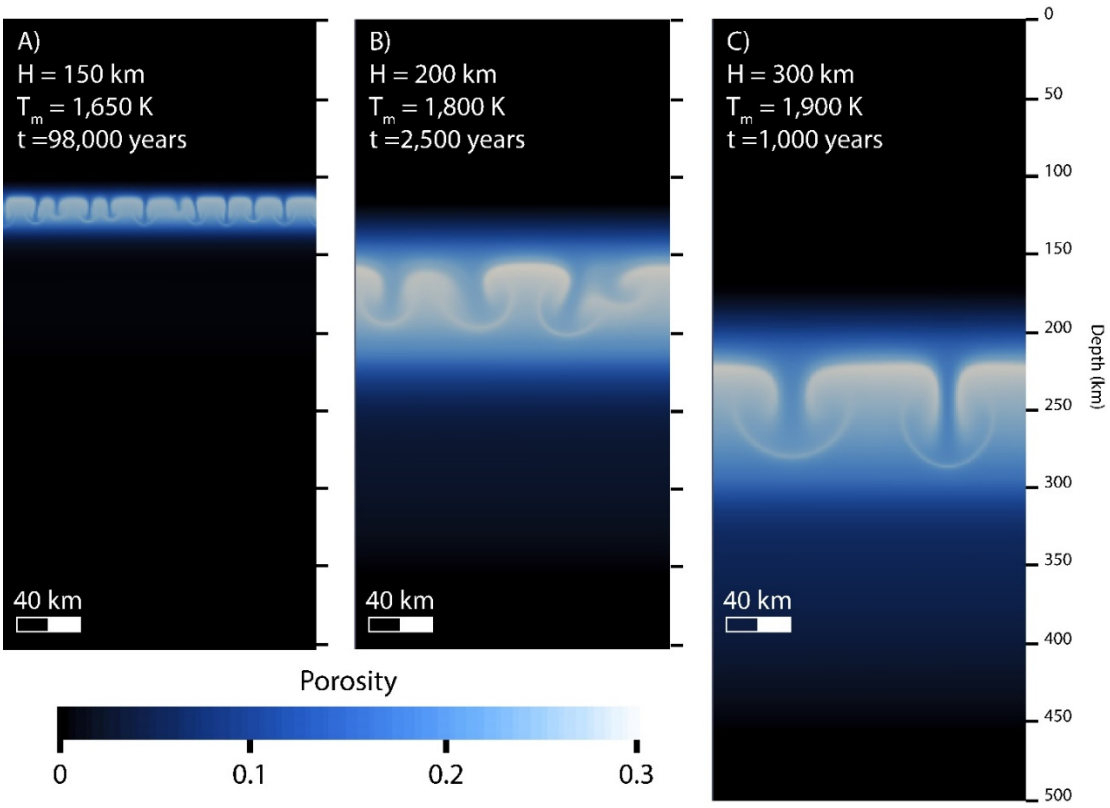

Figure 4.5 - Example model outputs for three model setups. Model A) is the same in as Figure 4.4. Model C) requires a thicker model domain in order to accommodate deeper melt generation.

The convective process focuses melt above upwelling centers in the decompaction channel, against the permeability barrier. As melt accumulates against this cold region, crystallization occurs, releasing heat and increasing the temperature of the surrounding area. Thermal erosion is not uniform but associated with upwelling. Thus, the melt pockets that develop at the upwellings rise over the model time through the nominal depth of the permeability barrier to the initially colder lithosphere. In the $T_m = 1450$ and $H = 50$ km model, the horizon of highest porosity rises from 124 km depth at 83,600 years (convection onset) to 112 km depth at 128,500 years (model termination) (Figure 4.4).

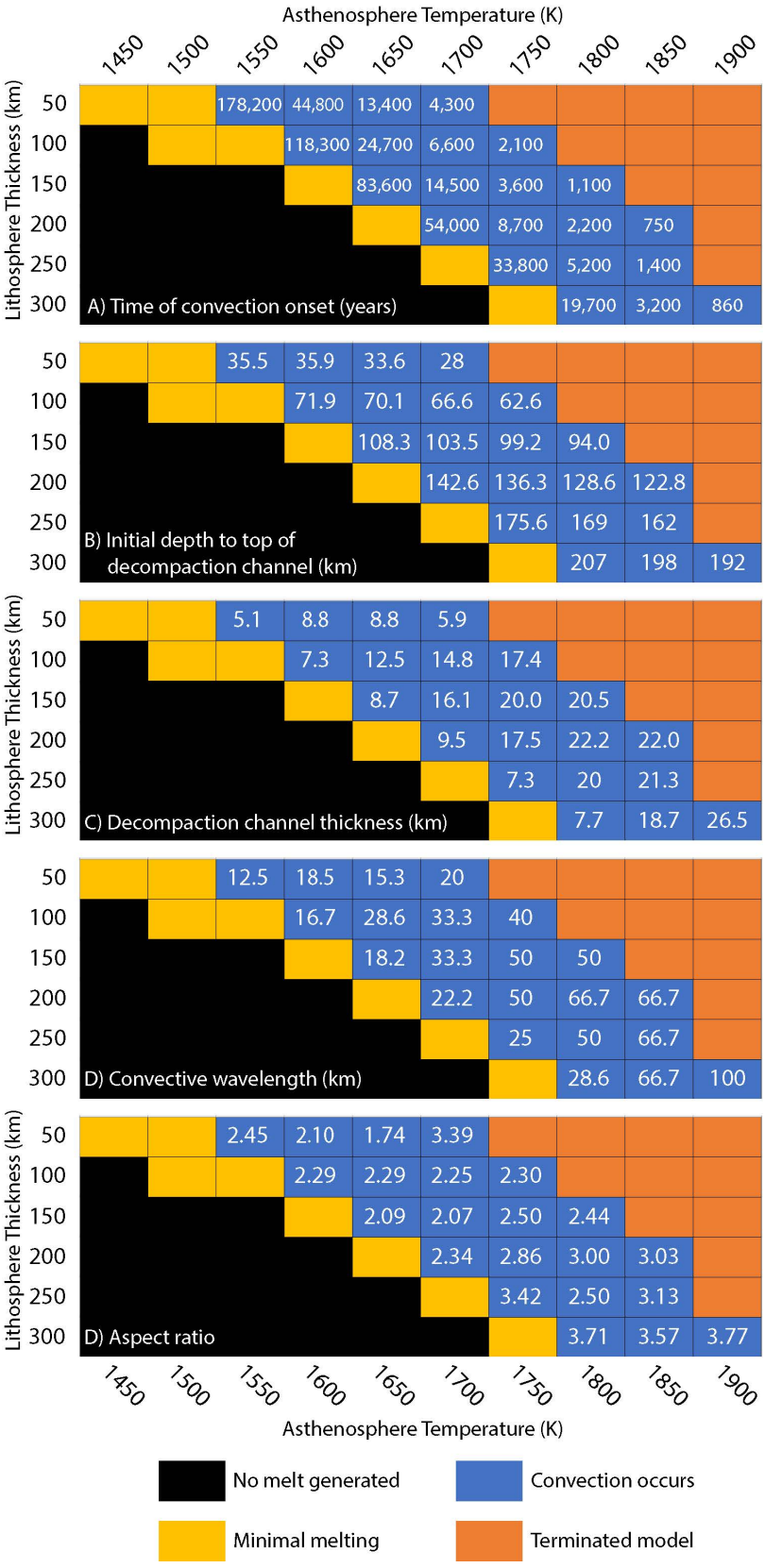
Asthenosphere Temperature (K)
1450
1500
1550
1600
1650
1700
1750
1800
1850
1900
Lithosphere Thickness (km)
50
100
150
200
250
300
178,200
44,800
13,400
4,300
118,300
24,700
6,600
2,100
83,600
14,500
3,600
1,100
54,000
8,700
2,200
750
33,800
5,200
1,400
19,700
3,200
860
A) Time of convection onset (years)
35.5
35.9
33.6
28
71.9
70.1
66.6
62.6
108.3
103.5
99.2
94.0
142.6
136.3
128.6
122.8
175.6
169
162
207
198
192
B) Initial depth to top of decompaction channel (km)
5.1
8.8
8.8
5.9
7.3
12.5
14.8
17.4
8.7
16.1
20.0
20.5
9.5
17.5
22.2
22.0
7.3
20
21.3
7.7
18.7
26.5
C) Decompaction channel thickness (km)
12.5
18.5
15.3
20
16.7
28.6
33.3
40
18.2
33.3
50
50
22.2
50
66.7
66.7
25
50
66.7
28.6
66.7
100
D) Convective wavelength (km)
2.45
2.10
1.74
3.39
2.29
2.29
2.25
2.30
2.09
2.07
2.50
2.44
2.34
2.86
3.00
3.03
3.42
2.50
3.13
3.71
3.57
3.77
D) Aspect ratio
No melt generated
Convection occurs
Minimal melting
Terminated model

Figure 4.6 (previous page) - Parameter domain and results of the 60 performed numerical models. Models in which convection was observed (highlighted in blue) display: A) Time after the initiation of the model of convection onset, B) The initial depth of the top of the decompaction channel in km, C) The thickness of the decompaction channel (δ) in km, D) the average spacing, or wavelength, of convective cells (λ) in km, and E) the aspect ratio of the convective cells (λ/δ). The models highlighted in orange terminated due to excessive melt accumulation leading to numerical problems as well as breakdown of the physical assumptions underlying model formulation.

The timing of convection initiation is dependent on the overall melt generation (Figure 4.6A). Thin lithospheres and hot asthenospheres generate larger amounts of melt which initiate convection earlier in the model run time, while thicker lithospheres and cooler asthenospheres reduce melt generation and initiate convection at a later time. As an example for asthenosphere temperature, in the $T_m = 1700$ and $H = 50$ km model, convection initiates after 4,300 years, while in the $T_m = 1700$ and $H = 200$ km model, convection initiates after 54,000 years. For lithosphere thickness, in the $T_m = 1650$ and $H = 200$ km model, convection initiates after 83,600 years, while in the $T_m = 1700$ and $H = 200$ km model, convection initiates after 1,100 years.

4.4 Discussion

4.4.1 Origin of Convection

The potential for convection in a viscous fluid layer can be assessed through the Rayleigh number. For thermally driven convection:

$$\mathrm{Ra}_{th} = \frac{\alpha \rho_{s_0} g \Delta T \delta^3}{\kappa \eta} \tag{4.3}$$

where α is the coefficient of thermal expansion, ρ_0 is the density of the material, ΔT is the temperature difference between the top and bottom of the layer, of thickness δ, κ is the thermal diffusivity, and η is the viscosity. Using the $T_m = 1650$ K and $H = 150$ km model as an example, where at convection initiation $\Delta T = 20$ K, $\delta = 8.7$ km, and $\eta = 10^{15}$ Pa s, the Rayleigh number is calculated to be 2,300. This is slightly higher than the critical Rayleigh number of ~1,000 [*Turcotte and Schubert*, 2014], suggesting that there is a thermal component to the observed convection.

To further test the temperature dependence of the modeled convective process, secondary models with $\alpha = 0$ were performed. All other model parameters remained the same. If $\alpha = 0$ then $Ra_{th} = 0$, however the numerical models produce convection in the decompaction channel. The observed convection initiates at the same time and produces the same wavelength spacing as the primary models. Therefore, thermal convection is not the dominant process that forms the observed circulation.

The observed solid melt convective process is initiated by drips that form at the relatively solid-rich and therefore dense roof of the decompaction channel, which contrasts with the more melt-rich and relatively melt rich core of the channel. This density contrast between the crystal-rich aggregate near the top of the channel and the melt-rich aggregate provides a more important driver of convection. We formulate a new Rayleigh number based on this density contrast:

$$\mathrm{Ra}_{\phi} = \frac{(\rho_s - \rho_m)\phi g \delta^3}{\kappa \eta} \tag{4.4}$$

where ϕ is the porosity in the decompaction channel, ρ_s is the solid density, and ρ_m is the melt density. Near the initiation of convection, the porosity is ~ 25%, yielding a Rayleigh number of 2.4×10^5.

Although we do not have a rigorous instability analysis here, this Rayleigh number is likely high enough to enable vigorous, time-dependent convection. Indeed, we see in our results individual downwellings that change over times, not the well-ordered stable convection cells of near-critical convection. Furthermore, the convection is dominated by downwellings, which is a characteristic of internally heated or equivalently cooled-from-the-top convection [e.g. *Davies and Richards*, 1992], consistent with our interpretation of the physical origin of convection in our models. Note that this formulation of crystallization-driven convection has no dependence on temperature contrasts or internal heating. Its main control is the thickness of the decompaction channel. Convection in Martian decompaction channels likely initiates due to the density differences between solid and melt.

4.4.2 Implications for volcano spacing

Melt must be able to breach the permeability barrier and reach the surface. In the numerical model, the permeability barrier maintains its overall depth but highly permeable pockets at the top of the decompaction channel rise as convection occurs. Melt is focused to these pockets where further crystallization and latent heat release occur. This increases the temperature of the surrounding material and elevates the level of the permeability barrier. As melt accumulates pressures will increase in the high porosity pockets, and at some point the overburden pressure of the lithosphere

will be surpassed and cracking and diking should initiate [e.g. *Cai and Bercovici*, 2013], providing a mechanism for melt to ascend to shallower depths than the relatively deep decompaction channel. Alternatively, the melt may rise as a mostly fluid diapir before initiating brittle failure when it reaches even shallower levels in the lithosphere [*Keller et al.,* 2013; *Cao et al.,* 2016]. In either case, melt will be focused over a length scale corresponding to the wavelength of the convective instability. All observed processes in the numerical model occur much deeper than the expected thickness of the crust [*Hauck and Phillips*, 2002], signifying that crustal processes such as compositional assimilation of crustal material are not significant to volcanic vent spacing.

4.4.3 Application to Syria Planum

Volcanic activity at Syria Planum tool place mostly in the Hesperian, 3.5 to 3.6 billion years ago [*Baptista et al.,* 2008]. A mantle temperature of 1650 K and thermal lithosphere thickness of 150 km is likely representative of this time period [*Hauck and Phillips,* 2002]. Therefore, we expect the wavelength spacing of our $T_m = 1650$ K and $H = 150$ km model to match the nearest neighbor spacing of Syria Planum volcanic vents, ~16.5 km [*Richardson et al.,* 2013].

In the $T_m = 1650$ K, $H = 150$ km numerical model (Figure 4.4), the initial downwellings create a topography with a wavelength of ~18 km which persist through the duration of the model. Considering model idealization, especially the limitations of a 2D modeling approach, the coincidence between the instability wavelength and the observe vent spacing is quite satisfactory.

As planetary bodies cool, the mantle cools and the thermal lithosphere thickens [e.g. *Hauck and Phillips*, 2002]. Therefore, the spacing of convective cells and volcanic vents is expected to shrink through time (Figure 4.6). This may be reflected in the geologic history of Mars, as fields of individual small shields are not observed in younger volcanic fields, such as the plains that surround the major Tharsis volcanoes. It may be impossible to preserve a relatively fine wavelength when magma must traverse a very thick lithosphere. In addition, these are each pockets of magma that may not contain enough heat to prevent full crystallization before reaching the surface. Melt may instead metasomatize the lithosphere [*Schools and Montési*, 2018] unless it takes advantage of a well-developed volcanic conduit that is formed independently from the process modeled here. Such a conduit may exist for example underneath the large, long-lived Tharsis volcanoes, which are the source of most of the late Hesperian and Amazonian flows in the region [e.g. *Schabert et al.,* 1978].

4.4.3 Model Limitations and Extrapolations

The 700 km spacing of the Tharsis Montes is not observable in the wavelength of the convective cells. This is largely due to the experimental design of the model, which only has a width of 200 km. The model domain size was chosen as a compromise between resolution of processes in the decompaction channel and computational expense of larger model domains. One complication of the constrained width in the numerical model is the accuracy of the recorded wavelength. Models with less melting and thinner decompaction channels trended towards smaller aspect ratios ($R_\lambda = 2.29$ when $T_m = 1600$ K and $H = 100$ km), while thick decompaction

channels trended towards larger aspect ratios ($R_\lambda = 3.77$ when $T_m = 1900$ K and $H = 300$ km) (Figure 4.6). The constrained width of the models limit the number of downwellings in the thicker decompaction models. If a 200 km wide model domain produces two downwellings, the spacing is 100 km; if three are produced, the spacing is 66.7 km. There can be no in between.

One way to compensate for the model width limitation is to use an average aspect ratio of the numerical models. The thickness of the generated decompaction channel is not affected by width of the model, therefore if a representative aspect ratio (R) for the convection can be determined, it can be used to calculate the expected convection wavelength:

$$\lambda = R\delta \tag{4.5}$$

The average convective aspect ratio of all models is ~2.7δ. Applying this value to thicker decompaction channels reduces the expected wavelength compared to the numerical model results (Figure 4.6). The $T_m = 1900$ K, $H = 300$ km numerical model produces a layer thickness of 26.5 km and a spacing of 100 km due to the boundary restrictions, but using Equation 4.5 and $R_\lambda = 2.7$, the spacing is calculated to be 72 km.

We were unable to model regions with large lithosphere thicknesses and high mantle temperatures, due to large amounts of melt generated, leading to porosities beyond the ~35% porous flow limit (Figure 4.6). If the trend observed in the convective models continues, it is possible that the thinnest lithospheres and hottest mantles may produce upwards of 700 km spacing, however it would likely only occur in the most extreme conditions. This may be representative of the initial emplacement

conditions of the large Tharsis shield volcanoes, assuming the volcanoes initiated very early in the history of Tharsis and that Tharsis has been underlain by a widespread hot melt source, or "superplume" at that time [*Harder and Christensen*, 1996]. If the aspect ratio described above is valid, then the decompaction channel at that time would have been ~260 km. Assuming a thin lithosphere of 50km, melting would have to initiate at least at 300 km depth, and probably deeper, requiring a mantle temperature in excess of 1900K. This temperature would require a major plume, but would also produce extremely high degrees of melting [*Schools and Montési*, 2018]. At that stage, the mantle would probably disaggregate and the physical processes modeled here would not be valid.

4.4.4 Comparison to the Earth

If conditions on ancient, volcanically active Mars were favorable to convective, melt-rich channels in the lithosphere, it is reasonable to speculate on the existence of similar convective channels on the Earth. As previously stated, decompaction channels likely exist at the base of the lithosphere in mid-ocean ridge settings, where they focus melt to the ridge axis [e.g. *Sparks and Parmentier*, 1991; *Spiegelman*, 1993, *Kelemen and Aharanov*, 1998; *Hebert and Montési,* 2010]. Convection has not been previously considered in these channels, likely for two related reasons. First, the permeability barrier and decompaction channel are sloped upwards towards the ridge axis, due to the plate cooling with age. This slope allows melt to flow upwards and not accumulate to the large thicknesses observed in these Mars models. This lack of accumulation leads to the second reason, which is the resulting thickness of these channels. For an upwelling column, which describes the

mantle under a mid-ocean ridge, the thickness of the decompaction channel is dependent on the mantle upwelling velocity (w), solid viscosity (η), porosity at the top of the channel (ϕ), density contrast between solid and melt ($\Delta\rho$), and the gravity (g):

$$\delta = \sqrt{\frac{w\eta\phi}{\Delta\rho g}} \tag{4.6}$$

from *Sparks and Parmentier* [1991]. Using the assumptions of *Sparks and Parmentier* [1991] for upwelling under a mid-ocean ridge, with an upwelling velocity of 1 cm/yr, a viscosity of 10^{19} Pa s, a maximum porosity of 20%, a density contrast of 500 kg/m^3, and an Earth gravity value of 9.8 m/s^2, the decompaction channel thickness is only 350 m. From equation 4.4 the Rayleigh number is $\sim 5 \times 10^{-3}$, which is likely too small for convection. Even reducing viscosity to 10^{15} Pa s leads to Ra $\sim 5 \times 10^{-5}$ as the decompaction channel would be only 3.6 m thick.

The lithosphere-asthenosphere boundary (LAB) underneath the continents, away from plate boundaries, may be a better analogue to the Martian models presented in this chapter. It has been hypothesized that there is a partially molten layer at the LAB underneath continents to accommodate plate motion over the asthenosphere [*Anderson*, 1989; *Mierdel et al.,* 2007]. Observed sharp seismic velocity gradients at the LAB also supports the possibility for a partially molten layer at this depth that may be ~11 km thick [*Rychert et al*., 2005; *Thybo*, 2006; *Rychert et al*., 2009]. Melt content is likely only a few per cent [*Rychert et al*., 2005; *Rychert et al*., 2009]. The strong dependence of the Rayleigh number on layer thickness can lead to $Ra \geq 1000$ if the viscosity is as lower than $\sim 10^{17}$ Pa s but this value

requires a higher melt content than inferred at the base of the lithosphere. In a younger Earth, with a hotter mantle capable of higher melt production, convective melt channels may have been possible.

4.5 Conclusion

As melt generated in the deep interior of Mars rises and reaches the lithosphere, it is expected to cool, crystallize and form a permeability barrier. We show here that for a broad range of expected lithosphere thicknesses and mantle temperatures, melt should accumulate in a growing decompaction channel underneath that barrier until the density contract between mostly the core channel core and mostly crystallized aggregates at the top of the channel triggered a convective instability. This crystallization-driven convection focuses melt and heat delivery at the top of the channel that start to thermally erode the lithosphere at regularly spaced points. While inaccessible by our current modeling capacity, these points of thermal erosion may develop into diapirs and dikes that could eventually form regularly spaced volcanic centers at the surface.

The spacing of Hesperian age volcanic vents at Syria Planum is similar to the wavelength of crystallization-driven convection for interior parameters appropriate for this time period. This brings confidence that this novel convection mechanism can influence observed geology. However, it may not be applicable to the entire history of the planet. The larger spacings as observed at shield volcanoes of the Tharsis region of Mars cannot be replicated in the performed models and may be generated by some larger scale melt focusing process. Melts generated at more recent time periods may

either reuse ancient passageways through the lithosphere, such as major central volcanoes, or crystallize completely at depth.

Further work is needed to stabilize the code in order to perform models with thin lithospheres and hot asthenospheres. These conditions should be explored as they likely represent the initial emplacement conditions of the oldest Martian volcanoes. Larger lateral model domains should be included to accurately capture the convection wavelength in thicker decompaction channels and 3D models would be needed link convection and volcano spacing in more detail. Further work is also needed to integrate brittle failure and cracking into the melt migration code. As the high porosity pockets rise against the permeability barrier, pressures may increase higher than the overburden pressure, imitating cracking and dike propagation from depth to the near surface [e.g. *Cai and Bercovici*, 2013].

Chapter 5: Modeling Melt Migration in the Lithosphere and Asthenosphere of Io

Abstract

Heat pipe processes have been proposed as an important heat loss mechanism for the early Earth, modern Io, and some exoplanets. However, fundamental aspects of heat pipes, such as their duration, are largely unknown. We use numerical and analytical models of melt migration to constrain the lifespan of Ionian heat pipes and explore convection as a mechanism for focusing asthenosphere melt to heat pipes. Heat pipe lifespans are calculated and found to be highly dependent on pipe width, ranging from ~10,000 years for a 1 km pipe to 6-7 million years for a 25 km pipe, most well beyond the existing 40 years of observational constraints. Melt ascent velocities in the heat pipe are adequate for supplying volcanic eruptions for hundreds to millions of years over a heat pipe lifespan. Smaller heat pipes, with widths less than 5-10 km close before the 2 million year time scale needed to recycle a 20 km thick lithosphere, while larger heat pipes may persist through several cycles if not forced closed by lithosphere collapse. Counterintuitively, upwellings in the asthenosphere do not efficiently supply melt to heat pipes. Instead, upwellings anticorrelated to heat pipe locations, that is, with downwellings directly underneath the heat pipe, pushing melt laterally along the base of the lithosphere towards heat pipes. The melt is extracted upward through the pipe as the solid travels downwards.

5.1 Introduction

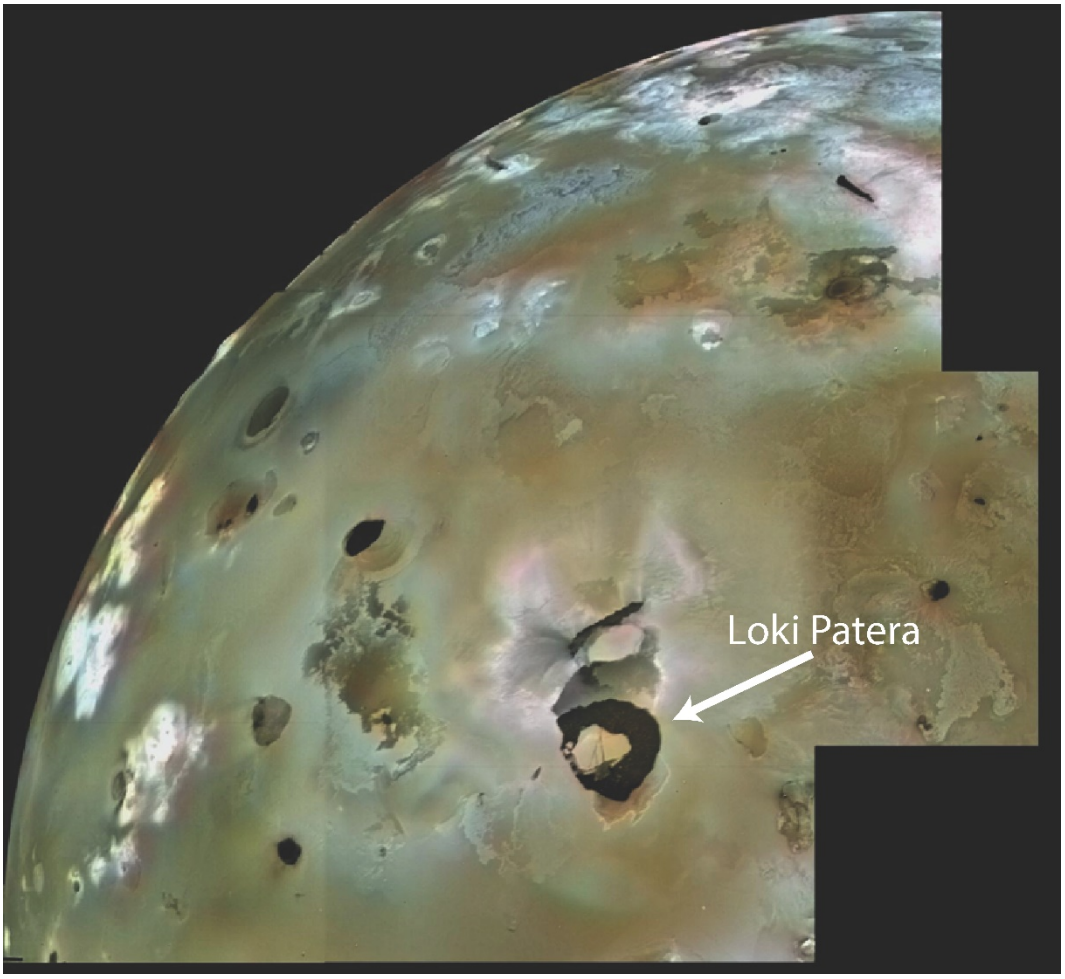

Figure 5.1 – Loki Patera and other volcanic features. Loki Patera consists of a lava lake (the black horseshoe shape, lower middle of the image), active since at least the 1979 flybys of Voyager 1. Loki Patera is 202 km in diameter. [*NASA/JPL/USGS*]

A mean motion resonance with Europa and Ganymede maintains a forced eccentricity in the orbit of Io around Jupiter ($e = 0.0041$, where $e = 0$ is perfectly circular and $e = 1$ is a parabolic trajectory) [*de Sitter*, 1928]. This eccentricity causes tidal heating inside of Io, intense enough to result in a high degree of interior melting [*Peale et al.,* 1979; *Khurana et al.,* 2011] and extensive, active surface volcanism (Figure 5.1) [*Hanel et al.,* 1979; *Morabito et al.,* 1979; *Smith et al.,* 1979; *McEwen et al.,* 1998; *Davies,* 2007]. The intensity and distribution of heating and melt in the

Ionian interior is a point of debate and estimates depend strongly on model parameters and methodology [e.g. *Peale et al.,* 1979; *Tackley et al.,* 2001; *Keszthelyi et al.,* 2007; *Steinke et al.,* 2020]. Nevertheless, the total surface power is measured to be $1.06 \pm 0.12 \times 10^{14}$ W [*Matson et al.,* 1981; *Veeder et al.*, 1994; 2012]. This yields an average heat flow of 2.529 ± 0.265 W/m^2 [*Davies et al.,* 2015], much higher than the average heat flow of the Earth: 0.087 W/m^2 [*Pollack et al.,* 1993].

If conduction is the primary heat transfer mechanism in the Ionian lithosphere, then the lithosphere must be very thin, only 4.5 km [*Peale et al.,* 1979; *Matson et al.,* 1981; *O'Reilly and Davies,* 1981]. However, the presence of mountains upwards of 10 km tall [*Carr et al.,* 1979] require a thicker lithosphere for support. The surface heat flux on Io also appears to be concentrated at discreet points, or "hot spots," which are locations of active volcanism (Figure 5.1) [*Hanel et al.,* 1979; *Veeder et al.,* 2009; 2011; 2012; 2015; *Davies et al.,* 2015]. The hot spot heat flow and required thick lithosphere suggest a heat transport mechanism unlike the plate tectonics of Earth or the stagnant lid conduction of Mars or the Moon.

Io likely transports heat through advection as magma rises from deeply rooted vents, or "heat pipes", to the surface [*O'Reilly and Davies,* 1981]. Heat pipes are either a singular conduit of magma, or network of conduits, which traverse the entire crust. The magma they carry erupts onto the surface, forming laterally extensive lava flows, lava lakes, and low-relief volcanic edifices called paterae. The lava flows cool to the ambient surface temperature of Io (-130°C) and are buried by subsequent lava flows and pyroclastic deposits. Lava flows are continuously buried until they reach the base of the crust, where they melt and mix into the partially molten asthenosphere.

The cycle continues as the melt in the asthenosphere is collected into the heat pipes and re-erupts to the surface.

The constant resurfacing and burial of surface material results in a relatively thick, cold lithosphere which is required to support Io's mountains. Based on a complete lack of impact craters on the surface of Io, the resurfacing must occur at a relatively high rate, likely ~1 cm/yr on average, with variations based on proximity to active volcanism [*Johnson et al.,* 1979; *Blaney et al.,* 1995; *Phillips,* 2000; *McEwen et al.,* 2004; *Kirchoff and McKinnon*, 2009]. The continuous resurfacing and melting results in an interesting characteristic unique to Io where the thermal lithosphere and the compositional crust all refer to the same outer layer of the body. These terms are used interchangeably in this chapter.

Beyond Io, heat pipe processes are increasingly invoked to explain the pre-plate tectonic Earth [*Moore and Webb*, 2013; *Kankanamge and Moore*, 2016], Venus [*Turcotte*, 1989; *Armann and Tackley*, 2012] and hypothesize on the nature of exoplanets [*Stern*, 2016; *Moore et al.,* 2017]. Despite recognition of their increasing importance, heat pipes themselves are rarely modeled or explored due to the complexity of the necessary melt migration processes. Beyond the notion that heat pipes must carry heat and melt in some way from the asthenosphere to the surface of Io, little or nothing is known about their structure, size, or lifespan.

In this chapter, we use recent advances in numerical modeling of melt migration to examine two unexplored aspects of heat pipe evolution. First, we use simple analytical calculations and numerical modeling to constrain the lifespan of heat pipes. Second, we create a numerical model of coupled solid-melt flow to

explore how melt is focused over large areas of the partially molten asthenosphere to the locations of heat pipes at the base of the lithosphere.

5.2 Heat pipe Closure

5.2.1 Introduction

Given the geologically rapid evolution of Io, which can completely recycle a 20 km lithosphere in 2 million years and produce thrust faulting that traverses the lithosphere *[Turtle et al.,* 2001; *McKinnon et al.,* 2001; *Jaeger et al.,* 2003; *Kirchoff and McKinnon*, 2009; *Bland and McKinnon*, 2016], it is unlikely heat pipes are a permanent feature. Beyond a structural closure through lithosphere collapse, the cooling and crystallization of melt in the pipe itself is expected. We explore the rate of this crystallization as a constraint on the closure and lifespan of heat pipes.

We assume a heat pipe structure consisting of a simple conduit from surface to base of lithosphere, with a slope at the base to encourage melt flow (Figure 5.2). It is unlikely that heat pipes are so simple. Presumably a magma plumbing system resembling terrestrial volcanic systems exists at shallower depths, and the deeper sections may be a more complex system encompassing many interconnected conduits of melt [e.g. *Cashman et al.,* 2017]. However, the heat pipes considered here are not an open conduit but consist of at most 30% melt distributed in a microscopic pore space. Thus, melt motion through the pipe, while not modeled in detail, is quite tortuous [e.g. *Zhu and Hirth*, 2003; *Miller et al.*, 2015] and slower than if assuming an open conduit. Our simple configuration allows for a first order constraint on the cooling and closure of heat pipes.

5.2.2 Methodology

We model heat pipe closure using two techniques. First, we create relatively simple two-dimensional, finite element models of melt flow in an idealized heat pipe. In order to assess the effect of melt migration on crystal growth on the heat pipe walls, we then use simple analytical techniques to model heat pipe closure as a Stefan problem [*Stefan*, 1891; *Vuik*, 1993], as applied to the cooling and crystallization of dikes [*Spohn et al.*, 1988].

5.2.2.1 Numerical model

Using the finite element code ASPECT 2.0.1 [*Kronbichler et al.,* 2012; *Heister et al.,* 2017; *Bangerth et al., 2018*; *Bangerth et al*., 2019] with melt migration [*Dannberg and Heister*, 2016; *Dannberg et al.,* 2019], we model the evolution of an idealized, pre-existing heat pipe in an Ionian lithosphere in two dimensions. For incompressible models with melt migration, ASPECT operates by solving a series of equations representing the conservation of mass and momentum, fluid (melt) flow, and temperature/heating describing the behavior of silicate melt moving through and interacting with a viscously deforming host. For an explanation of the equations solved in ASPECT with melt migration, see Appendix C. The main advantages of using ASPECT over other currently available finite element modeling packages are the included compaction physics and that the melt and solid matrix are both modeled as separate but related fields, so they can have diverging flow directions and velocities based on porosity, viscosities, and density contrasts (Appendix C, Equation C5).

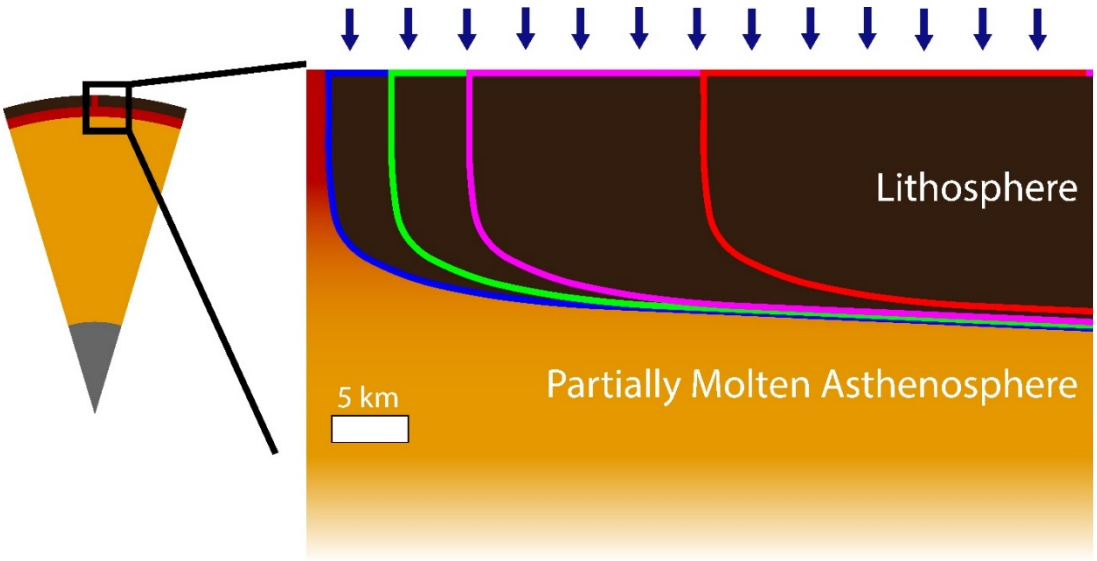

Figure 5.2 - Setup of heat pipe closure models. A 20 km thick lithosphere overlays 80 km of asthenosphere, only the top 10 km of which are shown here. The heat pipe is defined as an initial region of high porosity (melt content) on the left boundary. Models were run with four heat pipe radii: 1 km (blue), 5 km (green), 10 km (magenta), and 25 km (red). The model is resurfaced at 1.35 cm/yr (arrows).

The model set up consists of a 50 km wide by 100 km thick box representing a ~20 km thick lithosphere and ~80 km of upper asthenosphere. A heat pipe is modeled on the left of the model set up as a section of the lithosphere with the temperature of the asthenosphere. Depending the assumed adiabatic mantle temperature, the heat pipe contains 20 to 30% melt. Four separate models were performed with heat pipe widths of 1 km, 5 km, 10 km, and 25 km (Figure 5.2). The 1 km heat pipe was modeled with a resolution of 1 element cell per ~20 × 20 meters and the larger pipes were modeled at a resolution of 1 element cell per ~80 × 80 meters. ASPECT utilizes adaptive mesh refinement, however it is not utilized within the heat pipes in order to maintain a high resolution throughout the model run time. A slope is imposed on the base of the lithosphere, whereby the lithosphere is slightly

thinner near the pipe and thicker away from it, to facilitate melt flow to the base of the heat pipe (Figure 5.2). The effective thickness of the lithosphere is defined as:

$$H_{effective} = \frac{H}{\ln(W - r)} * \ln(x - r) \quad (5.1)$$

where H is the maximum lithosphere thickness (20 km), W is the width of the model domain (100 km), and r is the width of the heat pipe. This profile provides the slope seen in Figure 5.2.

The large 50 km by 80 km asthenosphere domain is modeled only to supply melt over the course of the model run. As the only relevant process occurring in this domain is the initial melt production, a course mesh of 1,250 × 1,250 meters per finite element is used. In reality, convection likely occurs in the asthenosphere, but it is ignored in this model, as the region of interest is the heat pipe itself.

The side boundaries are free slip and insulating. The bottom boundary is open to solid and melt flow. The top boundary has an imposed solid velocity of 1.35 cm/yr downwards, a simplification of the volcanic resurfacing of Io. For this simple model, where the primary interest is the closure rate of the pipe, the magma output through the top of the heat pipe and the resurfacing rate are not coupled. A fully coupled model would require a volcanic eruption and lava flow model to distribute the expelled magma across the surface, and likely outside the domain of the model.

The temperature of the asthenosphere is set to 1573 K, consistent with the eruption temperature constraints of *Keszthelyi et al*. [2007]. The initial temperature profile of the lithosphere is set to the steady state solution of the heat equation in a continuously buried lithosphere [*O'Reilly and Davies,* 1981]:

$$T = T_s + (T_m - T_s)\frac{e^{z/l} - 1}{e^{d/l} - 1} \tag{5.2}$$

where T_s is the surface temperature, T_m is the temperature of the mantle, d is the thickness of the lithosphere and $l = \kappa/v$, where κ is the thermal diffusivity and v is the burial rate. The burial rate is set to 1.35 cm/yr, matching the velocity of the resurfacing at the top boundary of the model.

We include several relevant sources of heat necessary to model the rise and crystallization of melt through a porous conduit. First, this model takes into account the release and consumption of latent heat due to melting and freezing. Second, this model accounts for adiabatic heating and cooling of both solid and melt as material rises. Third, shear heating and heat generated by melt segregation are included to account for the generation of heat as material flows along a solid boundary (i.e. the base of the lithosphere and side of the heat pipe). As the focus of this model is on the heat pipe itself, the internal tidal heating is not replicated. The long-term effect of tidal heating is to increase mantle temperature to the value used here, which is high enough that a melt fraction upwards of 25% is expected in the upper asthenosphere and the heat pipe. The heating and temperature equation to be solved in the numerical model is:

$$\begin{aligned} \bar{\rho} C_p \left(\frac{\partial T}{\partial t} + \mathbf{u}_s \cdot \nabla T\right) - \nabla \cdot k_{\text{thermal}} \nabla T \\ = T\Delta S\Gamma + \alpha T(\mathbf{u}_s \cdot \nabla p_s) + 2\eta(\dot{\varepsilon}_s : \dot{\varepsilon}_s) + \xi(\nabla \cdot \mathbf{u}_s)^2 \\ + \frac{\phi^2}{K_D}(\mathbf{u}_f - \mathbf{u}_s)^2 \end{aligned} \tag{5.3}$$

See Table 5.1 for a description of model variables and parameters.

Name	Symbol	Value	Unit	Equation
Temperature	T			(5.2)(5.3)(5.8) Appendix C
Surface temperature	T_s	113	K	(5.2)(5.5)
Asthenosphere temperature	T_m	1573	K	(5.2)(5.5)
Resurfacing rate	v	1.35	$\frac{cm}{yr}$	(5.2)
Lithosphere thickness	d	20	km	(5.2)
Thermal diffusivity	κ	$\frac{k_{thermal}}{\rho_s C_p}$		(5.2)(5.4)(5.8)(5.9) Appendix C
Reference solid density	ρ_{s_0}	3000	$\frac{kg}{m^3}$	(5.3)(5.5)(5.9) Appendix C
Thermal conductivity	$k_{thermal}$	4.7	$\frac{W}{m\,K}$	(5.2)(5.3)(5.4)(5.8)(5.9)
Phase weighted average density	$\bar{\rho}$		$\frac{kg}{m^3}$	(5.2) Appendix C
Specific Heat	C_p	1200	$\frac{J}{kg\,K}$	(5.3)(5.4)(5.5)(5.8)
Solid velocity	$\boldsymbol{u}_s$			(5.3)(5.8) Appendix C
Melt velocity	$\boldsymbol{u}_f$			(5.3)(5.8) Appendix C
Porosity	ϕ			(5.3)(5.8) Appendix C
Strain rate of the solid matrix	$\dot{\varepsilon}_s$			(5.3)(5.8) Appendix C
Darcy Coefficient	K_D	$\frac{k}{\eta_f}$		(5.3)(5.8) Appendix C
Melting/Freezing Rate	Γ	From melting model [*Katz et al.*, 2003]		(5.3)(5.8) Appendix C
Peridotite melting entropy change	ΔS	300	$\frac{J}{kg\,K}$	(5.3)
Time	t			(5.4) Appendix C
Latent heat of fusion	L	$\Delta S \times T_{solidus}$		(5.5)
Gravity	g	1.8	$\frac{m}{s^3}$	(5.6)(5.9)
Internal heating term	H	1.5×10^{-8}	$\frac{W}{kg}$	(5.8)(5.9)
Thermal expansivity	α	3×10^{-5}	$\frac{1}{K}$	(5.9) Appendix C
Reference permeability	k_0	10^{-8}	m^{-2}	Appendix C
Reference melt density	ρ_{f_0}	2500	$\frac{kg}{m^3}$	Appendix C
Reference bulk viscosity	ξ_0	10^{20}	$Pa\ s$	Appendix C
Reference Shear viscosity	η_0	5×10^{20}	$Pa\ s$	Appendix C
Melt viscosity	η_f	1	$Pa\ s$	Appendix C
Melt weakening parameter	a	27	$unitless$	Appendix C
Reference temperature	T_0	370	K	Appendix C

Table 5.1 - Variables and parameters for Ionian melt migration models and associated calculations

The melting model follows the parameterization of *Katz et al.* [2003] for dry peridotite. Dry peridotite is an acceptable approximation of the Ionian mantle due to the basaltic and kommatiitc lava flows on the surface, suggesting a peridotite-like mantle. Due to the constant melting of Io's interior and the ongoing widespread volcanic eruptions, Io is likely completely devolatilized. See *Keszthelyi and McEwan* [1997], *Keszthelyi et al.* [2007], and Chapter 3 of this dissertation for a petrological defense of a peridotitic Ionian mantle.

5.2.2.2 Stefan Problem

In order to determine the amount of time until heat pipe closure for heat pipes with width other than the four tested models, we also consider an analytical solution of the Stefan problem, typically applied to the cooling and crystallization of a dike or sea ice [*Stefan*, 1891; *Spohn et al.*, 1988; *Vuik*, 1993; *Turcotte and Schubert*, 2014]. In a Stefan problem, heat is transferred by diffusion between a molten body and a solid medium in contact with it, with an additional heat source resulting from crystallization at the interface between the two domains. Essentially the Stefan problem tracks the location of the boundary where solidification occurs, measured here as the location where $T = T_{\text{solidus}}$. The solution is complicated due to the latent heat of crystallization, where melt releases heat as it solidifies.

We use the formulation of *Turcotte and Schubert* [2014], where the position of the solidifying wall y_m changes over time t as:

$$y_m = 2\lambda_1\sqrt{\kappa t} \tag{5.4}$$

where κ is the thermal diffusivity and λ_1 is a constant value corresponding to the solidification boundary, given by:

$$\frac{L\sqrt{\pi}}{C_p(T_m - T_s)} = \frac{e^{\lambda_1^2}}{\lambda_1(1 - \mathrm{erf}\lambda_1)} \tag{5.5}$$

where L is the latent heat of fusion, C_p is the specific heat of the melt, T_m is the temperature of the molten material (the asthenosphere temperature), T_s is the temperature of the solid material (the surface temperature). Input parameters match those used in the numerical model and are shown in Table 1.

5.2.3 Results

Numerical models with heat pipe widths of 1, 5, 10, and 25 km were solved. The closure of the heat pipe is recorded as the location of the solidus temperature, ~1358 K, along a transect at 2 km depth (Figure 5.3). The solution of the Stefan problem using the numerical model parameters as inputs is also plotted on Figure 5.3 for reference.

Two main phenomena are observed to occur in the numerical models. First, melt is generated in the asthenosphere and rises to the base of the lithosphere. Melt generated underneath the heat pipe itself rises through the pipe to exit the model. Melt generated away from the heat pipe rises and accumulates under the base of the lithosphere, forming a decompaction channel [Spiegelman, 1993]. The melt at the base of the lithosphere travels upslope to supply the heat pipe with melt. However, the lateral flow at the base of the lithosphere is insufficient to balance melt accumulation and melt extraction at the heat pipe. Hence, the melt content and porosity of the decompaction channel away from the pipe increases over time while supply to the pipe is limited to the asthenosphere directly underneath the pipe. The consequences of this limited melt supply are explored in detail in the second series of

models presented in Section 5.3. For now, its main effect is to lead to progressive pipe closure.

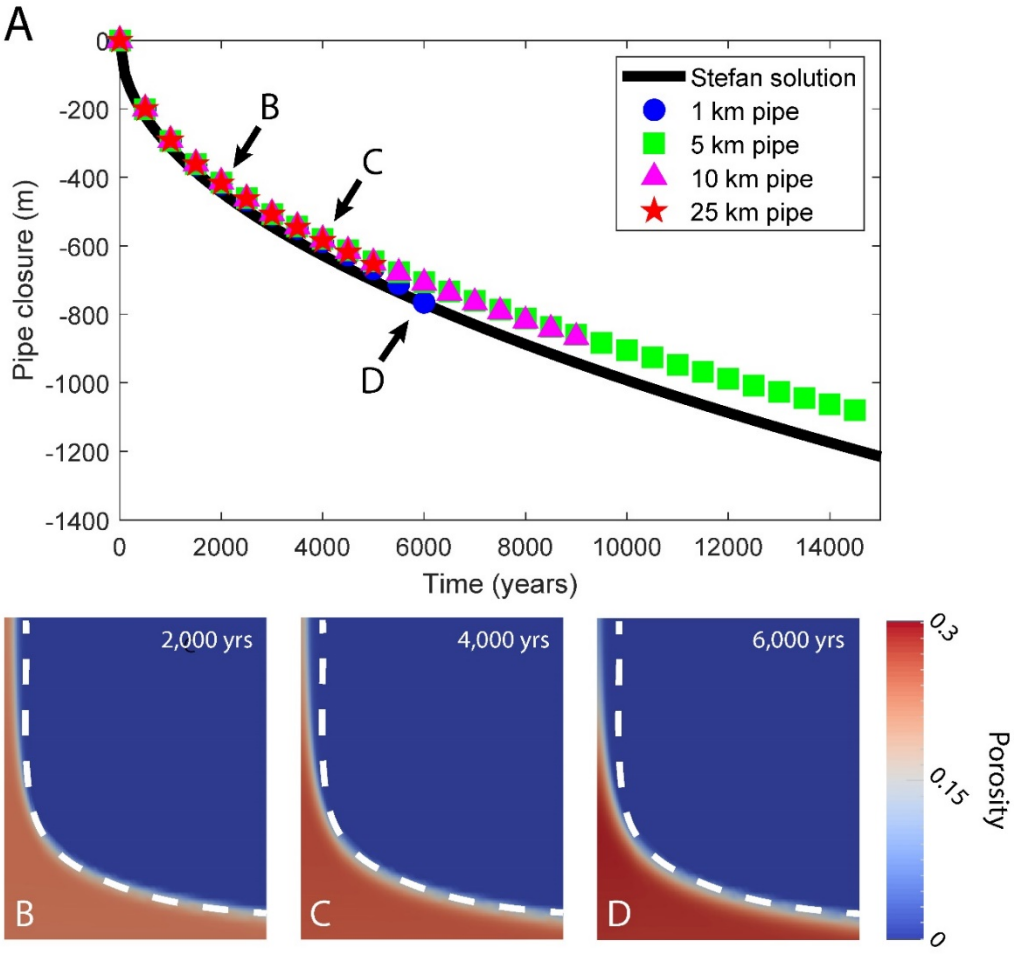

Figure 5.3 - A) Results of heat pipe closure numerical models (colored points) and solution to the idealized Stefan problem (solid black line). Results displayed as a plot of time in years vs. pipe closure, where pipe closure is recorded as the location of the solidus temperature, in meters, respective to original heat pipe width. B, C, and D) show example numerical results of pipe closure at 2,000 years, 4,000 years, and 6,000 years respectively for the 1 km width heat pipe. The white dashed line denotes the original 1 km width, and the depth where the pipe closure was recorded.

The second main phenomenon observed is these models is indeed that all the modeled heat pipes close over time. While in principle, melt from immediately below the pipe should replace upward-migrating melt already in the pipe, the pipe also loses

heat to the surrounding lithosphere. As this heat is not replenished by the rising melt, the heat pipe cools and the melt inside crystallizes against the side of the pipe, shrinking the width of the pipe (Figure 5.3).

Due to the large amounts of melt accumulating in the decompaction channel, the models terminate before complete heat pipe closure can be observed. The 1 km pipe numerical model terminates at ~6,000 years, the 5 km pipe model terminates at ~14,500 years, the 10 km pipe model terminates at ~9,000 years, and the 25 km pipe model terminates at ~5,000 years.

All four numerical models yield heat pipes with 25-35% melt, with melt ascent velocities of 5-10 meters per year over the course of the model runtimes. The 1 km width pipe yields reduced porosity and melt velocities (7% and 1 m/yr) at the end of the run time as the pipe cools and nears total closure. Porosity also decreases in the 25 km width pipe as the large pipe width efficiently removes the initial melt from the model. Near the end of the model run, the 25 km pipe model reduces pipe porosity to ~20%. In models with an intermediate pipe width, such as 5 km width pipe model of Figure 5.3 B though D, melt porosity inside the pipe actually increases as the pipe cools and flow becomes more restricted. A relatively high porosity is sustained by the high decompaction pressure despite the decreasing temperature. Porosity changes related to melt flux difference are relatively minor. Pipe closure is mainly the result of heat loss at the edge of the pipe.

5.2.4 Discussion

5.2.4.1 Predicted Pipe Closure

The predicted heat pipe closures of the numerical model are in general agreement with the Stefan problem solution (Figure 5.3A). The numerical models largely agree with each other, tracking the same closure rate of the heat pipe regardless of initial pipe diameter, with the exception of the very end of the 1 km model run. The heat pipes in the numerical model close slightly slower than the Stefan problem solution. The deviation is best seen at the termination of the 5 km numerical model, where after 14,500 years, the numerical pipe has shrunk by ~1080 m, but the analytical solution predicts 1195 m of closure, a ~10% discrepancy.

This discrepancy is likely due to the inclusion of shear heating and melt segregation in the numerical model, both of which generate heat that would counteract heat loss to the cold lithosphere that surrounds the pipe. As melt flows through the rock matrix and as material flows against the wall of the heat pipe, heat is generated. In the idealized Stefan problem, the only heat source considered is latent heat release due to the crystallization of the melt. Shear heating also likely explains why near the termination of the 1 km width numerical model, the closure rate increases. Porosity and melt velocity are reduced, therefore less shear heating occurs, and the pipe closes faster. Alternatively, as the heat pipe narrows and the walls become closer, the influence of the second wall may affect the temperature evolution and close the pipe at a quicker rate.

No numerical model was observed to close completely. Compete closure using the Stefan problem is expected after 9,480 years for the 1 km heat pipe, 236,980

years for the 5 km heat pipe, 947,940 years for the 10 km model, and 5,924,600 years for the 25 km model.

The largest eruptive center on Io is Loki Patera, which consists of a 202 km diameter lava lake (Figure 5.1). In the unlikely case where the surface expression is reflective of a 100 km width heat pipe, the Loki Patera heat pipe would close in 95 million years according to the Stefan solution. Smaller width heat pipes closure can be observed in Figure 5.3A. For example, a 100 m width heat pipe would be expected to close in ~100 years.

5.2.4.2 Pipe Closure Rates vs. Melt Ascent Rates vs. Resurfacing Rates

Heat pipe closure, as modeled here does not appear to be a significant barrier to melt extraction. In the numerical model, melt flows upwards in all four pipes at a velocity between 5 and 10 m/yr. If the 1 km heat pipe closes after ~10,000 years as described in the previous section and melt travels at 10 m/yr, melt can ascend 100 km, much more than the estimated lithospheric thickness of Io, permitting observed surface eruptions.

Melt ascent in the model is limited to porous flow along grain boundaries [i.e. *McKenzie,* 1984]. In reality, channelization and dike processes are likely to occur and facilitate melt ascent. Based on buoyant ascent due to the density contrast between the solid rock and melt, a simple estimate of melt ascent in a channelized heat pipe can be made:

$$c_{\text{channel}} = \frac{g(\rho_s - \rho_f)A_e}{8\pi\eta_f} = \frac{g(\rho_s - \rho_f)}{8\eta_f}\phi r^2 \qquad (5.6)$$

where $A_e = \pi r_e^2$ is the effective cross sectional area of the pipe, and where the effective radius, $r_e = r\sqrt{\phi}$, represents the radius of the pipe if all the distributed melt were collected into a smaller 100% melt conduit. At 30% melt in the pipe, assuming $\eta_f = 1$ Pa s, the simple channelized melt calculation yields an ascent rate of 10^{12} km/year (or 3×10^{-5} m/s) for a 1 km heat pipe, 13 orders of magnitude higher than the closure rate. Larger radius pipes increase channelization velocity as a function of r^2. If all the melt was collected in a single open conduit, melt flow would be so rapid that the pipe would almost instantaneously collapse on itself.

A single large column of pure melt is of course an unlikely scenario, and reality likely involves volcanic systems similar to those observed on earth, with networks of thin dikes. Even in this case, a network of thin channels in the porous heat pipe, the ascent velocity will be orders of magnitude larger than the closure rate. Even a 5 meter wide channel produces a melt velocity of 2.7×10^7km/yr melt velocities. The ascent velocity will depend greatly on the volcanic structure and pressurization of the melt. Geothermobarometry analysis of terrestrial samples suggest rapid melt ascent rates from 0.02 to 0.1 m/s are likely in the Earth's lower crust [*Mutch et al.,* 2019].

With a resurfacing rate of ~1 cm/yr, a 20 km Ionian lithosphere will completely recycle in 2 million years. The closure models suggest that if heat pipes are thin, as in the 1 km or 5 km model, pipes are transient features that disappear completely due to cooling over a single cycle of the lithosphere. Larger pipes such as the 25 km model appear to be more established features which persist through the evolution and recycling of the lithosphere. In the large widths, long life case it is

possible that lithosphere collapse (mountain generating thrust faulting, at the million year timescale of lithosphere resurfacing) terminates heat pipes abruptly rather than slow cooling.

5.2.4.3 Conduit Waves and Periodic Volcanism

Experiments have shown that fluid conduits in a viscous medium can support solitary waves [*Scott et al.,* 1986; *Olson and Christensen,* 1986; *Whitehead,* 1988]. A heat pipe, as modeled here, is fluid conduit in a viscous, solid lithosphere, therefore solitary waves may represent pulses of melt through the heat pipe. Short period pulses may be linked to periodic volcanic eruptions observed on Io [*de Kleer et al.,* 2019]. We adapt the formulations of *Olson and Christensen* [1986] to assess the timescale of magma pulses related to solitary waves:

$$t_{\text{pulse}} = c^{-1}\left(\frac{\eta_s A_e}{8\pi\eta_f}\right)^{1/2} \tag{5.7}$$

where c is the melt ascent velocity and A_e is the effective cross sectional area of the heat pipe, as in Equation 5.6. For the 1 km pipe with 30% melt in the pipe and the same parameters as the numerical, $t_{\text{pulse}} = 4.3 \times 10^9$ years. This is almost the age of the solar system, and obviously well beyond humanity's 40 years of observation of Io. A 40 year timescale is only achievable with a pipe radius of 10 nanometers. Larger pipes yield even longer wave periods. Solitary waves do not appear to be a significant driver of eruption periodicity.

5.3 Melt Focusing to Heat pipes

5.3.1 Introduction

One ancillary result of the modeling in the previous section is that the melt in the interior of Io is not predisposed to flow towards the base of heat pipes, even when given a reasonable slope (Equation 5.1, Figure 5.2). Due to the reduced gravity of Io compared to the Earth, the buoyant force associated with melt in the interior of Io is seemingly not large enough to initiate sufficient lateral flow upslope even with porosities as high as 40% in the decompaction channel, above the ~35% porosity limit of flow along grain boundaries. Instead melt accumulates at the base of the lithosphere, immediately above where it was generated, and decompacts the rock matrix, forming a high porosity decompaction channel which stores melt [e.g. *Sparks and Parmentier,* 1991]. The thickness and porosity of this layer appears to grow without limit over the course of the model runtime.

A relatively thin high porosity layer at the base of the lithosphere likely exists in Io [e.g. *Moore* 2003; *Keszthelyi et al.,* 2007; *Khuruna et al*., 2011], however it cannot grow uncontrollably to encompass the entire asthenosphere. The mantle of Io requires some degree of rigidity for tidal heating to occur, so there is an upper limit to the melt fraction of the asthenosphere [*Keszthelyi et al.,* 2007]. Some process must be occurring which redistributes melt throughout the asthenosphere or focuses melt to the base of heat pipes so that it may be erupted to the surface.

If melt cannot flow laterally to the base of heat pipes or sink into the lithosphere due to its density being lower than that of the solid mantle, then solid flow must occur to facilitate melt transport. The most likely candidate for solid flow in

planetary interiors is thermal convection. Solid convection of Io's asthenosphere is likely [*Moore* 2001; 2003] and seemingly necessary to explain the dissonance between surface distribution of hotspots and laterally variable models of heat production in the interior [*Tackley et al.,* 2001; *Hamilton et al.,* 2013]. Here we test solid convection as a possible mechanism for focusing melt to heat pipe centers.

5.3.2 Methodology

As in the heat pipe closure models, we use the finite element code ASPECT [*Kronbichler et al.,* 2012; *Heister et al.,* 2017; *Bangerth et al., 2018*; *Bangerth et al*., 2019] with melt migration [*Dannberg and Heister*, 2016; *Dannberg et al.,* 2019], however here we focus on melt distribution in the asthenosphere and base of the lithosphere rather than in the interior of the heat pipe. As previously described, ASPECT solves a series of equations necessary to model the behavior of silicate melt moving through and interacting with a viscously deforming host (Appendix C).

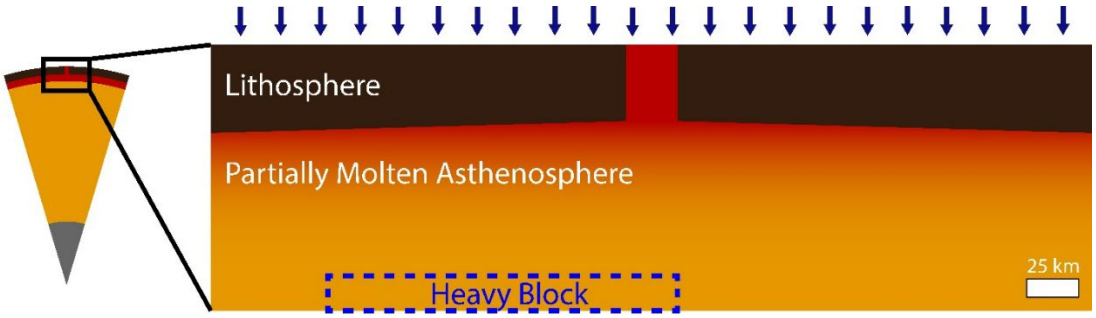

Figure 5.4 - Setup of melt focusing models including a simplified heat pipe with a width of 25 km. The dashed line outlines a slab of high-density material, which falls out of the model space in the initial timesteps. The resulting downwelling material initiates upwelling away from the initial slab location. The two discussed models start with the heavy slab away from the base of the pipe, to start an upwelling directly underneath the pipe (Figure 5.5A), or with the heavy slab under the pipe to start upwelling away from the pipe (Figure 5.5B). The right and left boundaries are periodic, so that the model domain represents a continuum of equally spaced heat pipes.

The initial conditions of the model consist of a two-dimensional box (Figure 5.4). The box is 75 km thick representing ~25 km of cold lithosphere and ~50 km of hot, upper asthenosphere. The box is 250 km wide. We include a 15 km wide pipe in the center of the model so that melt can be efficiently extracted from the system. Again, a small slope (~10˚) is implemented on the base of the lithosphere to accommodate melt flow. The top boundary flows inward at 1cm/yr, representing resurfacing. As this model represents only the lithosphere and upper asthenosphere, the bottom boundary is open to solid and melt flow.

The side boundaries are periodic, essentially mirroring each other, so that the model represents a series of two-dimensional heat pipes and underlying structures. The 250 km model width and periodic boundaries were chosen to replicate the average nearest neighbor spacing of hot spots on Io [*Hamilton et al*., 2013], with the assumption that similar melt focusing or distributing processes must be operating under each eruptive center.

As in the previous model, latent heat release, adiabatic heating, and shear heating terms are included. Differing from the model in the previous section, tidal heating is represented in this model as a simple constant heating term in the asthenosphere. We do not implement a full tidal heating calculation as this model is focused specifically on melt behavior at the base of the lithosphere. The addition of the heating term alters Equation (5.3) to:

$$\bar{\rho}C_p\left(\frac{\partial T}{\partial t}+\mathbf{u}_s\cdot\nabla T\right)-\nabla\cdot k_{\text{thermal}}\nabla T$$
$$=T\Delta S\Gamma+\alpha T(\mathbf{u}_s\cdot\nabla p_s)+2\eta(\dot{\varepsilon}_s:\dot{\varepsilon}_s)+\xi(\nabla\cdot\mathbf{u}_s)^2 \qquad (5.8)$$
$$+\frac{\phi^2}{K_D}\left(\mathbf{u}_f-\mathbf{u}_s\right)^2+\rho_s H$$

Convection is seeded using a novel method. Traditionally solid convection is initiated by using a hot thermal anomaly at the bottom of the model domain or by introducing a harmonic oscillation in the initial conditions. Since this model is above the solidus over most of the domain introducing a positive thermal anomaly would produce a large pocket of melt which preferentially flows upwards due to density contrast and insufficient solid motion is produced. A harmonic perturbation is also inadequate as the model domain is focused on the base of the lithosphere and the immediately underlying asthenosphere, not the whole thickness of a prospective convection system. The solution adopted in the presented models is to instead place heavy "blocks" into the bottom of the model domain (Figure 5.4). These blocks are given relatively high densities (4000 kg/m^3). Since the bottom of the domain is open to solid flow, these blocks "fall" out of the bottom of the model domain in the initial timesteps and create upwellings away from the original position of the blocks. As the blocks exit the model domain, they do not affect the model in any way other than initiating the upwellings and downwellings. The block is placed either away from the heat pipe to initiate an upwelling under the heat pipe, or under the heat pipe to initiate an upwelling away from the heat pipe. This initial condition is not reflective of

reality; however it adequately initiates the geologically ongoing process of interest for this study.

5.3.3 Results

5.3.3.1 No convection

In a control model with no convection, the results are the same as the previously described heat pipe lifespan section. Melt rises through the asthenosphere, collects and forces decompaction under the lithosphere. Melt does not flow laterally to the base of the heat pipe. After ~45,000 years, the porosity at the base of the lithosphere reaches upwards of 55%, well beyond the capability of the physics being modeled in ASPECT.

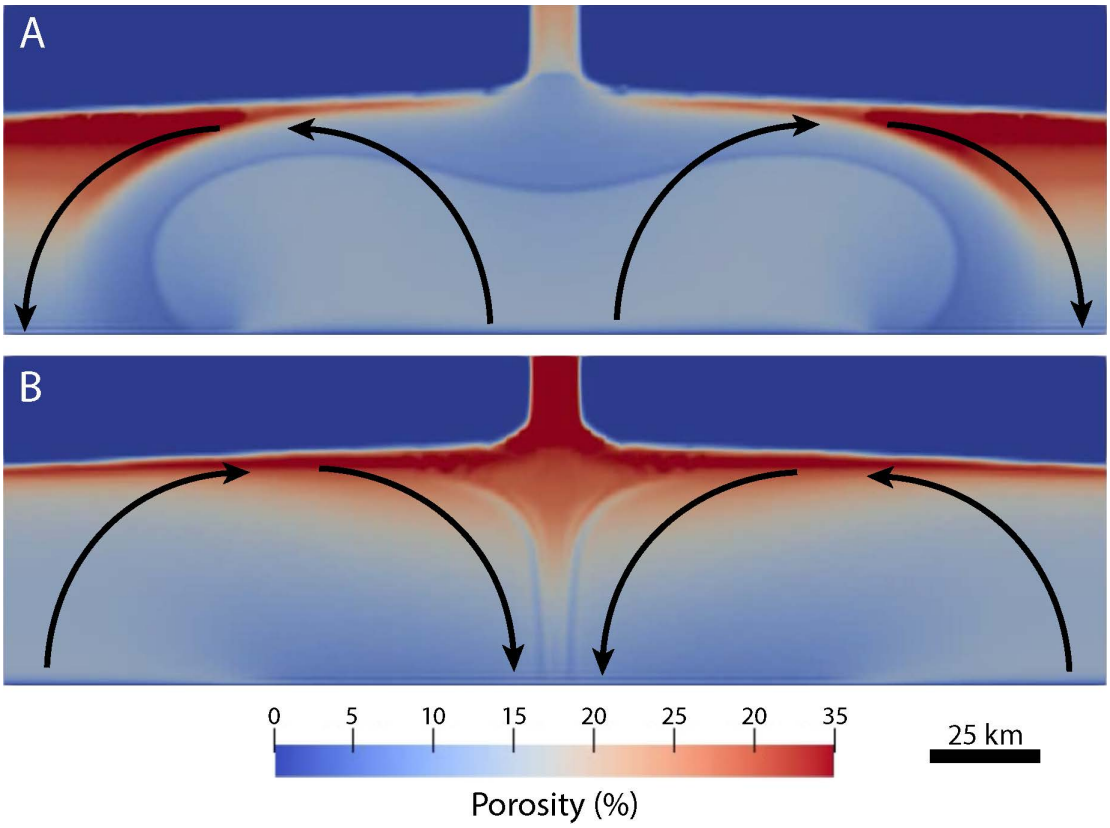

Figure 5.5 – Results of melt focusing models. A) The upwelling is seeded under the heat pipe. As the upwelling rises and encounters the base of the lithosphere, melt is

pushed laterally away from the heat pipe. As solid material downwells, melt collects in large masses at the base of the lithosphere, anticorrelated to heat pipe location. Snapshot is taken ~29,000 years into model run. B) The upwelling is seeded away from the heat pipe. Horizontal convergence towards the downwelling pushes melt towards the heat pipe. Melt preferentially travels upwards into the pipe as the solid downwells. Snapshot is taken ~50,000 years into model run.

5.3.3.2 Upwelling under the base of the heat pipe

Two heavy blocks, each 10 km thick and 50 km wide are placed at bottom right and left corners of the model domain. These blocks descend out of the model domain, fully exiting the calculation after ~34 years. Solid material follows the descending blocks creating a persistent downwelling. Between the two descending blocks, material rises from the bottom boundary, forming an upwelling centered below the heat pipe. Solid material upwells from the center of the model, spreads laterally against the base of the lithosphere, and descends at the edges of the model, creating an approximation of two convective cells in the model domain (Figure 5.5A).

The melt immediately underneath the heat pipe rises into the heat pipe; however, as the upwelling transitions into lateral flow against the base of the lithosphere, melt is pushed away from the heat pipe towards the left and right edges of the model domain. Due to the solid-melt density contrast, melt preferentially travels upwards, even at the solid downwelling. This creates a growing reservoir of melt, tens of kilometer's thick, anticorrelated to the location of the surface heat pipe. The heat pipe itself is starved of melt supply, and slowly begins to freeze and close. The model is terminated at ~29,000 years when porosity in the decompaction channel above the downwellings becomes too large for melt migration calculations.

5.3.3.3 Downwelling under the base of the heat pipe

In this model one heavy block, 10 km thick and 100 km wide, is placed at the bottom of the model, centered underneath the heat pipe. This block completely descends out of the model after ~35 years. The descending block kick starts a solid downwelling underneath the heat pipe and upwellings at the edges of the model, again approximating two convection cells albeit each shifted compared to the previous model. As the upwelling encounters the base of the lithosphere, lateral flow initiates towards the base of the heat pipe (Figure 5.5B).

Melt at the base of the lithosphere is pushed by the lateral solid flow towards the heat pipe. As in the previous model, the solid flow is directed downwards underneath the heat pipe but the melt preferentially travels upwards due to the solid-melt density contrast. Horizontal convergence and melt buoyancy combine to collect melt above the downwelling. In this model, melt is extracted by the heat pipe instead of accumulating under the lithosphere. A thin (~5 km) high porosity (~30 %) channel remains at the base of the lithosphere. In contrast to the previous model, the channel is stable over the model run and serves to accommodate melt flow to the heat pipe. While the melt is focused to the heat pipe, the limits of the modeled physical system are such that a steady configuration in which melt would be extracted at the same rate as it is supplied cannot be achieved. Instead, the model is terminated at ~50,000 years.

5.3.4 Discussion

5.3.4.1 Convective Assumption

Our assumption of thermally driven convection can be tested via a simple Rayleigh number analysis. For convection in an internally heated layer,

$$Ra = \frac{g\rho^2 \alpha H D^5}{\eta \kappa k_{\text{thermal}}} \tag{5.9}$$

where ρ and η are the density and viscosity respectively of the solid-melt aggregate and D is the thickness of the convecting layer. The density and viscosity are taken from the model and found to be $\rho \approx 2900$ kg/m^3 and $\eta \approx 10^{15}$ Pa s. Due to the associated fifth power, the thickness of the layer is significant to the calculated Rayleigh number. As described in the model set up, the entire asthenosphere is not being modeled, only the upper 50 km, so the true thickness of the layer is unclear. However, if only the modeled 50 km is used in the calculation, the Rayleigh number is found to be 3.4×10^8, well over the threshold of convection. Increasing the thickness further increases the Rayleigh number, therefore convection is the natural state of the modeled box and the forced initiation of convection is appropriate.

Finite amplitude convection models predict a horizontal velocity in internally heating convection cells of $u_0 \sim \frac{R_\lambda^2}{2\left(1+R_\lambda^4\right)^{\frac{1}{2}}} \frac{\kappa}{D} Ra_H^{\frac{1}{2}}$, where $R_\lambda = \frac{\lambda}{2D}$ is the ratio of convection wavelength to layer thickness [*Turcotte and Schubert,* 2014]. In our case, $R_\lambda = 2.5$ and $u_0 \sim 30$ m/yr. This motion being much faster than melt migration velocity, melt is efficiently entrained by solid convection, as we observe in our models.

5.3.4.2 Volcanoes Over Upwellings

The most significant result of this model is the counterintuitive notion that an eruption center overlays a downwelling. On the Earth we know rising plumes create hotspot volcanism and upwellings deliver melt to mid ocean ridges. On Io it appears that the most efficient arrangement for melt extraction actually occurs when the upwelling is as far from the heat pipe as possible, so that melt can be pushed laterally towards the extraction centers (Figure 5.6). Putting an upwelling underneath the heat pipe pushes most melt away from the extraction center and actually starves the heat pipe of melt and facilitates closure.

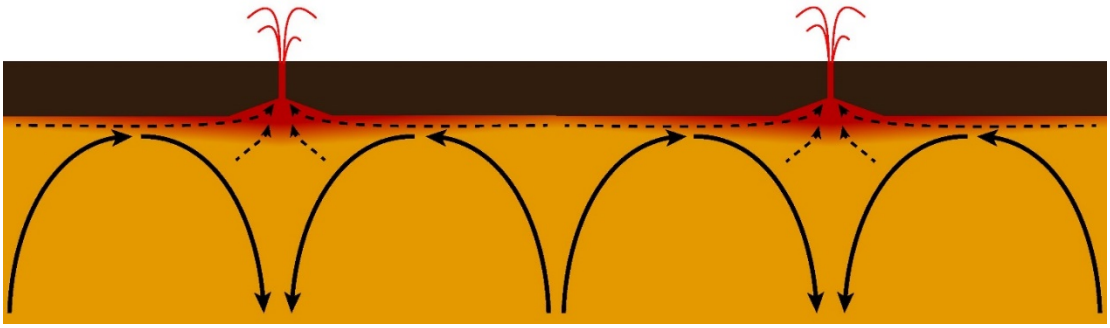

Figure 5.6 – Schematic of proposed convection-based melt focusing in the interior of Io. Upwellings are anticorrelated to the location of heat pipes. Upwellings push melt laterally along the base of the lithosphere to the heat pipes where melt can travel to the surface and erupt as lava flows.

On the Earth, volcanic centers overlay upwellings because the only melt available is from the upwelling. Volcanism reflects melt generation. On Io, melt is seemingly abundant in the asthenosphere and pathways for melt ascent are limited to the heat pipes, likely represented at the surface by only 173 active hotspots [*Hamilton et al.,* 2013]. The limited number of melt extraction points suggest that melt will accumulate unless some lateral force can push it towards a heat pipe.

Convective cells in the asthenosphere of Io are likely not rooted to lithospheric heat pipes. In reality, and especially considering the high Rayleigh

number deduced here, convective cells likely move through geologic time sometimes resulting in the efficient focusing of Figure 5.5B and 5.6 and other times accumulating melt away from active heat pipes as in Figure 5.5A. When melt accumulates at the base of the lithosphere away from a heat pipe, processes such as brittle failure, diking, and intrusive plutons [*Spencer et al.,* 2020] may occur, forcing melt upwards. Some combination of these processes likely initiates the formation of new heat pipes. It may also be possible that heat can be initiated by bolide impacts. The long duration of heat pipes, discussed in section 5.2 make it possible to see these structures as the scar in the lithosphere of specific events that may have happened millions of years ago.

Distribution of Io's near-equatorial volcanic heat flow, estimated from active hotspots, is systematically offset from models of tidal dissipation (Figure 5.7) [*Veeder et al.,* 2012; 2015; *Hamilton et al.,* 2013]. Regions of larger asthenospheric heat flux are expected to be the locations of magmatic upwellings. Therefore, assuming that more melt is generated at the maxima of tidal dissipation, lateral melt flow must be occurring below the base of the lithosphere of Io to deliver melt to the inferred hotspot clusters. Nonsynchronous rotation [*Radebaugh et al.,* 2001; *Schenk et al., 2001*, *Kirckoff et al.,* 2011] and regional favorability to melt ascent [*Hamilton et al.,* 2013] have been invoked to explain this offset; however, the results presented here suggest an alternative. While this project is focused on convection patterns in the upper asthenosphere and the spacing of individual heat pipes, the same upwelling-induced lateral flow may be occurring on a larger, deeper asthenosphere scale. Large deep asthenosphere upwellings may push melt laterally over several thousands of

kilometers where it can be focused to heat pipe clusters. Then the convective process active over tens of km presented here may focus melt to individual heat pipes.

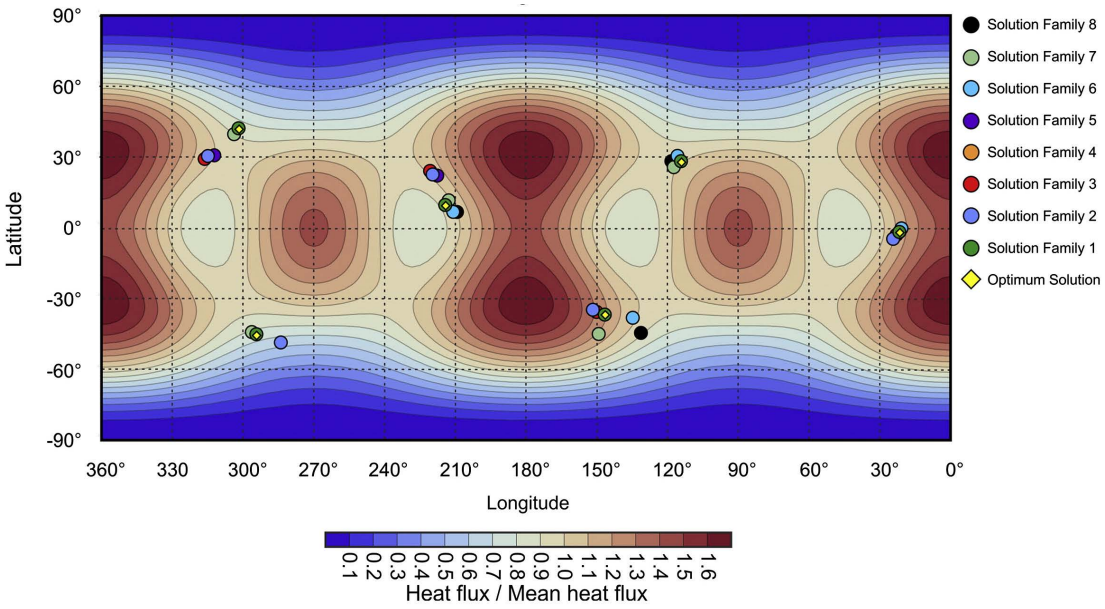

Figure 5.7 - Hot spot clusters plotted on expected heat flux from tidal dissipation modeling. *From Hamilton et al.* [2013]. Reprinted from *Earth and Planetary Science Letters, Vol. 361,* Authors C. W. Hamilton, C. D. Beggan, S. Still, M. Beuthe, R. M. C. Lopes, D. A. Williams, J. Radebaugh, W. Wright, Spatial distribution of volcanoes on Io: Implications for tidal heating and magma ascent, Pages 272-286, Copyright (2012), with permission from Elsevier.

5.3.4.3 Pipe Closure vs. Convective Velocities

In the downwelling centered model the convective velocity supplies melt to the heat pipe faster than the model can extract it. This suggests that in an efficient convective regime pipe closure is not impacted by melt supply, and large fluxes of melt travel through even the thinnest heat pipe over its lifespan.

The modeled upwellings travel at a velocity of ~10 m/yr. This matches the modeled velocity of melt in the heat pipe from the previous section. As discussed, melt likely channelizes in the heat pipe, creating a much larger melt velocity and flux. This increased flux would accommodate more melt flow into the base of the lithosphere and prevent the overwhelming heat pipe porosities which terminate the

downwelling centered model. Convective melt velocity is not a hurdle to melt flow in the heat pipe. However, an inefficient convection regime with an upwelling underneath the heat pipe starves the heat pipe of melt and facilitates pipe closure.

5.4 Concluding Remarks

The presented work attempts to begin the exploration of heat pipes as a dynamic process. The lifespan of heat pipes is highly dependent on the width of the heat pipe, where heat pipes with less than 1 km widths existing for less than 1000 years, while 100 km heat pipes could exist for several million years, longer than the total recycling of the lithosphere. In all but the sub 1 km widths, melt supply as measured by melt ascent rates and convective velocities is adequate to supply surface volcanism for hundreds to millions of years prior to heat pipe closure. Heat pipes are likely not the surface expression of asthenosphere upwellings. The overwhelming quantities of melt in the asthenosphere of Io require lateral motion at the base of the lithosphere towards heat pipes. This lateral motion is supplied by the lateral translation of upwellings anticorrelated to heat pipes

While focused on the lifespan and death of heat pipes, this work neglects the birth of heat pipes. The melt accumulation of the upwelling centered convection model (Figure 5.5A) suggests that melt may be focused to locations away from heat pipes. This accumulation of melt may initiate heat pipe formation through brittle cracking and intrusion, however the necessary physics for modeling these processes do not currently exist in numerical modeling codes for melt migration. Future modeling should attempt to develop the necessary code and include these processes. The same physical processes are likely necessary for melt channelization in the

existing heat pipes and would further refine model results, allowing for longer duration models involving the recycling of the lithosphere.

The presented model assumes the lithosphere resembles the simple model of *O'Reilly and Davies* [1981], where all melt and heat escapes Io's interior via heat pipes, and the rest of the surrounding lithosphere is cold from surface to asthenosphere. One possibility for future added nuance is intrusive magmatic processes. Efficient melt focusing to the base of heat pipes may not be an essential process if, like on the Earth, intrusive pluton emplacement accounts for most magmatic activity [*Spencer et al.,* 2020]. The models presented in this paper do not include the necessary physics for pluton emplacement but should be considered for future work.

Chapter 6: Summary of Results and Future directions

6.1 Summary of Significant Results

6.1.1 Permeability Barrier Evolution in the Martian Lithosphere

Permeability barrier formation is modeled in the lithosphere of Mars using a one-dimensional coupled petrological geodynamical model. At lower strain rates (< 10^{-15} s^{-1}), permeability barriers are found to form deep in the lithosphere. Higher strain rates (10^{-13} s^{-1}) create shallower permeability barriers. Including relatively small amounts of water (25 ppm) into the mantle source reduces mantle viscosity and yields shallower permeability barriers. Large amounts of water (1000 ppm) produce very shallow barriers, or no barriers at all, allowing melt to flow unimpeded to the near surface.

Deeper permeability barriers are likely linked to formation of localized volcanic edifices due to thermal instability channelization. Shallow barriers likely allow melt to percolate upwards over wider areas creating widespread volcanic flows. As Mars cools, permeability barriers become deeper, stopping widespread flows from forming and only permitting ascent to established edifices such as the shield volcanoes of the Tharsis region.

6.1.2 Permeability Barrier Evolution in the Ionian Lithosphere

Permeability barrier formation is modeled in the lithosphere of Io using a one-dimensional coupled petrological-geodynamical model. Due the cold thermal profile of the Ionian lithosphere, caused by the rapid volcanic resurfacing at the surface, the

permeability barrier is always produced at the base of the lithosphere. The permeability barrier can be elevated 100s of meters to several kilometers in areas of very high strain rate (10^{-9} s^{-1}) or low resurfacing rate (0.02 cm/yr).

As resurfacing controls the depth of the permeability barrier, the permeability barrier is expected to be deep near actively resurfacing areas and relatively shallow in inactive regions. The resultant regional slope of the permeability barrier likely concentrates melt to the inactive regions. Heat released from melt crystallization may increase the temperatures at depth of the permeability barrier, allowing further melt ascent, creating new heat pipes.

6.1.3 Convective Instabilities in Melt Horizons in the Martian Lithosphere

The formation of decompaction channels is modeled in two-dimensions in representations of various possible Martian lithospheres. The numerical models produce a convective process at depth in the lithosphere. This convective process focuses melt above upwellings and elevates melt upwards several kilometers relative to the nominal level of the permeability barrier. Melt is focused and elevated at the wavelength, or spacing, of the convective instability. This spacing is proposed to be linked to the spacing of volcanoes and volcanic vents at the Martian surface.

Initial conditions consisting of mantle temperatures ranging from 1450 K to 1900 K and lithosphere thicknesses from 50 km to 200 km are used to determine their relationship to the convective wavelength. Hotter mantles produce more melt, which create thicker decompaction channels and larger wavelength, therefore probably larger volcano spacing. Numerical modeling using expected Hesperian interior conditions of a mantle temperature of 1650 K and a lithospheric thickness of 150 km

yield a convective wavelength of 18.2 km, approximately matching the 16.5 km nearest neighbor spacing of the Hesperian aged Syria Planum region of Mars. Larger spacings such as those of the large Tharsis region shield volcanoes cannot be replicated in these models. Volcanism of younger than Hesperian age does not typically produce vent fields with regular spacing. It is possible that melt crystallizes completely inside the lithosphere and volcanism is restricted to locations where it is possible to reuse a preexisting volcanic conduit, for example at the previously formed Tharsis Montes.

6.1.3 Ionian Heat Pipe Processes

Numerical and analytical models of melt migration are used to determine the lifespan of Ionian heat-pipes and demonstrate the efficiency of convection as a melt focusing mechanism. Heat-pipe lifespans are found to be well predicted by the Stefan problem and are highly dependent on pipe radius. A 1 km pipe will fully close within ~10,000 years while a 25 km conduit of melt will close within 6-7 million years. Melt ascent velocities within the pipe are adequate for supplying hundreds to millions of years' worth of volcanism over the heat-pipe's lifespan. Smaller heat pipes (5-10 km) will close before the complete resurfacing of the lithosphere (~2 million years), but larger pipes will persist through several resurfacing events.

A solid convection pattern consisting of an upwelling positioned underneath a heat pipe is determined to be inefficient for melt extraction. In this set up melt will be focused to points away from heat pipes by lateral flow against the base of the lithosphere. Placing the upwelling away from the base of the heat pipe (with a downwelling beneath the heat pipe) causes lateral flow to push melt towards the heat

pipe. Melt preferentially travels up the heat pipe as the solid travels with the downwelling.

6.2 Future Directions

6.2.1 Potential Expansions to Mars and Io Projects

The big limitation of the numerical melt migration models presented is the lack of brittle or fracture physics. In the presented models, melt simply accumulates at impenetrable boundaries until it moves laterally or the model stops. In reality the overburden pressure of the above rock should eventually be surpassed by the pressure generated by the accumulating melt. This would initiate cracking and eventually create dike complexes which rapidly carry melt to the surface, or near surface magma chambers [*Cai and Bercovici,* 2016; *Havlin et al.,* 2013]. Further work is needed to implement brittle deformation physics into models with melt migration to capture this behavior.

One of the grand goals of geodynamical code development is the accurate integration of geochemistry and petrology into numerical models of solid and fluid flow. Essentially it would be ideal to create one code capable of the two- and three-dimensional finite element modeling of ASPECT, incorporating the petrology and thermodynamics of the MELTS software. Despite early efforts like GyPSM-S (Geodynamic and Petrological Synthesis Model for Subduction [*Hebert et al.,* 2009]), this code does not currently exist in a usable package due to the required complexity, and even an elegantly written code would require massive computing power to run even simple models. The continual development of large computer clusters will

eventually provide the computing power and groups like the ENKI project (ENabling Knowledge Integration) are working towards modeling coupled geochemical and geodynamical processes [*Ghiorso and Wolf,* 2019; *Wolf and Ghiorso,* 2019]. Eventually the models presented in this dissertation could be replicatedwithout petrological or geodynamical simplifications using this new architecture.

6.2.1 Prospective Planetary Bodies for Related Research

6.2.1.1 Earth

As discussed in the Chapter 4, the modern Earth likely does not have thick, convecting channels of melt at the base of the lithosphere. The Hadean or Archean Earth may have possessed internal temperatures high enough to create the necessary decompaction channels. The pre-plate tectonic Earth also likely released internal heat and melt in the form of heat pipes [*Moore and Webb*, 2013; *Kankanamge and Moore*, 2016]. It is possible that convection in the Hadean or Archean decompaction channel would have focused melt towards terrestrial heat pipes. Future work should model these decompaction channel and heat pipe processes for the ancient Earth, and investigate possible signals of wavelength volcanism in Archean terrains.

The modeling techniques used in this dissertation may apply to one type of location on the modern Earth, albeit at a shallower depth and smaller scale than modeled for Io and early Mars. Regional volcanic fields on the Earth, such as the Springer Volcanic Field in Arizona [*Connor et al.,* 1992] display a volcano spacing that is dependent on the regional geology. Melt migration models similar to those developed in this dissertation can created and expanded upon with knowledge of the regional structural geology and rock composition as model inputs to recreate the

volcanic history of the focus region. This can involve brittle deformation physics as described above, as the magma interacts with fault planes, and assimilation of the regional rock types. Models could be "ground-truthed" with geophysical measurements such as tomography from seismic lines. Model replication of extinct volcanic fields may lead to insights which can inform hazard assessment of volcanically active regions.

6.2.1.2 Venus

Understanding the interior conditions responsible for the atmospheric divergence of the Earth and Venus is critical to our understanding of the habitability of bodies in our solar system and exoplanets. The pressures and temperatures of the hellish Venusian surface make sustained geophysical probes of the planet's interior impossible with currently available technology. I propose to model the formation of plentiful, volcanic-tectonic surface features known as coronae (Figure 6.1), which appears to be unique to Venus [*Pronin and Stofan* 1990]. Coronae are likely the surficial expression of melt producing mantle processes such as plumes or delamination [*Smrekar and Stofan*, 1997]. Previous models of coronae formation do not include full two-phase flow melt migration. By integrating melt migration modeling at depth with melt extraction processes near the surface, such as dike generation, new, more accurate coronae topography and lava flow volume predictions can be generated. Matching of model output with actual radar imagery of corona topography, lava flow volume, and dike field orientation will constrain the mantle temperature, the thickness of the thermal and elastic lithospheres, and the stress state near the surface as determined by model initial conditions. By directly modeling melt flow, petrological constraints such as the

composition of the mantle and crust and volcanic outgassing can also be determined. Preliminary modeling also suggests that the complete resurfacing of Venus could be a related process to coronae formation. A full exploration of model parameters will help constrain the cooling history of the planet from complete resurfacing events to localized lave flows and corona formation.

Figure 6.1– Fotla Corona. The corona itself consists of the annulus of ridges and interior topography. The circular object to the north is a volcanic feature known as a pancake dome. Image is ~300 km across. [*NASA/JPL,* PhotoID: PIA00202]

6.2.1.3 Icy satellites

While this dissertation has focused on silicate melts, I am interested in applying this experience towards the icy moons of the outer solar system. Based on my experience with silicate melt modeling, I believe that it is possible to build a two-phase flow numerical model of water through the ice shell of Europa or other icy

satellites. This could either be implemented into the finite element code ASPECT, or built as a separate program for icy satellite modeling. The "petrology" is inherently simpler as it would involve modeling phase changes between solid and liquid H_2O (with possible complications of salts) as opposed to the litany of possible phases associated with silicate melts. I am interested in applying this model to investigate the formation of water or slush reservoirs for cryovolcanism or as intrusions, or melting events, resulting in chaos terrains.

One of the fundamental parameters in melt migration modeling is the density contrast between solid matrix and liquid melt. Since water ice is actually less dense than liquid water, I am very interested in the pressure differentials that must exist to force the denser water upwards. In particular, I am interested in applying brittle deformation and cracking, which must exist to accommodate some of the pressure, to models of water ascent in an icy shell. By including the effect of regional tectonic stresses, small and large scale brittle deformation would be included. Linking full two phase flow fluid migration with brittle failure would lead to new models of water/brine flow through icy shells, and lead to model input derived constraints on the structure of Europa's ice shell (which in turn could eventually be validated by the Europa Lander).

6.2.1.4 Exoplanets

The community is approaching one final frontier of planetary bodies. As telescopes become more and more powerful, details of exoplanetary orbits, atmospheres, and even surfaces will be revealed. Work has already been published on the interior conditions and structure of exoplanets [*Unterborn and Panero,* 2019], and

will continue to be refined with time. As melt carries both heat and volatiles from planetary interiors to the surface, evolutions of the models presented in this dissertation may be used to determine the habitability of known exoplanets.

Appendix A: Supporting Information for Chapter 2

This appendix has been published as the supplementary information for:

Schools, J. W., & Montési, L. G. (2018). The generation of barriers to melt ascent in the Martian lithosphere. *Journal of Geophysical Research: Planets*, *123*(1), 47-66. https://doi.org/10.1002/2017JE005396

A1 Introduction

The supporting figures presented here expand on the results of Figures 2.5, 2.6, and 2.7 of the main text to different oxygen fugacities (Figure A1), mantle water content (Figures A2 and A3), and rheological parameters (Figures A4 and A5). Figures A6 and A7 display the same information as FiguresA4 and A5 by showing the elevation, or distance, of the permeability barrier above the base of the lithosphere ($E = D_{base\ of\ lithosphere} - D_{permeabiity\ barrier}$). Additionally the SiO_2 content of melt generated from decompression and melt at the depth of the modeled permeability barrier is shown in Figures A3, A8, and A9. These results were all generated using the methods described in the main text.

Table A1 reports the mantle potential temperature and lithospheric thickness from the thermal evolution model of *Hauck and Phillips* [2002] used to link the calculations presented in the paper with the geological history of Mars.

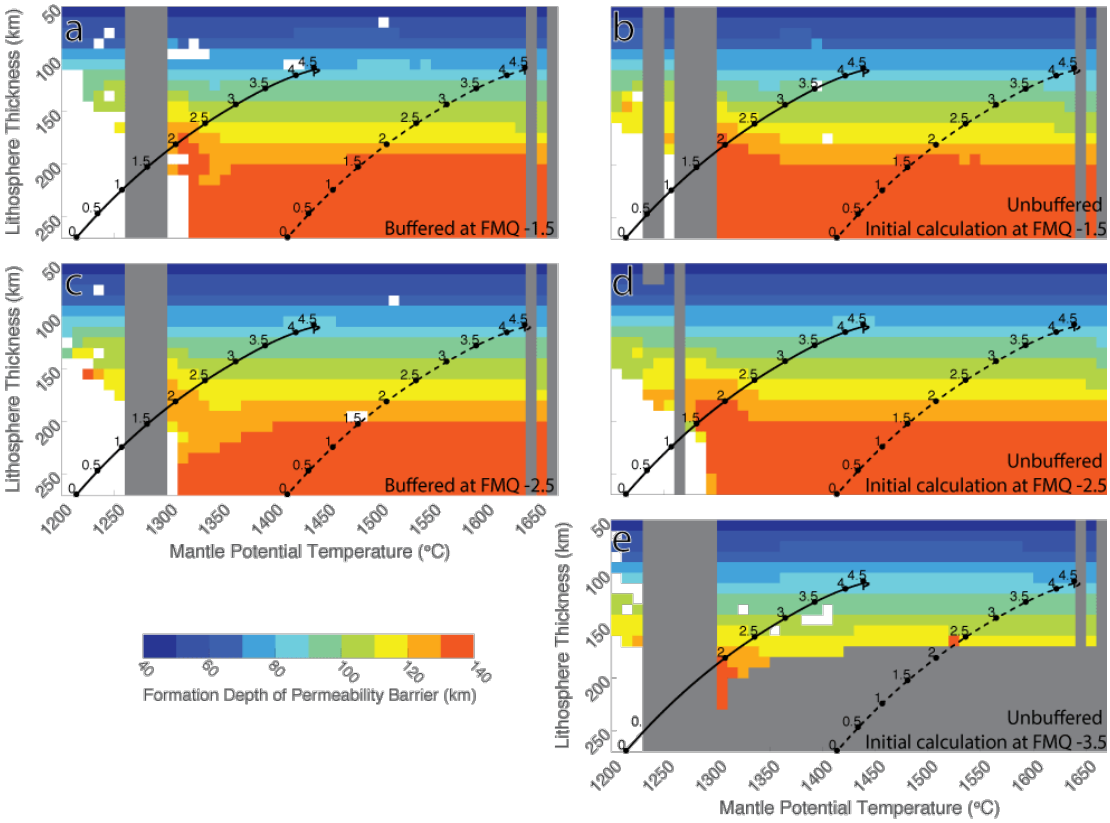

Figure A1. Depth of the permeability barrier predicted with an anhydrous mantle and a dry lithosphere deforming at a background strain rate of 10^{-15} s^{-1}, the same conditions as Figure 2.5a, but with varying oxygen fugacity conditions: (a) fully buffered in both the melting and crystallizing calculation at FMQ -1.5, (b) unbuffered but with an initial calculation at 4 GPa set to FMQ -1.5 to establish composition, (c) fully buffered at FMQ -2.5, (d) unbuffered with an initial calculation at FMQ -2.5, and (e) unbuffered with an initial calculation at FMQ -3.5. Colors and lines as in Figure 2.5.

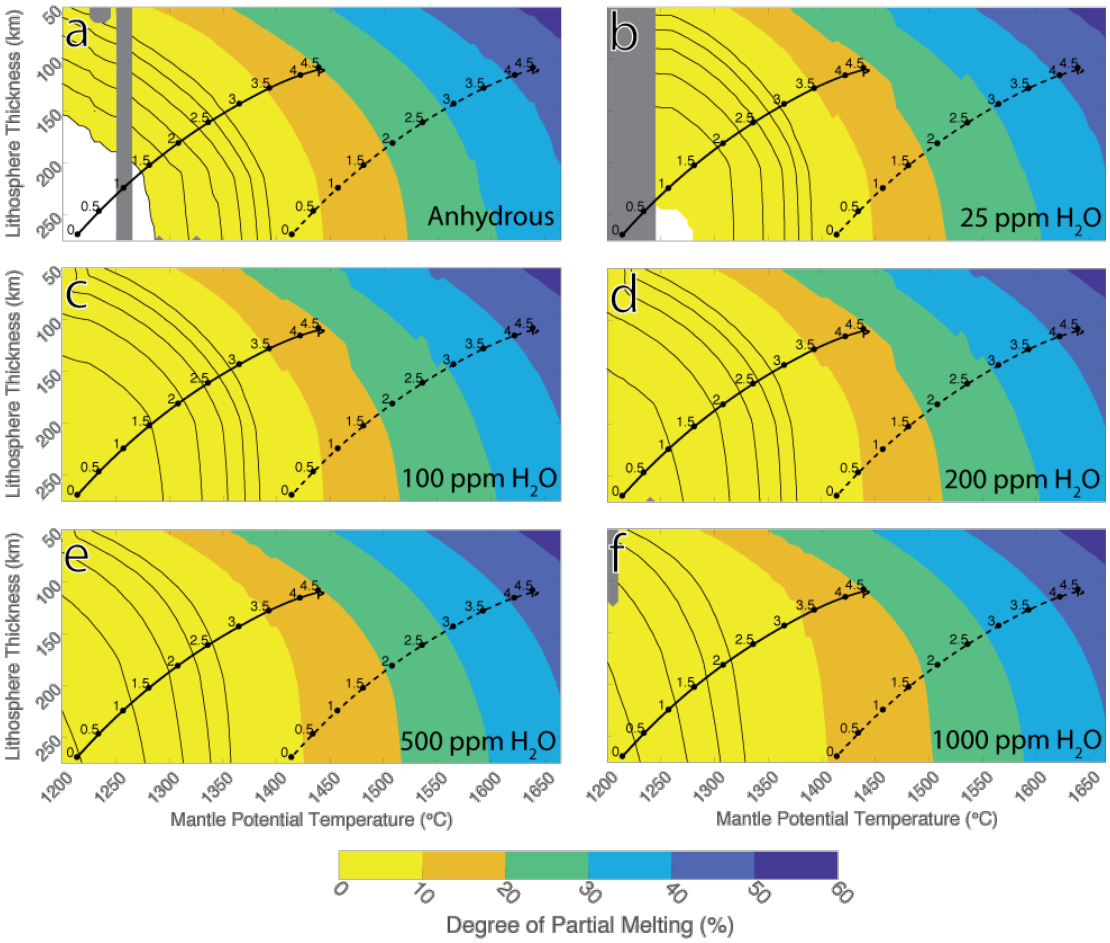

Figure A2. Degree of melting produced by decompression melting of (a) anhydrous Martian mantle and Martian mantle containing (b) 25 ppm H_2O, (c) 100 ppm H_2O, (d) 200 ppm H_2O, (e) 500 ppm H_2O, and (f) 1000 ppm H_2O, as a function of mantle potential temperature and lithospheric thickness. Colors and lines similar to Figure 2.4.

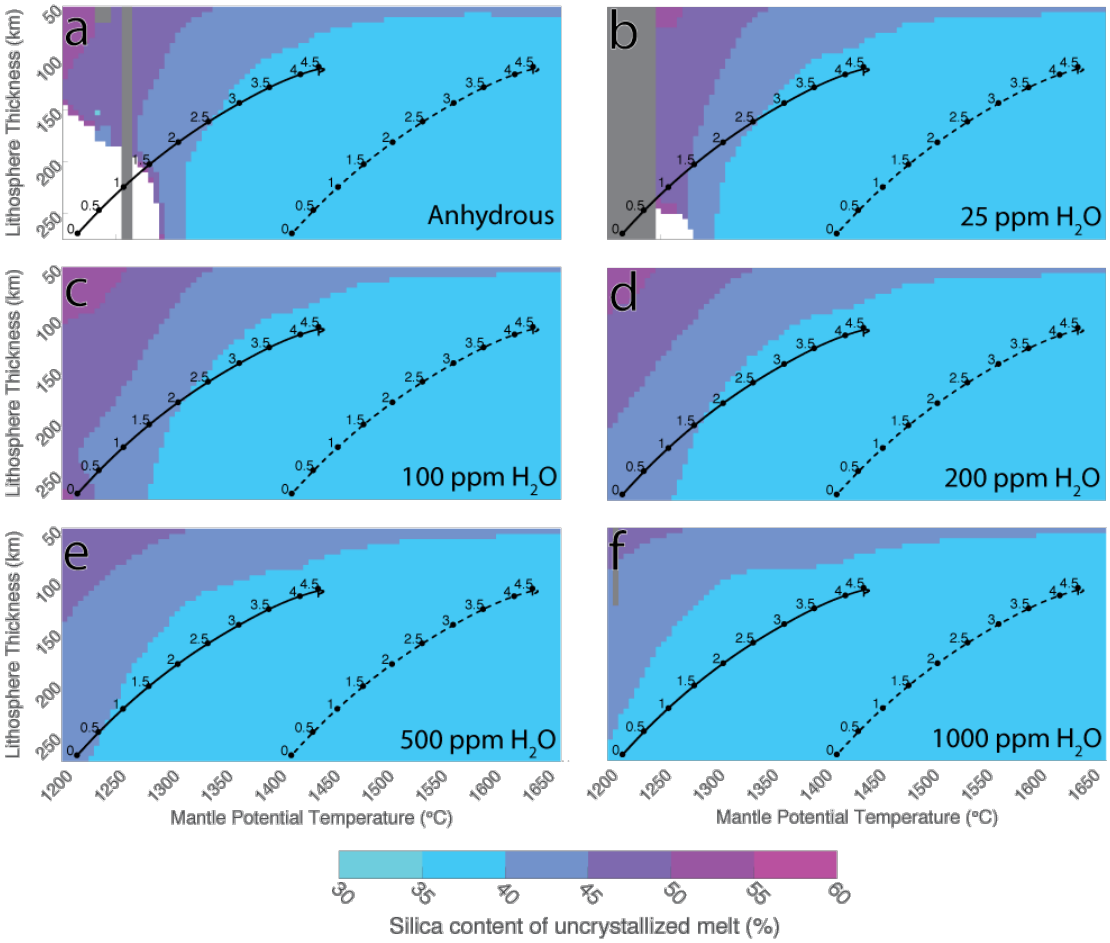

Figure A3. The silica content of melt generated by decompression melting of (a) anhydrous Martian mantle and Martian mantle containing (b) 25 ppm H_2O, (c) 100 ppm H_2O, (d) 200 ppm H_2O, (e) 500 ppm H_2O, and (f) 1000 ppm H_2O, as a function of mantle potential temperature and lithospheric thickness. Colors and lines similar to Figure 2.6.

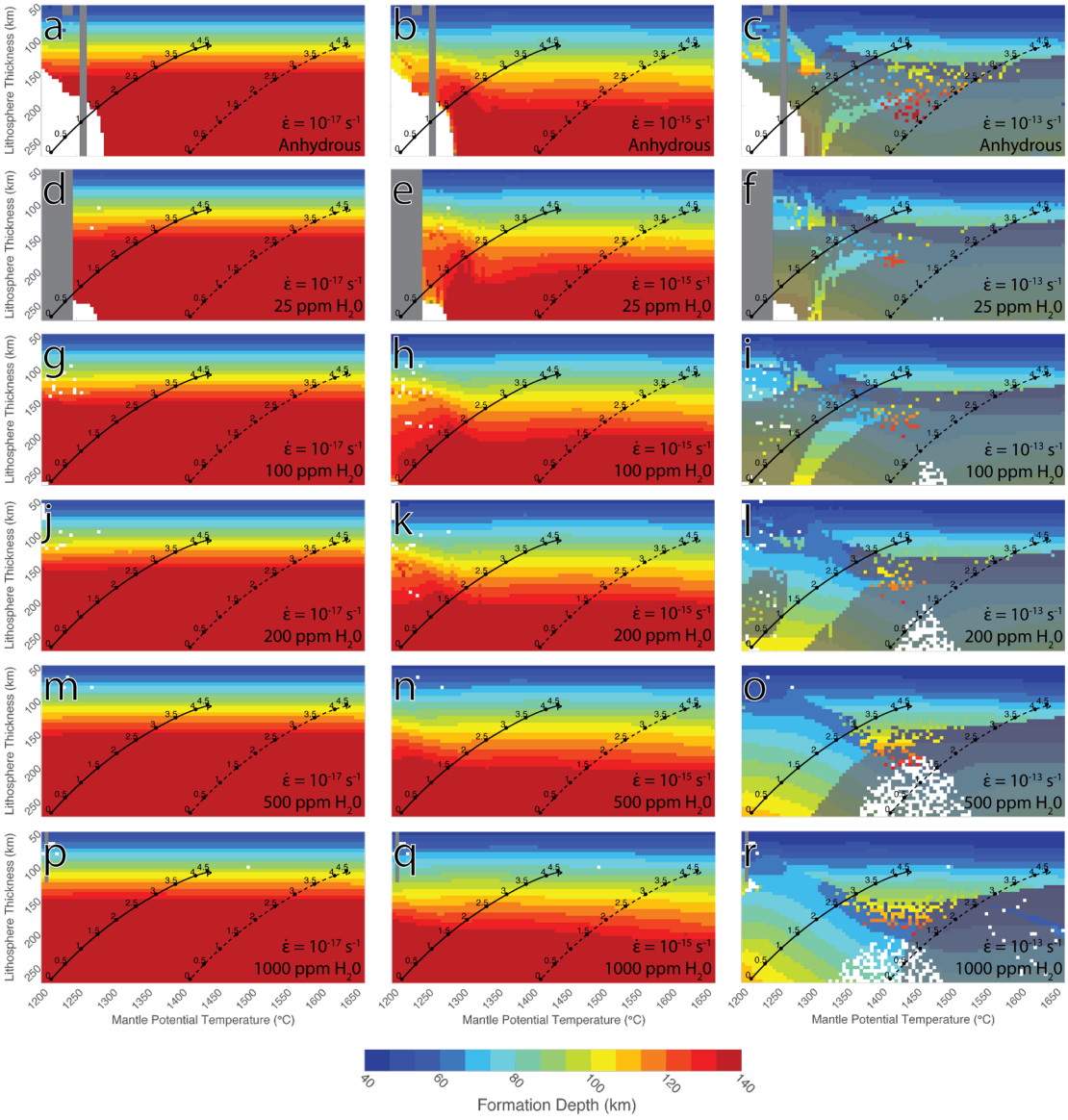

Figure A4. Depth of the permeability barrier as a function of mantle potential temperature and lithospheric thickness assuming a dry rheology, a background strain rate of $\dot{\varepsilon} = \mathbf{10^{-17}\ s^{-1}}$ (left column), $\dot{\varepsilon} = \mathbf{10^{-15}\ s^{-1}}$ (middle column), or $\dot{\varepsilon} = \mathbf{10^{-13}\ s^{-1}}$ (right column) and various water contents in the initial composition: a), b), and c): anhydrous mantle; d), e), and f): 25 ppm H_2O; g), h), and i): 100 ppm H_2O; j), k), and l): 200 ppm H_2O; m), n), and o): 500 ppm H_2O; p), q), and r): 1000 ppm H_2O. Colors and lines as in Figure 2.5.

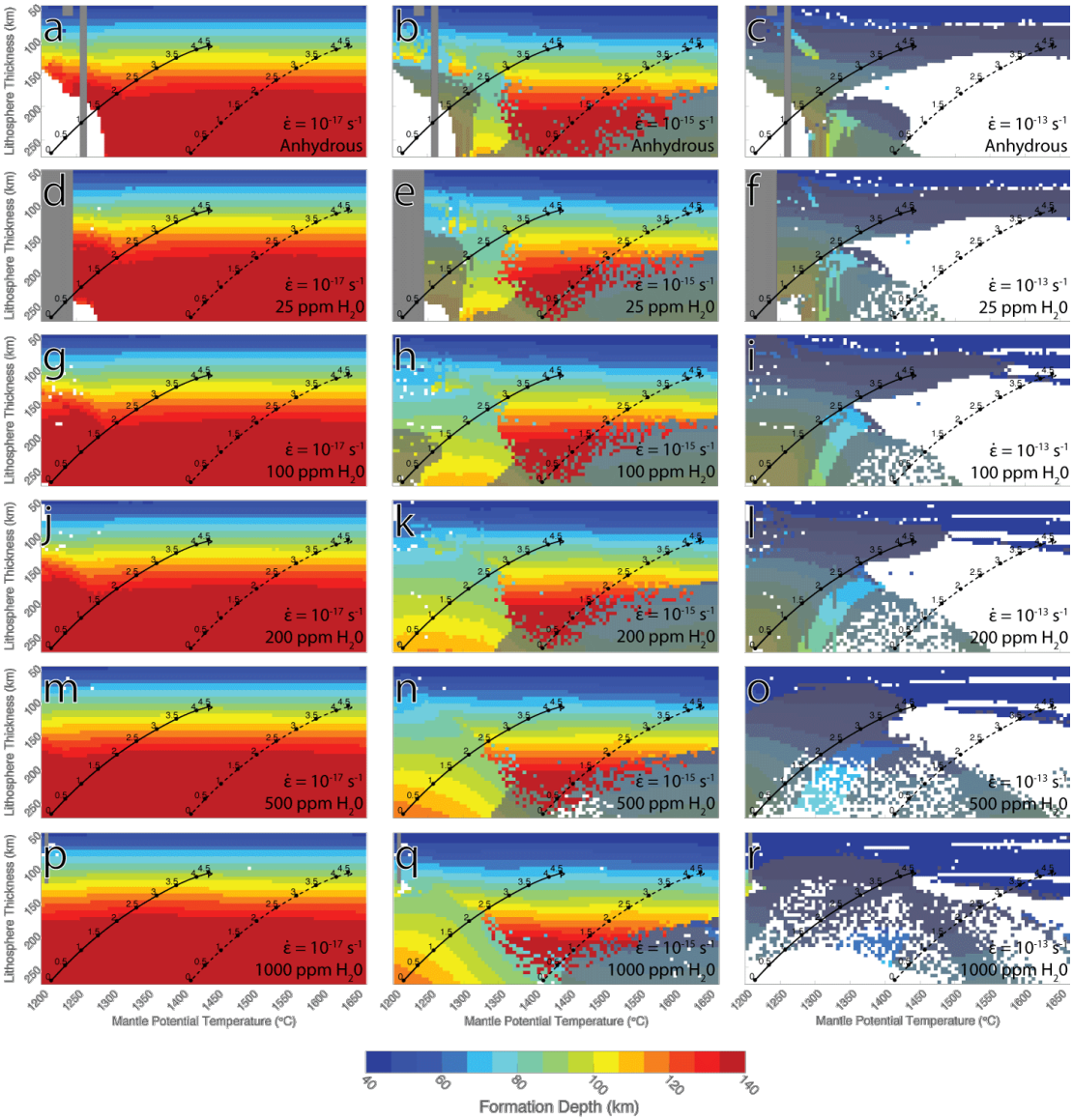

Figure A5. Same as Figure A4, but assuming a fully wet rheology.

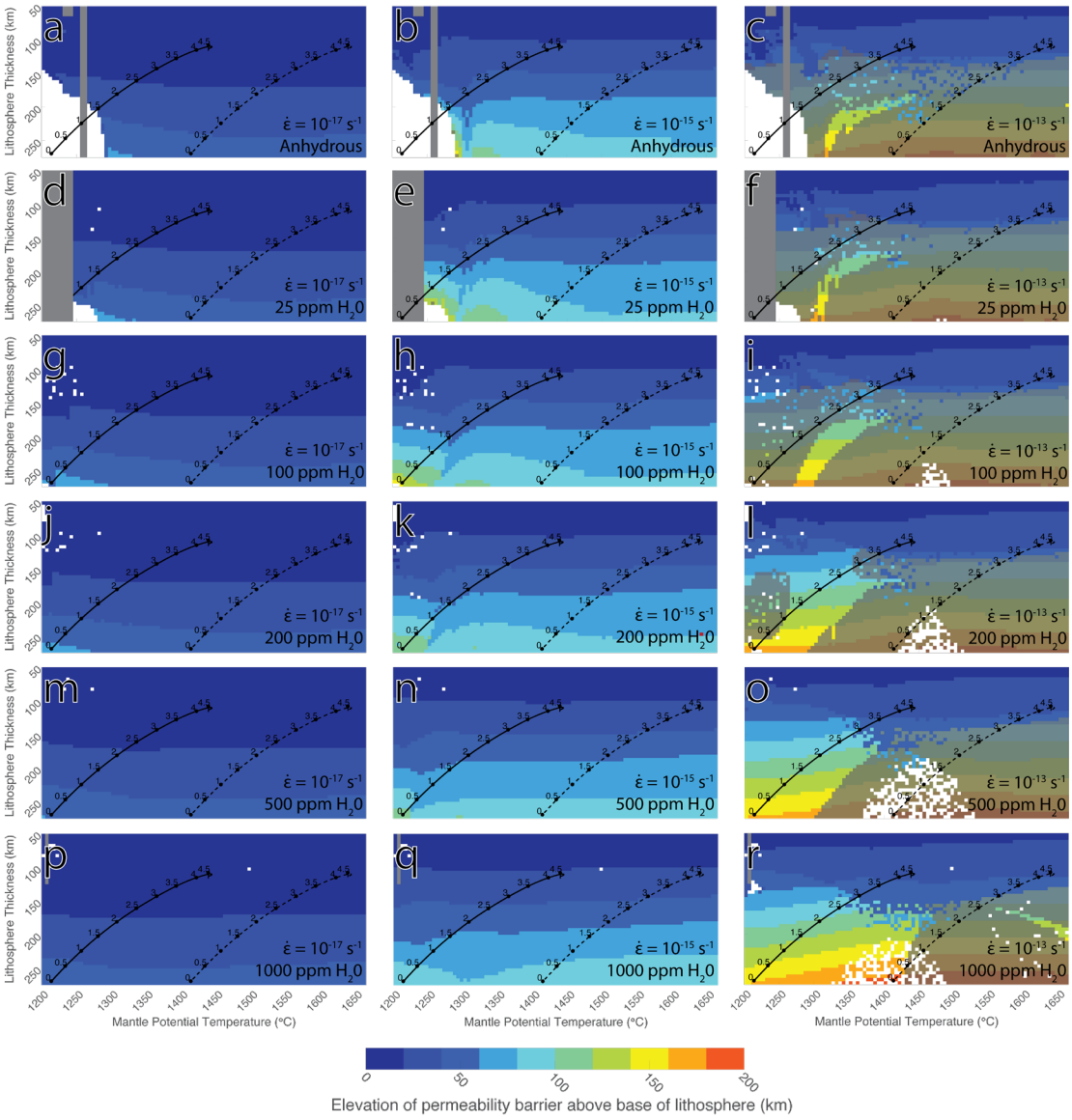

Figure A6. Elevation of formation of the permeability barrier above the base of the lithosphere calculated using dry rheological parameters. Panels corresponding to the calculations shown in Figure A4.

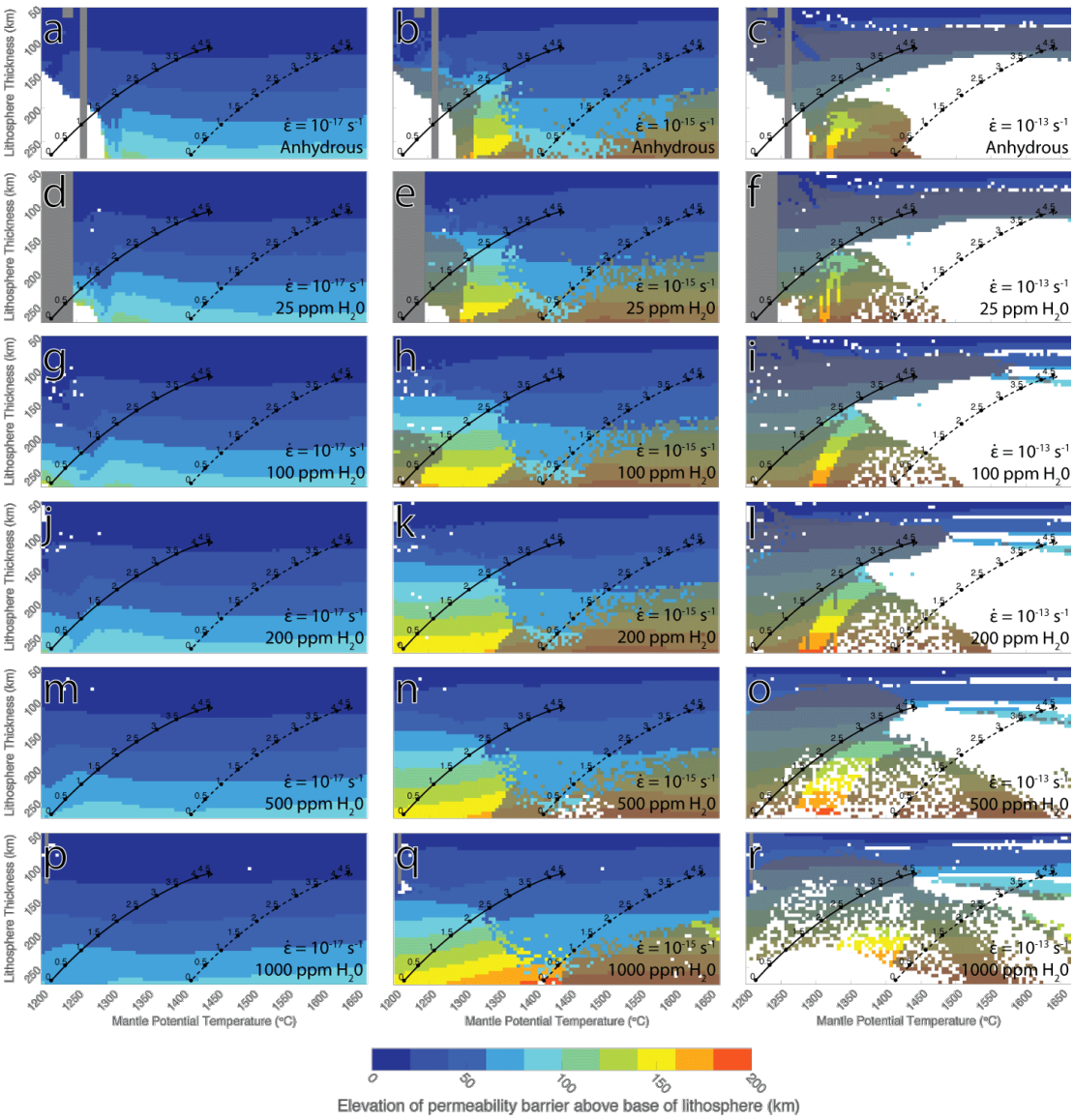

Figure A7. Same as Figure A6 but assuming a fully wet rheology. Panels corresponding to the calculations shown in Figure S5.

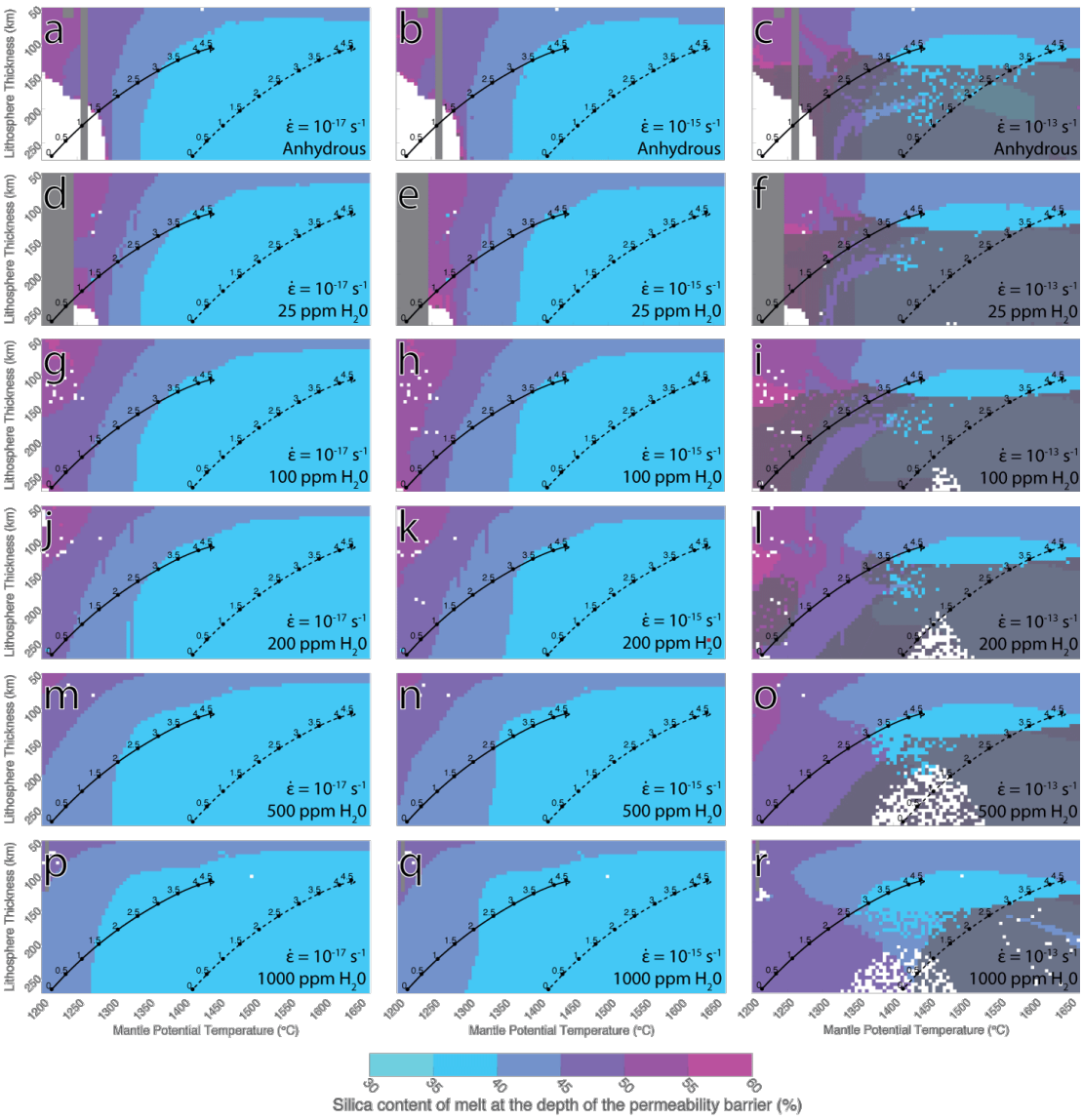

Figure A8. The silica content of melt at the depth of the permeability barrier as a function of mantle potential temperature calculated with a dry rheology. Panels corresponding to the calculations shown in Figure A4.

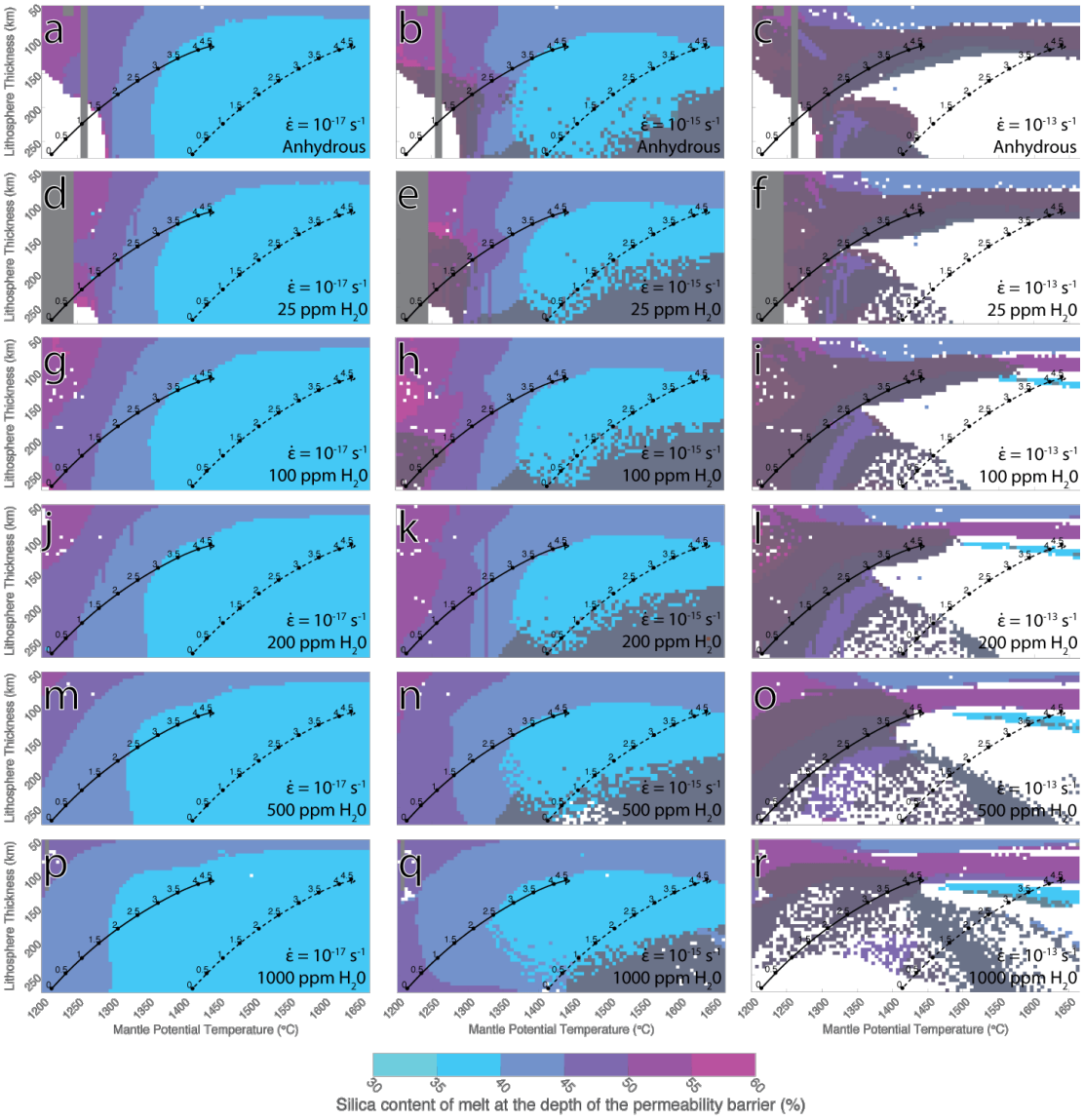

Figure A9. Same as Figure A8 but assuming a fully wet rheology. Panels corresponding to the calculations shown in Figure A5.

Age (Ga)	Lithospheric thickness (km)	Mantle Potential Temperature (°C)	MPT+200(°C)
4.5	108.0	1439	1639
4.0	115.3	1422	1622
3.5	127.8	1393	1593
3.0	143.0	1365	1565
2.5	161.0	1336	1536
2.0	181.0	1308	1508
1.5	202.4	1281	1481
1.0	24.4	1257	1457
0.5	246.8	1234	1434
0.0	269.3	1214	1414

Table A1. Lithospheric thickness and mantle potential temperature (MPT) at 0.5 billion year intervals from the models of *Hauck and Phillips* [2002]. The fourth column is the MPT calculated by *Hauck and Phillips* [2002] with an added 200°C to represent an anomalously hot mantle, as may be present in mantle plumes.

Appendix B: Supporting Information for Chapter 3

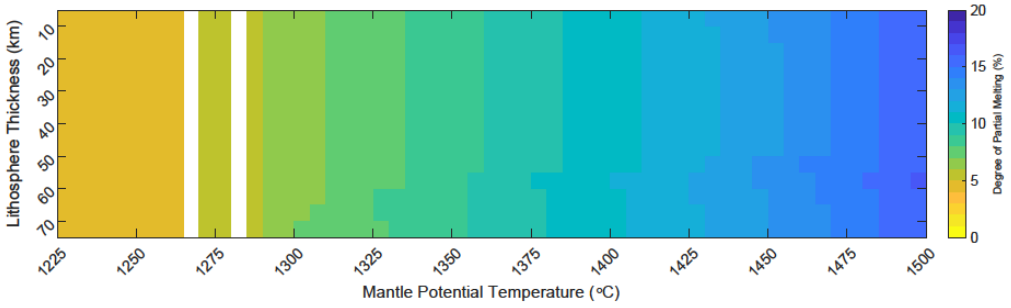

Figure B1 - Collected results of adiabatic melting calculations. These represent the composition of the melt produced in the mantle, before ascending through the lithosphere, as a function of the partial melt of the Ionian mantle. The partial melt produced largely depends on Mantle potential temperature, rather than lithospheric thickness.

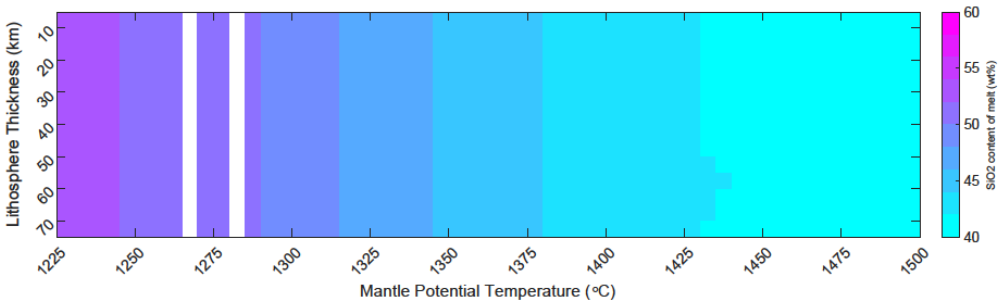

Figure B2 – SiO_2 content of the results of the adiabatic melting calculations. This is the SiO_2 content of the melt prior to ascent through the lithosphere.

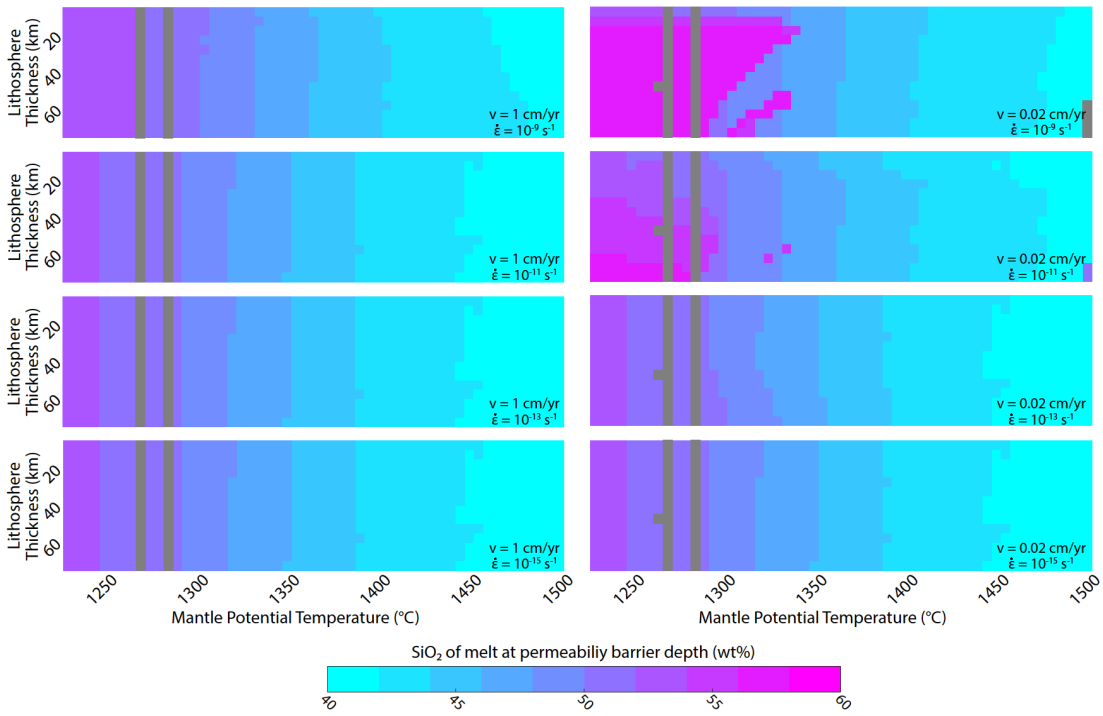

Figure B3 – SiO_2 content of the melt at the level of the permeability barrier. This is the SiO2 concentration of the melt that collects underneath the permeability barrier in the decompaction channel. This figure follows the format of Figure 3.3 in the main text.

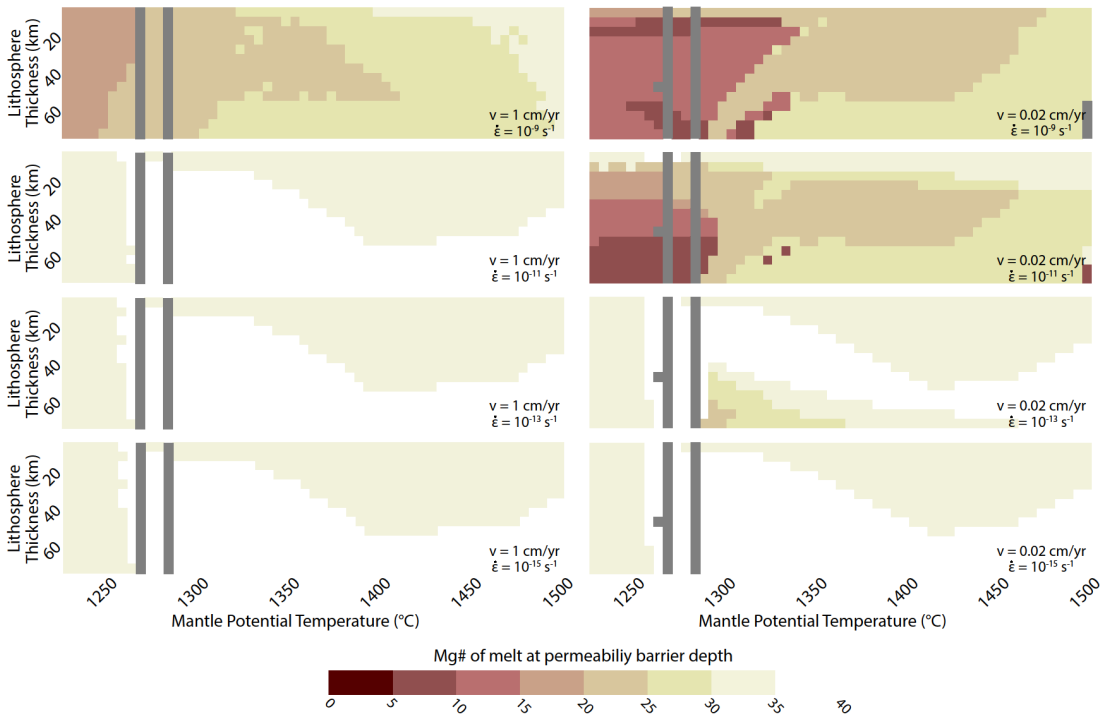

Figure B4 – Mg# of the melt at the level of the permeability barrier. This is the composition of the melt that collects underneath the permeability barrier in the decompaction channel. This figure follows the format of Figure 3.3 in the main text and Figure B3.

Appendix C: Equations Solved in the ASPECT Numerical Models

Here I present the calculations solved by the finite element modeling software ASPECT for the numerical models of Chapters 3 and 4. For derivations of these equations please refer to the citations within this text, particularly *Dannberg and Heister* [2016] and *Dannberg et al.* [2019].

For incompressible models, ASPECT 2.0.1 [*Kronbichler et al.,* 2012; *Heister et al.,* 2017; *Bangerth et al., 2018*; *Bangerth et al*., 2019] with melt migration [*Dannberg and Heister*, 2016; *Dannberg et al.,* 2019] operates by solving the following equations for conservation of mass and momentum (variables and parameters are defined in Table C1):

$$-\boldsymbol{\nabla}\cdot(2\boldsymbol{\eta}\dot{\boldsymbol{\varepsilon}}) + \boldsymbol{\nabla}\boldsymbol{p_f} + \boldsymbol{\nabla}\left(\sqrt{\boldsymbol{K'_D}}\overline{\boldsymbol{p}}_{\boldsymbol{c}}\right) = \overline{\boldsymbol{\rho}}\mathrm{g} \tag{1}$$

$$\begin{aligned}\boldsymbol{\nabla}\cdot \mathrm{u}_{\boldsymbol{s}} - \boldsymbol{\nabla}\cdot \boldsymbol{K_D}\boldsymbol{\nabla}\boldsymbol{p_f} - \boldsymbol{K_D}\boldsymbol{\nabla}\boldsymbol{p_f}\cdot\frac{\boldsymbol{\nabla}\boldsymbol{\rho_f}}{\boldsymbol{\rho_f}} \\ = -\boldsymbol{\nabla}\cdot\left(\boldsymbol{K_D}\boldsymbol{\rho_f}\mathrm{g}\right) + \boldsymbol{\Gamma}\left(\frac{\mathbf{1}}{\boldsymbol{\rho_f}} - \frac{\mathbf{1}}{\boldsymbol{\rho_s}}\right) - \frac{\boldsymbol{\phi}}{\boldsymbol{\rho_f}}\mathrm{u}_{\boldsymbol{s}}\cdot\boldsymbol{\nabla}\boldsymbol{\rho_f} \\ -\boldsymbol{K_D}\mathrm{g}\cdot\boldsymbol{\nabla}\boldsymbol{\rho_f}\end{aligned} \tag{2}$$

$$\sqrt{\boldsymbol{K'_D}}\boldsymbol{\nabla}\cdot\mathrm{u}_{\boldsymbol{s}} + \frac{\boldsymbol{K'_D}\overline{\boldsymbol{p}}_{\boldsymbol{c}}}{\boldsymbol{\xi}} = \mathbf{0} \tag{3}$$

advection in the porosity field is solved as:

$$\frac{\partial \boldsymbol{\phi}}{\partial \boldsymbol{t}} + \mathrm{u}_{\boldsymbol{s}} \cdot \boldsymbol{\nabla \phi} = \frac{\boldsymbol{\Gamma}}{\boldsymbol{\rho_s}} + (\mathbf{1} - \boldsymbol{\phi})(\boldsymbol{\nabla} \cdot \mathrm{u}_{\boldsymbol{s}}) \tag{4}$$

and melt velocity is computed as:

$$\mathrm{u}_{\boldsymbol{f}} = \mathrm{u}_{\boldsymbol{s}} - \frac{\boldsymbol{K_D}}{\boldsymbol{\phi}}\left(\boldsymbol{\nabla p_f} - \boldsymbol{\rho_f} \mathrm{g}\right) \tag{5}$$

The solution for temperature and heating is also solved. Heating terms vary between models and the relevant equations are located in the chapter text (Equation 4.2, 5.3, and 5.8).

K_D is the Darcy coefficient, where:

$$\boldsymbol{K_D} = \frac{\boldsymbol{k}}{\boldsymbol{\eta_f}} \tag{6}$$

K'_D is function used to scale the above formulations and address degeneracy in the system:

$$\boldsymbol{K'_D} = \sqrt{\frac{\boldsymbol{K_D}}{\boldsymbol{K_{D_0}}}} \tag{7}$$

The permeability, k, is dependent on the porosity as follows:

$$\boldsymbol{k = k_0\, \phi^3 (1 - \phi)^2} \tag{8}$$

Individual material properties vary with temperature and porosity and their relations follow for density of the solid and liquid phases:

$$\boldsymbol{\rho_{s,f} = \rho_{s_0,f_0}\left(1 - \alpha(T - T_{adi})\right)} \tag{9}$$

Compaction viscosity:

$$\xi(\phi, T) = \xi_0 \frac{\phi_0}{\phi} e^{(T-T_0)/T_0} \tag{10}$$

and shear viscosity of the solid matrix:

$$\eta(\phi) = \eta_0 e^{a(\phi-\phi_0)} \tag{11}$$

The melting/crystallization model follows the parameterization of *Katz et al.* [2003] for dry peridotite. The solidus at surface pressure is ~1360 K or ~1087˚C and increases with increasing pressure following a quadratic relationship. See *Katz et al.* [2003] for details and experimental constraints.

Symbol	Variables and Parameters
T_{adi}	Adiabatic temperature
ξ	Compaction viscosity
p_c	Compaction pressure
K_D	Darcy coefficient
$\dot{\varepsilon}$	Deviatoric strain rate
p_f	Fluid pressure
g	Gravity
ρ_f	Melt density
u_f	Melt velocity
η_f	Melt viscosity
a	Melt weakening parameter
Γ	Melting/freezing rate
k	Permeability
$\bar{\rho}$	Phase weighted average density
ϕ	Porosity
ξ_0	Reference bulk viscosity
ρ_{f_0}	Reference melt density
k_0	Reference permeability
ϕ_0	Reference porosity
η_0	Reference shear viscosity
ρ_{s_0}	Reference solid density

$\boldsymbol{T_0}$	Reference Temperature
$\boldsymbol{K'_D}$	Scaling factor for compaction pressure
$\boldsymbol{\eta}$	Shear viscosity
$\boldsymbol{\rho_s}$	Solid density
u_s	Solid velocity
$\boldsymbol{T}$	Temperature
$\boldsymbol{\alpha}$	Thermal expansivity
$\boldsymbol{t}$	Time

Table C1 - Variables and Parameters used in ASPECT numerical models. Relevant values are located in the chapter texts, Tables 4.1 and 5.1

Bibliography

Anderson, D. L. (1989). *Theory of the Earth*. Blackwell scientific publications.

Anderson, J. D., Sjogren, W. L., & Schubert, G. (1996). Galileo Gravity Results and the Internal Structure of Io. *Science*, *272*(5262), 709–712. https://doi.org/10.1126/science.272.5262.709

Anderson, J. D., Jacobson, R. A., Lau, E. L., Moore, W. B., & Schubert, G. (2001). Io's gravity field and interior structure. *Journal of Geophysical Research: Planets*, *106*(E12), 32963–32969. https://doi.org/10.1029/2000JE001367

Antoshechkina, P. M., & Asimow, P. D. (2010). Adiabat_1ph 3.0 and the MAGMA website: educational and research tools for studying the petrology and geochemistry of plate margins. *American Geophysical Union Fall Meeting, 2010*, ED41B-0644. https://ui.adsabs.harvard.edu/#abs/2010AGUFMED41B0644A/abstract

Antoshechkina, P. M., Asimow, P. D., Hauri, E. H., & Luffi, P. I. (2010). Effect of water on mantle melting and magma differentiation, as modeled using Adiabat_1ph 3.0. *American Geophysical Union Fall Meeting, 2010*, V53C-2264. https://ui.adsabs.harvard.edu/#abs/2010AGUFM.V53C2264A/abstract

Armann, M., & Tackley, P. J. (2012). Simulating the thermochemical magmatic and tectonic evolution of Venus's mantle and lithosphere: Two-dimensional models. *Journal of Geophysical Research: Planets*, *117*(E12), n/a-n/a. https://doi.org/10.1029/2012JE004231

Asimow, P. D., Dixon, J. E., & Langmuir, C. H. (2004). A hydrous melting and fractionation model for mid-ocean ridge basalts: Application to the Mid-Atlantic Ridge near the Azores. *Geochemistry, Geophysics, Geosystems*, *5*(1), n/a-n/a. https://doi.org/10.1029/2003GC000568

Asimow, P. D., & Ghiorso, M. S. (1998). Algorithmic modifications extending MELTS to calculate subsolidus phase relations. *American Mineralogist*, *83*(9–10), 1127–1132. https://doi.org/10.2138/am-1998-9-1022

Ave Lallemant, H. G., Mercier, J.-C. C., Carter, N. L., & Ross, J. V. (1980). Rheology of the upper mantle: Inferences from peridotite xenoliths. *Tectonophysics*, *70*(1–2), 85–113. https://doi.org/10.1016/0040-1951(80)90022-0

Bai, H., & Montési, L. G. J. (2015). Slip-rate-dependent melt extraction at oceanic transform faults. *Geochemistry, Geophysics, Geosystems*, *16*(2), 401–419. https://doi.org/10.1002/2014GC005579

Bai, H., Montési, L. G. J., & Behn, M. D. (2017). MeltMigrator: A MATLAB-based software for modeling three-dimensional melt migration and crustal thickness variations at mid-ocean ridges following a rules-based approach. *Geochemistry, Geophysics, Geosystems*, *18*(1), 445–456. https://doi.org/10.1002/2016GC006686

Baloga, S. M. (2003). Rheology of a long lava flow at Pavonis Mons, Mars. *Journal of Geophysical Research*, *108*(E7), 5066. https://doi.org/10.1029/2002JE001981

Balta, J. B., & McSween, H. Y. (2013). Application of the MELTS algorithm to Martian compositions and implications for magma crystallization. *Journal of Geophysical Research: Planets*, *118*(12), 2502–2519. https://doi.org/10.1002/2013JE004461

Bandfield, J. L. (2000). A Global View of Martian Surface Compositions from MGS-TES. *Science*, *287*(5458), 1626–1630. https://doi.org/10.1126/science.287.5458.1626

Banerdt, W. B., Smrekar, S. E., Banfield, D., Giardini, D., Golombek, M., Johnson, C. L., Lognonné, P., Spiga, A., Spohn, T., Perrin, C., Stähler, S. C., Antonangeli, D., Asmar, S., Beghein, C., Bowles, N., Bozdag, E., Chi, P., Christensen, U., Clinton, J., … Wieczorek, M. (2020). Initial results from the InSight mission on Mars. *Nature Geoscience*, *13*(3), 183–189. https://doi.org/10.1038/s41561-020-0544-y

Bangerth, W., Dannberg, J., Gassmoeller, R., & Heister, T. (2018). *Aspect V2.0.1*. Zenodo. https://doi.org/10.5281/ZENODO.1297145

Bangerth, W., Dannberg, J., Gassmoeller, R., Heister, T., & Others. (2020). *ASPECT: Advanced Solver for Problems in Earth's ConvecTion, User Manual*. 38178920 Bytes. https://doi.org/10.6084/M9.FIGSHARE.4865333

Baptista, A. R., Mangold, N., Ansan, V., Baratoux, D., Lognonné, P., Alves, E. I., Williams, D. A., Bleacher, J. E., Masson, P., & Neukum, G. (2008). A swarm of small shield volcanoes on Syria Planum, Mars. *Journal of Geophysical Research*, *113*(E9), E09010. https://doi.org/10.1029/2007JE002945

Baratoux, D., Pinet, P., Toplis, M. J., Mangold, N., Greeley, R., & Baptista, A. R. (2009). Shape, rheology and emplacement times of small martian shield volcanoes. *Journal of Volcanology and Geothermal Research*, *185*(1–2), 47–68. https://doi.org/10.1016/j.jvolgeores.2009.05.003

Baratoux, D., Toplis, M. J., Monnereau, M., & Sautter, V. (2013). The petrological expression of early Mars volcanism. *Journal of Geophysical Research: Planets*, *118*(1), 59–64. https://doi.org/10.1029/2012JE004234

Baratoux, D., Toplis, M. J., Monnereau, M., & Gasnault, O. (2011). Thermal history of Mars inferred from orbital geochemistry of volcanic provinces. *Nature*, *472*(7343), 338–341. https://doi.org/10.1038/nature09903

Bercovici, D., Ricard, Y., & Schubert, G. (2001). A two-phase model for compaction and damage: 1. General Theory. *Journal of Geophysical Research: Solid Earth*, *106*(B5), 8887–8906. https://doi.org/10.1029/2000JB900430

Barrell, J. (1914). The strength of the Earth's crust. *The Journal of Geology, 22*(7), 655-683. https://doi.org/10.1086/622181

Bertka, C. M., & Holloway, J. R. (1994). Anhydrous partial melting of an iron-rich mantle II: Primary melt compositions at 15 kbar. *Contributions to Mineralogy and Petrology*, *115*(3), 323–338. https://doi.org/10.1007/BF00310771

Bland, M. T., & McKinnon, W. B. (2016). Mountain building on Io driven by deep faulting. *Nature Geoscience*, *9*(6), 429–432. https://doi.org/10.1038/ngeo2711

Blaney, D. (1995). Volcanic Eruptions on Io: Heat Flow, Resurfacing, and Lava Composition. *Icarus*, *113*(1), 220–225. https://doi.org/10.1006/icar.1995.1020

Bouvier, A., Blichert-Toft, J., & Albarède, F. (2009). Martian meteorite chronology and the evolution of the interior of Mars. *Earth and Planetary Science Letters*, *280*(1–4), 285–295. https://doi.org/10.1016/j.epsl.2009.01.042

Boynton, W., Taylor, G. J., Karunatillake, S., Reedy, R. C., & Keller, J. M. (2008). Elemental abundances determined via the Mars Odyssey GRS. In J.

F. Bell (Ed.), *The Martian Surface: Composition, Mineralogy, and Physical Properties*, Cambridge Planetary Science Series (pp. 105– 124). New York: Cambridge University Press.

Brown, M., & Solar, G. S. (1998). Shear-zone systems and melts: Feedback relations and self-organization in orogenic belts. *Journal of Structural Geology*, *20*(2–3), 211–227. https://doi.org/10.1016/S0191-8141(97)00068-0

Bryan, S. E., Peate, I. U., Peate, D. W., Self, S., Jerram, D. A., Mawby, M. R., Marsh, J. S. (Goonie), & Miller, J. A. (2010). The largest volcanic eruptions on Earth. *Earth-Science Reviews*, *102*(3–4), 207–229. https://doi.org/10.1016/j.earscirev.2010.07.001

Buck, W. R. (1991). Modes of continental lithospheric extension. *Journal of Geophysical Research: Solid Earth*, *96*(B12), 20161–20178. https://doi.org/10.1029/91JB01485

Bunte, M. K., Williams, D. A., Greeley, R., & Jaeger, W. L. (2010). Geologic mapping of the Hi'iaka and Shamshu regions of Io. *Icarus*, *207*(2), 868–886. https://doi.org/10.1016/j.icarus.2009.12.006

Cai, Z., & Bercovici, D. (2013). Two-phase damage models of magma-fracturing. *Earth and Planetary Science Letters*, *368*, 1–8. https://doi.org/10.1016/j.epsl.2013.02.023

Cai, Z., & Bercovici, D. (2016). Two-dimensional magmons with damage and the transition to magma-fracturing. *Physics of the Earth and Planetary Interiors*, *256*, 13–25. https://doi.org/10.1016/j.pepi.2016.03.002

Cao, W., Kaus, B. J. P., & Paterson, S. (2016). Intrusion of granitic magma into the continental crust facilitated by magma pulsing and dike-diapir interactions: Numerical simulations. *Tectonics*, *35*(6), 1575–1594. https://doi.org/10.1002/2015TC004076

Carr, M. H., Greeley, R., Blasius, K. R., Guest, J. E., & Murray, J. B. (1977). Some Martian volcanic features as viewed from the Viking orbiters. *Journal of Geophysical Research*, *82*(28), 3985–4015. https://doi.org/10.1029/JS082i028p03985

Carr, M. H., Masursky, H., Strom, R. G., & Terrile, R. J. (1979). Volcanic features of Io. *Nature*, *280*(5725), 729–733. https://doi.org/10.1038/280729a0

Carr, M. H. (1973). Volcanism on Mars. *Journal of Geophysical Research*, *78*(20), 4049–4062. https://doi.org/10.1029/JB078i020p04049

Carr, M. H. (1974). Tectonism and volcanism of the Tharsis Region of Mars. *Journal of Geophysical Research*, *79*(26), 3943–3949. https://doi.org/10.1029/JB079i026p03943

Carr, M. H., & Head, J. W. (2010). Geologic history of Mars. *Earth and Planetary Science Letters*, *294*(3–4), 185–203. https://doi.org/10.1016/j.epsl.2009.06.042

Carr, M. H., McEwen, A. S., Howard, K. A., Chuang, F. C., Thomas, P., Schuster, P., Oberst, J., Neukum, G., & Schubert, G. (1998). Mountains and Calderas on Io: Possible Implications for Lithosphere Structure and Magma Generation. *Icarus*, *135*(1), 146–165. https://doi.org/10.1006/icar.1998.5979

Cashman, K. V., Sparks, R. S. J., & Blundy, J. D. (2017). Vertically extensive and unstable magmatic systems: A unified view of igneous processes. *Science*, *355*(6331), eaag3055. https://doi.org/10.1126/science.aag3055

Cattermole, P. (1987). Sequence, rheological properties, and effusion rates of volcanic flows at Alba Patera, Mars. *Journal of Geophysical Research: Solid Earth*, *92*(B4), E553–E560. https://doi.org/10.1029/JB092iB04p0E553

Ceuleneer, G., & Rabinowicz, M. (2013). Mantle Flow and Melt Migration Beneath Oceanic Ridges: Models Derived from Observations in Ophiolites. In J. P. Morgan, D. K. Blackman, & J. M. Sinton (Eds.), *Geophysical Monograph Series* (pp. 123–154). American Geophysical Union. https://doi.org/10.1029/GM071p0123

Cheadle, M. J. (1989). Properties of texturally equilibrated two-phase aggregates (Doctoral dissertation, University of Cambridge). https://ethos.bl.uk/OrderDetails.do?uin=uk.bl.ethos.253845

Clow, G. D., & Carr, M. H. (1980). Stability of sulfur slopes on Io. *Icarus*, *44*(2), 268–279. https://doi.org/10.1016/0019-1035(80)90022-6

Connolly, J. A. D., Schmidt, M. W., Solferino, G., & Bagdassarov, N. (2009). Permeability of asthenospheric mantle and melt extraction rates at mid-ocean ridges. *Nature*, *462*(7270), 209–212. https://doi.org/10.1038/nature08517

Coogan, L. A. (2003). Contaminating the lower crust in the Oman ophiolite. *Geology*, *31*(12), 1065. https://doi.org/10.1130/G20129.1

Costa, A., Caricchi, L., & Bagdassarov, N. (2009). A model for the rheology of particle-bearing suspensions and partially molten rocks. *Geochemistry, Geophysics, Geosystems*, *10*(3), n/a-n/a. https://doi.org/10.1029/2008GC002138

Crumpler, L. S., & Aubele, J. C. (1978). Structural evolution of Arsia Mons, Pavonis Mons, and Ascreus Mons: Tharsis region of Mars. *Icarus*, *34*(3), 496–511. https://doi.org/10.1016/0019-1035(78)90041-6

Dannberg, J., & Gassmöller, R. (2018). Chemical trends in ocean islands explained by plume–slab interaction. *Proceedings of the National Academy of Sciences*, *115*(17), 4351–4356. https://doi.org/10.1073/pnas.1714125115

Dannberg, J., Gassmöller, R., Grove, R., & Heister, T. (2019). A new formulation for coupled magma/mantle dynamics. *Geophysical Journal International*, ggz190. https://doi.org/10.1093/gji/ggz190

Dannberg, J., & Heister, T. (2016). Compressible magma/mantle dynamics: 3-D, adaptive simulations in ASPECT. *Geophysical Journal International*, *207*(3), 1343–1366. https://doi.org/10.1093/gji/ggw329

Davies, A. G. (2007). *Volcanism on Io* Cambridge University Press.

Davies, A. G., Veeder, G. J., Matson, D. L., & Johnson, T. V. (2015). Map of Io's volcanic heat flow. *Icarus*, *262*, 67–78. https://doi.org/10.1016/j.icarus.2015.08.003

Davies, G. F., & Richards, M. A. (1992). Mantle Convection. *The Journal of Geology*, *100*(2), 151–206. https://doi.org/10.1086/629582

de Kleer, K., Nimmo, F., & Kite, E. (2019). Variability in Io's Volcanism on Timescales of Periodic Orbital Changes. *Geophysical Research Letters*, *46*(12), 6327–6332. https://doi.org/10.1029/2019GL082691

de Pater, I., de Kleer, K., Davies, A. G., & Ádámkovics, M. (2017). Three decades of Loki Patera observations. *Icarus*, *297*, 265–281. https://doi.org/10.1016/j.icarus.2017.03.016

de Sitter, W. (1928). Orbital elements determining the longitude of Jupiter's satellites, derived from observations. *Annalen van de Sterrewacht te Leiden, 16*, B1-B96. https://ui.adsabs.harvard.edu/#abs/1928AnLei..16B...1D/abstract

Detrick, R. S., Buhl, P., Vera, E., Mutter, J., Orcutt, J., Madsen, J., & Brocher, T. (1987). Multi-channel seismic imaging of a crustal magma chamber along the East Pacific Rise. *Nature*, *326*(6108), 35–41. https://doi.org/10.1038/326035a0

Dreibus, G., & Wänke, H. (1987). Volatiles on Earth and Mars: A comparison. *Icarus*, *71*(2), 225–240. https://doi.org/10.1016/0019-1035(87)90148-5

Dreibus, G., & Wänke, H. (1985). Mars, a volatile-rich planet. *Meteoritics*, **20**, 367– 381. https://ui.adsabs.harvard.edu/#abs/1985Metic..20..367D/abstract

Dziewonski, A. M., & Anderson, D. L. (1981). Preliminary reference Earth model. *Physics of the Earth and Planetary Interiors*, *25*(4), 297–356. https://doi.org/10.1016/0031-9201(81)90046-7

El Maarry, M. R., Gasnault, O., Toplis, M. J., Baratoux, D., Dohm, J. M., Newsom, H. E., Boynton, W. V., & Karunatillake, S. (2009). Gamma-ray constraints on the chemical composition of the martian surface in the Tharsis region: A signature of partial melting of the mantle? *Journal of Volcanology and Geothermal Research*, *185*(1–2), 116–122. https://doi.org/10.1016/j.jvolgeores.2008.11.027

England, P. C., & Katz, R. F. (2010). Melting above the anhydrous solidus controls the location of volcanic arcs. *Nature*, *467*(7316), 700–703. https://doi.org/10.1038/nature09417

Evans, Rob. L., Hirth, G., Baba, K., Forsyth, D., Chave, A., & Mackie, R. (2005). Geophysical evidence from the MELT area for compositional controls on oceanic plates. *Nature*, *437*(7056), 249–252. https://doi.org/10.1038/nature04014

Fagereng, Å., & Biggs, J. (2019). New perspectives on 'geological strain rates' calculated from both naturally deformed and actively deforming rocks. *Journal of Structural Geology*, *125*, 100–110. https://doi.org/10.1016/j.jsg.2018.10.004

Freed, A. M., & Bürgmann, R. (2004). Evidence of power-law flow in the Mojave desert mantle. *Nature*, *430*(6999), 548–551. https://doi.org/10.1038/nature02784

Galilei, G. (1610). *Sidereus nuncius*. Apud Thomam Baglionum. https://doi.org/10.5479/sil.95438.39088015628597

Garcia, R. F., Khan, A., Drilleau, M., Margerin, L., Kawamura, T., Sun, D., Wieczorek, M. A., Rivoldini, A., Nunn, C., Weber, R. C., Marusiak, A. G., Lognonné, P., Nakamura, Y., & Zhu, P. (2019). Lunar Seismology: An Update on Interior Structure Models. *Space Science Reviews*, *215*(8), 50. https://doi.org/10.1007/s11214-019-0613-y

Garry, W. B., Zimbelman, J. R., & Gregg, T. K. P. (2007). Morphology and emplacement of a long channeled lava flow near Ascraeus Mons Volcano, Mars. *Journal of Geophysical Research: Planets*, *112*(E8). https://doi.org/10.1029/2006JE002803

Ghiorso, M. S., Hirschmann, M. M., Reiners, P. W., & Kress, V. C. (2002). The pMELTS: A revision of MELTS for improved calculation of phase relations and major element partitioning related to partial melting of the mantle to 3 GPa: pMELTS, A REVISION OF MELTS. *Geochemistry, Geophysics, Geosystems*, *3*(5), 1–35. https://doi.org/10.1029/2001GC000217

Ghiorso, M. S., & Sack, R. O. (1995). Chemical mass transfer in magmatic processes IV. A revised and internally consistent thermodynamic model for the interpolation and extrapolation of liquid-solid equilibria in magmatic systems at elevated temperatures and pressures. *Contributions to Mineralogy and Petrology*, *119*(2–3), 197–212. https://doi.org/10.1007/BF00307281

Ghiorso, M. S., & Wolf, A. S. (2019). Thermodynamic Modeling Using ENKI: 1. Overview and Phase Equilibrium Applications. *American Geophysical Union Fall Meeting, 2019*, ED53F-0897. https://ui.adsabs.harvard.edu/abs/2019AGUFMED53F0897G/abstract

Glaze, L. S., Baloga, S. M., & Stofan, E. R. (2003). A methodology for constraining lava flow rheologies with MOLA. *Icarus*, *165*(1), 26–33. https://doi.org/10.1016/S0019-1035(03)00171-4

Greeley, R. (1973). Mariner 9 Photographs of Small Volcanic Structures on Mars. *Geology*, *1*(4), 175–180. https://doi.org/10.1130/0091-7613(1973)1<175:MPOSVS>2.0.CO;2

Greeley, R. (2005). Fluid lava flows in Gusev crater, Mars. *Journal of Geophysical Research*, *110*(E5), E05008. https://doi.org/10.1029/2005JE002401

Greeley, R., Bridges, N. T., Crown, D. A., Crumpler, L., Fagents, S. A., Mouginis-Mark, P. J., & Zimbelman, J. R. (2000). Volcanism on the Red Planet: Mars. In J. R. Zimbelman & T. K. P. Gregg (Eds.), *Environmental Effects on Volcanic Eruptions* (pp. 75–112). Springer US. https://doi.org/10.1007/978-1-4615-4151-6_4

Greeley, R., & Spudis, P. D. (1981). Volcanism on Mars. *Reviews of Geophysics*, *19*(1), 13. https://doi.org/10.1029/RG019i001p00013

Gregg, T. K. P., & Williams, S. N. (1996). Explosive Mafic Volcanoes on Mars and Earth: Deep Magma Sources and Rapid Rise Rate. *Icarus*, *122*(2), 397–405. https://doi.org/10.1006/icar.1996.0132

Gualda, G. A. R., Ghiorso, M. S., Lemons, R. V., & Carley, T. L. (2012). Rhyolite-MELTS: A Modified Calibration of MELTS Optimized for Silica-rich, Fluid-bearing Magmatic Systems. *Journal of Petrology*, *53*(5), 875–890. https://doi.org/10.1093/petrology/egr080

Hallis, L. J., Taylor, G. J., Nagashima, K., & Huss, G. R. (2012). Magmatic water in the martian meteorite Nakhla. *Earth and Planetary Science Letters*, *359–360*, 84–92. https://doi.org/10.1016/j.epsl.2012.09.049

Hamecher, E. A., Antoshechkina, P. M., Ghiorso, M. S., & Asimow, P. D. (2012). The molar volume of FeO–MgO–Fe2O3–Cr2O3–Al2O3–TiO2 spinels. *Contributions to Mineralogy and Petrology*. https://doi.org/10.1007/s00410-012-0790-0

Hamilton, C. W., Beggan, C. D., Still, S., Beuthe, M., Lopes, R. M. C., Williams, D. A., Radebaugh, J., & Wright, W. (2013). Spatial distribution of volcanoes on Io:

Implications for tidal heating and magma ascent. *Earth and Planetary Science Letters*, *361*, 272–286. https://doi.org/10.1016/j.epsl.2012.10.032

Hamilton, V. E., Wyatt, M. B., McSween, H. Y., & Christensen, P. R. (2001). Analysis of terrestrial and Martian volcanic compositions using thermal emission spectroscopy: 2. Application to Martian surface spectra from the Mars Global Surveyor Thermal Emission Spectrometer. *Journal of Geophysical Research: Planets*, *106*(E7), 14733–14746. https://doi.org/10.1029/2000JE001353

Hanel, R., Conrath, B., Flasar, M., Kunde, V., Lowman, P., Maguire, W., Pearl, J., Pirraglia, J., Samuelson, R., Gautier, D., Gierasch, P., Kumar, S., & Ponnamperuma, C. (1979). Infrared Observations of the Jovian System from Voyager 1. *Science*, *204*(4396), 972–976. https://doi.org/10.1126/science.204.4396.972-a

Harder, H., & Christensen, U. R. (1996). A one-plume model of martian mantle convection. *Nature*, *380*(6574), 507–509. https://doi.org/10.1038/380507a0

Hauber, E., Brož, P., Jagert, F., Jodłowski, P., & Platz, T. (2011). Very recent and wide-spread basaltic volcanism on Mars. *Geophysical Research Letters*, *38*(10), n/a-n/a. https://doi.org/10.1029/2011GL047310

Hauck, S. A. (2002). Thermal and crustal evolution of Mars. *Journal of Geophysical Research*, *107*(E7), 5052. https://doi.org/10.1029/2001JE001801

Havlin, C., Parmentier, E. M., & Hirth, G. (2013). Dike propagation driven by melt accumulation at the lithosphere–asthenosphere boundary. *Earth and Planetary Science Letters*, *376*, 20–28. https://doi.org/10.1016/j.epsl.2013.06.010

Head, J. W. (2002). Northern lowlands of Mars: Evidence for widespread volcanic flooding and tectonic deformation in the Hesperian Period. *Journal of Geophysical Research*, *107*(E1), 5003. https://doi.org/10.1029/2000JE001445

Hebert, L. B., & Montési, L. G. J. (2010). Generation of permeability barriers during melt extraction at mid-ocean ridges. *Geochemistry, Geophysics, Geosystems*, *11*(12), n/a-n/a. https://doi.org/10.1029/2010GC003270

Hebert, L. B., & Montési, L. G. J. (2011). Melt extraction pathways at segmented oceanic ridges: Application to the East Pacific Rise at the Siqueiros transform.

Geophysical Research Letters, *38*(11), n/a-n/a. https://doi.org/10.1029/2011GL047206

Hebert, L. B., Antoshechkina, P., Asimow, P., & Gurnis, M. (2009). Emergence of a low-viscosity channel in subduction zones through the coupling of mantle flow and thermodynamics. *Earth and Planetary Science Letters*, *278*(3–4), 243–256. https://doi.org/10.1016/j.epsl.2008.12.013

Heister, T., Dannberg, J., Gassmöller, R., & Bangerth, W. (2017). High accuracy mantle convection simulation through modern numerical methods – II: Realistic models and problems. *Geophysical Journal International*, *210*(2), 833–851. https://doi.org/10.1093/gji/ggx195

Hellebrand, E. (2002). Garnet-field Melting and Late-stage Refertilization in "Residual" Abyssal Peridotites from the Central Indian Ridge. *Journal of Petrology*, *43*(12), 2305–2338. https://doi.org/10.1093/petrology/43.12.2305

Herd, C. D. K., Borg, L. E., Jones, J. H., & Papike, J. J. (2002). Oxygen fugacity and geochemical variations in the martian basalts: Implications for martian basalt petrogenesis and the oxidation state of the upper mantle of Mars. *Geochimica et Cosmochimica Acta*, *66*(11), 2025–2036. https://doi.org/10.1016/S0016-7037(02)00828-1

Herzberg, C., Asimow, P. D., Arndt, N., Niu, Y., Lesher, C. M., Fitton, J. G., Cheadle, M. J., & Saunders, A. D. (2007). Temperatures in ambient mantle and plumes: Constraints from basalts, picrites, and komatiites. *Geochemistry, Geophysics, Geosystems*, *8*(2), n/a-n/a. https://doi.org/10.1029/2006GC001390

Hetényi, G., Molinari, I., Clinton, J., Bokelmann, G., Bondár, I., Crawford, W. C., Dessa, J.-X., Doubre, C., Friederich, W., Fuchs, F., Giardini, D., Gráczer, Z., Handy, M. R., Herak, M., Jia, Y., Kissling, E., Kopp, H., Korn, M., Margheriti, L., … Živčić, M. (2018). The AlpArray Seismic Network: A Large-Scale European Experiment to Image the Alpine Orogen. *Surveys in Geophysics*, *39*(5), 1009–1033. https://doi.org/10.1007/s10712-018-9472-4

Hiesinger, H. (2004). The Syrtis Major volcanic province, Mars: Synthesis from Mars Global Surveyor data. *Journal of Geophysical Research*, *109*(E1), E01004. https://doi.org/10.1029/2003JE002143

Hiesinger, H., Head, J. W., & Neukum, G. (2007). Young lava flows on the eastern flank of Ascraeus Mons: Rheological properties derived from High Resolution Stereo Camera (HRSC) images and Mars Orbiter Laser Altimeter (MOLA) data. *Journal of Geophysical Research*, *112*(E5), E05011. https://doi.org/10.1029/2006JE002717

Hirth, G., & Kohlstedt, D. (2003). Rheology of the upper mantle and the mantle wedge: A view from the experimentalists. In J. Eiler (Ed.), *Geophysical Monograph Series* (Vol. 138, pp. 83–105). American Geophysical Union. https://doi.org/10.1029/138GM06

Hirth, G., & Kohlstedt, D. L. (1996). Water in the oceanic upper mantle: Implications for rheology, melt extraction and the evolution of the lithosphere. *Earth and Planetary Science Letters*, *144*(1–2), 93–108. https://doi.org/10.1016/0012-821X(96)00154-9

Hollister, L., & Crawford, M. L. (1986). Melt-enhanced deformation: A major tectonic process. *Geology*, *14*(7), 558–561. https://doi.org/10.1130/0091-7613(1986)14<558:MDAMTP>2.0.CO;2

Hulme, G. (1976). The determination of the rheological properties and effusion rate of an Olympus Mons lava. *Icarus*, *27*(2), 207–213. https://doi.org/10.1016/0019-1035(76)90004-X

Hutton, D. H. W. (1988). Granite emplacement mechanisms and tectonic controls: Inferences from deformation studies. *Earth and Environmental Science Transactions of the Royal Society of Edinburgh*, *79*(2–3), 245–255. https://doi.org/10.1017/S0263593300014255

Ivanov, M. A., & Head, J. W. (2006). Alba Patera, Mars: Topography, structure, and evolution of a unique late Hesperian–early Amazonian shield volcano. *Journal of Geophysical Research*, *111*(E9), E09003. https://doi.org/10.1029/2005JE002469

Izquierdo, K., Lekić, V., & Montési, L. G. J. (2020). A Bayesian approach to infer interior mass anomalies from the gravity data of celestial bodies. *Geophysical Journal International*, *220*(3), 1687–1699. https://doi.org/10.1093/gji/ggz544

Jaeger, W. L. (2003). Orogenic tectonism on Io. *Journal of Geophysical Research*, *108*(E8), 12-1-12–18. https://doi.org/10.1029/2002JE001946

Jaeger, W. L., Keszthelyi, L. P., McEwen, A. S., Dundas, C. M., & Russell, P. S. (2007). Athabasca Valles, Mars: A Lava-Draped Channel System. *Science*, *317*(5845), 1709–1711. https://doi.org/10.1126/science.1143315

James, P. B., Smith, D. E., Byrne, P. K., Kendall, J. D., Melosh, H. J., & Zuber, M. T. (2019). Deep Structure of the Lunar South Pole-Aitken Basin. *Geophysical Research Letters*, *46*(10), 5100–5106. https://doi.org/10.1029/2019GL082252

Johnson, T. V., Cook, A. F., Sagan, C., & Soderblom, L. A. (1979). Volcanic resurfacing rates and implications for volatiles on Io. *Nature*, *280*(5725), 746–750. https://doi.org/10.1038/280746a0

Kankanamge, D. G. J., & Moore, W. B. (2016). Heat transport in the Hadean mantle: From heat pipes to plates. *Geophysical Research Letters*, *43*(7), 3208–3214. https://doi.org/10.1002/2015GL067411

Karato, S. (2010). Rheology of the Earth's mantle: A historical review. *Gondwana Research*, *18*(1), 17–45. https://doi.org/10.1016/j.gr.2010.03.004

Karato, S. (1984). Grain-size distribution and rheology of the upper mantle. *Tectonophysics*, *104*(1–2), 155–176. https://doi.org/10.1016/0040-1951(84)90108-2

Kargel, J., Carlson, R., Davies, A., Fegley, B., Gillespie, A., Greeley, R., Howell, R., Jessup, K. L., Kamp, L., Keszthelyi, L., Lopes, R., MacIntyre, T., Marchis, F., McEwen, A., Milazzo, M., Perry, J., Radebaugh, J., Schaefer, L., Schmerr, N., … Zolotov, M. (2003). Extreme volcanism on Io: Latest insights at the end of Galileo era. *Eos, Transactions American Geophysical Union*, *84*(33), 313. https://doi.org/10.1029/2003EO330001

Karunatillake, S., Wray, J. J., Squyres, S. W., Taylor, G. J., Gasnault, O., McLennan, S. M., Boynton, W., El Maarry, M. R., & Dohm, J. M. (2009). Chemically striking regions on Mars and Stealth revisited. *Journal of Geophysical Research*, *114*(E12), E12001. https://doi.org/10.1029/2008JE003303

Katz, R. F., Spiegelman, M., & Langmuir, C. H. (2003). A new parameterization of hydrous mantle melting. *Geochemistry, Geophysics, Geosystems*, *4*(9), n/a-n/a. https://doi.org/10.1029/2002GC000433

Kelemen, P. B., Hirth, G., Shimizu, N., Spiegelman, M., & Dick, H. J. (1997). A review of melt migration processes in the adiabatically upwelling mantle beneath oceanic spreading ridges. *Philosophical Transactions of the Royal Society of London. Series A: Mathematical, Physical and Engineering Sciences*, *355*(1723), 283–318. https://doi.org/10.1098/rsta.1997.0010

Kelemen, P. B., & Aharonov, E. (2013). Periodic Formation of Magma Fractures and Generation of Layered Gabbros in the Lower Crust Beneath Oceanic Spreading Ridges. In W. Roger Buck, P. T. Delaney, J. A. Karson, & Y. Lagabrielle (Eds.), *Geophysical Monograph Series* (pp. 267–289). American Geophysical Union. https://doi.org/10.1029/GM106p0267

Kelemen, P. B., Shimizu, N., & Salters, V. J. M. (1995). Extraction of mid-ocean-ridge basalt from the upwelling mantle by focused flow of melt in dunite channels. *Nature*, *375*(6534), 747–753. https://doi.org/10.1038/375747a0

Keller, T., Katz, R. F., & Hirschmann, M. M. (2017). Volatiles beneath mid-ocean ridges: Deep melting, channelised transport, focusing, and metasomatism. *Earth and Planetary Science Letters*, *464*, 55–68. https://doi.org/10.1016/j.epsl.2017.02.006

Keller, T., May, D. A., & Kaus, B. J. P. (2013). Numerical modelling of magma dynamics coupled to tectonic deformation of lithosphere and crust. *Geophysical Journal International*, *195*(3), 1406–1442. https://doi.org/10.1093/gji/ggt306

Keszthelyi, L., Jaeger, W. L., Turtle, E. P., Milazzo, M., & Radebaugh, J. (2004). A post-Galileo view of Io's interior. *Icarus*, *169*(1), 271–286. https://doi.org/10.1016/j.icarus.2004.01.005

Keszthelyi, L., Jaeger, W., Milazzo, M., Radebaugh, J., Davies, A. G., & Mitchell, K. L. (2007). New estimates for Io eruption temperatures: Implications for the interior. *Icarus*, *192*(2), 491–502. https://doi.org/10.1016/j.icarus.2007.07.008

Keszthelyi, L., & McEwen, A. (1997). Magmatic Differentiation of Io. *Icarus*, *130*(2), 437–448. https://doi.org/10.1006/icar.1997.5837

Khurana, K. K., Jia, X., Kivelson, M. G., Nimmo, F., Schubert, G., & Russell, C. T. (2011). Evidence of a Global Magma Ocean in Io's Interior. *Science*, *332*(6034), 1186–1189. https://doi.org/10.1126/science.1201425

Kiefer, W. S., & Li, Q. (2009). Mantle convection controls the observed lateral variations in lithospheric thickness on present-day Mars. *Geophysical Research Letters*, *36*(18), L18203. https://doi.org/10.1029/2009GL039827

Kirby, S. H., & Kronenberg, A. K. (1987). Rheology of the lithosphere: Selected topics. *Reviews of Geophysics*, *25*(6), 1219. https://doi.org/10.1029/RG025i006p01219

Kirchoff, M. R., & McKinnon, W. B. (2009). Formation of mountains on Io: Variable volcanism and thermal stresses. *Icarus*, *201*(2), 598–614. https://doi.org/10.1016/j.icarus.2009.02.006

Kirchoff, M. R., McKinnon, W. B., & Bland, M. T. (2020). Effects of faulting on crustal stresses during mountain formation on Io. *Icarus*, *335*, 113326. https://doi.org/10.1016/j.icarus.2019.05.028

Kirchoff, M. R., McKinnon, W. B., & Schenk, P. M. (2011). Global distribution of volcanic centers and mountains on Io: Control by asthenospheric heating and implications for mountain formation. *Earth and Planetary Science Letters*, *301*(1–2), 22–30. https://doi.org/10.1016/j.epsl.2010.11.018

Korenaga, J., Holbrook, W. S., Kent, G. M., Kelemen, P. B., Detrick, R. S., Larsen, H.-C., Hopper, J. R., & Dahl-Jensen, T. (2000). Crustal structure of the southeast Greenland margin from joint refraction and reflection seismic tomography. *Journal of Geophysical Research: Solid Earth*, *105*(B9), 21591–21614. https://doi.org/10.1029/2000JB900188

Korenaga, J., & Kelemen, P. B. (1997). Origin of gabbro sills in the Moho transition zone of the Oman ophiolite: Implications for magma transport in the oceanic lower crust. *Journal of Geophysical Research: Solid Earth*, *102*(B12), 27729–27749. https://doi.org/10.1029/97JB02604

Korenaga, J., & Kelemen, P. B. (1998). Melt migration through the oceanic lower crust: a constraint from melt percolation modeling with finite solid diffusion. *Earth and Planetary Science Letters, 156*(1), 1-12. https://doi.org/10.1016/S0012-821X(98)00004-1

Kronbichler, M., Heister, T., & Bangerth, W. (2012). High accuracy mantle convection simulation through modern numerical methods: High accuracy

mantle convection simulation. *Geophysical Journal International*, *191*(1), 12–29. https://doi.org/10.1111/j.1365-246X.2012.05609.x

Ksanfomaliti, L. V., Zubkova, V. M., Morozov, N. A., & Petrova, E. V. (1982). Microseisms at the VENERA-13 and VENERA-14 Landing Sites. *Soviet Astronomy Letters, 8,* 241. https://ui.adsabs.harvard.edu/abs/1982SvAL....8..241K

Lapen, T. J., Righter, M., Brandon, A. D., Debaille, V., Beard, B. L., Shafer, J. T., & Peslier, A. H. (2010). A Younger Age for ALH84001 and Its Geochemical Link to Shergottite Sources in Mars. *Science*, *328*(5976), 347–351. https://doi.org/10.1126/science.1185395

Le Corvec, N., Menand, T., & Lindsay, J. (2013). Interaction of ascending magma with pre-existing crustal fractures in monogenetic basaltic volcanism: An experimental approach. *Journal of Geophysical Research: Solid Earth*, *118*(3), 968–984. https://doi.org/10.1002/jgrb.50142

Le Roux, V., Bodinier, J.-L., Tommasi, A., Alard, O., Dautria, J.-M., Vauchez, A., & Riches, A. J. V. (2007). The Lherz spinel lherzolite: Refertilized rather than pristine mantle. *Earth and Planetary Science Letters*, *259*(3–4), 599–612. https://doi.org/10.1016/j.epsl.2007.05.026

Lodders, K., & Fegley, B. (1997). An Oxygen Isotope Model for the Composition of Mars. *Icarus*, *126*(2), 373–394. https://doi.org/10.1006/icar.1996.5653

Longhi, J. "Magmatic processes on Mars: Insights from SNC meteorites." *Lunar and Planetary Science Conference.* Vol. 21. 1990. https://ui.adsabs.harvard.edu/#abs/1990LPI....21..716L/abstract

Lunine, J. I., & Stevenson, D. J. (1982). Formation of the galilean satellites in a gaseous nebula. *Icarus*, *52*(1), 14–39. https://doi.org/10.1016/0019-1035(82)90166-X

Magde, L. S., & Sparks, D. W. (1997). Three-dimensional mantle upwelling, melt generation, and melt migration beneath segment slow spreading ridges. *Journal of Geophysical Research: Solid Earth*, *102*(B9), 20571–20583. https://doi.org/10.1029/97JB01278

Magde, L. S., Sparks, D. W., & Detrick, R. S. (1997). The relationship between buoyant mantle flow, melt migration, and gravity bull's eyes at the Mid-Atlantic Ridge between 33°N and 35°N. *Earth and Planetary Science Letters*, *148*(1–2), 59–67. https://doi.org/10.1016/S0012-821X(97)00039-3

Matson, D. L., Ransford, G. A., & Johnson, T. V. (1981). Heat flow from Io (JI). *Journal of Geophysical Research*, *86*(B3), 1664. https://doi.org/10.1029/JB086iB03p01664

McBirney, A. R. (1995). Mechanisms of differentiation in the Skaergaard Intrusion. *Journal of the Geological Society*, *152*(3), 421–435. https://doi.org/10.1144/gsjgs.152.3.0421

McCauley, J. F., Carr, M. H., Cutts, J. A., Hartmann, W. K., Masursky, H., Milton, D. J., Sharp, R. P., & Wilhelms, D. E. (1972). Preliminary mariner 9 report on the geology of Mars. *Icarus*, *17*(2), 289–327. https://doi.org/10.1016/0019-1035(72)90003-6

McCubbin, F. M., Hauri, E. H., Elardo, S. M., Vander Kaaden, K. E., Wang, J., & Shearer, C. K. (2012). Hydrous melting of the martian mantle produced both depleted and enriched shergottites. *Geology*, *40*(8), 683–686. https://doi.org/10.1130/G33242.1

McEwen, A. S. (2000). Galileo at Io: Results from High-Resolution Imaging. *Science*, *288*(5469), 1193–1198. https://doi.org/10.1126/science.288.5469.1193

McEwen, A., Turtle, E., Hibbard, K., Reynolds, E., & Adams, E. (2014). Io Volcano Observer (IVO): Budget travel to the outer Solar System. *Acta Astronautica*, *93*, 539–544. https://doi.org/10.1016/j.actaastro.2012.05.028

McEwen, A. S., Keszthelyi, L., Geissler, P., Simonelli, D. P., Carr, M. H., Johnson, T. V., Klaasen, K. P., Breneman, H. H., Jones, T. J., Kaufman, J. M., Magee, K. P., Senske, D. A., Belton, M. J. S., & Schubert, G. (1998). Active Volcanism on Io as Seen by Galileo SSI. *Icarus*, *135*(1), 181–219. https://doi.org/10.1006/icar.1998.5972

McEwen, A. S., Keszthelyi, L. P., Lopes, R., Schenk, P. M., & Spencer, J. R. (2004). The lithosphere and surface of Io. In *Jupiter: The Planet, Satellites and Magnetosphere*, 307-328.

McEwen, A. S., Simonelli, D. P., Senske, D. R., Klaasen, K. P., Keszthelyi, L., Johnson, T. V., Geissler, P. E., Carr, M. H., & Belton, M. J. S. (1997). High-temperature hot spots on Io as Seen by the Galileo solid state imaging (SSI) Experiment. *Geophysical Research Letters*, *24*(20), 2443–2446. https://doi.org/10.1029/97GL01956

McGovern, P. J., Grosfils, E. B., Galgana, G. A., Morgan, J. K., Rumpf, M. E., Smith, J. R., & Zimbelman, J. R. (2015). Lithospheric flexure and volcano basal boundary conditions: Keys to the structural evolution of large volcanic edifices on the terrestrial planets. *Geological Society, London, Special Publications*, *401*(1), 219–237. https://doi.org/10.1144/SP401.7

McGovern, P. J., Solomon, S. C., Smith, D. E., Zuber, M. T., Simons, M., Wieczorek, M. A., Phillips, R. J., Neumann, G. A., Aharonson, O., & Head, J. W. (2002). Localized gravity/topography admittance and correlation spectra on Mars: Implications for regional and global evolution. *Journal of Geophysical Research: Planets*, *107*(E12), 19-1-19–25. https://doi.org/10.1029/2002JE001854

McKenzie, D. (1984). The Generation and Compaction of Partially Molten Rock. *Journal of Petrology*, *25*(3), 713–765. https://doi.org/10.1093/petrology/25.3.713

McKinnon, W. B., Schenk, P. M., & Dombard, A. J. (2001). Chaos on Io: A model for formation of mountain blocks by crustal heating, melting, and tilting. *Geology*, *29*(2), 103–106. https://doi.org/10.1130/0091-7613(2001)029<0103:COIAMF>2.0.CO;2

McSween, H. Y. (2004). Basaltic Rocks Analyzed by the Spirit Rover in Gusev Crater. *Science*, *305*(5685), 842–845. https://doi.org/10.1126/science.3050842

McSween, H. Y., Murchie, S. L., Crisp, J. A., Bridges, N. T., Anderson, R. C., Bell, J. F., Britt, D. T., Brückner, J., Dreibus, G., Economou, T., Ghosh, A., Golombek, M. P., Greenwood, J. P., Johnson, J. R., Moore, H. J., Morris, R. V., Parker, T. J., Rieder, R., Singer, R., & Wänke, H. (1999). Chemical, multispectral, and textural constraints on the composition and origin of rocks at the Mars Pathfinder landing site. *Journal of Geophysical Research: Planets*, *104*(E4), 8679–8715. https://doi.org/10.1029/98JE02551

McSween, H. Y. (1985). SNC meteorites: Clues to Martian petrologic evolution? *Reviews of Geophysics*, *23*(4), 391. https://doi.org/10.1029/RG023i004p00391

McSween, H. Y. (1994). What we have learned about Mars from SNC meteorites. *Meteoritics*, *29*(6), 757–779. https://doi.org/10.1111/j.1945-5100.1994.tb01092.x

Mège, D., & Masson, P. (1996). A plume tectonics model for the Tharsis province, Mars. *Planetary and Space Science*, *44*(12), 1499–1546. https://doi.org/10.1016/S0032-0633(96)00113-4

Mierdel, K., Keppler, H., Smyth, J. R., & Langenhorst, F. (2007). Water solubility in aluminous orthopyroxene and the origin of Earth's asthenosphere. *Science, 315*(5810), 364-368. https://doi.org/10.1126/science.1135422

Miller, K. J., Montési, L. G. J., & Zhu, W. (2015). Estimates of olivine–basaltic melt electrical conductivity using a digital rock physics approach. *Earth and Planetary Science Letters*, *432*, 332–341. https://doi.org/10.1016/j.epsl.2015.10.004

Miller, K. J., Zhu, W., Montési, L. G. J., & Gaetani, G. A. (2014). Experimental quantification of permeability of partially molten mantle rock. *Earth and Planetary Science Letters*, *388*, 273–282. https://doi.org/10.1016/j.epsl.2013.12.003

Montési, L. G. J. (2001). Concentric dikes on the flanks of Pavonis Mons: Implications for the evolution of martian shield volcanoes and mantle plumes. In R. E. Ernst & K. L. Buchan, *Mantle plumes: Their identification through time*. Geological Society of America. https://doi.org/10.1130/0-8137-2352-3.165

Montési, L. G. J. (2003). Clues to the lithospheric structure of Mars from wrinkle ridge sets and localization instability. *Journal of Geophysical Research*, *108*(E6), 5048. https://doi.org/10.1029/2002JE001974

Montési, L. G. J., & Behn, M. D. (2007). Mantle flow and melting underneath oblique and ultraslow mid-ocean ridges. *Geophysical Research Letters*, *34*(24), L24307. https://doi.org/10.1029/2007GL031067

Montési, L. G. J., Behn, M. D., Hebert, L. B., Lin, J., & Barry, J. L. (2011). Controls on melt migration and extraction at the ultraslow Southwest Indian Ridge 10°–

16°E. *Journal of Geophysical Research*, *116*(B10), B10102. https://doi.org/10.1029/2011JB008259

Moore, W. (2001). The Thermal State of Io. *Icarus*, *154*(2), 548–550. https://doi.org/10.1006/icar.2001.6739

Moore, W. B. (2003). Tidal heating and convection in Io. *Journal of Geophysical Research*, *108*(E8), 5096. https://doi.org/10.1029/2002JE001943

Moore, H. J., Arthur, D. W. G., & Schaber, G. G. (1978). Yield strengths of flows on the Earth, Mars, and Moon. In *Lunar and planetary science conference proceedings* (Vol. 9, pp. 3351-3378). https://ui.adsabs.harvard.edu/#abs/1978LPSC....9.3351M/abstract

Moore, W. B., Simon, J. I., & Webb, A. A. G. (2017). Heat-pipe planets. *Earth and Planetary Science Letters*, *474*, 13–19. https://doi.org/10.1016/j.epsl.2017.06.015

Moore, W. B., & Webb, A. A. G. (2013). Heat-pipe earth. *Nature, 501*(7468), 501-505. https://doi.org/10.1038/nature12473

Morabito, L. A., Synnott, S. P., Kupferman, P. N., & Collins, S. A. (1979). Discovery of Currently Active Extraterrestrial Volcanism. *Science*, *204*(4396), 972–972. https://doi.org/10.1126/science.204.4396.972

Mouginis-Mark, P. J., Wilson, L., Head, J. W., Brown, S. H., Lynn Hall, J., & Sullivan, K. D. (1984). Elysium planitia, mars: Regional geology, volcanology, and evidence for volcano-ground ice interactions. *Earth, Moon and Planets*, *30*(2), 149–173. https://doi.org/10.1007/BF00114309

Mouginis-Mark, P., & Yoshioka, M. T. (1998). The long lava flows of Elysium Planita, Mars. *Journal of Geophysical Research: Planets*, *103*(E8), 19389–19400. https://doi.org/10.1029/98JE01126

Mutch, E. J. F., Maclennan, J., Shorttle, O., Edmonds, M., & Rudge, J. F. (2019). Rapid transcrustal magma movement under Iceland. *Nature Geoscience 12*, 569–574. https://doi.org/10.1038/s41561-019-0376-9

Nahm, A. L., & Schultz, R. A. (2010). Evaluation of the orogenic belt hypothesis for the formation of the Thaumasia Highlands, Mars. *Journal of Geophysical Research*, *115*(E4), E04008. https://doi.org/10.1029/2009JE003327

Neumann, G. A. (2004). Crustal structure of Mars from gravity and topography. *Journal of Geophysical Research*, *109*(E8), E08002. https://doi.org/10.1029/2004JE002262

Nicholson, H., Condomines, M., Fitton, J. G., Fallick, A. E., Gr Nvold, K., & Rogers, G. (1991). Geochemical and Isotopic Evidence for Crustal Assimilation Beneath Krafla, Iceland. *Journal of Petrology*, *32*(5), 1005–1020. https://doi.org/10.1093/petrology/32.5.1005

Nicoli, G., Moyen, J. & Stevens, G. (2016). Diversity of burial rates in convergent settings decreased as Earth aged. *Scientific Reports 6*, 26359 https://doi.org/10.1038/srep26359

Nimmo, F. (2002). Why does Venus lack a magnetic field? *Geology*, *30*(11), 987–990. https://doi.org/10.1130/0091-7613(2002)030<0987:WDVLAM>2.0.CO;2

Olson, P., & Christensen, U. (1986). Solitary wave propagation in a fluid conduit within a viscous matrix. *Journal of Geophysical Research*, *91*(B6), 6367. https://doi.org/10.1029/JB091iB06p06367

O'Reilly, T. C., & Davies, G. F. (1981). Magma transport of heat on Io: A mechanism allowing a thick lithosphere. *Geophysical Research Letters*, *8*(4), 313–316. https://doi.org/10.1029/GL008i004p00313

Pasckert, J. H., Hiesinger, H., & Reiss, D. (2012). Rheologies and ages of lava flows on Elysium Mons, Mars. *Icarus*, *219*(1), 443–457. https://doi.org/10.1016/j.icarus.2012.03.014

Peale, S. J., Cassen, P., & Reynolds, R. T. (1979). Melting of Io by Tidal Dissipation. *Science*, *203*(4383), 892–894. https://doi.org/10.1126/science.203.4383.892

Petford, N. (1995). Segregation of tonalitic-trondhjemitic melts in the continental crust: The mantle connection. *Journal of Geophysical Research: Solid Earth, 100*(B8), 15735-15743. https://doi.org/10.1029/94JB03259

Pfiffner, O. A., & Ramsay, J. G. (1982). Constraints on geological strain rates: Arguments from finite strain states of naturally deformed rocks. *Journal of Geophysical Research: Solid Earth*, *87*(B1), 311–321. https://doi.org/10.1029/JB087iB01p00311

Phillips, C. B. (2000). Voyager and Galileo SSI views of volcanic resurfacing on Io and the search for geologic activity on Europa (Doctoral dissertation, University of Arizona). https://repository.arizona.edu/handle/10150/289119

Phillips, R. J., Zuber, M. T., Smrekar, S. E., Mellon, M. T., Head, J. W., Tanaka, K. L., Putzig, N. E., Milkovich, S. M., Campbell, B. A., Plaut, J. J., Safaeinili, A., Seu, R., Biccari, D., Carter, L. M., Picardi, G., Orosei, R., Mohit, P. S., Heggy, E., Zurek, R. W., … Marinangeli, L. (2008). Mars North Polar Deposits: Stratigraphy, Age, and Geodynamical Response. *Science*, *320*(5880), 1182–1185. https://doi.org/10.1126/science.1157546

Plescia, J. (2000). Geology of the Uranius Group Volcanic Constructs: Uranius Patera, Ceraunius Tholus, and Uranius Tholus. *Icarus*, *143*(2), 376–396. https://doi.org/10.1006/icar.1999.6259

Plescia, J. B. (1991). Wrinkle ridges in Lunae Planum Mars: Implications for shortening and strain. *Geophysical Research Letters*, *18*(5), 913–916. https://doi.org/10.1029/91GL01070

Plescia, J. B. (2004). Morphometric properties of Martian volcanoes. *Journal of Geophysical Research*, *109*(E3), E03003. https://doi.org/10.1029/2002JE002031

Plescia, J. B., & Saunders, R. S. (1979). The chronology of the Martian volcanoes. In *Lunar and Planetary Science Conference Proceedings* (Vol. 10, pp. 2841-2859). https://ui.adsabs.harvard.edu/#abs/1979LPSC...10.2841P/abstract

Pollack, H. N., Hurter, S. J., & Johnson, J. R. (1993). Heat flow from the Earth's interior: Analysis of the global data set. *Reviews of Geophysics*, *31*(3), 267. https://doi.org/10.1029/93RG01249

Pronin, A. A., & Stofan, E. R. (1990). Coronae on Venus: Morphology, classification, and distribution. *Icarus*, *87*(2), 452–474. https://doi.org/10.1016/0019-1035(90)90148-3

Putirka, K. (2008). Excess temperatures at ocean islands: Implications for mantle layering and convection. *Geology*, *36*(4), 283. https://doi.org/10.1130/G24615A.1

Radebaugh, J., Keszthelyi, L. P., McEwen, A. S., Turtle, E. P., Jaeger, W., & Milazzo, M. (2001). Paterae on Io: A new type of volcanic caldera? *Journal of*

Geophysical Research: Planets, *106*(E12), 33005–33020. https://doi.org/10.1029/2000JE001406

Rathbun, J. A., & Spencer, J. R. (2006). Loki, Io: New ground-based observations and a model describing the change from periodic overturn. *Geophysical Research Letters*, *33*(17), L17201. https://doi.org/10.1029/2006GL026844

Rathbun, J. A., Spencer, J. R., Davies, A. G., Howell, R. R., & Wilson, L. (2002). Loki, Io: A periodic volcano: LOKI. *Geophysical Research Letters*, *29*(10), 84-1-84–4. https://doi.org/10.1029/2002GL014747

Rathbun, J. A., & Spencer, J. R. (2010). Ground-based observations of time variability in multiple active volcanoes on Io. *Icarus*, *209*(2), 625–630. https://doi.org/10.1016/j.icarus.2010.05.019

Rawlinson, N., Pozgay, S., & Fishwick, S. (2010). Seismic tomography: A window into deep Earth. *Physics of the Earth and Planetary Interiors*, *178*(3–4), 101–135. https://doi.org/10.1016/j.pepi.2009.10.002

Ricard, Y., Bercovici, D., & Schubert, G. (2001). A two-phase model for compaction and damage: 2. Applications to compaction, deformation, and the role of interfacial surface tension. *Journal of Geophysical Research: Solid Earth*, *106*(B5), 8907–8924. https://doi.org/10.1029/2000JB900431

Richardson, J. A., Bleacher, J. E., & Glaze, L. S. (2013). The volcanic history of Syria Planum, Mars. *Journal of Volcanology and Geothermal Research*, *252*, 1–13. https://doi.org/10.1016/j.jvolgeores.2012.11.007

Rieder, R., Economou, T., Wänke, H., Turkevich, A., Crisp, J., Brückner, J., Dreibus, G., & McSween, H. Y. (1997). The Chemical Composition of Martian Soil and Rocks Returned by the Mobile Alpha Proton X-ray Spectrometer: Preliminary Results from the X-ray Mode. *Science*, *278*(5344), 1771.1-1774. https://doi.org/10.1126/science.278.5344.1771

Rodrigue, C.M. (2009) Orders of relief and the regional geography of Mars. Paper presented at the *Association of American Geographers*, Las Vegas, 22–27 Mar 2009. http://web.csulb.edu/~rodrigue/geog441541/mercatorMOLA.jpg

Rondenay, S., Montési, L. G. J., & Abers, G. A. (2010). New geophysical insight into the origin of the Denali volcanic gap: Denali volcanic gap. *Geophysical Journal*

International, *182*(2), 613–630. https://doi.org/10.1111/j.1365-246X.2010.04659.x

Rudge, J. F., Bercovici, D., & Spiegelman, M. (2011). Disequilibrium melting of a two phase multicomponent mantle. *Geophysical Journal International, 184*(2), 699-718. https://doi.org/10.1111/j.1365-246X.2010.04870.x

Ruedas, T., Tackley, P. J., & Solomon, S. C. (2013a). Thermal and compositional evolution of the martian mantle: Effects of phase transitions and melting. *Physics of the Earth and Planetary Interiors*, *216*, 32–58. https://doi.org/10.1016/j.pepi.2012.12.002

Ruedas, T., Tackley, P. J., & Solomon, S. C. (2013b). Thermal and compositional evolution of the martian mantle: Effects of water. *Physics of the Earth and Planetary Interiors*, *220*, 50–72. https://doi.org/10.1016/j.pepi.2013.04.006

Rychert, C. A., Fischer, K. M., & Rondenay, S. (2005). A sharp lithosphere–asthenosphere boundary imaged beneath eastern North America. *Nature, 436*(7050), 542-545. https://doi.org/10.1038/nature03904

Rychert, C. A., & Shearer, P. M. (2009). A global view of the lithosphere-asthenosphere boundary. *Science, 324*(5926), 495-498. https://doi.org/10.1126/science.1169754

Sagan, C. (1979). Sulphur flows on Io. *Nature*, *280*(5725), 750–753. https://doi.org/10.1038/280750a0

Schaber, G. G. (1982). Syrtis major: A low-relief volcanic shield. *Journal of Geophysical Research*, *87*(B12), 9852. https://doi.org/10.1029/JB087iB12p09852

Schaber, G. G., Horstman, K. C., & Dial Jr, A. L. (1978). Lava flow materials in the Tharsis region of Mars. In *Lunar and Planetary Science Conference Proceedings* (Vol. 9, pp. 3433-3458). https://ui.adsabs.harvard.edu/#abs/1978LPSC....9.3433S/abstract

Schenk, P., Hargitai, H., Wilson, R., McEwen, A., & Thomas, P. (2001). The mountains of Io: Global and geological perspectives from Voyager and Galileo. *Journal of Geophysical Research: Planets*, *106*(E12), 33201–33222. https://doi.org/10.1029/2000JE001408

Schenk, P. M. (1998). Origin of Mountains on Io by Thrust Faulting and Large-Scale Mass Movements. *Science*, *279*(5356), 1514–1517. https://doi.org/10.1126/science.279.5356.1514

Schenk, P. M., Wilson, R. R., & Davies, A. G. (2004). Shield volcano topography and the rheology of lava flows on Io. *Icarus*, *169*(1), 98–110. https://doi.org/10.1016/j.icarus.2004.01.015

Schmeling, H., Marquart, G., & Grebe, M. (2018). A porous flow approach to model thermal non-equilibrium applicable to melt migration. *Geophysical Journal International, 212*(1), 119-138. https://doi.org/10.1093/gji/ggx406

Schools, J., & Montesi, L. (2017). *The Generation Of Barriers To Melt Ascent In The Martian Lithosphere: Melts Calculations* [Data set]. Zenodo. https://doi.org/10.5281/ZENODO.1037653

Schools, J., & Montési, L. G. J. (2018). The Generation of Barriers to Melt Ascent in the Martian Lithosphere. *Journal of Geophysical Research: Planets*, *123*(1), 47–66. https://doi.org/10.1002/2017JE005396

Schultz, R. A., & Lin, J. (2001). Three-dimensional normal faulting models of the Valles Marineris, Mars, and geodynamic implications. *Journal of Geophysical Research: Solid Earth*, *106*(B8), 16549–16566. https://doi.org/10.1029/2001JB000378

Scott, D. R., Stevenson, D. J., & Whitehead, J. A. (1986). Observations of solitary waves in a viscously deformable pipe. *Nature*, *319*(6056), 759–761. https://doi.org/10.1038/319759a0

Self, S., Schmidt, A., & Mather, T. A. (2014). Emplacement characteristics, time scales, and volcanic gas release rates of continental flood basalt eruptions on Earth. In G. Keller & A. C. Kerr, *Volcanism, Impacts, and Mass Extinctions: Causes and Effects*. Geological Society of America. https://doi.org/10.1130/2014.2505(16)

Smith, B. A., Soderblom, L. A., Johnson, T. V., Ingersoll, A. P., Collins, S. A., Shoemaker, E. M., Hunt, G. E., Masursky, H., Carr, M. H., Davies, M. E., Cook, A. F., Boyce, J., Danielson, G. E., Owen, T., Sagan, C., Beebe, R. F., Veverka, J., Strom, R. G., Mccauley, J. F., … Suomi, V. E. (1979). The Jupiter System

Through the Eyes of Voyager 1. *Science*, *204*(4396), 951–972. https://doi.org/10.1126/science.204.4396.951

Smith, P. M., & Asimow, P. D. (2005). Adiabat_1ph: A new public front-end to the MELTS, pMELTS, and pHMELTS models. *Geochemistry, Geophysics, Geosystems*, *6*(2). https://doi.org/10.1029/2004GC000816

Smrekar, S. E. (1997). Corona Formation and Heat Loss on Venus by Coupled Upwelling and Delamination. *Science*, *277*(5330), 1289–1294. https://doi.org/10.1126/science.277.5330.1289

Solomon, S. C., & Head, J. W. (1982). Evolution of the Tharsis Province of Mars: The importance of heterogeneous lithospheric thickness and volcanic construction. *Journal of Geophysical Research*, *87*(B12), 9755. https://doi.org/10.1029/JB087iB12p09755

Solomon, S. C., & Head, J. W. (1990). Heterogeneities in the thickness of the elastic lithosphere of Mars: Constraints on heat flow and internal dynamics. *Journal of Geophysical Research*, *95*(B7), 11073. https://doi.org/10.1029/JB095iB07p11073

Sparks, D. W., & Parmentier, E. M. (1991). Melt extraction from the mantle beneath spreading centers. *Earth and Planetary Science Letters*, *105*(4), 368–377. https://doi.org/10.1016/0012-821X(91)90178-K

Spencer, D. C., Katz, R. F., & Hewitt, I. J. (2020). Magmatic Intrusions Control Io's Crustal Thickness. *Journal of Geophysical Research: Planets*, *125*(6). https://doi.org/10.1029/2020JE006443

Spiegelman, M. (1993). Physics of melt extraction: Theory, implications and applications. *Philosophical Transactions of the Royal Society of London. Series A: Physical and Engineering Sciences*, *342*(1663), 23–41. https://doi.org/10.1098/rsta.1993.0002

Spiegelman, M., Kelemen, P. B., & Aharonov, E. (2001). Causes and consequences of flow organization during melt transport: The reaction infiltration instability in compactible media. *Journal of Geophysical Research: Solid Earth, 106*(B2), 2061-2077. https://doi.org/10.1029/2000JB900240

Spiegelman, M., & Kenyon, P. (1992). The requirements for chemical disequilibrium during magma migration. *Earth and Planetary Science Letters, 109*(3-4), 611-620. https://doi.org/10.1016/0012-821X(92)90119-G

Spohn, T., Hort, M., & Fischer, H. (1988). Numerical simulation of the crystallization of multicomponent melts in thin dikes or sills: 1. The liquidus phase. *Journal of Geophysical Research: Solid Earth*, *93*(B5), 4880–4894. https://doi.org/10.1029/JB093iB05p04880

Stefan, J. (1891). Ueber die Theorie der Eisbildung, insbesondere über die Eisbildung im Polarmeere. *Annalen der Physik*, *278*(2), 269–286. https://doi.org/10.1002/andp.18912780206

Steinke, T., Hu, H., Höning, D., van der Wal, W., & Vermeersen, B. (2020). Tidally induced lateral variations of Io's interior. *Icarus*, *335*, 113299. https://doi.org/10.1016/j.icarus.2019.05.001

Stern, R. J. (2016). Is plate tectonics needed to evolve technological species on exoplanets? *Geoscience Frontiers*, *7*(4), 573–580. https://doi.org/10.1016/j.gsf.2015.12.002

Svensen, H., Corfu, F., Polteau, S., Hammer, Ø., & Planke, S. (2012). Rapid magma emplacement in the Karoo Large Igneous Province. *Earth and Planetary Science Letters*, *325–326*, 1–9. https://doi.org/10.1016/j.epsl.2012.01.015

Tackley, P. (2001). Three-Dimensional Simulations of Mantle Convection in Io. *Icarus*, *149*(1), 79–93. https://doi.org/10.1006/icar.2000.6536

Tanaka, K. L., Robbins, S. J., Fortezzo, C. M., Skinner, J. A., & Hare, T. M. (2014). The digital global geologic map of Mars: Chronostratigraphic ages, topographic and crater morphologic characteristics, and updated resurfacing history. *Planetary and Space Science*, *95*, 11–24. https://doi.org/10.1016/j.pss.2013.03.006

Taylor, G. J. (2013). The bulk composition of Mars. *Geochemistry*, *73*(4), 401–420. https://doi.org/10.1016/j.chemer.2013.09.006

Taylor, N. C., Johnson, J. H., Herd, R. A., & Regan, C. E. (2020). What can Olympus Mons tell us about the Martian lithosphere? *Journal of Volcanology and Geothermal Research*, 106981. https://doi.org/10.1016/j.jvolgeores.2020.106981

Tesauro, M., Kaban, M., Cloetingh, S., Hardebol, N., & Beekman, F. (2007). 3D strength and gravity anomalies of the European lithosphere. *Earth and Planetary Science Letters*, *263*(1–2), 56–73. https://doi.org/10.1016/j.epsl.2007.08.035

Thompson, R. N., Riches, A. J. V., Antoshechkina, P. M., Pearson, D. G., Nowell, G. M., Ottley, C. J., Dickin, A. P., Hards, V. L., Nguno, A.-K., & Niku-Paavola, V. (2007). Origin of CFB Magmatism: Multi-tiered Intracrustal Picrite-Rhyolite Magmatic Plumbing at Spitzkoppe, Western Namibia, during Early Cretaceous Etendeka Magmatism. *Journal of Petrology*, *48*(6), 1119–1154. https://doi.org/10.1093/petrology/egm012

Thybo, H. (2006). The heterogeneous upper mantle low velocity zone. *Tectonophysics, 416*(1-4), 53-79. https://doi.org/10.1016/j.tecto.2005.11.021

Toomey, D., Allen, R., Barclay, A., Bell, S., Bromirski, P., Carlson, R., Chen, X., Collins, J., Dziak, R., Evers, B., Forsyth, D., Gerstoft, P., Hooft, E., Livelybrooks, D., Lodewyk, J., Luther, D., McGuire, J., Schwartz, S., Tolstoy, M., … Wilcock, W. (2014). The Cascadia Initiative: A Sea Change In Seismological Studies of Subduction Zones. *Oceanography*, *27*(2), 138–150. https://doi.org/10.5670/oceanog.2014.49

Turcotte, D. L. (1989). A heat pipe mechanism for volcanism and tectonics on Venus. *Journal of Geophysical Research: Solid Earth*, *94*(B3), 2779–2785. https://doi.org/10.1029/JB094iB03p02779

Turcotte, D., & Schubert, G. (2014). *Geodynamics:* (3rd ed.). Cambridge University Press. https://doi.org/10.1017/CBO9780511843877

Turtle, E. P., Jaeger, W. L., Keszthelyi, L. P., McEwen, A. S., Milazzo, M., Moore, J., Phillips, C. B., Radebaugh, J., Simonelli, D., Chuang, F., & Schuster, P. (2001). Mountains on Io: High-resolution Galileo observations, initial interpretations, and formation models. *Journal of Geophysical Research: Planets*, *106*(E12), 33175–33199. https://doi.org/10.1029/2000JE001354

Turtle, E. P., Jaeger, W. L., & Schenk, P. M. (2007). Ionian mountains and tectonics: Insights into what lies beneath Io's lofty peaks. In Io After Galileo (pp. 109-131). Springer.

Unterborn, C. T., & Panero, W. R. (2019). The Pressure and Temperature Limits of Likely Rocky Exoplanets. *Journal of Geophysical Research: Planets*, *124*(7), 1704–1716. https://doi.org/10.1029/2018JE005844

Usui, T., Alexander, C. M. O., Wang, J., Simon, J. I., & Jones, J. H. (2012). Origin of water and mantle–crust interactions on Mars inferred from hydrogen isotopes and volatile element abundances of olivine-hosted melt inclusions of primitive shergottites. *Earth and Planetary Science Letters*, *357–358*, 119–129. https://doi.org/10.1016/j.epsl.2012.09.008

Valentine, G., & Krogh, K. (2006). Emplacement of shallow dikes and sills beneath a small basaltic volcanic center – The role of pre-existing structure (Paiute Ridge, southern Nevada, USA). *Earth and Planetary Science Letters*, *246*(3–4), 217–230. https://doi.org/10.1016/j.epsl.2006.04.031

Vaucher, J., Baratoux, D., Toplis, M. J., Pinet, P., Mangold, N., & Kurita, K. (2009). The morphologies of volcanic landforms at Central Elysium Planitia: Evidence for recent and fluid lavas on Mars. *Icarus*, *200*(1), 39–51. https://doi.org/10.1016/j.icarus.2008.11.005

Veeder, G. J., Davies, A. G., Matson, D. L., & Johnson, T. V. (2009). Io: Heat flow from dark volcanic fields. *Icarus*, *204*(1), 239–253. https://doi.org/10.1016/j.icarus.2009.06.027

Veeder, G. J., Davies, A. G., Matson, D. L., Johnson, T. V., Williams, D. A., & Radebaugh, J. (2012). Io: Volcanic thermal sources and global heat flow. *Icarus*, *219*(2), 701–722. https://doi.org/10.1016/j.icarus.2012.04.004

Veeder, G. J., Davies, A. G., Matson, D. L., Johnson, T. V., Williams, D. A., & Radebaugh, J. (2015). Io: Heat flow from small volcanic features. *Icarus*, *245*, 379–410. https://doi.org/10.1016/j.icarus.2014.07.028

Veeder, G. J., Davies, A. G., Williams, D. A., Matson, D. L., Johnson, T. V., & Radebaugh, J. (2011). Io: Heat flow from dark paterae. *Icarus*, *212*(1), 236–261. https://doi.org/10.1016/j.icarus.2010.09.026

Veeder, G. J., Matson, D. L., Johnson, T. V., Blaney, D. L., & Goguen, J. D. (1994). Io's heat flow from infrared radiometry: 1983–1993. *Journal of Geophysical Research*, *99*(E8), 17095. https://doi.org/10.1029/94JE00637

Vera, E. E., Mutter, J. C., Buhl, P., Orcutt, J. A., Harding, A. J., Kappus, M. E., Detrick, R. S., & Brocher, T. M. (1990). The structure of 0- to 0.2-m.y.-old oceanic crust at 9°N on the East Pacific Rise from expanded spread profiles. *Journal of Geophysical Research*, *95*(B10), 15529. https://doi.org/10.1029/JB095iB10p15529

von Bargen, N., & Waff, H. S. (1986). Permeabilities, interfacial areas and curvatures of partially molten systems: Results of numerical computations of equilibrium microstructures. *Journal of Geophysical Research*, *91*(B9), 9261. https://doi.org/10.1029/JB091iB09p09261

Vuik, C. (1993) Some historical notes about the Stefan problem. *Nieuw Archief voor Wiskunde, 4e Serie*, *11*, 157-167. http://ta.twi.tudelft.nl/nw/users/vuik/papers/DUT-TWI-93-07.pdf

Wänke, H., & Dreibus, G. (1994). Chemistry and accretion history of Mars. *Philosophical Transactions of the Royal Society of London. Series A: Physical and Engineering Sciences*, *349*(1690), 285–293. https://doi.org/10.1098/rsta.1994.0132

Wanless, V. D., Perfit, M. R., Ridley, W. I., & Klein, E. (2010). Dacite Petrogenesis on Mid-Ocean Ridges: Evidence for Oceanic Crustal Melting and Assimilation. *Journal of Petrology*, *51*(12), 2377–2410. https://doi.org/10.1093/petrology/egq056

Wark, D. A., & Watson, E. B. (1998). Grain-scale permeabilities of texturally equilibrated, monomineralic rocks. *Earth and Planetary Science Letters*, *164*(3–4), 591–605. https://doi.org/10.1016/S0012-821X(98)00252-0

Warner, N. H. (2003). Evolved lavas on Mars? Observations from southwest Arsia Mons and Sabancaya volcano, Peru. *Journal of Geophysical Research*, *108*(E10), 5112. https://doi.org/10.1029/2002JE001969

Weatherley, S. M., & Katz, R. F. (2010). Plate-driven mantle dynamics and global patterns of mid-ocean ridge bathymetry. *Geochemistry, Geophysics, Geosystems*, *11*(10), n/a-n/a. https://doi.org/10.1029/2010GC003192

Werner, S. C. (2009). The global martian volcanic evolutionary history. *Icarus*, *201*(1), 44–68. https://doi.org/10.1016/j.icarus.2008.12.019

White, J. D. L., Bryan, S. E., Ross, P.-S., Self, S., & Thordarson, T. (2009). Physical volcanology of continental large igneous provinces: Update and review. In T. Thordarson, et al. (Eds.), *Studies in Volcanology: The Legacy of George Walker*, Special Publications of IAVCEI (Vol. 2, pp. 291– 321).

Whitehead, J. A. (1988). Fluid Models of Geological Hotspots. *Annual Review of Fluid Mechanics*, *20*(1), 61–87. https://doi.org/10.1146/annurev.fl.20.010188.000425

Wieczorek, M. A., Neumann, G. A., Nimmo, F., Kiefer, W. S., Taylor, G. J., Melosh, H. J., Phillips, R. J., Solomon, S. C., Andrews-Hanna, J. C., Asmar, S. W., Konopliv, A. S., Lemoine, F. G., Smith, D. E., Watkins, M. M., Williams, J. G., & Zuber, M. T. (2013). The Crust of the Moon as Seen by GRAIL. *Science*, *339*(6120), 671–675. https://doi.org/10.1126/science.1231530

Wilkins, S. J., Schultz, R. A., Anderson, R. C., Dohm, J. M., & Dawers, N. H. (2002). Deformation rates from faulting at the Tempe Terra extensional province, Mars. *Geophysical Research Letters*, *29*(18), 31-1-31–34. https://doi.org/10.1029/2002GL015391

Williams, D. A., Greeley, R., Fergason, R. L., Kuzmin, R., McCord, T. B., Combe, J.-P., Head, J. W., Xiao, L., Manfredi, L., Poulet, F., Pinet, P., Baratoux, D., Plaut, J. J., Raitala, J., & Neukum, G. (2009). The Circum-Hellas Volcanic Province, Mars: Overview. *Planetary and Space Science*, *57*(8–9), 895–916. https://doi.org/10.1016/j.pss.2008.08.010

Williams, D. A., & Howell, R. R. (2007). Active volcanism: Effusive eruptions. In *Io After Galileo*, 133-161. Springer, Berlin, Heidelberg.

Wilson, B. M. (2007*). Igneous petrogenesis a global tectonic approach* (2nd ed.). Springer Science & Business Media. https://doi.org/10.1007/978-1-4020-6788-4

Wilson, L., Scott, E. D., & Head, J. W. (2001). Evidence for episodicity in the magma supply to the large Tharsis volcanoes. *Journal of Geophysical Research: Planets*, *106*(E1), 1423–1433. https://doi.org/10.1029/2000JE001280

Wise, D. U., Golombek, M. P., & McGill, G. E. (1979). Tharsis province of Mars: Geologic sequence, geometry, and a deformation mechanism. *Icarus*, *38*(3), 456–472. https://doi.org/10.1016/0019-1035(79)90200-8

Wolf, A. S., & Ghiorso, M. S. (2019). Thermodynamic Modeling Using ENKI: 2. Extending Existing Models. *American Geophysical Union Fall Meeting, 2019*, ED52A-05. https://ui.adsabs.harvard.edu/abs/2019AGUFMED52A..05W/abstract

Wyatt, M. B., & McSween, H. Y. (2002). Spectral evidence for weathered basalt as an alternative to andesite in the northern lowlands of Mars. *Nature*, *417*(6886), 263–266. https://doi.org/10.1038/417263a

Wyatt, M. B., McSween, H. Y., Tanaka, K. L., & Head, J. W. (2004). Global geologic context for rock types and surface alteration on Mars. *Geology*, *32*(8), 645. https://doi.org/10.1130/G20527.1

Xiao, L., Huang, J., Christensen, P. R., Greeley, R., Williams, D. A., Zhao, J., & He, Q. (2012). Ancient volcanism and its implication for thermal evolution of Mars. *Earth and Planetary Science Letters*, *323–324*, 9–18. https://doi.org/10.1016/j.epsl.2012.01.027

Zhu, W., Gaetani, G. A., Fusseis, F., Montesi, L. G. J., & De Carlo, F. (2011). Microtomography of Partially Molten Rocks: Three-Dimensional Melt Distribution in Mantle Peridotite. *Science*, *332*(6025), 88–91. https://doi.org/10.1126/science.1202221

Zhu, Wenlu, & Hirth, G. (2003). A network model for permeability in partially molten rocks. *Earth and Planetary Science Letters*, *212*(3–4), 407–416. https://doi.org/10.1016/S0012-821X(03)00264-4

Zimbelman, J. R. (1985). Estimates of rheologic properties for flows on the Martian volcano Ascraeus Mons. *Journal of Geophysical Research*, *90*(S01), 157. https://doi.org/10.1029/JB090iS01p00157

Zimbelman, J. R. (1998). Emplacement of long lava flows on planetary surfaces. *Journal of Geophysical Research: Solid Earth*, *103*(B11), 27503–27516. https://doi.org/10.1029/98JB01123

Zimbelman, J. R., & Edgett, K. S. (1992). The Tharsis Montes, Mars: Comparison of volcanic and modified landforms. *In Proceedings of Lunar and Planetary Science, volume 22*. Lunar and Planetary Institute. https://hdl.handle.net/20.500.11753/1563

Zolotov, M. Yu., & Fegley, B. (1999). Oxidation State of Volcanic Gases and the Interior of Io. *Icarus*, *141*(1), 40–52. https://doi.org/10.1006/icar.1999.6164

Zuber, M. T., Smith, D. E., Watkins, M. M., Asmar, S. W., Konopliv, A. S., Lemoine, F. G., Melosh, H. J., Neumann, G. A., Phillips, R. J., Solomon, S. C., Wieczorek, M. A., Williams, J. G., Goossens, S. J., Kruizinga, G., Mazarico, E., Park, R. S., & Yuan, D.-N. (2013). Gravity Field of the Moon from the Gravity Recovery and Interior Laboratory (GRAIL) Mission. *Science*, *339*(6120), 668–671. https://doi.org/10.1126/science.1231507

Zuber, Maria T. (1995). Wrinkle Ridges, Reverse Faulting, and the Depth Penetration of Lithospheric Strain in Lunae Planum, Mars. *Icarus*, *114*(1), 80–92. https://doi.org/10.1006/icar.1995.1045